Università degli Studi di Pavia

Doctoral Thesis

Control Applications in the Context of Industry 4.0

Author:
Giacomo Galuppini

Supervisor:
Prof. Lalo Magni

PhD in Electronic, Computer and Electric Engineering

Identification and Control of Dynamic Systems Laboratory
Department of Industrial and Information Engineering

UNIVERSITÀ DEGLI STUDI DI PAVIA

Abstract

Faculty of di Engineering
Department of Industrial and Information Engineering

PhD in Electronic, Computer and Electric Engineering

Control Applications in the Context of Industry 4.0

by Giacomo GALUPPINI

The Industry 4.0 approach represents the driving force behind the current industrial research and development activities. The spread of smart sensors and actuators, tightly connected in the Industrial Internet of Things, offers a wide range of possibilities for the application of control methodologies to tackle very different control problems. In addition, the huge amount of data captured by sensors can be exploited to develop and validate very accurate models of the processes under control, thus allowing to perform preliminary studies in a simulated environment and move to the real plant only when the control approach is sufficiently consolidated.

In this framework, this Thesis faces three different control problems with the application of various control methodologies. In particular, a Proportional-Intergral-Derivative is adopted to perform fine regulation of magnetic field in Fast Field Cycling Nuclear Magnetic Resonance experiments, with a closed-loop based on an ad-hoc virtual sensor for magnetic field measurements. Both the design of the virtual sensor and the synthesis of the regulator are studied in simulation first, then successfully applied to the real plant.

The second task faced in this work is service pressure regulation in Water Distribution Networks. Different control algorithms (frequency domain and optimal control) are developed and tested in a simulated environment to investigate how to take advantage of the improved communication capabilities made available by *wired* networks, where pressure sensors and control valves are connected by wire to a digital control unit.

Finally, the last application faced in this Thesis is related to smart warehousing, and deals with the control of mechanical systems with actuators affected by deadzone nonlinerity. In particular, two different Model Predictive Control approaches are tested both in simulation and on a laboratory scale version of an overhead travelling crane, with the aim of assessing their performances in term of accuracy, robustness and computational honour.

The results obtained in the above case studies stresses how the application of consolidated control methodologies, available from control theory, allows to successfully face the new challenges that arise by the Industry 4.0 context.

Contents

1 Introduction 3

I Model Based Design of a Field Frequency Lock System for Nuclear Magnetic Resonance Applications 5

2 Introduction 7

3 Basics of NMR 9
- 3.1 Spin and Energy Levels . . . 9
- 3.2 NMR Hardware . . . 14
- 3.3 NMR Continuous Wave Spectroscopy . . . 15
- 3.4 Spin Physics: a Classical Interpretation . . . 15
- 3.5 The Vector Model and Pulsed NMR . . . 17
  - 3.5.1 Pulsed NMR . . . 19
  - 3.5.2 Continuous Wave Versus Pulsed NMR . . . 19
- 3.6 The NMR Spectrum . . . 21
  - 3.6.1 Dipolar Magnetic Interaction . . . 21
  - 3.6.2 Effect of Molecular Motion . . . 22
  - 3.6.3 Effect of Non Homogeneous Field . . . 23

4 Relaxometry 25
- 4.1 Spin-Lattice Relaxation . . . 25
  - 4.1.1 Origins of Spin-Lattice Relaxation and Relation to Molecular Motions . . . 27
- 4.2 Spin-Spin Relaxation . . . 28
  - 4.2.1 Origins of Spin-Spin Relaxation and Relation to Molecular Motions . . . 29
- 4.3 Measuring the Relaxation Time Constants . . . 30
  - 4.3.1 Pulse calibration: the Angle sequence . . . 30
  - 4.3.2 Measuring T1: the Inversion-Recovery Sequence . . . 30
  - 4.3.3 Measuring T2: The Carr-Purcell-Meiboom-Gill (CPMG) Sequence 31
- 4.4 An Introduction to Fast Field Cycling NMR . . . 32

5 Non-Homogeneous Magnetic Field, Echoes and Steady State Free Precession 37
- 5.1 Magnetic Field Inhomogeneity and Echo . . . 37
- 5.2 Steady State Free Precession . . . 40

6 The NMR Field Frequency Lock 43
- 6.1 NMR Lock . . . 43
- 6.2 Locking the FFC-NMR . . . 45
- 6.3 Lock Pulse Sequencies . . . 45

6.3.1 Low Repetition Rate (LRR) Lock Pulses 47
6.3.2 High Repetition Rate (HRR) Lock Pulses 47

7 NMR Hardware and Firmware 49
7.1 Probe and Transmitter/Receiver 49
7.2 Magnets 49
7.2.1 Superconducting Magnet 50
7.2.2 Permanent Magnet 51
7.2.3 IDentIFY Magnet Prototype 51
7.3 Signal Detection 52
7.3.1 Phase Sensitive Detection 52
7.3.2 Quadrature Detection 53
7.4 Acquisition Chain Digital Implementation 55

8 Models for NMR Steady State Free Precession 57
8.1 An (Only Apparent) Contradiction 57
8.2 Bloch Equations 57
8.3 Discrete Time Nonlinear Model for Bulk Magnetization 60
8.3.1 Linearised Model 62
8.4 Static Steady State Model and Linear Region 62
8.5 Model Comparison: Simulated Step Response 64
8.5.1 Discrete time Non Linear Model and Linearised Model 65
8.5.2 Bloch Equations and Discrete time Non Linear Model 67
8.6 Model Validation 71
8.7 Bloch-Based Isochromat Model 72
8.7.1 Model Validation 74

9 Closed-Loop Design 79
9.1 Synthesis of the Regulator 80

10 Experimental trials 83
10.1 NMR Lock Setup 83
10.2 NMR Sensor Models 84
10.2.1 Silicone 84
10.2.2 Copper Sulphate 86
10.3 Process Model 87
10.4 Experimental Validation Trials 88
10.4.1 Silicone 88
10.4.2 Copper Sulphate 89
10.5 Synthesis of the Regulator 89
10.5.1 Silicone 90
10.5.2 Copper sulphate 91
10.6 Closed-loop Trials 91
10.6.1 Silicone 91
10.6.2 Copper Sulphate 92
10.7 Effect of Lock System on the Main NMR Experiment 93

11 Conclusion and Future Work 97

II Service Pressure Regulation in Water Distribution Newtorks 99

12 Introduction 101

13 Basics of Hydrodynamics 103
13.1 Fluid Motion . . . 103
13.2 The Continuity Equation . . . 104
13.3 The Energy Conservation Principle . . . 105
13.4 Total Head Line and Piezometric Line . . . 106

14 Elastic Unsteady Flow 109
14.1 Elastic Unsteady Flow Equations . . . 111
14.1.1 Method of Characteristics . . . 111
14.2 Integration of Unsteady Flow Equations . . . 112

15 Case Studies and Numerical Model for Plant Simulations 115
15.1 Numerical Model for Plant Simulations . . . 117

16 Pressure Control Strategies Based on Dynamic Models 119
16.1 Working Points . . . 119
16.2 Dynamic Models . . . 121
16.3 Control . . . 125
16.4 PI Regulators . . . 127
16.5 Filtered PI Regulators and Smith Predictor . . . 132
16.6 Linear Quadratic Gaussian Control . . . 136
16.7 Linear Quadratic Gaussian Control with Shaping Functions . . . 139

17 Stability Analysis and PI Design Based on Higer Order Models 143
17.1 PI Gain Design Based on Higher Order Models . . . 143
17.2 Improving Robustness and Cost of Control with FPI-SP RTC Algorithms 149
17.2.1 Stability Analysis of FPI-SP RTC Algorithm . . . 150
17.2.2 Cost of Control of FPI-SP RTC Algorithm . . . 151
17.3 Water Distribution Network . . . 151
17.3.1 Stability and Robustness Analysis . . . 152
17.4 Discussion of Results . . . 155

18 Discussion of Results and Future Work 157
18.1 Pressure Control Strategy Based on Steady State Models . . . 157
18.2 Analysis of Performances . . . 158

III Model Predictive Control of a Laboratory Scale Overhead Travelling Crane Affected by Deadzone Nonlinearity 163

19 Introduction 165

20 Plant Description and Model Identification 167
20.1 Deadzone . . . 168
20.2 Saturation . . . 168
20.3 DC Motor . . . 169

21 MPC General Framework **173**
21.1 Multiparametric Programming and Explicit MPC 174
21.1.1 Multiparametric Programming 174
21.1.2 Explicit MPC 175
21.1.3 Explicit Hybrid MPC 175
21.2 Kalman Filter and Speed Estimation 176

22 Simulations and Experiments **177**
22.1 Hybrid MPC Controller 177
22.1.1 Problem Formulation 177
22.1.2 Simulations 179
22.2 MPC with Equivalent Saturation 179
22.2.1 Problem Formulation 180
22.2.2 Simulations 181
22.3 Robustness with Respect to Deadzone Model Uncertainties 181
22.3.1 Hybrid MPC 182
22.3.2 Equivalent Saturation MPC 182
22.3.3 Comparison and Remarks 183
22.4 Experimental Results 183
22.4.1 Hybrid MPC 184
22.4.2 Equivalent Saturation MPC 185

23 Conclusions and Future Work **187**

24 Conclusion **191**

Bibliography **193**

List of Figures

3.1 The nucleus as a spinning charged particle carries an angular momentum L and a magnetic momentum μ 10
3.2 A nucleus in a magnetic field has a potential energy W which depends on the angle θ. 10
3.3 The *spin up* and *spin down* states of a nucleus in a constant magnetic field. 11
3.4 Energy gap between two consecutive energy levels. 11
3.5 Boltzmann's distribution of spin populations as function of the absolute temperature. Note that near room temperatures (300 $°K$) the number of low and high energy particles is nearly equal. 12
3.6 a) A nucleus moves to the upper energy level when absorbing an energy quantum b) As a consequence of the application of a quantum of energy, a nucleus falls to the lower energy state and releases another quantum of energy. 13
3.7 At thermal equilibrium the lowest energy state is the more populated, therefore the number of absorbed energy quanta is higher than that of emitted ones. The consequence is an overall Absorption of energy. . . 14
3.8 The oscillating magnetic field B_{RF} can be interpreted as the superposition of the counter rotating fields B_1' and B_1''. 16
3.9 The oscillating magnetic field B_{RF} can be interpreted as the superposition of the counter rotating fields B_1' and B_1''. 16
3.10 When the rotating magnetic field and the precessing nucleus run at the same angular speed it is possible to change the precession angle of the nucleus. 17
3.11 In a rotating reference frame $x'y'z'$ with the same angular speed of vector $\mathbf{M}$, the latter remains still. 18
3.12 Motion of the bulk magnetization $\mathbf{M}$ in the rotating frame $x'y'z'$ when the rotating magnetic field is applied. 18
3.13 The *Free Induction Decay* (FID) signal collected in the xy plane. 19
3.14 The M_x and M_y FIDs can be considered as the product of a cosine or sine wave for an exponential decay with constant $T2$. Some noise $n(t)$ is present as well in this example. The Fourier transform of the x FID gives a Lorentzian peak in for the absorption spectrum, while the Fourier transform of the y FID generates the dispersion spectrum. The same result can be interpreted as the convolution of the Fourier transforms of the sin and cos waves, which are deltas placed at the resonance frequency, with the complex Fourier transform of the exponential, which defines the shape for the absorption and dispersion spectra. 20

3.15 Example of local fields are generated by the nuclei which carry a dipole magnetic momentum. Flux lines show how the local fields change the effective value of B_0 seen by each nucleus. In particular a) shows the local field generated by nucleus 1 acting on nucleus 2 (b_{21}) while b) shows the local field generated by nucleus 2 acting on nucleus 1 (b_{12}). . . 21
3.16 Origin of the spectral widening due to magnetic dipolar interaction between nuclei. 22
3.17 The shape of the spectrum is the result of the interactions of many nuclei in the sample. 22
3.18 Absorption spectrum for protons in water as ice b) Absorption spectrum for protons in water as liquid. 23

4.1 When a nucleus moves from one energy level to the other one, both populations change their value. 26
4.2 The Spin-Lattice relaxation described as the change of spin populations. The rate of transition is proportional to the deviation of population from its equilibrium value. 26
4.3 (a) The process of longitudinal relaxation shows a time behaviour described by an exponential of time constant $T1$. (b) The process of transverse relaxation shows a time behaviour described by a decaying exponential of time constant $T2$ in the rotating reference frame. . . 27
4.4 Transverse time constant ($T2$) profile in red and longitudinal time constant ($T1$) profile in blue as function of the correlation frequency of molecular motion in log-log scale. 28
4.5 a) When all the contributions share the same phase angle, coherence is obtained and M_{xy} reaches its maximum value. b) When a preferred phase angle exists, coherence is generated and a non-zero value of M_{xy} can be measured. c) When individual contributions show a random phase distribution, no coherence is generated and the resulting M_{xy} is null. d) Individual contributions brought by each spin sum up into M_{xy}. 29
4.6 The Angle sequence consists of a series of increasing duration pulses. The signal generated in such a way gets its maximum value when the duration of the corresponding pulse completely brings the magnetization to the transverse plane. When no signal is collected the magnetization is expected to be aligned to the ˘z' direction, hence the corresponding pulse is a 180° one. 31
4.7 The Inversion-Recovery sequence is a couple of $180° - 90°$ pulses spaced τ seconds. 32
4.8 Time evolution of M_z during an Inversion-Recovery sequence. 33
4.9 The CPMG sequence is a couple of $90° - 180°$ pulses spaced τ seconds. After another τ seconds an echo signal is collected. 33
4.10 Time evolution of the bulk magnetization vector **M** during a *CPMG* sequence. Note how the different components of **M** rotate at different angular speeds in the rotating frame and how thay refocus after the application of the 180° pulse. 34
4.11 A complete CPMG execution. Notice that each single FID has time constant $T2^*$, while the overall signal envelope has time constant $T2$. . 35
4.12 The magnetic field evolution during a basic FFC-NMR experiment. . . 35

5.1 A Lorentzian shaped NMR spectrum where the *Full Witdh at Half Maximum* is indicated as Γ. . . . 38
5.2 The *spin-echo* following a pair of pulses. . . . 38
5.3 Evolution of four isochromats in the rotating reference frame as the consequence of a couple of 90° pulses [18]. . . . 39
5.4 Evolution of four isochromats in the rotating reference frame as the consequence of three consecutive 90° pulses [18]. . . . 39
5.5 The steady-state condition of both the longitudinal and transverse components of the magnetization obtained with a train of evenly spaced pulses. . . . 40
5.6 With evenly spaced pulses spin echoes and stimulated echoes grow and reach a maximum in correspondence of the arrival of a new pulse. 40
5.7 The Steady State Free Precession regime of the magnetization occurs when the repetition time is shorter than the decay of FID signal. This means that the signal never dies and echoes sum up with the residual signal. . . . 41

6.1 Precession of the bulk magnetization vector in the rotating reference frame $x'y'z'$. . . . 44
6.2 The dispersion spectrum as function of the frequency deviation from the receiver one. . . . 45
6.3 Sequence of Low Repetition Rate pulses with repetition time T. These are typically 90° pulses and generate a complete FID signal. . . . 46
6.4 A Phase-Locked Loop approach for the FFL system. The PSD compares the frequency of the FID signal to the reference one and outputs the error signal that is proportional to the frequency deviation. Then the controller generates a field correction on the basis of the error signal. 46
6.5 Sequence of High Repetition Rate pulses with repetition time $T << T1, T2$. The low power pulses allow reaching a steady state condition where the signal is not decaying anymore. . . . 47

7.1 The tuned circuit in the probe is composed of an inductance (the coil used for generating the pulses) and two capacitors (match and tune) . 50
7.2 Block scheme for a quadrature detector: the signal coming from the probe is multiplied by a cosinusoidal reference on the real path and then filtered. On the imaginary path the incoming signal is multiplied by a sinusoidal reference and then it is passed through the low pass filter. This allows to obtain the real and imaginary signals. . . . 53
7.3 Absorption and dispersion mode spectra. . . . 54
7.4 (A) Complex Fourier Transform of M'_x. (B) Complex Fourier Transform of M'_y. . . . 55
7.5 Absorption and dispersion mode spectra. The sum the real part of the real channel and the imaginary part of the imaginary channel allows to obtain the abosrption mode spectrum correctly setup to distinguish among positive and negative frequencies. The difference if the imaginary part of the real channel from the real part of the imaginary channel allows to build up the dispersion mode spectrum correctly placed in frequency. . . . 55

7.6 The acquisition chain. The incoming signal is digitized by means of a 12 *bit* ADC with sampling frequency f_s of 400 MHz. Then the digital signal goes through the quadrature detector. Notice that the two low pass filters also introduce a decimation factor R. In the end signals (Real, Imaginary, Module, Phase) are sent to a DAC. 56

8.1 HRR pulse sequence used for the DNLM. Pulses are spaced T instants. The k-th pulse starts at time t_k and lasts t_w instants. It rotates $\mathbf{M}$ of an angle θ. 60
8.2 The xyz rotating reference frame. Each RF pulse rotates M of an angle θ. The field deviation generates a drift in the xy plane indicated as ϕ. . 61
8.3 Plot of the curve relating the y component of the transverse magnetization at steady state to the magnetic field deviation. Note that the shape of the curve is that of a dispersion mode profile. 64
8.4 *Simulation 1*. Step response comparison for DNLM (blue, solid line) and LM (red, dashed line). 66
8.5 *Simulation 2*. Step response comparison for DNLM (blue, solid line) and LM (red, dashed line). 66
8.6 *Simulation 3*. Step response comparison for DNLM (blue, solid line) and LM (red, dashed line). 66
8.7 *Simulation 1*. Step response comparison for BE (blue, solid line) and DNLM (red, dashed line). 68
8.8 *Simulation 2*. Step response comparison for BE (blue, solid line) and DNLM (red, dashed line). 68
8.9 *Simulation 2*. Detail: DNLM does not take into account inter-pulse oscillations of the transverse magnetisation. 69
8.10 *Simulation 3*. Step response comparison for BE (blue, solid line) and DNLM (red, dashed line). 69
8.11 *Simulation 4*. Step response comparison for BE (blue, solid line) and DNLM (red, dashed line). 69
8.12 *Simulation 5*. Step response comparison for BE (blue, solid line) and DNLM (red, dashed line). 70
8.13 *Simulation 6*. Step response comparison for BE (blue, solid line) and DNLM (red, dashed line). 70
8.14 *Simulation 6*. Detail: when the strongest simulated disturbance acts on the system, both BE and DNLM oscillate around a steady state value. As expected, not all oscillations are present in the discrete time version. 70
8.15 Graphical interpretation of isochromat decomposition used in BBIM. . 73
8.16 Simulation 1 (a) and Simulation 2 (b). $BBIM$ simulations show the effect of field inhomogeneity on the SSFP of the virtual sample. The sensitivity to the field deviation and the width of the linear region are both affected. 74
8.17 Normalized Lorentzian distributions of the isochromats in a strongly homogeneous field (a) and in a non-homogeneous field (b). 74
8.18 Trial 1.2. Behaviour of the transverse magnetization $M_y(t)$ in real experiment (a) and in the $BBIM$ simulated one (b). 75
8.19 Trial 2.2. Behaviour of the transverse magnetization $M_y(t)$ in real experiment (a) and in the $BBIM$ simulated one (b). 75

9.1 Block scheme with transfer function for the FFL. $u(t)$ is the voltage control action, $u_{sat}(t)$ is the saturated voltage control action, $\Delta I^*(t)$ is the current control action. $\Delta I(t)$ is the overall current deviation from the resonance condition; it is the sum of the current from the power supply, $\Delta I_{ps}(t)$, and the current disturbance $\Delta I_d(t)$; $\Delta B(t)$ is the overall field deviation seen by the NMR sample; it is the sum of the field deviation from the magnet, $\Delta B_{mag}(t)$, and the field disturbance $\Delta B_d(t)$; $M_y(t)$ is the y component of the transverse magnetization in the rotating frame, $\tilde{M}_y(t)$ is its low-pass filtered version; $N(t)$ is measurement noise; $e(t)$ is the error signal feeding the regulator. . . 79

10.1 Silicone sample. Input-output data for CLS identification of the transfer function model. Top: $M_y(t)$ step response data from BBIM model and filtered data. Bottom: magnetic field deviation $\Delta B(t)$. 84
10.2 Silicone sample. Comparison of identification data $M_y(t)$ and transfer function model prediction $\hat{M}_y(t)$. 85
10.3 Silicone sample. Detail of input-output data for CLS identification of the transfer function model. 85
10.4 Copper sulphate sample. Input-output data for CLS identification of the transfer function model. Top: $M_y(t)$ step response data from BBIM model and filtered data. Bottom: magnetic field deviation $\Delta B(t)$. 86
10.5 Comparison of identification data $M_y(t)$ and transfer function model prediction $\hat{M}_y(t)$. 86
10.6 Silicone sample. (A) Experimental Input-output data for identification of the process model. Top: $M_y(t)$ step response data. Bottom: voltage control action $u(t)$. (B) Comparison of experimental identification data $M_y(t)$ and process model prediction $\hat{M}_y(t)$. 88
10.7 Copper sulphate sample. (A) Experimental Input-output data for identification of the process model. Top: $M_y(t)$ step response data. Bottom: voltage control action $u(t)$. (B) Comparison of experimental identification data $M_y(t)$ and process model prediction $\hat{M}_y(t)$. 89
10.8 Loop functions $L(s)$ in case of silicone sample (solid, blue line), and of copper sulphate sample (dashed, red line). 90
10.9 Silicone sample. Closed-loop response to a current step disturbance. Top: feedback signal $M_y(t)$ Bottom: voltage control action $u(t)$. 92
10.10 Silicone sample. Open-loop (A) and closed-loop (B) response to a 1 Hz sinusoidal disturbance. Top: feedback signal $M_y(t)$ Bottom: voltage control action $u(t)$. 92
10.11 Silicone sample. Open-loop (A) and closed-loop (B) response to a 10 Hz sinusoidal disturbance. Top: feedback signal $M_y(t)$ Bottom: voltage control action $u(t)$. 93
10.12 Copper sulphate sample. Closed-loop response to a current step disturbance. Top: feedback signal $M_y(t)$ Bottom: voltage control action $u(t)$. 93
10.13 Copper sulphate sample. Open-loop (A) and closed-loop (B) response to a 10 Hz sinusoidal disturbance. Top: feedback signal $M_y(t)$ Bottom: voltage control action $u(t)$. 94
10.14 Copper sulphate sample. Open-loop (A) and closed-loop (B) response to a 50 Hz sinusoidal disturbance. Top: feedback signal $M_y(t)$ Bottom: voltage control action $u(t)$. 94

10.15 Copper sulphate sample. Open-loop (A) and closed-loop (B) response to a 100 Hz sinusoidal disturbance. Top: feedback signal $M_y(t)$ Bottom: voltage control action $u(t)$. 95
10.16 Copper sulphate sample. Main NMR experiment without lock system (A) and with lock system (B), in presence of a 10 Hz sinusoidal disturbance. 95
10.17 Copper sulphate sample. Main NMR experiment without lock system (A) and with lock system (B), in presence of a 50 Hz sinusoidal disturbance. 96

13.1 A flow line is tangent to the velocity vector in each point P of the flow field. 103
13.2 A flow tube example: black lines represent the closed curve, blue lines are flux lines. 104
13.3 Pipe with variable cross section. 104
13.4 Pipe with variable cross section. 105
13.5 Graphical representation of Bernoulli equation for an ideal fluid. 106
13.6 Graphical representation of Bernoulli equation for a real fluid. 107

14.1 Conceptual example of the water hammer effect. 110
14.2 Representation of characteristic lines for the integrated equations of elastic unsteady flow, applied to a pipe of length L. 113

15.1 Case Study A: topology of the water distribution system. 115
15.2 Case Study A: demand profile. 116
15.3 Case Study B: topology of the WDN 116
15.4 Case Study B: (A) Demand profiles. (B) Source pressure head profile. . 117

16.1 Case Study A: identification data. Top: pressure variation $\delta h(t)$. Bottom: valve variation $\delta\alpha(t)$. 121
16.2 Case Study A: comparison of model and system output with identification data. 122
16.3 Case Study A: comparison of model and system output with validation data. 122
16.4 The local loss coefficient ξ as function of the valve closure α and the straight line tangent to the curve in the working point. 123
16.5 Absolute value of the gain of the linearised system μ_a as function of the flow Q. 123
16.6 Identification data for Case Study B. Top: pressure variation $\delta h(t)$. Bottom: valve variation $\delta\alpha(t)$. 124
16.7 Case Study B: Comparison of model and system output with identification data. 124
16.8 Case Study B: Comparison of model and system output with validation data. 125
16.9 SISO system for control purposes. 125
16.10 Antiwindup control scheme for PI regulators. 126
16.11 Case Study A: design of loop functions for PI_{na}, PI and FPI regulators. 129
16.12 Case Study A: closed-loop simulation with PI_{na} and demand offset -0.03 m^3/s. Top: pressure $h(t)$ and pressure setpoint h_{sp}. Middle: demand $D(t)$. Bottom: valve closure $\alpha(t)$. 129

16.13 Case Study A: closed-loop simulation with PI algorithm. Top: pressure $h(t)$ and pressure setpoint h_{sp}. Middle: demand $D(t)$. Bottom: valve closure $\alpha(t)$. 130
16.14 Case Study A: closed-loop simulation with PI algorithm and opening of a fire hydrant. Top: pressure $h(t)$ and pressure setpoint h_{sp}. Middle: demand $D(t)$. Bottom: valve closure $\alpha(t)$. 130
16.15 Case Study B: design of loop functions for PI and FPI regulators. . . . 131
16.16 Case Study B: closed-loop simulation with PI algorithm and demand profile A. Top: pressure $h(t)$ and pressure setpoint h_{sp}. Middle: demand $D(t)$. Bottom: valve closure $\alpha(t)$. 132
16.17 Case Study B: closed-loop simulation with PI algorithm and demand profile B. Top: pressure $h(t)$ and pressure setpoint h_{sp}. Middle: demand $D(t)$. Bottom: valve closure $\alpha(t)$. 132
16.18 Control scheme with Smith Predictor. 133
16.19 Antiwindup control scheme for FPI regulators with Smith Predictor. . 133
16.20 Case Study A: closed-loop simulation with FPI algorithm and opening of a fire hydrant. Top: pressure $h(t)$ and pressure setpoint h_{sp}. Middle: demand $D(t)$. Bottom: valve closure $\alpha(t)$. 134
16.21 Control scheme for the LQG regulator, featuring integral action and Smith Predictor 136
16.22 Case Study A: closed-loop simulation with $ILQG$ algorithm and opening of a fire hydrant. Top: pressure $h(t)$ and pressure setpoint h_{sp}. Middle: demand $D(t)$. Bottom: valve closure $\alpha(t)$. 138
16.23 Control scheme for LQG control with disturbances prefiltering. 139
16.24 Shaping functions used for disturbances prefiltering. 140
16.25 Case Study A: closed-loop simulation with $ILQG - SF$ algorithm and opening of a fire hydrant. Top: pressure $h(t)$ and pressure setpoint h_{sp}. Middle: demand $D(t)$. Bottom: valve closure $\alpha(t)$. 140

17.1 Step response identification data and model prediction. Top: measured (solid, blue line) and predicted (magenta, dashed line) pressure variation $\delta h(t)$. Bottom: valve variation $\delta\alpha(t)$. 145
17.2 Left: Bode diagram of $G_{ah}(s)$. Right, blue solid line: Bode diagram of $L(s)$ with PI_{na} algorithm. Right, red dashed line: Bode diagram of $L(s)$ with PI algorithm. 145
17.3 Step response identification data and model prediction from $\tilde{G}_{ah}(s)$. Top: measured (solid, blue line) and predicted (magenta, dashed line) pressure variation $\delta h(t)$. Bottom: valve variation $\delta\alpha(t)$. 146
17.4 Left: Bode diagram of $\tilde{G}_{ah}(s)$. Right, blue solid line: Bode diagram of $\tilde{L}(s)$ with PI_{na} algorithm. Right, red dashed line: Bode diagram of $\tilde{L}(s)$ with PI algorithm. 146
17.5 Step response identification data and model prediction from $\tilde{G}_{ah}^{lf}(s)$. Top: measured (solid, blue line) and predicted (magenta, dashed line) pressure variation $\delta h(t)$. Bottom: valve variation $\delta\alpha(t)$. 147
17.6 Left: Bode diagram of $\tilde{G}_{ah}^{lf}(s)$. Right, blue solid line: Bode diagram of $\tilde{L}^{lf}(s)$ with PI_{na} algorithm. Right, red dashed line: Bode diagram of $\tilde{L}^{lf}(s)$ with PI algorithm. 147
17.7 Nyquist diagrams of $\tilde{L}^{lf}(s)$. Left: PI_{na} algorithm. Centre: PI algorithm. Right: $FPI - SP$ algorithm. 148

17.8 Closed-loop simulation with $PIna$ (blue, solid line) and $FPI - SP$ (orange, dashed line) algorithms. Top: pressure $h(t)$ and pressure setpoint h_{sp}. Middle: demand $D(t)$. Bottom: valve closure $\alpha(t)$. 149
17.9 Control sensitivity functions for the $PIna$ (solid, blue line) and $FPI - SP$ (red, dashed line) algorithms. 149
17.10 Left: Bode diagram of $G_{ah}(s)$. Right, blue solid line: Bode diagram of $L(s)$ with PI_{na} algorithm. Right, red dashed line: Bode diagram of $L(s)$ with $FPI - SP$ algorithm. 150
17.11 Left: Bode diagram of $\tilde{G}_{ah}^{lf}(s)$. Right, blue solid line: Bode diagram of $\tilde{L}^{lf}(s)$ with PI_{na} algorithm. Right, red dashed line: Bode diagram of $\tilde{L}^{lf}(s)$ with $FPI - SP$ algorithm. 150
17.12 Step response identification data and model prediction from $\tilde{G}_{ah}(s)$. Top: measured (solid, blue line) and predicted (magenta, dashed line) pressure variation $\delta h(t)$. Bottom: valve variation $\delta\alpha(t)$. 152
17.13 Left: Bode diagram of $\tilde{G}_{ah}(s)$. Right, blue solid line: Bode diagram of $\tilde{L}(s)$ with a PI algorithm. Right, red dashed line: Bode diagram of $\tilde{L}(s)$ with a FPI-SP algorithm. 152
17.14 WDN: (a) Nyquist diagrams of $\tilde{L}(s)$. Left: PI algorithm. Right FPI-SP algorithm. (b) Nyquist diagrams of $\tilde{L}^{hf}(s)$. Left: PI algorithm. Right FPI-SP algorithm. 153
17.15 WDN: Step response identification data and model prediction from $\tilde{G}_{ah}^{hf}(s)$. Top: measured (solid, blue line) and predicted (magenta, dashed line) pressure variation $\delta h(t)$. Bottom: valve variation $\delta\alpha(t)$. . 154
17.16 WDN: Left: Bode diagram of $\tilde{G}_{ah}^{hf}(s)$. Right, blue solid line: Bode diagram of $\tilde{L}^{hf}(s)$ with a PI algorithm. Right, red dashed line: Bode diagram of $\tilde{L}^{hf}(s)$ with a $FPI - SP$ algorithm. 154
17.17 WDN: Closed-loop simulation with PI (blue, solid line) and $FPI - SP$ (orange, dashed line) algorithms. Top: pressure $h(t)$ and pressure setpoint h_{sp}. Middle: flow discharge at the valve site $Q(t)$. Bottom: valve closure $\alpha(t)$. 155

18.1 Case Study A: closed-loop simulation with $P\ on\ \xi$ algorithm and opening of a fire hydrant. Top: pressure $h(t)$ and pressure setpoint h_{sp}. Middle: demand $D(t)$. Bottom: valve closure $\alpha(t)$. 158
18.2 Case Study A: regulation error as function of the demand offset. 160
18.3 Case Study A: cost of control as function of the demand offset. 160

19.1 The laboratory scale overhead travelling crane used for experiments. . 166

20.1 System response to a sinusoidal input. 168
20.2 Left: a generic deadzone acting on signal $u(t)$. Right: a generic saturation acting on signal $u(t)$. 169
20.3 Block scheme for the the actuator. Signals in the scheme: $u(t)$ is a generic voltage input to the actuator; $u_{sat}(t)$ is the saturated voltage input; $u_{dz}(t)$ is the voltage input after the deadzone; $v(t)$ is the speed; $p(t)$ is the position. Note that mixed notation is used. 169
20.4 Conceptual block scheme for grey-box identification. 170
20.5 Validation of $G(s)$. The dashed, red line is the real position from the Plant, the solid, blue line is the predicted position from $G(s)$. 171

22.1 A generic deadzone acting on signal $u(k)$ as a piecewise-affine function associated to logical conditions. 178
22.2 Block scheme for Hybrid MPC approach. 178
22.3 Hybrid MPC. Above: plot of simulated position $p(t)$. Below: plot of simulated MPC control action $u_{mpc}(t)$. 179
22.4 Left: inverse deadzone applied to a generic signal $u(t)$. Right: equivalence of signals $u_{es}(t)$ and $u_{dz}(t)$. 179
22.5 Block scheme for ES MPC approach. 180
22.6 ES MPC. Above: plot of simulated position $p(t)$. Below: plot of simulated control action $u_{id}(t)$. 181
22.7 Hybrid MPC with uncertain deadzone. Above: plot of simulated position $p(t)$. Below: plot of simulated MPC control action $u_{mpc}(t)$. 182
22.8 ES MPC with uncertain deadzone. Above: plot of simulated position $p(t)$. Below: plot of simulated control action $u_{id}(t)$. 182
22.9 ES MPC with uncertain deadzone (re-tuning). Above: plot of simulated position $p(t)$. Below: plot of simulated control action $u_{id}(t)$. 183
22.10 Hybrid MPC real experiments. Above: plot of position $p(t)$. Below: plot of MPC control action $u_{mpc}(t)$. 184
22.11 ES MPC real experiments. Above: plot of position $p(t)$. Below: plot of actual control action $u_{id}(t)$. 184

List of Tables

3.1 Examples of spin numbers and gyromagnetic ratios of some common nuclei. . . . 9

7.1 Superconducting magnet time constant identification trials. Estimated time constant for each applied voltage step. . . . 50

8.1 Comparison of DNLM and LM: parameters of the NMR virtual sample and parameters of the lock sequence used for simulations. . . . 65
8.2 Comparison of DNLM and LM: amplitude of field step disturbance. . . . 65
8.3 Comparison of BE and DNLM: parameters of the NMR virtual sample used for simulations. . . . 67
8.4 Comparison of BE and DNLM: parameters of the lock sequence and amplitude of step disturbances used for simulations. . . . 67
8.5 Details of lock sequences used for NMR trials. . . . 71
8.6 Details of samples used for NMR trials. . . . 71
8.7 Comparison of model-predicted steady state values of M_y to real ones after the application of a step field disturbance. . . . 72
8.8 Parameters of the virtual sample used for BBIM simulations. . . . 74
8.9 Parameters of the experiment for BBIM simulation. . . . 75
8.10 Comparison of $\hat{SS}_{BBIM}$ to real SS after the application of a step field disturbance. . . . 76
8.11 Comparison of $\hat{ST}_{BBIM}$ to real ST after the application of a step field disturbance. . . . 76

10.1 Details of the lock samples. . . . 83
10.2 Details of the lock sequence. . . . 84
10.3 Power of imaginary component of NMR signal with and without lock system, in presence of external current disturbance. . . . 96

16.1 Case Study A: performance of PI_{na} algorithm for different demand offsets. . . . 128
16.2 Case Study A: performance of PI algorithm for different demand offsets. 128
16.3 Case Study B: Performance of PI algorithm for different demand profiles. . . . 131
16.4 Case Study A: performance of FPI algorithm for different demand offsets. . . . 134
16.5 Case Study B: Performance of FPI algorithm for different demand profiles. . . . 135
16.6 Case Study A: performance of $ILQG$ algorithm for different demand offsets. . . . 138
16.7 Case Study B: Performance of $ILQG$ algorithm for different demand profiles. . . . 139

16.8 Case Study A: performance of $ILQG - SF$ algorithm for different demand offsets. 141

17.1 Robustness indicators for the PI_{na} and PI RTC algorithms based on $L(s)$. 143
17.2 Robustness indicators for the PI_{na} and PI RTC algorithms based on $\tilde{L}(s)$. 144
17.3 WDN: robustness indicators for the PI and $FPI - SP$ RTC algorithms based on $\tilde{L}(s)$. 153

18.1 Performance of $P\ on\ \xi$ algorithm for different demand offsets. 158
18.2 Case Study B: Performance of $PI\ on\ \xi$ algorithm for different demand profiles. 159
18.3 Case Study B: performance comparison of algorithms tested on the WDN with Demand A. 159
18.4 Case Study B: performance comparison of algorithms tested on the WDN with Demand B. 159

Chapter 1

Introduction

The concept of Industry 4.0 was first proposed at the Hannover Fair with the *Industry 4.0 Initiative*, and the *Industry 4.0 manifesto* published in 2013 by the German National Academy of Science and Engineering. Since then, more and more companies have embraced the Industry 4.0 approach, with the establishment of *smart* factories, products and services. Nowadays, the Industry 4.0 approach represents the driving force of industrial development in many fields, ranging from manufacturing to water management systems [1, 2, 3, 4, 5]. The context of Industry 4.0 is characterised by the presence of advanced sensor networks, with the integration of the Internet of Things (IoT) concept in the industrial environment [6, 7]. Such sensors collect huge amount of data, which are usually stored in the Cloud to be accessible by all the smart agents connected to the Industrial IoT network and involved in the production and management processes. The result is a complete digitalisation of the information characterising the plant [8, 9]. Virtualisation of factory processes is also made possible by the huge sensing capability promoted by the Industry 4.0 approach: a virtual version of the plant (digital twin) is a key to improve management and optimisation, and help developing ad hoc fault detection and predictive maintenance solutions, thus improving productivity and quality of the product/service [10]. Big Data management and analysis and model identification techniques have therefore become crucial technologies that allow turning the collected data into useful information [8]. Finally, the spread of smart actuators, tightly connected with smart sensors and processing units in the Industrial IoT network, makes it possible not just to monitor, but also to interact with the plant and control it in real time, by means of feedback control loops. This completes the integration of physical and virtual components of the plant and gives rise to the so called Cyber Physical Systems (CPSs) [11, 12]. In this scenario, control theory assumes a crucial role [13]. In fact, only a proper design of control algorithms allows to take maximum advantage of both sensing and communication capabilities of smart plants, in terms of performances. This Thesis exploits the tools of control system theory to face very different control problems related to three different field of applications. Frequency domain, optimal and predictive control algorithms are developed on the digital twin first, and then successfully tested on the real plant.

The first task faced in this Thesis is the design of a control loop to perform fine regulation of magnetic field in nuclear magnetic resonance applications, thus allowing to obtain more precise and repeatable results. To overcome magnetic field sensing limitations, a *virtual* sensor, based on a parallel magnetic resonance experiment, is first designed and optimised. To this end, an accurate model of the process is first developed and validated. This digital twin features both the hardware and the physical components of the process, and is exploited for the development of Proportional Integral Derivative control algorithms, which are then implemented and tested on the real plant.

The second field of application of control theory faced in this Thesis is pressure control in water distribution networks, with the final aim of reducing leakage and extend infrastructure lifetime. In particular, in the context of “Water 4.0”, the spread of wired water distribution networks, where sensors and actuators are connected by wire to control units, allows to develop new control approaches working with high sampling rates. In this Thesis, both frequency domain and optimal control algorithms are tuned and tested in a simulated environment, to highlight the benefit of this new possibility. All the proposed algorithms outperform a benchmark algorithm, which works with longer sampling times.

The last topic of this Thesis is related to the context of smart warehousing. In this case, the goal is to develop and test different Model Predictive Control approaches to overcome structural limitations of the plant, resulting in nonlinearities such as deadzone, typically affecting the mechanical systems employed in warehousing. In particular, the case study is a laboratory scale version of an overhead travelling crane, whose actuators are affected by severe deadzone and saturation of the control action.

The Thesis is therefore organised in three main sections, one for each application. In each of them, the control problem is first described from a high-level point of view, as well as its context, with useful references to the literature. Then the physics required to allow a proper understanding of the application is introduced. The control problem is then reformulated in a formal way and different solutions described in detail. Both simulations and experiments on the real plant are performed to assess the performances of the proposed approaches. Finally, further insight on possible research developments is also reported in each conclusion section.

Part I

Model Based Design of a Field Frequency Lock System for Nuclear Magnetic Resonance Applications

Chapter 2

Introduction

Nuclear Magnetic Resonance (NMR) is an incredibly powerful spectroscopic technique which allows to identify unknown products of chemical reactions, to study properties of organic composites or to gather information about molecular motions. The NMR principle is also the basis for Magnetic Resonance Imaging (MRI) which is a powerful, non-invasive medical imaging technique [14, 15, 16, 17, 18]. During an NMR experiment, the sample containing the material under investigation is placed in a magnetic field: the behaviour of the sample depends on both the kind of material and the field strength. NMR techniques require then very stable and homogeneous magnetic field so that this behaviour is only defined by the physical characteristics of the sample. In fact, if the magnetic field drifts during time, measures may not be accurate. Moreover, a common procedure to improve the Signal to Noise Ratio (SNR) is to cumulate several scans of the same sample. If the field changes from scan to scan, this procedure does not allow to improve the results [14, 15, 16, 17, 18]. All these aspects point out the need for a closed-loop control of the magnetic field, called *Field Frequency Lock* (FFL) system. A precision of few parts per million (ppm) is often required with the modern spectrometers. Typical magnetic field sensors cannot be used for such an accurate task, as they may not be granular enough or fast enough to cope with field disturbances. The solution is that of using the NMR experiment as a virtual sensor of the applied magnetic field, setting up a parallel experiment capable of providing a suitable signal for feedback [16, 19]. The usual approach for the loop closure is the use a Proportional (P) or Proportional-Intergral (PI) controller, which is tuned on the basis of heuristic rules. Just few works try to face the problem using a model-based approach [19, 20]. New NMR techniques such as Fast Field-Cycling NMR (FFC-NMR) [21, 22] add new requirements to the FFL system: in addition to static precision, constraints on the settling time of the closed-loop are required. This stresses the need to develop reliable models for the entire process, ranging from the magnet used for generating the magnetic field to the NMR physics itself, and to properly exploit the tools of control system theory to design a closed-loop system that can cope with the above specifications. All these points are covered in this work, which aims at developing and testing on a real FFC-NMR setup a methodology for the design of the closed-loop control of the magnetic field. In particular, a simulator of the process is developed, based on physical models of the different components along the control loop. A black-box approach for the identification of simplified, linear models to be exploited for control is then proposed: a proper model structure is chosen according to the response of the system to a step input, and the values of its parameters defined by means of input-output identification. A methodology for the synthesis of Proportional-Intergral-Derivative (PID) controllers, based on linear models, is then developed in the simulated environment. Finally, the overall closed-loop approach is tested on the real plant and its performances evaluated, with particular focus on how the new FFL positively affects the results of NMR experiments.

This part of the Thesis is organised as follows: the NMR phenomenon is first described in details in order to understand the physics behind the process (Chapters 3-5). Then the FFL is introduced in Chapter 6, where the different approaches to the problem are also investigated. Chapter 7 is devoted to the analysis of the experimental setup, both hardware and firmware, and to develop its description in terms of block schemes. Chapter 8 concerns the analysis of mathematical models for the description of the NMR phenomenon. Models are investigated and compared each other, then the behaviour of predicted NMR is compared to real data collected from trials. Chapter 9 describes the methodology for the synthesis of the PID regulator, and the closed-loop implementation. Finally, Chapter 10 describes the experimental trials performed to asses the correctness of the methodology.

This work is carried out in collaboration with Stelar s.r.l [23], a leader company in the realization of NMR and FFC-NMR instrumentation based in Mede (Italy) since 1984. As a research activity, this thesis is part of European project "Improving Diagnosis by Fast Field-Cycling MRI" (IDentIFY), which aims to develop a FFC-NMR setup capable of capturing information that is invisible to standard NMR techniques [24]. The results here presented are published as [25, 26].

Chapter 3

Basics of NMR

In this first chapter the phenomenon of Nuclear Magnetic Resonance (NMR) is introduced starting from the very basic considerations from quantum mechanics. A simplified case study of non-interacting particles is taken in consideration, thus allowing to give a first description of Continuous Wave (CW) spectroscopy. Then the *vector model* from classical physics is introduced and investigated in the same simplified case study, allowing to understand modern Fourier Transform (FT) NMR techniques. A more realistic environment is then introduced by considering interactions between nuclei, making it possible to better understand the information which can be obtained from NMR spectroscopy. For further details refer to [14, 15, 16, 17, 18].

3.1 Spin and Energy Levels

Spin is an intrinsic form of quantized angular momentum carried by atomic nuclei, as if they were spinning as shown in Figure 3.1. The angular momentum **L** can be expressed as:

$$\mathbf{L} = \frac{h}{2\pi} I = \hbar I \tag{3.1}$$

where $h = 6.626 \times 10^{-34}\ J\ s$ is the Planck constant; $\hbar = h/2\pi$ is the reduced Planck constant; $I = 0, 1/2, 1, 3/2, \ldots$ is the *spin quantum number*, and it is a positive integer or semi-integer, depending on the nucleus. The values I can assume are strictly related to the number of protons and neutrons in the nucleus. If we introduce the atomic number Z (i.e. the number of protons in the nucleus) and the mass number A (i.e. the overall number of protons and neutrons in the nucleus) one can state that:

- if both A and Z are even, then $I = 0$;
- if A is odd, then I is half-integer;
- if A is even and Z is odd, then I is integer.

Nucleus		γ [10^2 $rad/(s \times G)$]	*Spin I*
1H	Proton	267.513	1/2
2H	Deuterium	41.065	1
13C	Carbon	67.262	1/2
17O	Oxygen	-36.264	5/2

TABLE 3.1: Examples of spin numbers and gyromagnetic ratios of some common nuclei.

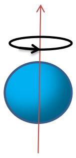

FIGURE 3.1: The nucleus as a spinning charged particle carries an angular momentum L and a magnetic momentum μ

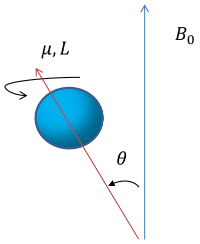

FIGURE 3.2: A nucleus in a magnetic field has a potential energy W which depends on the angle θ.

As far as nuclei carry some electric charge, the angular spin momentum $\mathbf{L}$ is always associated and parallel to a quantized magnetic momentum $\boldsymbol{\mu}$ measured in $[J/G]$:

$$\boldsymbol{\mu} = \gamma \mathbf{L} = \gamma \hbar I \tag{3.2}$$

where γ is the gyromagnetic ratio and depends on the nucleus. Table 3.1 shows some examples of nuclear specie with their spin value and gyromagnetic ratio. Note that γ can assume both positive and negative values, thus defining the sense of precession.

When a nucleus with a magnetic moment $\boldsymbol{\mu}$ is placed in a constant magnetic field $\mathbf{B}_0$ its potential magnetic energy depends on the component aligned with the field.

Considering Figure 3.2, energy W can be written as:

$$W = -\mu B_0 = -\mu |\mathbf{B}_0| cos(\theta) \tag{3.3}$$

with $\theta \in [0; \pi]$.
Note that the minus indicates the fact that the state aligned with the magnetic field is the low energy one.

According to quantum mechanics, energy transfer is quantized, therefore not all the orientations are possible. Consider the case of a single nucleus with $I = 1/2$. The only possible orientations are those parallel or anti-parallel with respect to the magnetic field (this means that $\theta = 0, \pi$), as seen in Figure 3.3.

It follows that only two energy levels are possible, and considering (3.2) and (3.3) they can be written as

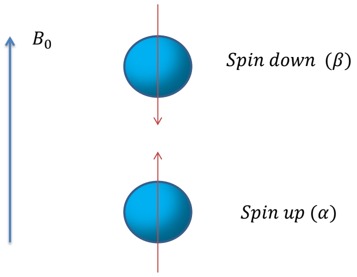

FIGURE 3.3: The *spin up* and *spin down* states of a nucleus in a constant magnetic field.

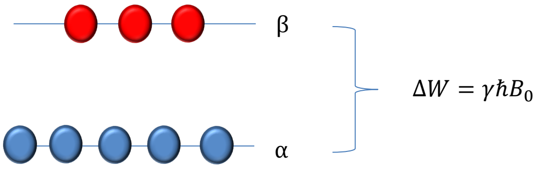

FIGURE 3.4: Energy gap between two consecutive energy levels.

$$W\uparrow = -\mu|\mathbf{B}_0|cos(\pi) = \frac{1}{2}\gamma\hbar B_0 \tag{3.4}$$
$$W\downarrow = -\mu|\mathbf{B}_0|cos(0) = -\frac{1}{2}\gamma\hbar B_0 \tag{3.5}$$

With the arrow referring to the alignment of the spin with respect to the magnetic field, the so called *up* (or α) and *down* (or β) spin state.

If a nucleus with $I = 1$ is considered, then three orientations and three energy levels are possible. In particular those related to $\theta = 0, \pi/2, \pi$, as described in the following:

$$W\downarrow = \mu B_0 = \gamma\hbar B_0 \tag{3.6}$$
$$W\rightarrow = 0 \tag{3.7}$$
$$W\uparrow = -\mu B_0 = -\gamma\hbar B_0 \tag{3.8}$$

In general the number of possible orientations (and of energy levels) is $2I + 1$.

From now on, reference will be made to the specific case $I = 1/2$ unless differently stated. Let now consider the energy gap between the two spin states. It is straightforward to compute:

$$\Delta W = \mu B_0 - (-\mu B_0) = 2\mu B_0 = 2(\frac{1}{2}\gamma\hbar)B_0 = \gamma\hbar B_0 \tag{3.9}$$

It can be shown that in general this is the energy gap between two consecutive spin levels, as shown in Figure 3.4.

So, to change the orientation of a nucleus it is necessary to bridge the energy gap

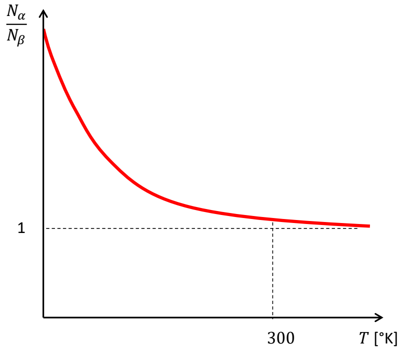

FIGURE 3.5: Boltzmann's distribution of spin populations as function of the absolute temperature. Note that near room temperatures (300 $^\circ K$) the number of low and high energy particles is nearly equal.

between the two spin states, that means to provide exactly ΔW by an electromagnetic wave. Recall that the energy of an electromagnetic wave that is absorbed at a time by a nucleus W_{em} is quantized as well (energy quantum), and is given by:

$$W_{em} = h\nu \tag{3.10}$$

where ν is the frequency expressed in $[Hz]$.

By equating W_{em} and ΔW, the correct frequency ν_0 to make a single nucleus jump to the closest energy level can be computed as follows:

$$W_{em} = \Delta W \implies h_0 = \gamma\hbar B_0 \tag{3.11}$$

therefore:

$$\nu_0 = \frac{\gamma}{2\pi} B_0 \tag{3.12}$$

$$\omega_0 = \gamma B_0 \tag{3.13}$$

The ω_0 represents the resonance frequency of the nucleus and is called *Larmor Frequency*.

Up to now a single, isolated nucleus was taken into consideration. Consider now a set of N identical nuclei with $I = 1/2$ and an uniform magnetic field $\mathbf{B}_0$. If the temperature was 0 $^\circ K$, all of them would be at the minimum energy state. If not, the minimum energy state is still the most probable, but thermal excitation may be enough to make some nucleus jump to the other state. At thermal equilibrium, the distribution of spins in the two energy levels is predicted by Boltzmann's equation:

$$\frac{N_\alpha}{N_\beta} = e^{\frac{\Delta W}{kT}} \tag{3.14}$$

where N_α and N_β are the number of nuclei in the energy levels α and β respectively, ΔW is the energy gap, k is the Boltzmann constant and T is the absolute temperature measured in $[^\circ K]$. Boltzmann's distribution as function of the absolute temperature is shown in Figure 3.5.

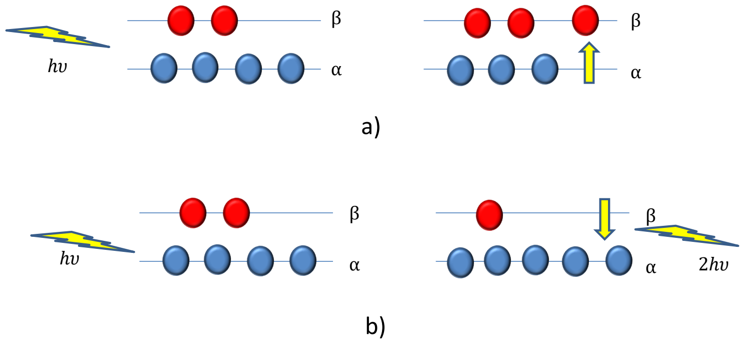

FIGURE 3.6: a) A nucleus moves to the upper energy level when absorbing an energy quantum b) As a consequence of the application of a quantum of energy, a nucleus falls to the lower energy state and releases another quantum of energy.

In particular, at room temperature (300 $^\circ K$), in a field of about 1000 G, Boltzmann's equation predicts that the N_α and N_β are nearly equal. Applying these hypotheses it is possible to obtain an approximated formula. The difference of population ΔN is defined as $\Delta N = N_\alpha - N_\beta$.

From Boltzmann's equation one can write:

$$N_\alpha = N_\beta e^{\frac{\Delta W}{kT}} \tag{3.15}$$

then:

$$\Delta N = N_\beta e^{\frac{\Delta W}{kT}} - N_\beta = N_\beta (e^{\frac{\Delta W}{kT}} - 1) \tag{3.16}$$

Introducing a first order expansion for the exponential, one gets to:

$$\Delta N \approx N_\beta \frac{\Delta W}{kT} \tag{3.17}$$

and recalling that $\Delta W = 2\mu B_0$, it is possible to write:

$$\Delta N \approx N_\beta \frac{2\mu B_0}{kT} \tag{3.18}$$

Finally, since N is the overall number of nuclei, it is possible to introduce the above hypothesis and write:

$$\begin{cases} N = N_\alpha + N_\beta \\ N_\alpha \approx N_\beta \end{cases} \tag{3.19}$$

hence:

$$2N_\beta \approx N \tag{3.20}$$

the difference of population ΔN can be therefore approximated as:

$$\Delta N \approx N \frac{\mu B_0}{kT} \tag{3.21}$$

At this point, when the electromagnetic pulse is applied, two opposite phenomena are possible (see Figure 3.6):

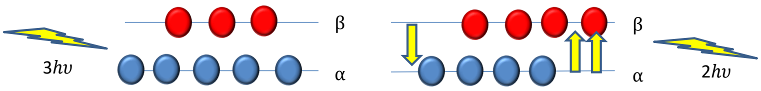

FIGURE 3.7: At thermal equilibrium the lowest energy state is the more populated, therefore the number of absorbed energy quanta is higher than that of emitted ones. The consequence is an overall Absorption of energy.

- *absorption*: a nucleus jumps from the low energy state to the higher one, absorbing some energy;
- *emission*: a nucleus falls from the high energy state to the lower one, emitting some energy.

According to 3.14, as $\Delta W \geq 0$, then $N_\alpha \geq N_\beta$, so the dominant effect is always absorption. Figure 3.7 shows a possible evolution of the spin population as consequence of the interaction with an electromagnetic wave providing three energy quanta.

The frequency of the electromagnetic wave which allows to move the spin from one energy level to the upper (which is also the frequency of the electromagnetic wave they emit when falling to the low energy state) depends on the nuclear specie of the nuclei, so its observation provide information about the compound under investigation. Notice that this frequency falls in the Radio Frequency (RF) range, therefore the applied electromagnetic wave is typically called *RF wave* or *RF pulse*. Before explaining a first NMR spectroscopy technique, an overview of the hardware necessary to carry out an NMR experiment is necessary and is introduced in the following.

3.2 NMR Hardware

In the following section the experimental setup for NMR is explored. The probe is a metal tube containing the sample, the transmitter and receiver circuitry; it is placed into the magnetic field $\mathbf{B}_0$. The transmitter circuit is used to apply a proper RF wave to the sample, the receiver one is necessary to record the output signal of the NMR experiments. The magnet used for generating $\mathbf{B}_0$ can be a superconducting or a resistive one, so a dedicated power supply is needed to obtain the desired value of the field. For superconducting magnets vacuum and cooling systems are necessary as well to keep the magnet itself in the superconducting state. The input signal is generated by a pulse sequence generator and sent to the transmitter. The output signal coming from the probe is amplified and digitized with an ADC. At this point it can undergo various software elaborations to extract the desired information.

3.3 NMR Continuous Wave Spectroscopy

To better understand how the property of spin can be exploited to obtain information about an unknown sample, the technique of NMR Continuous Wave (CW) spectroscopy is now introduced. CW spectroscopy analyses the resonance frequency of the nuclei in the sample to obtain information about their nuclear species, since different nuclear species resonate at different frequencies. A first possible procedure to perform an NMR experiment can be summarised in the following steps:

- generate $\mathbf{B}_0$ with a magnet and wait for the spins to settle in the different energy levels;
- apply an input to the sample with a slowly varying the frequency, using the transmission coil;
- the resonance frequency ω_0 depends on both the nuclear specie and the strength of $\mathbf{B}_0$;
- the receiver coil records energy changes to build up the absorption spectrum.

3.4 Spin Physics: a Classical Interpretation

The analysis of how spins move across the different energy levels allows to understand how CW spectroscopy works. Nevertheless, spin property can be also exploited in other NMR experiments which instead require an explanation of resonance in terms of classical physics. Relation (3.13) does not show any dependence on h, which is typical of quantum mechanics, thus it can be obtained by applying classical physics principles as well. Think of a nucleus as a top, both spinning and precessing along the magnetic field. The latter applies a torque that pushes the top towards the field itself. Notice that in the classical interpretation of the phenomenon all orientations are possible. It is important to remark that for positive values of γ precession of nuclei about the magnetic field occurs in clockwise (negative) direction. A minus should then appear in the above relation when it is interpreted as the precession angular speed. It is then possible to write:

$$\boldsymbol{\omega}_0 = -\gamma \mathbf{B}_0 \tag{3.22}$$

Let introduce a reference frame with the z axis directed along $\mathbf{B}_0$. The electromagnetic wave of frequency ω' is then applied in such a way that its associated magnetic field $\mathbf{B}_{RF}$ lies in the xy plane, so that no interference with the main field $\mathbf{B}_0$ occurs. The magnetic field is time dependent and can be written as:

$$\mathbf{B}_{RF}(\omega' t) = 2B_1 cos(\omega' t) \tag{3.23}$$

It can be decomposed in two fields $\mathbf{B}_1'$, rotating at speed $\boldsymbol{\omega}'$ and with magnitude B_1, and $\mathbf{B}_1''$, rotating at speed $-\boldsymbol{\omega}'$ and with magnitude B_1, as shown in Figures 3.8 and 3.9.

Only if $\boldsymbol{\omega}' = \boldsymbol{\omega}_0$ one of the two components is always in phase with the precessing nucleus and can fully interact with it, allowing to obtain the maximum effect when trying to change the nucleus orientation. This is shown in Figure 3.10. The other component instead does not influence the nucleus. On the contrary, if the two angular speeds are very different, the rotating field and the nucleus get out of phase and the effects gets averaged to zero. This behaviour can be extended to a set of N nuclei with some additional considerations.

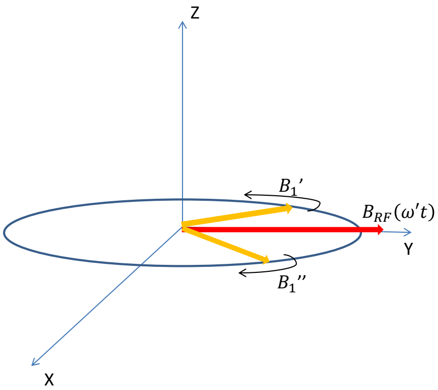
Z
B_1'
$B_{RF}(\omega' t)$
Y
B_1''
X

FIGURE 3.8: The oscillating magnetic field B_{RF} can be interpreted as the superposition of the counter rotating fields B_1' and B_1''.

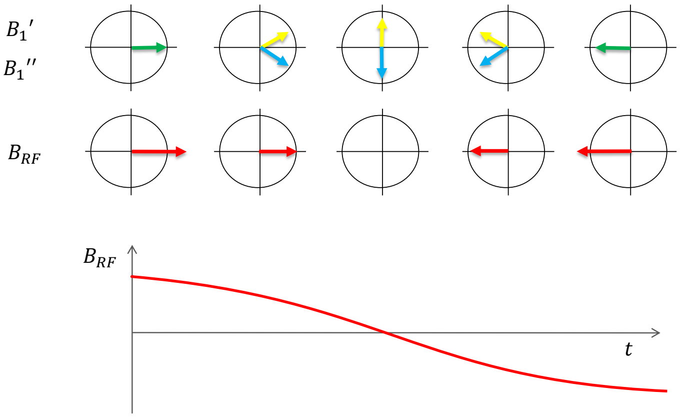
B_1'
B_1''
B_{RF}
B_{RF}
t

FIGURE 3.9: The oscillating magnetic field B_{RF} can be interpreted as the superposition of the counter rotating fields B_1' and B_1''.

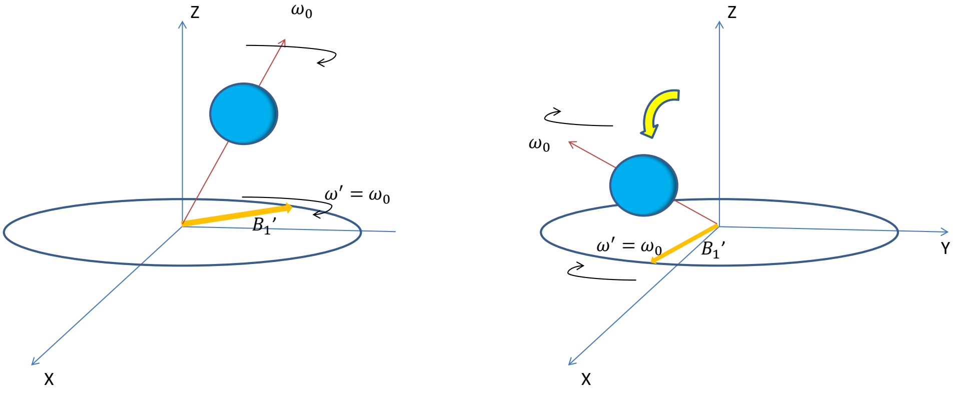

(A) (B)

FIGURE 3.10: When the rotating magnetic field and the precessing nucleus run at the same angular speed it is possible to change the precession angle of the nucleus.

3.5 The Vector Model and Pulsed NMR

Consider a set of N identical nuclei with $I = 1/2$ and an uniform magnetic field $\mathbf{B}_0$. The overall effect of their magnetic moments sums up into the nuclear magnetization vector $\mathbf{M}$ (also known as *bulk magnetization vector*). At thermal equilibrium the favoured orientation for all $\boldsymbol{\mu}_i$ is along $\mathbf{B}_0$, thus $\mathbf{M}$ is along $\mathbf{B}_0$ and, recalling 3.1, its magnitude can be written as:

$$M = \frac{(NB_0\mu^2)}{kT} = \mu\Delta N \tag{3.24}$$

If for some reason $\mathbf{M}$ is not aligned with $\mathbf{B}_0$, it starts precessing along $\mathbf{B}_0$ at speed $\boldsymbol{\omega}_0$ as given by (3.22). Let introduce a new reference frame $x'y'z'$ that rotates along $\mathbf{B}_0$ at speed $\boldsymbol{\omega}_0$, with z' directed as z. From now on this frame will be called *rotating reference frame*. At this point the effect of $\mathbf{B}_0$ is not evident and $\mathbf{M}$ is not moving with respect to the new frame, as reported in Figure 3.11.

Let now apply the RF pulse with the associated field $\mathbf{B}_1$ perpendicular to $\mathbf{B}_0$. Since $\mathbf{B}_1$ rotates at speed $\boldsymbol{\omega}_0$, $\mathbf{B}_1$ remains still in the new frame and is the only active magnetic field. Hence $\mathbf{M}$ starts precessing along $\mathbf{B}_1$ at speed:

$$\boldsymbol{\omega}_1 = -\gamma\mathbf{B}_1 \tag{3.25}$$

In a time interval t, $\mathbf{M}$ spans over an angle θ with respect to the z axis given by:

$$\theta = \omega_1 t = -\gamma B_1 t \tag{3.26}$$

Since the NMR signal is collected on the xy plane, the NMR signal is maximized when $\mathbf{M}$ lies into that plane. A 90° displacement allows to bring $\mathbf{M}$ into the xy plane. From (3.26) it is easy to see that to achieve this goal the pulse must last for τ instants such that:

$$-\gamma B_1\tau = \frac{\pi}{2} \tag{3.27}$$

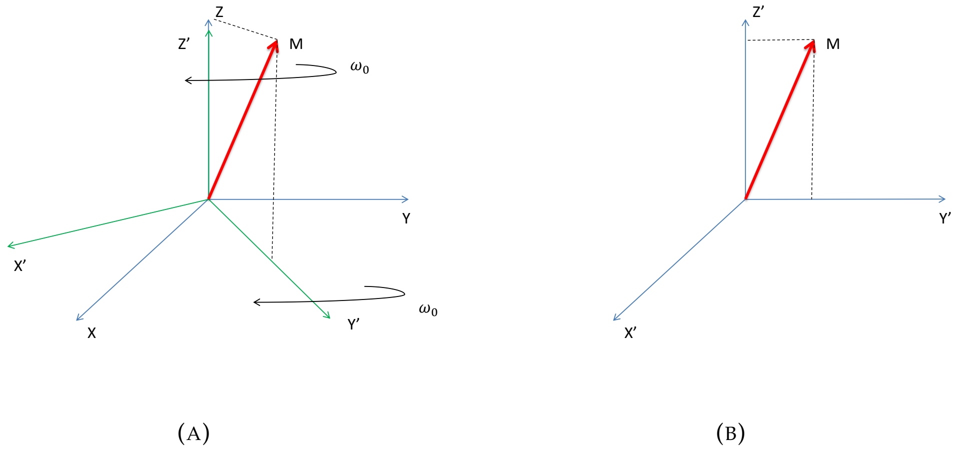

(A) (B)

FIGURE 3.11: In a rotating reference frame $x'y'z'$ with the same angular speed of vector **M**, the latter remains still.

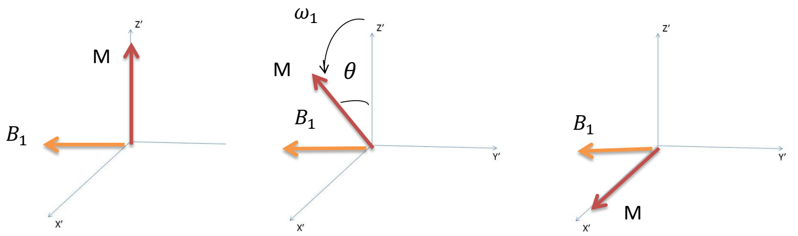

FIGURE 3.12: Motion of the bulk magnetization **M** in the rotating frame $x'y'z'$ when the rotating magnetic field is applied.

The procedure is resumed in Figure 3.12.

Back in the still frame, **M** is now perpendicular with respect to $\mathbf{B}_0$. The RF wave must be then switched off. At this point **M** starts precessing about $\mathbf{B}_0$ while moving back to the equilibrium position. This process is called *relaxation* (see Chapter 4 for further details). Let the components of **M** along the x, y, z axis as M_x, M_y and M_z respectively. It is possible to distinguish between longitudinal relaxation (about M_z) and transverse relaxation (about M_x and M_y). As the receiving coil is placed perpendicularly with respect to $\mathbf{B}_0$, an induced electromotive force results in the sensing circuitry from the motion of **M** from the 90° displaced position back to the equilibrium one (M_x or M_y are sensed). This voltage oscillates at frequency ω_0 and it is called *Free Induction Decay* (FID). An example is depicted in Figure 3.13. The exponential envelope of this signal has time constant called $T2$ or *Spin-Spin* time constant.

If the signal relative to M_x is sensed, the Fourier Transform (FT) of FID signal gives the so called absorption spectrum. The input for the FT is a cos-like wave multiplied by an exponential. In terms of spectra this is a convolution of the two signals, and leads to a Lorentzian-shaped absorption peak placed in correspondence of the resonance frequency. If instead M_y is sensed (or it is obtained via a 90° displacement

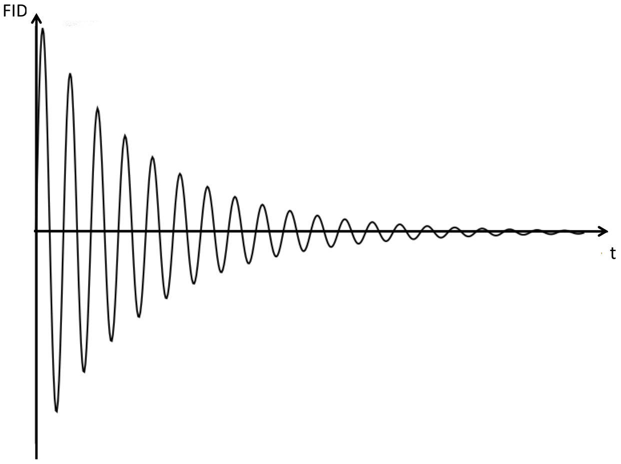

FIGURE 3.13: The *Free Induction Decay* (FID) signal collected in the xy plane.

of M_x) it is possible to obtain the so called dispersion spectrum. In this case the input for the FT is a sin-like wave multiplied by an exponential. Again, a convolution must be performed in the frequency domain (see Figure 3.14 for a full example). Since we are dealing with signals in two dimensions (x and y components), we need to rely on the complex FT, which provides a couple of spectra (the real one and the imaginary one) for each input signal (see Chapter 7 for details). Note that the amplitude of the FID signal is related to $\mathbf{M}$, which in turn depends on the number of nuclei. Then the area of the spectrum depends on the number of nuclei as well: the more the nuclei, the largest the area. This method to obtain the NMR spectrum is called *Fourier Transform NMR* or *Pulsed NMR*.

3.5.1 Pulsed NMR

The Pulsed NMR technique allows to obtain an NMR spectrum as the FT of a FID signal. The analysis of the spectrum allows then to obtain different information about the sample. The steps needed to obtain the spectrum are the following:

- generate $\mathbf{B}_0$ with a magnet and put the sample in it;
- apply a 90° RF pulse with the transmission coil to bring the magnetization vector in the transverse plane;
- collect the FID via the receiver coil;
- perform FT of FID to obtain the spectrum.

3.5.2 Continuous Wave Versus Pulsed NMR

Both CW and FT NMR techniques allow to obtain a proper spectrum. Still, CW spectroscopy is inefficient in comparison with FT since it probes the NMR response at individual frequencies in succession. On the contrary, with FT NMR it is necessary to acquire a single FID to obtain information about all the frequencies characterizing the response of the sample. Still, both these NMR experiments provide low Signal to

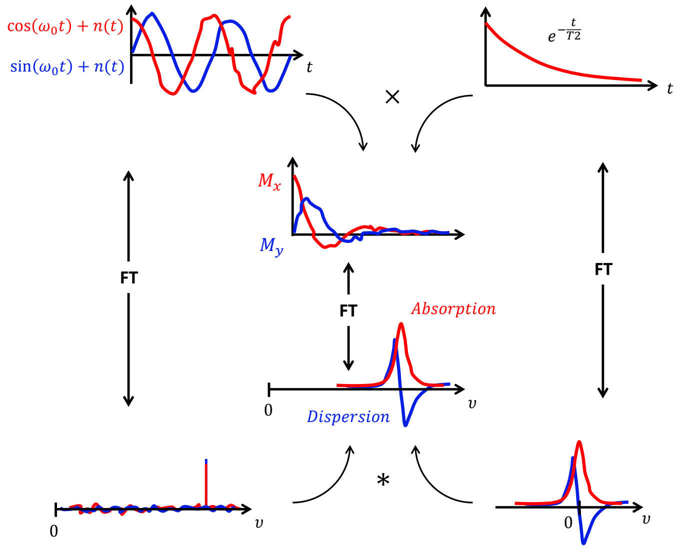
$\cos(\omega_0 t) + n(t)$
$\sin(\omega_0 t) + n(t)$
t
$e^{-\frac{t}{T2}}$
t
×
M_x
M_y
FT
FT
FT
Absorption
Dispersion
0
v
*
0
v
0
v

Figure 3.14: The M_x and M_y FIDs can be considered as the product of a cosine or sine wave for an exponential decay with constant $T2$. Some noise $n(t)$ is present as well in this example. The Fourier transform of the x FID gives a Lorentzian peak in for the absorption spectrum, while the Fourier transform of the y FID generates the dispersion spectrum. The same result can be interpreted as the convolution of the Fourier transforms of the sin and cos waves, which are deltas placed at the resonance frequency, with the complex Fourier transform of the exponential, which defines the shape for the absorption and dispersion spectra.

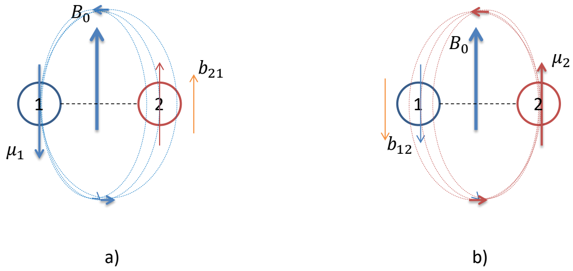

a) b)

FIGURE 3.15: Example of local fields are generated by the nuclei which carry a dipole magnetic momentum. Flux lines show how the local fields change the effective value of B_0 seen by each nucleus. In particular a) shows the local field generated by nucleus 1 acting on nucleus 2 (b_{21}) while b) shows the local field generated by nucleus 2 acting on nucleus 1 (b_{12}).

Noise Ratio (SNR). To overcome this problem it is possible to acquire many signals and perform an average. This requires a stable $\mathbf{B}_0$ as the resonance frequency is related to the magnetic field. Then SNR then increases as the square root of the number of scans. The process becomes quite long this way, in particular with CW NMR. For these reasons new spectrometers are based on FT.

3.6 The NMR Spectrum

Up to this point we have considered the NMR spectrum obtained via CW NMR or as the FT transform of the FID signal obtained via pulsed NMR. Nevertheless, position and shape of an NMR spectrum can be directly related to a series of physical phenomena, such as interaction between nuclei, molecular motion and presence of spatially non-homogeneous magnetic field. The following will be then devoted to the analysis of the spectrum as the result of these phenomena.

3.6.1 Dipolar Magnetic Interaction

Up to now we have considered $\mathbf{B}_0$ as the only magnetic field acting on the probe, but each magnetized nucleus provides a small contribution to the overall magnetic field. Let focus on z contributions only in the simple case of two interacting nuclei i and j. Let define $\mathbf{b}_{ij}$ as the local field generated by nucleus j and acting on i. Let also define $\mathbf{B}_{Tot}$ the overall magnetic field experienced by each nucleus. Then the following holds

$$\omega_{0i} = -\gamma B_{Tot_i} = -\gamma(B_0 + b_{ij}) \tag{3.28}$$

$$\omega_{0j} = -\gamma B_{Tot_j} = -\gamma(B_0 + b_{ji}) \tag{3.29}$$

Figure 3.15 highlights the direction of local fields seen by the nuclei according to the flux lines.

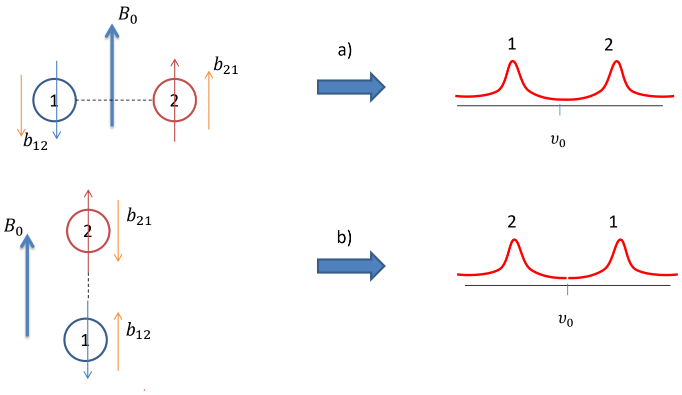

FIGURE 3.16: Origin of the spectral widening due to magnetic dipolar interaction between nuclei.

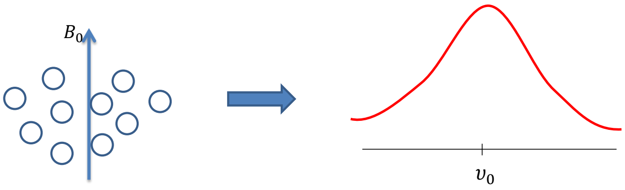

FIGURE 3.17: The shape of the spectrum is the result of the interactions of many nuclei in the sample.

The interaction between $\mathbf{B}_0$ and $\mathbf{b}_{ij}$ is defined by the relative position of the nuclei, therefore different cases are possible: Joining line of the two nuclei is perpendicular to $\mathbf{B}_0$, $\mathbf{b}_{12}$ is opposite to $\mathbf{B}_0$ and $\mathbf{b}_{21}$ is parallel to $\mathbf{B}_0$. Nucleus 1 resonates at lower frequency with respect to the expected ν_0 frequency and nucleus 2 resonates at higher frequency. Joining line is parallel to $\mathbf{B}_0$, $\mathbf{b}_{12}$ is parallel to $\mathbf{B}_0$ and $\mathbf{b}_{21}$ is opposite to $\mathbf{B}_0$. Nucleus 2 resonates at lower frequency with respect to the expected ν_0 frequency and nucleus 1 resonates at higher frequency. Figure 3.16 illustrates these possible situations.

With N nuclei all these effects coexists and all the mutual couplings should be considered. The result is a wider absorption spectrum, as depicted in Figure 3.17.

3.6.2 Effect of Molecular Motion

The state of the compound in the probe affects the shape of the spectrum. Consider for instance two samples containing water, one as ice, the other as liquid, both obtained with $B_0 = 10000\ G$. Absorption spectrums for ice and water are shown in Figure 3.18. The latter is narrower and higher with respect to the former. This is due to molecular motion, which is much reduced in solids. Every water molecule rotates about $\mathbf{B}_0$, thus the local field seen by a generic H nucleus changes over time. The overall effect is therefore an "average". Recall that a narrow peak is also higher as

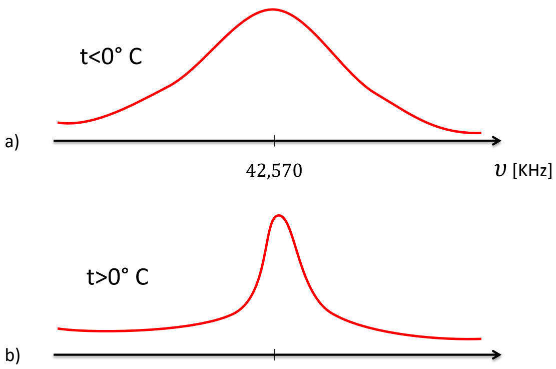

FIGURE 3.18: Absorption spectrum for protons in water as ice b) Absorption spectrum for protons in water as liquid.

the area of the signal depends on the number of nuclei N but does not depend on the state of the probe.

3.6.3 Effect of Non Homogeneous Field

Another aspect that impacts on the shape of the NMR spectrum is the uniformity of the applied magnetic field. If $\mathbf{B}_0$ is not perfectly homogeneous the precession frequency of some nuclei is different from the Larmor one. Suppose we divide our probe in many small cubes of equal volume. The external field in each of them is

$$\mathbf{B}_0, \mathbf{B}_0 \pm \Delta\mathbf{B}, \mathbf{B}_0 \pm 2\Delta\mathbf{B}, \ldots$$

Apply the 90° pulse and move to the rotating reference frame. Only the component of $\mathbf{M}$ due to the cube seeing $\mathbf{B}_0$ is still, the others rotate both clockwise and counterclockwise (recall (3.22)). This results in a faster decay of the FID signal, since the contributions become randomly oriented very fast and their sum goes to zero. The absorption spectrum is then wider than the expected one because nuclei resonate at many different frequencies, according to the effective value of $\mathbf{B}_0$ they experience. One cannot distinguish enlarging due to dipolar interactions or intermolecular interactions or molecular motion from that due to field inhomogeneity. It is said that the resolution of the spectrum is worsened. The effect of a non-homogeneous magnetic field will be further discussed in Chapter 5.

Chapter 4

Relaxometry

In this chapter the phenomenon of relaxation, which was introduced in Chapter 3, is described in details. Relaxation is the process by which the spins in the sample move towards an equilibrium. In order to attain this, the nuclei move from an energy level to another until the spin populations reach those predicted by Boltzmann's equation (3.14). The study of relaxation allows to:

- determine the design of the experiment;
- study physical properties of the analysed material;
- determine inter-nuclear distances in a molecule;
- study molecular motions.

Recall that spins result in a magnetization vector **M**, which at thermal equilibrium is aligned with the external field $\mathbf{B}_0$. The application of a RF pulse of a suitable frequency and duration can rotate **M** of 90°. Once the RF pulse is switched off, the so called relaxation phase occurs: **M** moves back to the equilibrium precessing around $\mathbf{B}_0$. As stated in the previous chapter, relaxation can be distinguished into longitudinal (also known as *spin-lattice*) and transverse (also known as *spin-spin*). Note that while the first involves energy exchange, the latter does not. In the following we explain in detail both processes and their origins. For further details refer to [14, 15, 16, 17, 18].

4.1 Spin-Lattice Relaxation

Spin-lattice relaxation is the process that brings the component of **M** along $\mathbf{B}_0$, M_z, back to its equilibrium value. From a microscopic point of view this means that some nuclei change their spin orientation so to obtain a minimum energy configuration. This leads to a release of energy from the nuclei to the rest of the probe (*lattice*). At each time instant t, M_z is proportional to the difference of population:

$$M_z(t) \propto \Delta N(t) = (N_\alpha(t) - N_\beta(t)) \tag{4.1}$$

Given a proper coefficient K_z , the previous relation can be rewritten as follows:

$$M_z(t) = K_z(N_\alpha(t) - N_\beta(t)) = (n_\alpha(t) - n_\beta(t)) \tag{4.2}$$

where:

$$n_\alpha(t) = K_z N_\alpha(t) \tag{4.3}$$

$$n_\beta(t) = K_z N_\beta(t) \tag{4.4}$$

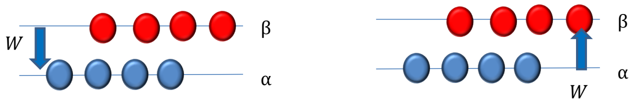

FIGURE 4.1: When a nucleus moves from one energy level to the other one, both populations change their value.

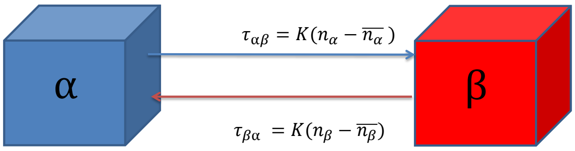
α
β
$\tau_{\alpha\beta} = K(n_\alpha - \overline{n_\alpha})$
$\tau_{\beta\alpha} = K(n_\beta - \overline{n_\beta})$

FIGURE 4.2: The Spin-Lattice relaxation described as the change of spin populations. The rate of transition is proportional to the deviation of population from its equilibrium value.

If $n_\alpha(t)$ and $n_\beta(t)$ are not the equilibrium values, transitions between the two spin levels (recall that we assumed $I = 1/2$) must occur for some nuclei. Notice that a loss of population in level β means an increase of population in level α and vice-versa, as it appears in Figure 4.1. The rate of transition from a population i to a population j is proportional to the deviation of population i from its equilibrium value. Let $\overline{n_i}$ be the equilibrium value for a generic population i. If this phenomenon is modelled as a first order process, the system can be represented as in Figure 4.2. The rate of transition from population i to population j , denoted τ_{ij} ,is given by:

$$\tau_{ij} = K(n_i(t) - \overline{n_i}) \tag{4.5}$$

where K is a suitable constant. Then, omitting for simplicity the time dependences, one can write:

$$\frac{dn_\alpha}{dt} = -K(n_\alpha(t) - \overline{n_\alpha}) + K(n_\beta(t) - \overline{n_\beta}) \tag{4.6}$$

$$\frac{dn_\beta}{dt} = K(n_\alpha(t) - \overline{n_\alpha}) - K(n_\beta(t) - \overline{n_\beta}) \tag{4.7}$$

$$\tag{4.8}$$

$$\begin{aligned}
\frac{dM_z}{dt} &= \frac{d(n_\alpha - n_\beta)}{dt} = && (4.9)\\
&= -K(n_\alpha(t) - \overline{n_\alpha}) + K(n_\beta(t) - \overline{n_\beta}) - K(n_\alpha(t) - \overline{n_\alpha}) + K(n_\beta(t) - \overline{n_\beta}) && (4.10)\\
&= -2K(n_\alpha - n_\beta) + 2K(\overline{n_\alpha} - \overline{n_\beta}) && (4.11)\\
&= -2K(M_z - (\overline{n_\alpha} - \overline{n_\beta})) && (4.12)
\end{aligned}$$

Defining the equilibrium of M_z ,M_0, as:

$$M_0 = \overline{n_\alpha} - \overline{n_\beta} \tag{4.13}$$

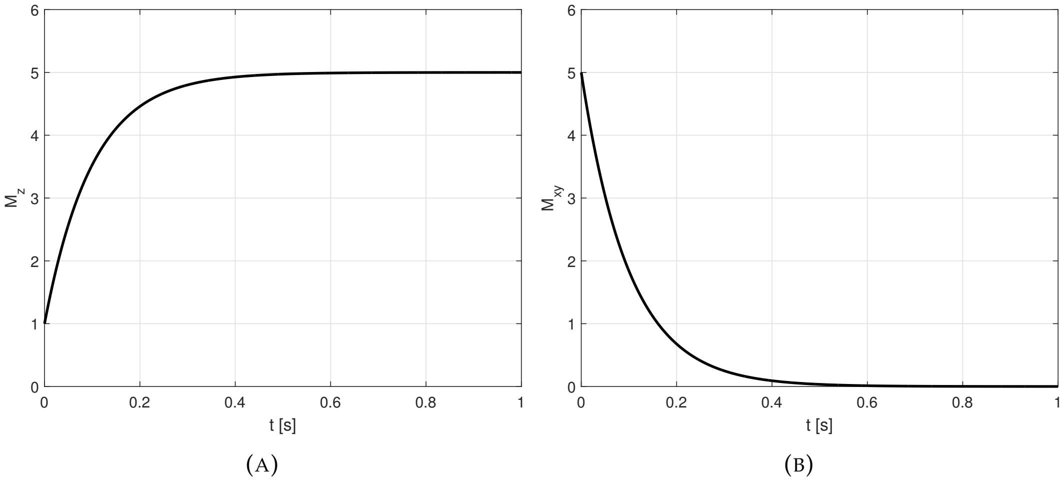

FIGURE 4.3: (a) The process of longitudinal relaxation shows a time behaviour described by an exponential of time constant $T1$. (b) The process of transverse relaxation shows a time behaviour described by a decaying exponential of time constant $T2$ in the rotating reference frame.

it is possible to obtain:

$$\frac{dM_z}{dt} = -2K(M_z - M_0) \tag{4.14}$$

$$\frac{dM_z}{dt} = -R_z(M_z - M_0) \tag{4.15}$$

$$\tag{4.16}$$

with $R_Z = 2K$.

The rate of change of M_z is therefore proportional to the deviation of M_z from its equilibrium value, M_0, with a constant R_z. Integration gives:

$$M_z(t) = (M_z(0) - M_0)e^{-\frac{t}{T1}} + M_0 \tag{4.17}$$

where $T1 = 1/R_z$ is the longitudinal or spin-lattice relaxation time constant. The relaxation profile appears in Figure 4.3a.

4.1.1 Origins of Spin-Lattice Relaxation and Relation to Molecular Motions

As recalled in the previous section, relaxation involves transitions between energy levels. Such transitions can be caused by local transverse magnetic fields which are oscillating at the Larmor frequency. The effect produced by each of these local fields is the same of a small RF pulse, i.e. the rotation of group of spins of some angle depending on the intensity and on the duration of the pulse. Still, when an RF pulse is applied, all of the spins experience the same oscillating field. Each local transverse field instead only affects a few spins and in the whole they are the cause of relaxation. These fields vary randomly in direction and magnitude and this randomness brings to equilibrium. Local fields are generated within the sample due to dipolar interactions, as seen in Chapter 3, and their time varying behaviour is strictly related to random motion of molecules, in particular rotations, thermal agitation, and collisions between the molecules themselves. Consider two identical nuclei with

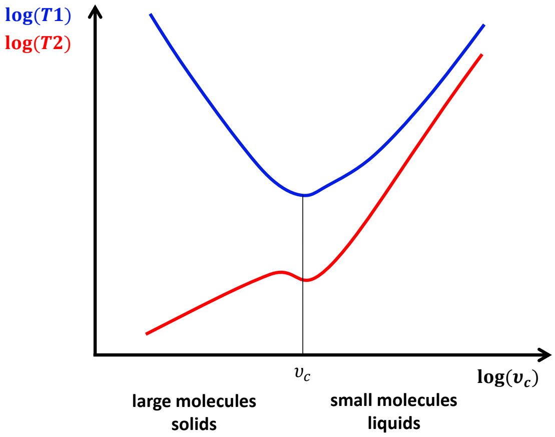

FIGURE 4.4: Transverse time constant ($T2$) profile in red and longitudinal time constant ($T1$) profile in blue as function of the correlation frequency of molecular motion in log-log scale.

$I = 1/2$. Let $\mathbf{b}_{12}(t)$ be the local field generated by nucleus 2 and acting on nucleus 1 at time t. Because of molecular motion, the distance between nuclei and their relative position changes over time and so $\mathbf{b}_{12}(t)$ does. This shows a «random» behaviour. Let J_x and J_y be the spectra of the x and y components of $\mathbf{b}_{12}(t)$. Their harmonics at frequency ν_0 can change some nuclear spin orientation, acting just as a small RF pulse, thus affecting $T1$. In particular it turns out that:

$$\frac{1}{T1} \propto (J_x(\nu_0) + J_y(\nu_0)) \tag{4.18}$$

Since the process of relaxation is affected by molecular motion, a common way of investigating it is NMR relaxometry. Information can be obtained by relating the relaxation time constant to the so called «correlation frequency» ν_c. For rotational motion, ν_c is an estimate of the number of rotations of an angle π experienced by a molecule per second; for diffusion motion the correlation period τ_c is an estimate of the time needed for two identical molecules to change their relative distance by a length equal to their molecular diameter (collision diameter). For slow motions ($\nu_c << \nu_0$) $T1$ decreases as ν_c increases and it depends on ν_0 . For fast motions ($\nu_c >> \nu_0$) $T1$ increases as ν_c increases and it does not depend on ν_0 .

Note also that ν_c increases as the temperature increases. A graph resuming all the previous considerations is represented in Figure 4.4.

4.2 Spin-Spin Relaxation

The spin-spin relaxation is the process by which the component of $\mathbf{M}$ perpendicular to $\mathbf{B}_0$, call it M_{xy}, tends to zero. This does not require any energy exchange since no transition among energy levels may be involved in the process. Instead, spin-spin relaxation and is mainly due to a phase shift between nuclear spins. The process of *spin-spin relaxation*, also called *transverse relaxation* is described by:

$$M_{xy} = M_{xy}(0)e^{-\frac{t}{T2}} \tag{4.19}$$

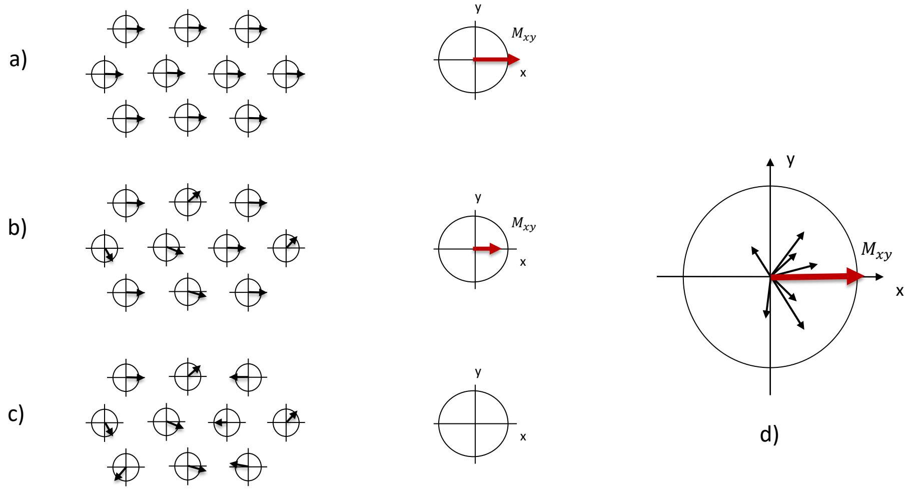

FIGURE 4.5: a) When all the contributions share the same phase angle, coherence is obtained and M_{xy} reaches its maximum value. b) When a preferred phase angle exists, coherence is generated and a non-zero value of M_{xy} can be measured. c) When individual contributions show a random phase distribution, no coherence is generated and the resulting M_{xy} is null. d) Individual contributions brought by each spin sum up into M_{xy}.

where $T2$ is the spin-spin or transverse relaxation time constant. The time evolution of the transverse magnetization M_{xy} in the rotating reference frame is shown in Figure 4.3b. Note that M_{xy} goes to zero before the longitudinal magnetization M_z has reached the equilibrium value M_0 along z. Then the following relation is always verified:

$$T2 \leq T1 \tag{4.20}$$

4.2.1 Origins of Spin-Spin Relaxation and Relation to Molecular Motions

Each spin in the sample gives rise to a small contribution to the bulk magnetization. Transverse contributions precess at the Larmor frequency in the xy plane (see Figure 4.5). Let us call *phase* ϕ the angle measured with respect to the x axis. If phases are random all contributions elide each other, so M_{xy} is zero (see Figure 4.5.c). If instead a preferred direction exists M_{xy} is different from zero (see Figure 4.5.a and 4.5.b). This situation is referred to as *coherence* in quantum mechanics. The application of a 90° pulse generates transverse magnetization. Transverse relaxation destroys this coherence by destroying the alignment of the contributions. Coherence is destroyed in two ways.

- Secular contribution makes the contributions jump to new positions at random (local fields oscillating close to the Larmor frequency). This is the same mechanism that brings to longitudinal relaxation. Anything that causes longitudinal relaxation also causes transverse relaxation.

- Non secular contribution makes the contributions get different phases as a result of precession at different frequencies (local constant fields).

Recall that the component of each local field **b** directed along $\mathbf{B}_0$ slightly changes the resonance frequency ν_0. The contribution given by local field is different for each nucleus, thus they all rotate at slightly different frequencies (non secular component). After the 90° pulse they still precede at different frequencies so that the overall contribution to M_{xy} tends to zero. In this respect $T2$ is inversely proportional to the bandwidth Δ of the spectrum: the largest the spectral linewidth the more the different frequencies in the game. If the contributions of **b** directed along $\mathbf{B}_0$ change randomly over time due to molecular motion, just the continuous component can dephase nuclear magnetic moments. Therefore, being J_z the spectrum of the z component of **b**, one can state that:

$$\frac{1}{T2} \propto J_z(0) \tag{4.21}$$

The behavior of $T2$ as function of the correlation frequency ν_c is reported in Figure 4.4, in particular one can approximate it as:

$$\frac{1}{T2} \propto \nu_c \tag{4.22}$$

4.3 Measuring the Relaxation Time Constants

The following section is devoted to the explanation of the basic pulse sequences that allow to measure the relaxation time constants, even in presence of non-homogeneous magnetic field. A preliminary discussion on how it is possible to correctly define duration and power of each pulse is also given. For this purpose it is convenient to introduce the rotating reference frame $x'y'z'$ described in Chapter 3, as it allows to hide oscillations so that the behaviour of both the magnitude M_{xy} and M_z is more evident.

4.3.1 Pulse calibration: the Angle sequence

Before introducing the pulse sequences which allow to measure $T1$ and $T2$ it is necessary to define the correct couple (intensity, duration) to tilt the magnetization vector of the desired angle. Let B_1 be the magnitude associated to the RF pulse. From now on we assume B_1 intensity as fixed and we define the correct duration of pulses (Recall (3.26)). The procedure of pulse calibration requires to apply a series of pulses of increasing duration and to collect the response signal. Figure 4.6 shows the behaviour of the collected signal intensity. It is maximum for the pulse tilting the magnetization down to the $x'y'$ plane: the associated duration will be the duration of a 90° pulse. Instead the collected signal intensity is zero for the pulse duration associated to a 180° pulse. Sometimes it is easier to discover a null point rather than a maximum, since the maximum value of the signal is not known a priori. Therefore one can define the duration of the 180° pulse verifying where the signal is null and then obtain the 90° pulse duration by halving the duration of the 180° pulse.

4.3.2 Measuring T1: the Inversion-Recovery Sequence

The procedure to measure the spin-lattice time constant $T1$ uses the Inversion-Recovery sequence, which is based on the following steps:

a) Apply a 180° pulse so that **M** is directed as $-z'$ and wait for a time interval τ;

b) apply a 90° pulse to bring **M** into the $x'y'$ plane and read the magnitude of the FID signal: its initial value is proportional to $M(\tau)$;

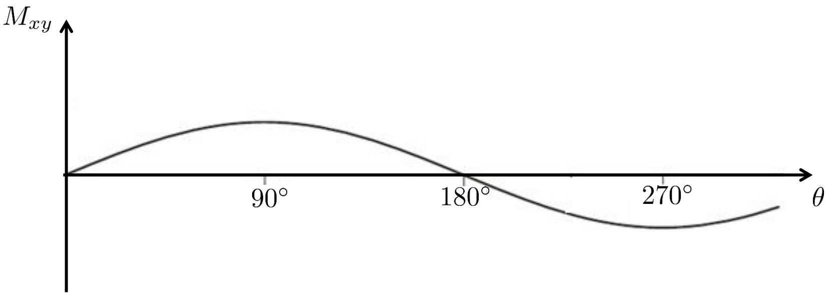

FIGURE 4.6: The Angle sequence consists of a series of increasing duration pulses. The signal generated in such a way gets its maximum value when the duration of the corresponding pulse completely brings the magnetization to the transverse plane. When no signal is collected the magnetization is expected to be aligned to the ˘z' direction, hence the corresponding pulse is a 180° one.

c) repeat changing τ to build up the law describing spin-lattice relaxation and to compute $T1$.

The procedure is resumed in Figures 4.7 and 4.8 which show the pulse sequence and the evolution of the magnetization. It is important to notice that in this way **M** is forced to undergo spin-lattice relaxation from $-M_0$ to M_0, that is twice the theoretical range (from 0 to M_0). This advantage is obtained thanks to the first inverting 180° pulse which brings the magnetization to $-z'$. The obtained profile follows the relation:

$$M_{zIR}(t) = M_0(1 - 2e^{-\frac{t}{T1}}) \tag{4.23}$$

4.3.3 Measuring T2: The Carr-Purcell-Meiboom-Gill (CPMG) Sequence

In the case of $\mathbf{B}_0$ completely uniform, in order to measure $T2$, it would be sufficient to apply a 90° pulse and study the FID signal, which is proportional to **M**. If this hypothesis is not fulfilled, FID decay is mainly due to the lack of homogeneity in B_0. A suitable sequence of pulses, called Carr-Purcell-Meiboom-Gill (CPMG), is then needed to correctly measure $T2$ even in presence of this issue. When dealing with a non-uniform magnetic field in fact, the FID signal decays faster. The time constant $T2^*$ is introduced and defined as:

$$\frac{1}{T2^*} = \frac{1}{T2} + \frac{1}{T2'} \tag{4.24}$$

where $T2'$ accounts for the effect of field inhomogeneity.

Suppose we divide our probe in many small cubes of equal volume. The external field in each of them is:

$$\mathbf{B}_0, \mathbf{B}_0 \pm \Delta\mathbf{B}, \mathbf{B}_0 \pm 2\Delta\mathbf{B}, \ldots \tag{4.25}$$

Then:

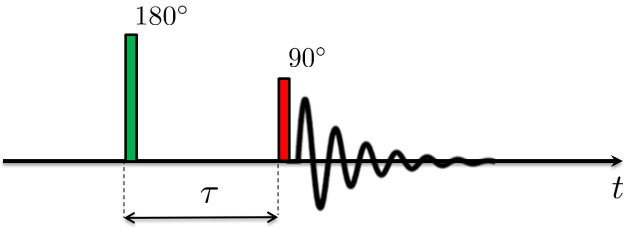

FIGURE 4.7: The Inversion-Recovery sequence is a couple of $180^\circ - 90^\circ$ pulses spaced τ seconds.

a) apply a 90° pulse to bring **M** to the $x'y'$ plane;

b) wait for a time interval τ. During this interval only the contributions to **M** of the cube with $\mathbf{B}_0$ are still (in the rotating reference frame), while the others rotate both clockwise and counterclockwise, as stated by Equation (3.22). Apply then a 90° pulse so that each component reverses with respect to B_1. This operation does not change the rotational speed;

c) after another time interval τ all the components meet together again, providing as a result a signal called *echo* (see Chapter 5 for further details), then they restart dephasing;

d) go back to b).

The CPMG evolution is shown step by step in Figure 4.10, while Figure 4.9 resumes the basic pulse couple. Still, since $T2$ relaxation occurs, the amplitude of the echo signal depends on the time interval τ and on the value of $T2$. $T2$ is the decay time constant of the echoes envelope, as it appears in Figure 4.11, where a complete sequence is performed.

4.4 An Introduction to Fast Field Cycling NMR

Conventional NMR experiments are carried out relying on the presence of a magnetic field with time invariant magnitude, which was previously called $\mathbf{B}_0$. As the name suggests, FFC NMR is instead a technique based on a time-varying magnetic field, which is required to closely follow a particular profile (see Figure 4.12) during the experiment. FFC-NMR is a key tool in relaxometry to highlight even small differences in close values of $T1$. Let us focus on $T1$: it is known that the value of $T1$ of a given tissue changes as function of the applied magnetic field strength. The idea is to highlight differences in $T1$ between different substances by means of a proper field profile, which is reported in Figure 4.12. Note that, while a low value of B_0 would allow to better distinguish substances, this would result in poor SNR with a standard procedure. This motivates the use of FFC NMR approach. The experiment consists of three phases:

- Prepolarisation: Nuclear spin polarization is built up in this phase, at field strength B_{pol};

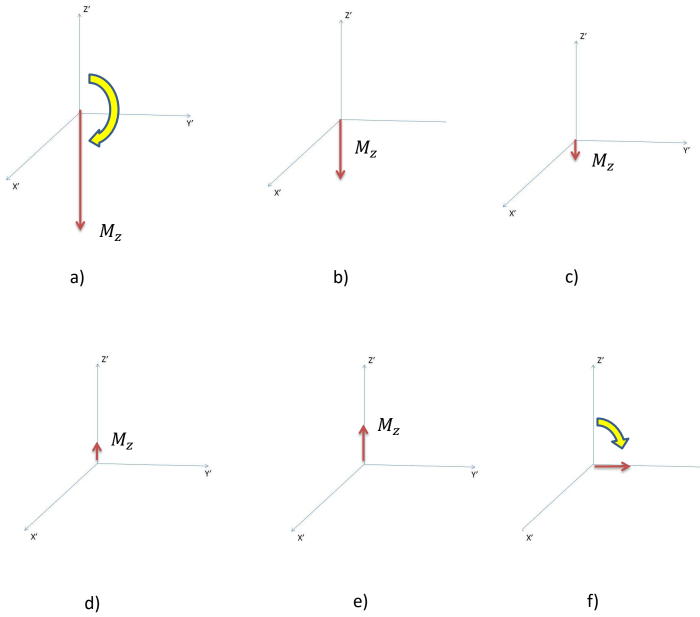

FIGURE 4.8: Time evolution of M_z during an Inversion-Recovery sequence.

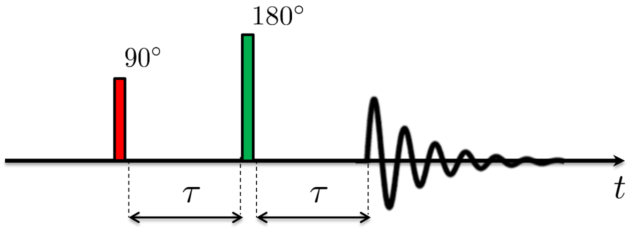

FIGURE 4.9: The CPMG sequence is a couple of $90° - 180°$ pulses spaced τ seconds. After another τ seconds an echo signal is collected.

- Evolution: Spin-Lattice ($T1$) relaxation occurs during this time interval, at field strength B_{rel};
- Detection: a 90° pulse brings the rest of the magnetization down to the $x'y'$ plane where it is sensed by the receiver coil, at field strength B_{acq}. This last phase allows to perform measures at higher field, thus providing a better SNR. This sequence is repeated with different relaxation time in order to measure $T1$ as function of B_{rel}.

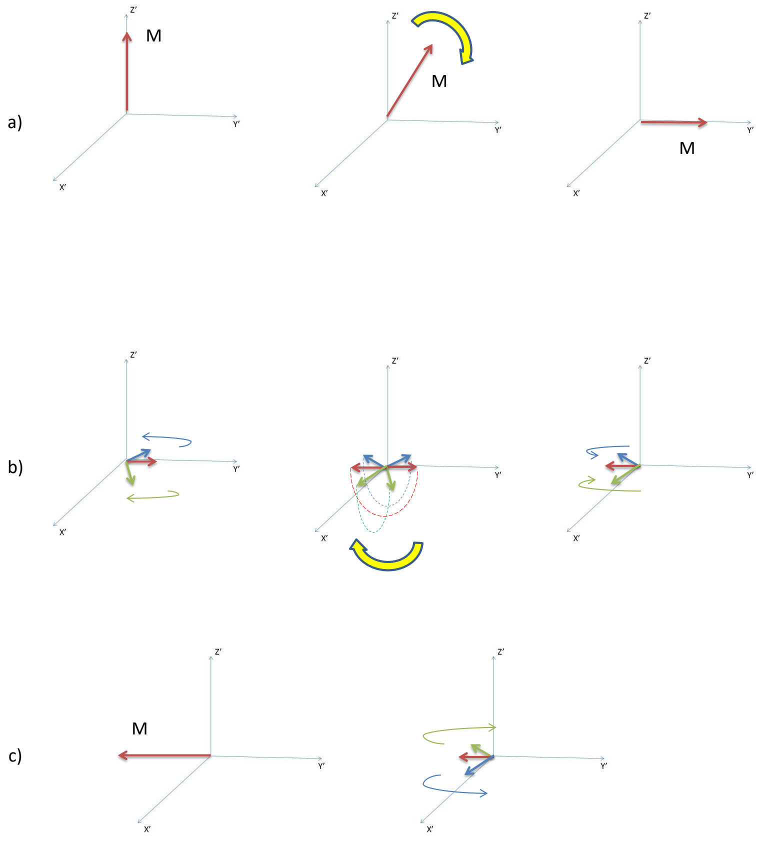
a)
z'
M
y'
x'
z'
M
y'
x'
z'
y'
M
x'
b)
z'
y'
x'
z'
y'
x'
z'
y'
x'
c)
z'
M
y'
x'
z'
y'
x'

FIGURE 4.10: Time evolution of the bulk magnetization vector **M** during a *CPMG* sequence. Note how the different components of **M** rotate at different angular speeds in the rotating frame and how thay refocus after the application of the 180° pulse.

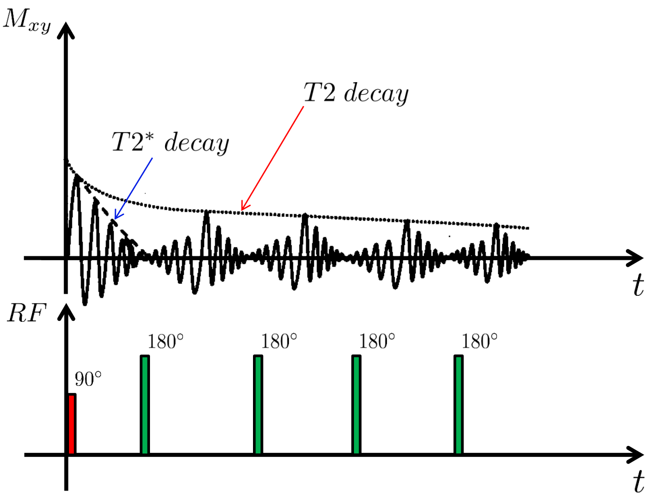
M_{xy}
$T2$ $decay$
$T2^*$ $decay$
t
RF
90°
180°
180°
180°
180°
t

FIGURE 4.11: A complete CPMG execution. Notice that each single FID has time constant $T2^*$, while the overall signal envelope has time constant $T2$.

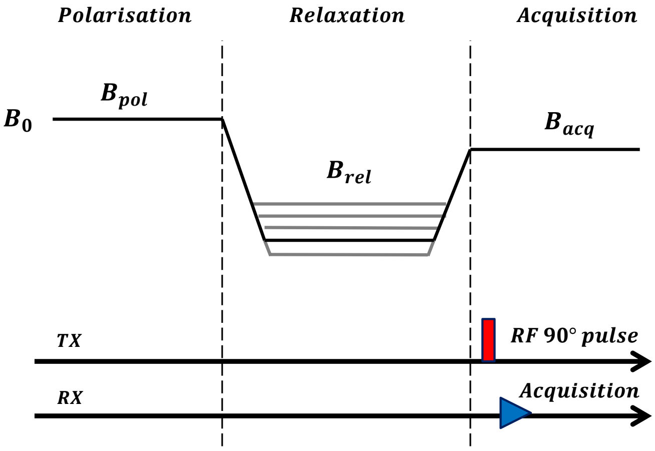
Polarisation
Relaxation
Acquisition
B_0
B_{pol}
B_{rel}
B_{acq}
TX
RF 90° pulse
RX
Acquisition

FIGURE 4.12: The magnetic field evolution during a basic FFC-NMR experiment.

Chapter 5

Non-Homogeneous Magnetic Field, Echoes and Steady State Free Precession

This final chapter of the theoretical introduction to NMR investigates the effects of a non-homogeneous magnetic field. The phenomenon of echo is typically related to the field inhomogeneity and it is therefore considered in this chapter. At the end a qualitative description of the Steady State Free Precession (SSFP) of transverse magnetization is introduced. For further details refer to [18, 27, 28, 29].

5.1 Magnetic Field Inhomogeneity and Echo

Recall that if $\mathbf{B}_0$ is not perfectly homogeneous, the FID exponential envelope has time constant $T2^*$ defined as in 4.24. The faster decay corresponds also to a wider spectrum, since from 4.24 is straightforward that:

$$T2^* < T2 \tag{5.1}$$

Figure 5.1 depicts an example of the Lorentzian shaped NMR spectrum $S(f)$, centred at zero frequency. The latter can be described by:

$$S(f) = \frac{T2^*}{1 + (2\pi f T2^*)^2} \tag{5.2}$$

It is straightforward that both peak value and width are related to $T2^*$. Recall that the area depends on the number of spins in the sample. The *Full Witdh at Half Maximum* Γ is the quantity used to represent the width of the spectral line and it is defined as:

$$\Gamma = \frac{1}{\pi T2^*} \tag{5.3}$$

The mechanism behind this effect is that of loss of coherence: each group of spins i seeing the same magnitude of magnetic field B_{0i} precesses at a given frequency ω_{0i}. Each group is called *isochromat*. In the rotating reference frame each isochromat precesses at angular speed which corresponds to the difference between its speed in the fixed frame xyz and the speed of the rotating frame Ω_0. This results in dephasing of contributions and in transverse relaxation of the bulk magnetization. The wider the spectrum the more the isochromats precessing at different frequencies, resulting in a faster decay and a shorter $T2^*$. The different values of B_{0i} are due to both spin-spin interaction and field inhomogeneity. While the loss of coherence due to spin-spin interaction is not reversible the one caused by non-homogeneous field is reversible:

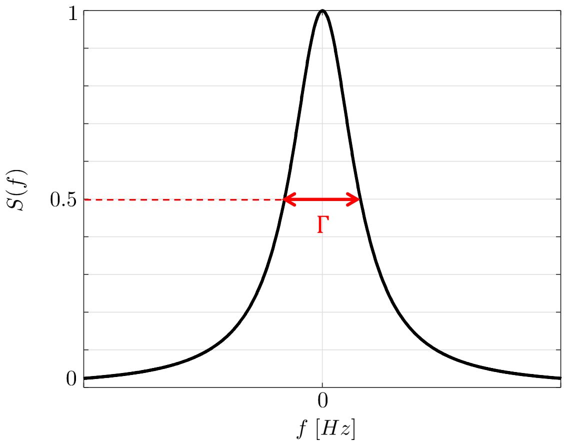

FIGURE 5.1: A Lorentzian shaped NMR spectrum where the *Full Witdh at Half Maximum* is indicated as Γ.

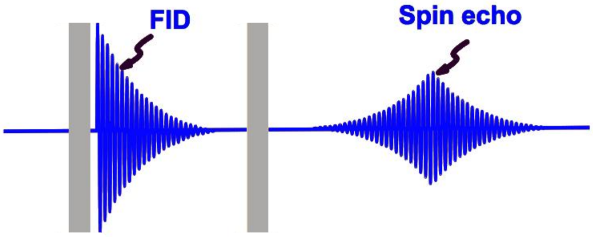

FIGURE 5.2: The *spin-echo* following a pair of pulses.

contributions may rephase generating the phenomenon of echo. When two successive RF pulses are applied to the sample a *Spin Echo* (SE) is generated. The second pulse allows in fact refocusing of spins that have dephased due to static field inhomogeneities. The time interval from the first RF pulse to the echo maximum is called *Echo Time* (TE) and lasts twice the interval between pulses. The signal collected on the transverse plane is represented in Figure 5.2.

In particular a 90° and a 180° pulses are the key of many NMR experiments, such as CPMG that allows to measure $T2$ even in presence of non-homogeneous field. When other flip angles are used, the echo is called *Hahn echo*. For sake of simplicity let consider a couple of 90° pulses. Figure 5.3 shows the evolution of four isochromats.

Assume that isochromats a and b move faster than c and d. The first pulse brings the bulk magnetization down to the $x'y'$ plane (a). At this point contributions start dephasing according to the effective field they see (b). When the second pulse arrives isochromats a and b are not affected as they exactly lie on the x' axis (c), therefore a and b keep on precessing and refocus on the y' axis (d - e - f). Contributions c and d

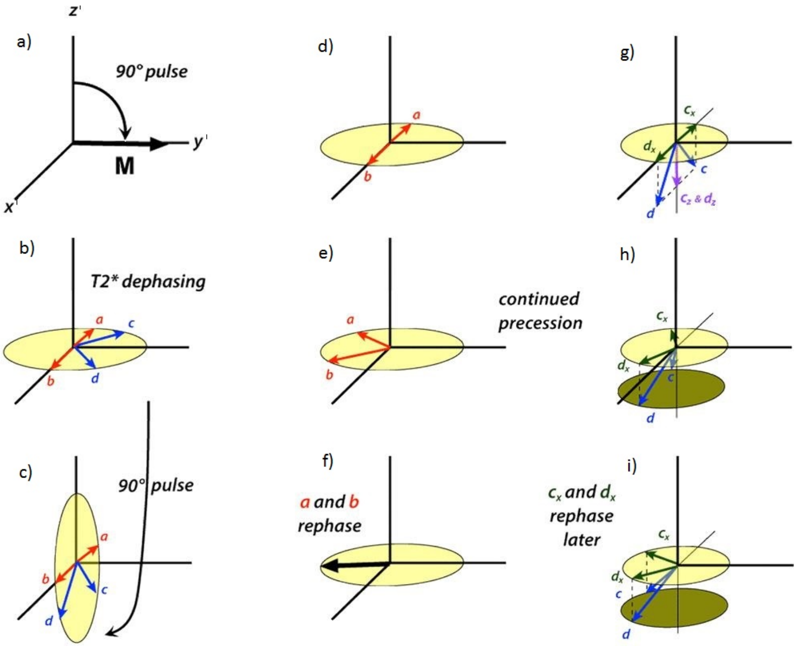
a)
z'
90° pulse
y'
M
x'
b)
T2* dephasing
a
c
b
d
c)
90° pulse
a
b
c
d
d)
a
b
e)
continued precession
a
b
f)
a and b rephase
g)
c_x
d_x
c
c_z & d_z
d
h)
c_x
d_x
c
d
i)
c_x and d_x rephase later
c_x
d_x
c
d

FIGURE 5.3: Evolution of four isochromats in the rotating reference frame as the consequence of a couple of 90° pulses [18].

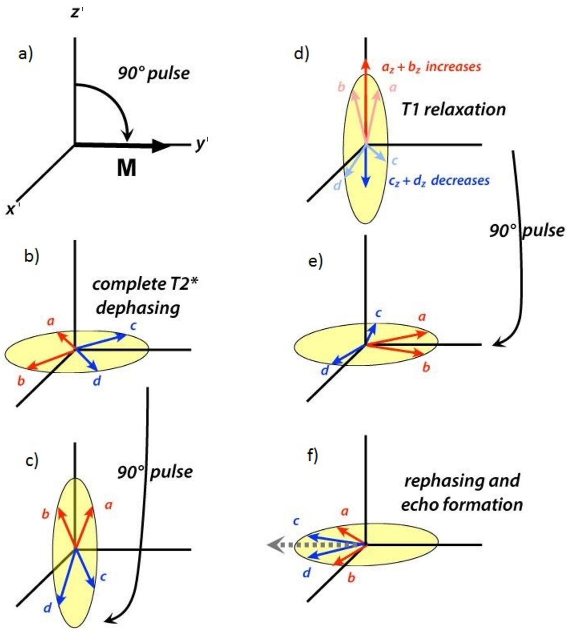
a)
z'
90° pulse
y'
M
x'
b)
complete T2* dephasing
a
c
b
d
c)
90° pulse
b
a
c
d
d)
$a_z + b_z$ increases
b
a
T1 relaxation
c
$c_z + d_z$ decreases
d
90° pulse
e)
c
a
d
b
f)
rephasing and echo formation
c
a
d
b

FIGURE 5.4: Evolution of four isochromats in the rotating reference frame as the consequence of three consecutive 90° pulses [18].

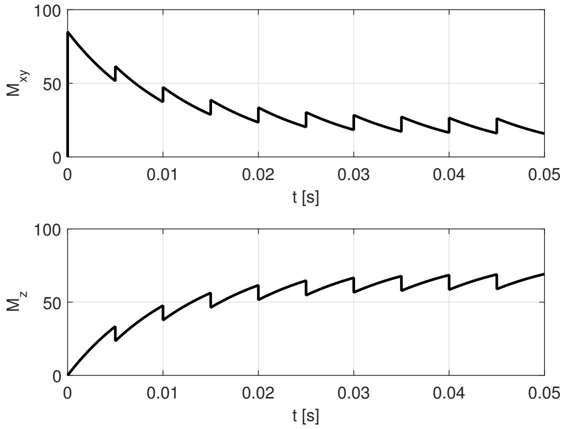

FIGURE 5.5: The steady-state condition of both the longitudinal and transverse components of the magnetization obtained with a train of evenly spaced pulses.

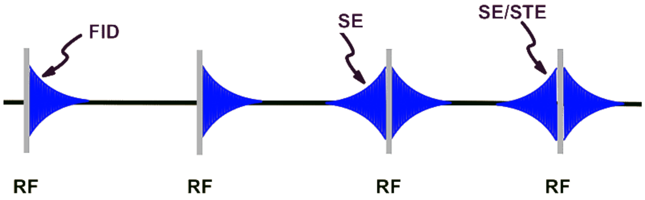

FIGURE 5.6: With evenly spaced pulses spin echoes and stimulated echoes grow and reach a maximum in correspondence of the arrival of a new pulse.

instead are brought to the $x'z'$ plane (c). From now on their components along z will decrease according to $T1$ relaxation: we focus on their components in the $x'y'$ plane, that keep on precessing (g). They are going to refocus as well (h - i), but their echo is going to have a smaller amplitude with respect to that produced by isochromats a and b because part of the magnetization was lost while contributions were locked to the z' axis. In addition the echo will occur later as precession of c and d is slower as stated before. What happens if three pulses are applied? An example is reported in Figure 5.4. Again, let stay with 90° pulses. After the first pulse (a) $T2^*$ decay occurs and contribution precess in the $x'y'$ plane (b). Then the second RF pulse is applied and brings contributions in the $x'z'$ plane (c). At this point they all undergo $T1$ relaxation (d) until the last 90° pulse arrives and brings what is left of the four isochromats back into the $x'y'$ plane (e). Precession is then resumed and the so called *Stimulated Echo* (STE) is going to grow as soon as contributions refocus (f).

5.2 Steady State Free Precession

Up to now the phenomenon of echo was generated by a set of two pulses (SE) or three pulses (STE). Consider now a train of identical RF pulses, evenly spaced, with

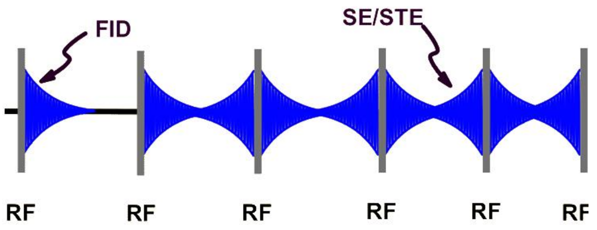

FIGURE 5.7: The Steady State Free Precession regime of the magnetization occurs when the repetition time is shorter than the decay of FID signal. This means that the signal never dies and echoes sum up with the residual signal.

repetition time T. Suppose $T < T1$ and $T > T2$. In this condition pulses arrive before the M_z has returned to its equilibrium value M_0. So the transverse magnetization M_{xy} reaches a steady state value in a short time as well. The steady state situation is depicted in Figure 5.5. Recall that every pair of RF pulses generates a SE and that every triad of pulses produces a STE. As pulses are evenly spaced both kind of echoes occur at the same time, which is also the time of arrival of a new RF pulse, giving rise to a signal like the one in Figure 5.6. If $T < T2^*$, both FIDs and echoes do not reach zero during T, so their contributions sum up and the transverse magnetization never dies out completely. This allows to reach a new steady state condition even in presence of non uniform magnetic field distribution. The SSFP sequence and the resulting signals are shown in Figure 5.7 .

Chapter 6

The NMR Field Frequency Lock

From now on, assume that $\mathbf{B}_0$ is always aligned with the z or z' axis of the reference frame. The magnitude B_0 will be then coinciding with the z component. For sake of simplicity, reference will be made to B_0 for both cases. Similarly, the precession angular speed related to B_0 will be simply referred to as ω_0.
To obtain good results from any NMR experiment, it is necessary guarantee a magnetic field strength B_0 with a very precise value which does not oscillate over time. This, for example, allows to repeat scans in order to improve the SNR or to perform very precise $T1$ and $T2$ measures. Note that, if B_0 drifts or oscillates during time, it is not possible to compare different FID acquisitions since the frequency ω_0, generated by B_0, may not be the same (ω_0 has to be *locked*, i.e. it has to be kept constant). In order to guarantee an accurate achievement of the desired value of B_0, a closed-loop approach can be used. The level of precision required by NMR application is very high, which implies that field sensors must have thin granularity. In addition, note that it is not possible to place any sensor in the sample. This implies that measures may be affected by field inhomogeneity. In order to overcome these problems it is possible to setup a parallel NMR experiment over a known nuclear specie contained in the sample. This allows to measure the frequency deviation, thus estimating the real field experienced by the sample. This chapter is devoted to a theoretical introduction to the Field Frequency Lock (FFL) system, a closed-loop technique to keep B_0 as stable as possible. In particular, we discuss FFL implementation both for general purpose NMR and FFC-NMR. Moreover, a high level analysis of the different pulse sequences for the NMR Lock setup is given. For the lock theoretical introduction, refer to [14, 15, 16, 17, 18, 19], which can be consulted for further details.

6.1 NMR Lock

The classical NMR experiments include an acquisition channel to read the signal related to protons in the sample. In order to realize the lock system a second channel will be necessary. The latter will be used to sense field deviations inside the sample relying on a known nucleus: the deuterium (2H). Deuterium is used in many solvents as its resonance frequency is very far from the one of H. Note that in NMR experiments magnetic fields are measured according to the H resonance frequency they generate (see Equation 3.22). In this respect, a 200 MHz instrument provides 2H resonance at 30.7 MHz, which is quite far from the H resonance frequency (i.e. 200 MHz).

The second channel, here named *lock channel*, continuously detects the 2H signal and monitors its frequency. Any drift in the magnetic field will cause a drift of the deuterium frequency as well. This drift can be detected since the nuclear specie is

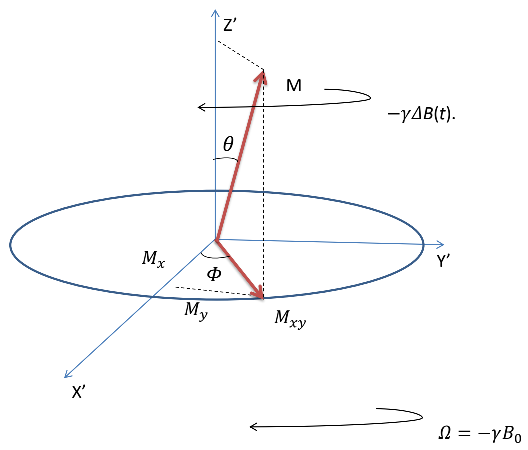

FIGURE 6.1: Precession of the bulk magnetization vector in the rotating reference frame $x'y'z'$.

well known and it can be used as error signal in a feedback loop that adjusts the field strength.

Recall that a RF pulse properly applied to the sample tilts the magnetization **M** of an angle θ with respect to the z axis. In the laboratory frame, **M** precesses about the z axis at a frequency:

$$\omega_0 + \Delta\omega = -\gamma(B_0 + \Delta B) \tag{6.1}$$

where ΔB is the field drift, only acting in the z direction.

In the rotating frame $x'y'z'$, (which rotates at speed $\Omega = \omega_0$, see Figure 6.1), the transverse component of the bulk magnetization, M_{xy}, rotates with frequency:

$$\Delta\omega = -\gamma\Delta B \tag{6.2}$$

In the following, when performing a 90° pulse, we assume that **M** is brought entirely on the x' axis. Therefore, at time t, the angle between M_{xy} and the x' axis, $\phi(t)$, is given by:

$$\phi(t) = \int_0^t -\gamma\Delta B(t)dt \tag{6.3}$$

Under these conditions, M_y can be used to estimate the field drift ΔB. Such value can be used in a closed-loop control scheme in order to bring ΔB to zero. Let consider the dispersion spectrum of the NMR signal in the rotating reference frame. When the magnetic field is exactly at B_0, the spectrum is the one in black in Figure 6.2, that has value zero for $\omega = \omega_0$. If the applied magnetic field is greater than B_0, the spectrum becomes the one in red in Figure 6.2, which presents a negative value for $\omega = \omega_0$. Similarly, when $\Delta B < 0$, the spectrum becomes the one depicted in blue in Figure 6.2, which presents a positive value for $\omega = \omega_0$. We can therefore use the measured value of the dispersion spectrum at $\omega = \omega_0$ in order to stabilise the field. Unfortunately this method works only for small values of ΔB. In fact, if ΔB increases over a certain value, the dispersion spectrum at $\omega = \omega_0$ increases instead of decreasing. In addition, if ΔB decreases over a certain value, the dispersion spectrum at $\omega = \omega_0$ decreases instead of increasing. Moreover, the dispersion

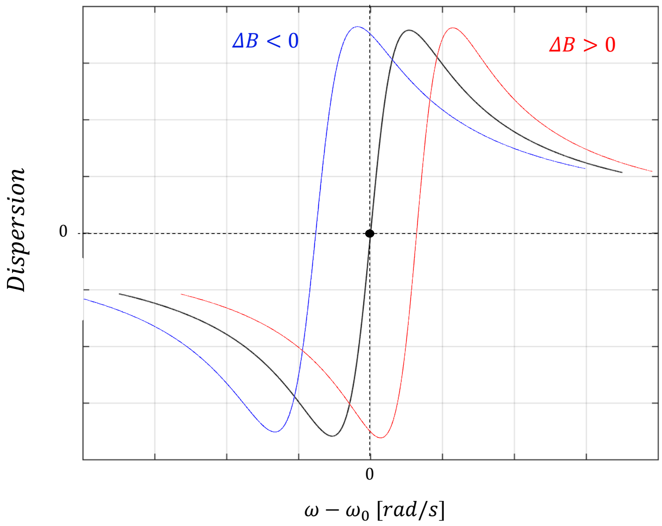

FIGURE 6.2: The dispersion spectrum as function of the frequency deviation from the receiver one.

spectrum at $\omega = \omega_0$ is almost zero for $|\Delta B|$ greater than a certain threshold. This behaviour limits the application of FFL to the compensation of small values of ΔB. In this respect the NMR lock experiment can be considered a sort of sensor which is characterized by thin granularity, high sensitivity and fast dynamic response but narrow linear range.

6.2 Locking the FFC-NMR

The FFL is a key technique used in NMR application that can be adapted to FFC NMR as well. In fact, FFC-NMR requires the main magnetic field to follow a particular profile during time, then requires it to stay as still as possible at the desired value during the detection phase (see Chapter 4.4 for details). In addition, the magnetic field must move from the evolution value to the detection one in a limited interval of time t_A, that has to be very short ($t_A < 10$ $msec$), independently of the sample under analysis. This opens up a completely new control problem, but the lock system is still the key to obtain the desired behaviour of the detection field. As discussed above, this particular kind of FFL must also guarantee a maximum *locking time*, requiring a deep knowledge of the whole system under control. This also motivates a model-based approach for the synthesis of the controller and the focus on mathematical description of the NMR signal, on the magnet and on the acquisition chain treated in the following chapters.

6.3 Lock Pulse Sequencies

Different pulse sequences allow to obtain NMR signals which can be exploited as lock signals. Nevertheless, each kind of lock signal provides different characteristics which really define the approach to the problem.

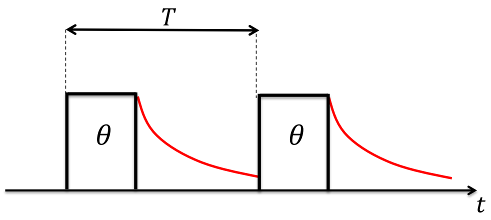

FIGURE 6.3: Sequence of Low Repetition Rate pulses with repetition time T. These are typically 90° pulses and generate a complete FID signal.

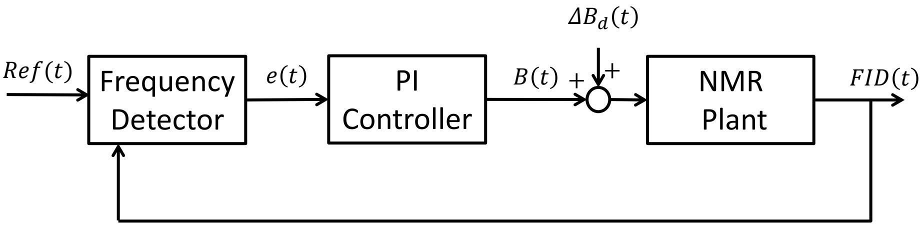
ΔB_d(t)
Ref(t)
Frequency Detector
e(t)
PI Controller
B(t)
+
+
NMR Plant
FID(t)

FIGURE 6.4: A Phase-Locked Loop approach for the FFL system. The PSD compares the frequency of the FID signal to the reference one and outputs the error signal that is proportional to the frequency deviation. Then the controller generates a field correction on the basis of the error signal.

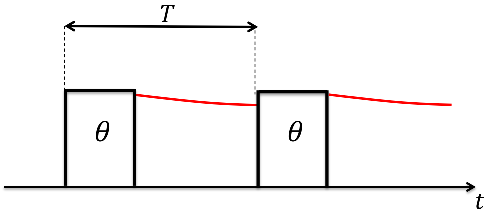

FIGURE 6.5: Sequence of High Repetition Rate pulses with repetition time $T << T1, T2$. The low power pulses allow reaching a steady state condition where the signal is not decaying anymore.

6.3.1 Low Repetition Rate (LRR) Lock Pulses

FFL systems can be categorized according to their pulse sequence parameters: based on the pulses repetition time T, they can be divided in *Low Repetition Rate* (LRR) and *High Repetition Rate* (HRR). In the LRR FFL the NMR response is generated by a train of high-power pulses at a low repetition rate (tenth of Hz). Typically these pulses provide a tilt angle $\theta = \pi/2$, with $T > T1$. The collected signal is then the actual FID, as in Figure 6.3. The LRR FFL samples the FID and uses a *Phase-Locked Loop* (PLL) to drive the FID frequency to the transmitter one. The PLL is based on a Frequency Detector, which outputs a signal proportional to the difference of the FID frequency and the frequency of the transmitter. Then this signal is then used as error signal for the controller. The overall closed-loop scheme is shown in Figure 6.4, where the controller is a PI. The last part of the FID signal can no longer be used to provide a measure of the resonant frequency as the SNR is too low to obtain a reliable computation of the frequency deviation. The system must wait for the next pulse to excite again the sample. An integrator is typically used to maintain the level of the correction field during pulses and to preserve locking condition. This PLL approach is anyway ineffective at attenuating high frequency fluctuations, as the frequency changes in the FID are not sensed instantaneously. Examples of PLL implementation can be found in [19, 30, 20, 31].

6.3.2 High Repetition Rate (HRR) Lock Pulses

This class includes low power, high repetition rate pulses are applied to the sample to bring it into SSFP regime. In fact the steady state value of the transverse magnetization is strictly related to the frequency deviation from the resonance condition. The HRR class of FFL excites the nuclei with a series of low-power pulses at a high repetition rate (several kHz). Each pulse must provide the same tilt angle $\theta << \pi/2$ with $T << T1, T2$ to reach a steady state condition. Under this hypothesis M_{xy} is approximated as constant in each inter-pulse interval, as in Figure 6.5. When a field deviation is present, the dispersion signal is non-zero and can be used as error signal for the control loop with reference set to zero. This approach can face higher frequency magnetic field fluctuations with respect to the LRR class as it updates more frequently. This also implies that there is a short time to perform computations. Moreover, this system is approximately linear only in a small region around the resonant condition, thus it is unable to handle disturbance amplitudes larger than the width of this linear region. However, the need for a controller able to providing locking in a short time interval (tenths of milliseconds) forces the choice to the HRR class of sequences. Hence a model for the description of the SSFP regime is needed. Examples of HRR approach for lock systems can be found in [19].

Chapter 7

NMR Hardware and Firmware

In this chapter a detailed description of the hardware and firmware used for NMR experiment is given. In particular focus is on the elements which characterize the signal which will be used as feedback for the Lock system, such as the probe, the magnet and the quadrature detector. Relevant transfer functions are derived as well. At the end the digital implementation of the acquisition chain is introduced. Further details can be found in [14, 15, 16, 17, 18, 32].

7.1 Probe and Transmitter/Receiver

The probe is a cylindrical tube (non-magnetic metal tube in standard spectrometer, glass tube in FFC-NMR) which contains the sample to be analysed and is inserted into the bore of the magnet. The key component of the probe is the so called *tuned circuit* (see Figure 7.1), which allows to excite the sample and to collect the NMR signal. It is composed of a coil and two capacitors. The inductance and the capacitances are designed so that the resulting tuned circuit they form is resonant at the Larmor frequency. The two capacitors play slightly different roles: the *tune* capacitor is used to set the frequency of the LC circuit while the *match* one is used to maximize the power transfer between the probe and the transmitter/receiver. Notice that the same coil is used both as transmitter and receiver. When working as transmitter the coil is used to apply the RF wave to the sample, when working as receiver it is used as sensor to collect the FID signal. The radiofrequency (RF) oscillator generates a low power signal which needs to be boosted to be properly applied to the sample. An amplifier is therefore used to push this small signal to a proper power. In addition, as the RF pulse is only applied for a short time, this signal has to be *gated*. The switching of the gate is typically controlled by means of a dedicated control line.

7.2 Magnets

The main magnetic field B_0 can be generated by different kinds of magnets. In the context of NMR, typical choices for magnets are permanent, superconducting and resistive magnets. Permanent magnets can provide a fixed magnetic field B_0, characterised by high stability (problems are only due to thermal derives); in this work, a permanent magnet will be used to perform experiments to characterise the lock sample dynamic behaviour. Superconducting magnets allow to generate different values of B_0, with good stability performances. Still, they are not suitable for FFC NMR since their dynamic response is very slow and does not allow to quickly switch from the different magnetic field levels. Finally, resistive magnets provide very fast

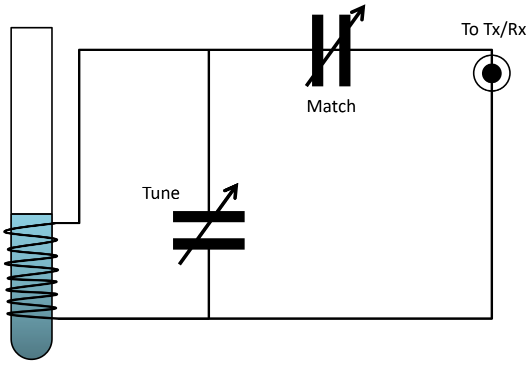

FIGURE 7.1: The tuned circuit in the probe is composed of an inductance (the coil used for generating the pulses) and two capacitors (match and tune)

Voltage Step [*V*]	1	2	−1	−2	0.5
Time Constant [*s*]	1.7161	1.5682	1.3729	1.5868	1.201

TABLE 7.1: Superconducting magnet time constant identification trials. Estimated time constant for each applied voltage step.

dynamic responses, but typically generate a magnetic field affected by stability problems arising from current oscillations. The different magnets are now discussed in detail.

7.2.1 Superconducting Magnet

A HTS 2T superconducting magnet is considered, which is capable of providing suitable values for the generated field. At low temperatures (less than $6°K$) the resistance goes very close to zero. Thus cooling the magnet is crucial to obtain good results. For this purpose different cryogenic fluids like *Galden* can be used. In addition the whole assembly is placed in a vacuum flask to further reduce the heat flow. In order to introduce current in the magnet when it is operating in persistent current mode, the joint between superconductive and regular wire is heated up by means of thermoresistive actuators. At the end of the operation the joint is cooled again to open the circuit. The main current is injected by means of a microprocessor controlled, low voltage power supply. This device needs a control loop to avoid abrupt current changes as this may lead to eddy currents and mechanical stress for the assembly which is a very large inductor ($L = 0.1\ H$). Considering the high inductance L and very low resistance R of the magnet it is clear that the magnet reacts quite slowly to changes in the current set point. This must be seriously taken into account when designing the control loop for the lock system, as the output of the controller will generate a correction field actuated via current. Therefore a model for the magnet must be developed. A first order low pass model can fit the behaviour of the magnet, hence the parameters needed to write its transfer function are a static gain μ_{mag} and a time constant τ_{mag}. The static relation between current and field is almost linear up to $60\ A$ ($1423, 1\ G$ magnetic field) and then starts saturating. Typical values for NMR proton resonance is about $21\ A$ (i.e. a Larmor frequency of about $21\ MHz$), while for deuterium it is even lower, so there is no need at this point to introduce a look-up table or a polynomial approximation for the nonlinear region of the curve as these current values fall into the linear one. The proportionality coefficient will represent the static gain of the magnet transfer function. To model the magnet around this working point as a first order low pass filter, it is instead necessary to define its time constant. The resistance depends on the temperature and goes very close to zero at working conditions. Still, its value at working point is not known, therefore it is not possible to compute the time constant by referring to the usual formula for RL circuits. It is necessary to evaluate it from experimentally collected data. The desired current is generated applying a voltage step over a 200Ω resistance via a voltage buffer. The usual procedure includes to apply step variations of the main current and measure the relative field variation. The field may not be really homogeneous within the probe: a measure performed outside of it may not represent exactly the field experienced by nuclei. In addition a small-signal model of the magnet around its working point will be developed; the field variations may be very small, so a very fine granular magnetic field sensor is required. To overcome these two problems it is possible to obtain a measure of the magnetic field inside the probe directly from the NMR experiment. According to (6.2), the field deviation is expected to closely represent the frequency deviation one.

Stelar acquisition software provides precise estimation of the NMR signal deviation frequency $\Delta\omega$ from the analysis of the NMR signals itself. This estimation will be considered for the evaluation of the magnet time constant. The experiment design is the following:

- Voltage steps of $1V$, $2V$, $-1V$,$-2V$, $0.5V$ are generated;
- NMR signals are collected using Stelar software and the deviation frequency $\Delta\omega$ is estimated.

Matlab Identification Toolbox [33] is exploited to estimate for each experiment the parameters of a first order transfer function. Note that a pure delay is introduced in the model to take into account possible delays into the application of the input step (which is done via software). The resulting time constants are shown in Table 7.1. The mean of the five estimations is used in the final model for the magnet, which results:

$$\tilde{G}_{mag}(s) = \frac{\Delta B(s)\ [G]}{\Delta V(s)\ [V]} = \frac{\mu_{mag}\mu_{ps}C}{1+s\tau_{ps}} = \frac{230.767}{1+1.4879s} \tag{7.1}$$

at a working point of 21.4 A, providing a magnetic field of 5007.6 G.

7.2.2 Permanent Magnet

A permanent magnet is also used for NMR model investigation and validation as it provides a much more stable field than the HTS magnet introduced above. The permanent magnet generates a B_0 magnetic field of about 5000 G, which is comparable to the one produced at working point by the superconducting magnet.

7.2.3 IDentIFY Magnet Prototype

The main magnet which will be used for closed-loop experimental trial is a resistive magnet, developed by Stelar [23] for the IDentify Project. This magnet is able to cope with the strict time requirements of the FFC experiment, allowing fast switches of the magnetic field and, at the same time, guaranteeing the desired level of homogeneity throughout the NMR sample. The magnet is equipped with a dedicated power supply developed by IECO [34] for the IDentify Project. The power supply features an internal control loop with integral action, tuned to provide no oscillations in the closed-loop step response and a closed-loop bandwidth of about 10 KHz.

The control action is introduced by summing the control current to the overall current reference of the power supply. Let therefore denote the current control action as ΔI^*. The power supply unit is then modelled as a first order transfer function relating ΔI_{ps}, i.e. the power supply current deviation from the resonance condition, to ΔI^*:

$$G_{ps}(s) = \frac{\Delta I_{ps}\ [A]}{\Delta I^*\ [A]} = \frac{\mu_{ps}}{1 + s\tau_{ps}} \tag{7.2}$$

The magnet is instead modelled as a static gain:

$$\mu_{mag} = \frac{\Delta B_{mag}\ [G]}{\Delta I\ [A]} \tag{7.3}$$

with ΔB_{mag} the magnet field deviation from the resonance condition.

7.3 Signal Detection

In the following the approaches used for signal detection are introduced. These approaches allow to obtain absorption and dispersion spectra used in NMR applications. The introduction of the rotating reference frame, as defined in Chapter 3, allows to remove FID oscillations and consequently to focus on the envelope decay. It also moves the NMR spectrum at zero frequency rather than at the Larmor one. In order to obtain this result, a *Phase Sensitive Detector* (PSD) or a *Quadrature Detector* (QD) has to be introduced in the acquisition channel.

7.3.1 Phase Sensitive Detection

The *Phase Sensitive Detector* (PSD) is a powerful method for seeing very small signals in presence of heavy noise and to move the signal to the desired frequency range. To understand how it works, let define a couple of simple signal. Let v_i be the signal from the probe, a FID signal:

$$v_i = M_x = v_{i0} cos(\omega_i t) e^{-\frac{t}{T2}} \tag{7.4}$$

Let v_r be a reference signal oscillating at the Larmor frequency:

$$v_r = v_{r0} cos(\omega_0 t) \tag{7.5}$$

Note that in this way ω_0 represents the receiver frequency. These signals are multiplied together so that the detected signal is given by:

$$v_i v_r = v_{i0} v_{r0} e^{-\frac{t}{T2}} cos(\omega_i t) cos(\omega_0 t) = v_{i0} v_{r0} e^{-\frac{t}{T2}} (cos(\omega_i - \omega_0)t + cos(\omega_i + \omega_0)t) \tag{7.6}$$

A low pass filter is used to cancel the term with frequency $\omega_i + \omega_0$ and the final detected signal oscillates at $\Delta\omega = \omega_i - \omega_0$:

$$M'_x = \frac{1}{2} v_{i0} v_{r0} e^{-\frac{t}{T2}} cos(\omega_i - \omega_0)t \tag{7.7}$$

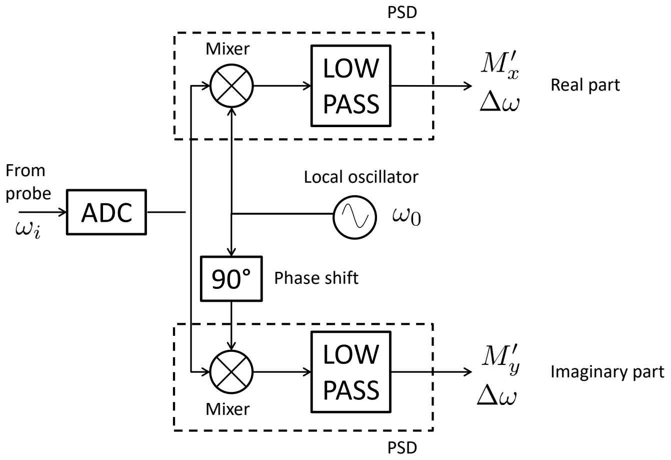

FIGURE 7.2: Block scheme for a quadrature detector: the signal coming from the probe is multiplied by a cosinusoidal reference on the real path and then filtered. On the imaginary path the incoming signal is multiplied by a sinusoidal reference and then it is passed through the low pass filter. This allows to obtain the real and imaginary signals.

The FT of this signal gives the NMR spectrum centered at zero frequency when in resonance. If only the real channel M_x is used to build an NMR spectrum it is not possible to distinguish between a ω_i and a $-\omega_i$ rotation of the vector from the supplied data. In fact the FT of a cosinusoidal signal has positive peaks at both ω_i and $-\omega_i$. This implies that after the FT one cannot discriminate positive and negative frequencies. In order to solve the problem both the M_x and M_y are used as input into the complex FT, which is designed to deal with two dimensional signals. The two orthogonal input are called the *real* (M_x) and *imaginary* (M_y) channels. A proper combination of the complex FT of the two signals allows in fact to obtain a spectrum which allows to discriminate among positive and negative rotations. This approach is called *quadrature detection* and is the method of detection on modern spectrometers and imagers.

7.3.2 Quadrature Detection

Quadrature Detection (QD) involves the collection of time domain NMR data related to both M_x and M_y .This is done via two separate receiver coils or via a single one with the presence of a 90° phase delay unit. Figure 7.2 shows a complete block scheme for a QD. Note that complex FT generates two spectra for each input signal: one is called *real* spectrum, the other *imaginary* spectrum.

The signal coming from the probe is running at frequency ω_i, which is expected to be close to the Larmor frequency ω_0 but not exactly the same. The local oscillator generates a wave at a reference frequency ω_0 , i.e. the receiver frequency is set to be equal to the Larmor one. The inputs to the first PSD are the reference signal and the one from the receiver. The output M'_x is therefore a cosinusoidal wave running at the difference of the frequency of the input signals ($\Delta\omega$):

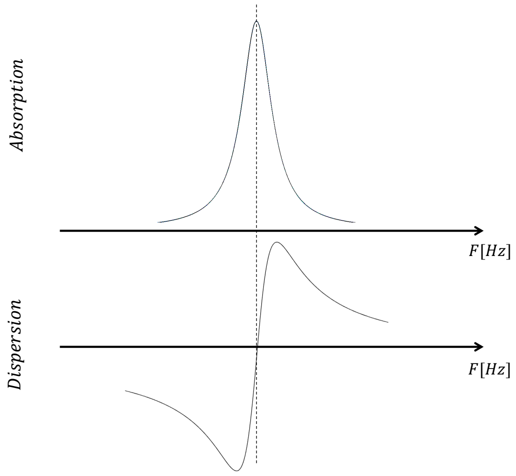

FIGURE 7.3: Absorption and dispersion mode spectra.

$$M'_x = \frac{1}{2} v_{i0} v_{r0} e^{-\frac{t}{T2}} cos\Delta\omega t \tag{7.8}$$

The inputs of the second PSD are identical to the first except for the phase of the reference signal that is shifted by 90°. The output M'_y is therefore similar to the first PSD one except that it has a 90° phase difference:

$$M'_y = \frac{1}{2} v_{i0} v_{r0} e^{-\frac{t}{T2}} sin\Delta\omega t \tag{7.9}$$

The two outputs are the real and imaginary FIDs in the rotating reference frame. Both are used as inputs to the complex FT. The real output,M'_x,is the x component of the FID in the rotating reference frame. The imaginary output, M'_y , is the y component of the FID in the rotating reference frame. The complex FT produces a real spectrum and an imaginary spectrum for each of the input signal, therefore the output of the QD is a set of four spectra. For the purpose of better understanding the effect of the quadrature detection method, the manipulation of spectra that allows to build up a conventional NMR absorption and dispersion spectra (Figure 7.3) from the quadrature-collected FIDs is now introduced. Assume that the signal from the probe to be:

$$v_i = M_x = v_{i0} cos(\omega_i t) e^{-\frac{t}{T2}} \tag{7.10}$$

According to the previous discussion one has:

$$M'_x = \frac{1}{2} v_{i0} v_{r0} e^{-\frac{t}{T2}} cos\Delta\omega t \tag{7.11}$$

$$M'_y = \frac{1}{2} v_{i0} v_{r0} e^{-\frac{t}{T2}} sin\Delta\omega t \tag{7.12}$$

The application of the complex FT to M'_x produces a real and an imaginary spectrum, as depicted in Figure 7.4a. For the real channel, these are labelled the real spectrum of the real channel (Re ft(M'_x)) and the imaginary spectrum of the real channel (Im ft(M'_x)). The application of the complex FT to M'_y produces a real and an imaginary spectrum, as depicted in Figure 7.4b. For the imaginary channel, these are labelled the real spectrum of the imaginary channel (Re ft(M'_y)) and the imaginary

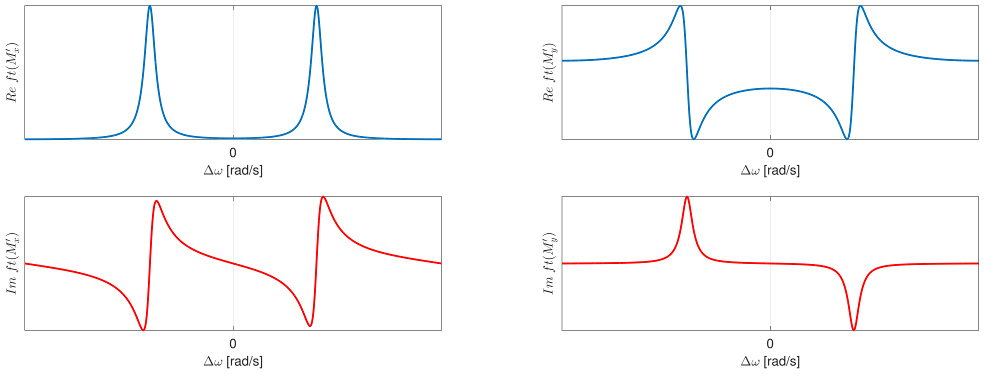

(A) (B)

FIGURE 7.4: (A) Complex Fourier Transform of M'_x. (B) Complex Fourier Transform of M'_y.

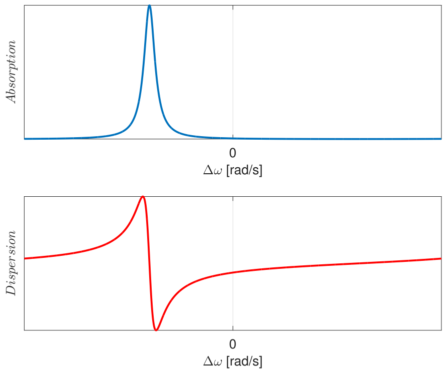

FIGURE 7.5: Absorption and dispersion mode spectra. The sum the real part of the real channel and the imaginary part of the imaginary channel allows to obtain the abosrption mode spectrum correctly setup to distinguish among positive and negative frequencies. The difference if the imaginary part of the real channel from the real part of the imaginary channel allows to build up the dispersion mode spectrum correctly placed in frequency.

spectrum of the real imaginary (Im ft(M'_y)).Recall that 0 Hz is the Larmor Frequency in the rotating frame.

To obtain the overall absorption spectrum the real of the real and the imaginary of the imaginary are required, as follows:

$$Absorption = Re\ ft(M'_x) + Im\ ft(M'_y) \tag{7.13}$$

The overall dispersion spectrum is produced in a similar manner using the imaginary spectrum from the real channel and the real channel of the imaginary spectrum:

$$Dispersion = Re\ ft(M'_y) - Im\ ft(M'_x) \tag{7.14}$$

The reconstructed absorption and dispersion spectra are reported in Figure 7.5.

7.4 Acquisition Chain Digital Implementation

A digital implementation on *Field Programmable Gate Array* (FPGA) of the acquisition chain allows to deal with very fast signals and achieve at the same time great

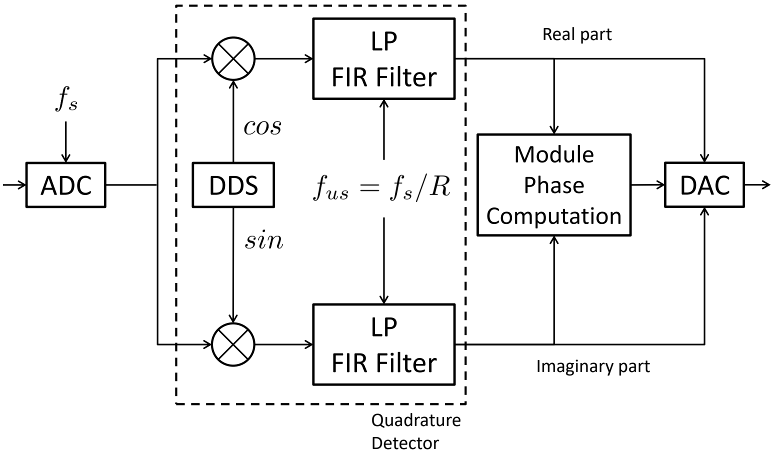

FIGURE 7.6: The acquisition chain. The incoming signal is digitized by means of a 12 *bit* ADC with sampling frequency f_s of 400 *MHz*. Then the digital signal goes through the quadrature detector. Notice that the two low pass filters also introduce a decimation factor R. In the end signals (Real, Imaginary, Module, Phase) are sent to a DAC.

flexibility. The signal coming from the probe is first amplified by means of a low noise amplifier. Then it is ready to be digitalised using a fast ADC. In particular a 12 *bit*, 400 *MHz* sampling frequency ADC is used. The digital signal goes through the quadrature detection steps which were introduced before. All the components of the detector are realized on the FPGA. The sinusoidal and cosinusoidal reference waves for the mixers are generated using a *Direct Digital Synthesizer* (DDS). The low pass filter is implemented as a *Finite Input Response* (FIR) filter with cut frequency of 700 *KHz*. After the filter the sampling frequency is reduced to 1.4 *MHz*, which is still consistent with Nyquist theorem: signals coming out of the filter run at frequencies which are lower than 700 *KHz*, therefore the new sampling frequency is always greater than twice that frequency. The overall system is depicted in Figure 7.6.

The system gives as output the real signal, the imaginary signal, module and phase. In a standard NMR application these signals undergo further filtering and elaboration, and then they are sent to a 16 *bit* DAC. For lock purposes instead the imaginary signal will be compared to a reference and the difference will feed the regulator. Then the compensation signal will be sent to the system through the 16 *bit* DAC. In a continuous-time framework the transfer function from the probe to the DAC, when the latter works in a linear way, can be approximated as:

$$G_{qd}(s) = \frac{\mu_{qd}}{1 + s\tau_{qd}} \tag{7.15}$$

Chapter 8

Models for NMR Steady State Free Precession

As it was previously discussed, the synthesis of the regulator will be driven by a mathematical description of the phenomenon, so that a good control of precision, settling time and disturbance rejection can be obtained. In this section a set of models for the NMR running in SSFP regime are investigated and compared each other, then they are validated using real data collected from NMR trials.

8.1 An (Only Apparent) Contradiction

The NMR models introduced in this chapter are based on parameters that change quite frequently and in some cases radically. So, tuning a regulator that guarantees good performances for any possible values of the parameters is difficult. In addition, only some of these parameters are known a priori (T, θ,γ), but others have to be directly measured from the process. This seems a contradiction as the Lock system is meant to improve these measures. Still, many NMR and FFC-NMR experiment needs at least a rough estimation of these parameters to be properly set up in terms of timing and field strength, so this way of operating is not unusual. Moreover, a model-based lock system exploits these initial estimations to tune the regulator, which should be parametrised and is recomputed every time one of the parameters changes.

8.2 Bloch Equations

During an NMR experiment, the behaviour of the bulk magnetization vector **M** in the stationary reference frame can be described by the following set of differential equations, known as Bloch Equations [35]:

$$\frac{dM_x(t)}{dt} = \gamma\left(\mathbf{M}(t) \times \mathbf{B}(t)\right)_x - \frac{M_x(t)}{T2} = \gamma\left(M_y(t)B_z(t) - M_z(t)B_y(t)\right) - \frac{M_x(t)}{T2} \tag{8.1}$$

$$\frac{dM_y(t)}{dt} = \gamma\left(\mathbf{M}(t) \times \mathbf{B}(t)\right)_y - \frac{M_y(t)}{T2} = \gamma\left(M_z(t)B_x(t) - M_x(t)B_z(t)\right) - \frac{M_y(t)}{T2} \tag{8.2}$$

$$\begin{aligned}\frac{dM_z(t)}{dt} &= \gamma\left(\mathbf{M}(t) \times \mathbf{B}(t)\right)_z - \frac{M_z(t) - M_0}{T1} = \gamma\left(M_x(t)B_y(t) - M_y(t)B_x(t)\right) + \\ &\quad - \frac{M_z(t) - M_0}{T1}\end{aligned} \tag{8.3}$$

where:

- $M_x(t)$,$M_y(t)$,$M_z(t)$ are the three components of bulk magnetization vector $\mathbf{M}$ in the stationary reference frame;
- $B_x(t)$,$B_y(t)$,$B_z(t)$ are the components of the overall magnetic field $B(t)$ experienced by nuclei in the sample, i.e. $\mathbf{B}(t) = B_0(t) + B_1(t) + \Delta B(t)$;
- M_0 is the equilibrium value of the magnetization;
- $T1$, $T2$ are the relaxation time constants;
- γ is the gyromagnetic ratio;
- $(\mathbf{M}(t) \times \mathbf{B}(t))_i$ is the component of the matrix product of $\mathbf{M}(t)$ and $\mathbf{B}(t)$ along the generic axis i.

For $T1$,$T2 \to \infty$ (i.e. no relaxation occurs), Bloch Equations describe the Larmor precession about the z axis.

$$\frac{dM_x(t)}{dt} = \gamma\left(\mathbf{M}(t) \times \mathbf{B}(t)\right)_x \tag{8.4}$$

$$\frac{dM_y(t)}{dt} = \gamma\left(\mathbf{M}(t) \times \mathbf{B}(t)\right)_y \tag{8.5}$$

$$\frac{dM_z(t)}{dt} = \gamma\left(\mathbf{M}(t) \times \mathbf{B}(t)\right)_z \tag{8.6}$$

Let introduce the complex quantities $M_{xy}(t)$ and $B_{xy}(t)$ to describe what happens in the xy plane.

$$M_{xy}(t) = M_x(t) + iM_y(t) \quad \overline{M}_{xy}(t) = M_x(t) - iM_y(t) \tag{8.7}$$

$$B_{xy}(t) = B_x(t) + iB_y(t) \quad \overline{B}_{xy}(t) = B_x(t) - iB_y(t) \tag{8.8}$$

Bloch Equations can be written in the following formulation:

$$\frac{dM_x(t)}{dt} = \gamma\left(M_{xy}(t)B_z(t) - M_z(t)B_{xy}(t)\right) - \frac{M_{xy}(t)}{T2} \tag{8.9}$$

$$\frac{dM_z(t)}{dt} = \gamma\left(M_{xy}(t)\overline{B}_{xy}(t) - M_{xy}(t)\overline{B}_{xy}(t)\right) - \frac{M_z(t) - M_0}{T1} \tag{8.10}$$

Let now introduce the rotating reference frame $x'y'z'$ with $z = z'$ and let Ω be its angular speed. Then:

$$M'_{xy}(t) = e^{i\Omega t} M_{xy}(t) \tag{8.11}$$

$$M'_z(t) = M_z(t) \tag{8.12}$$

Performing derivative one obtains:

$$\begin{aligned}
\frac{dM'_{xy}(t)}{dt} &= e^{i\Omega t}\frac{dM_{xy}(t)}{dt} + i\Omega M'_{xy}(t) && (8.13)\\
&= e^{i\Omega t}\left[-i\gamma\left(M_{xy}(t)B_z(t) - M_z(t)B_{xy}(t)\right) - \frac{M_{xy}(t)}{T2}\right] + i\Omega M'_{xy}(t) && (8.14)\\
&= \left[-i\gamma\left(M_{xy}(t)e^{i\Omega t}B_z(t) - M_z(t)B_{xy}(t)e^{i\Omega t}\right) - \frac{M_{xy}(t)}{T2}\right] + i\Omega M'_{xy}(t) && (8.15)\\
&= -i\gamma\left(M'_{xy}(t)B'_z(t) - M_z(t)B'_{xy}(t)\right) + i\Omega M'_{xy}(t) - \frac{M_{xy}(t)}{T2} && (8.16)\\
& && (8.17)\\
\frac{dM'_z(t)}{dt} &= \frac{i\gamma}{2}\left(M_{xy}(t)\overline{B}_{xy}(t) - \overline{M}_{xy}(t)B_{xy}(t)\right) - \frac{M_z(t) - M_0}{T1} && (8.18)
\end{aligned}$$

Since $z = z'$, $B'_z = B_0 + \Delta B(t)$, so it is possible to write:

$$\begin{aligned}
\frac{dM'_{xy}(t)}{dt} &= -i\gamma\left(M'_{xy}(t)(B_0 + \Delta B(t)) - M_z(t)B'_{xy}(t)\right) + i\Omega M'_{xy}(t) - \frac{M_{xy}(t)}{T2} && (8.19)\\
&= -i\gamma M'_{xy}(t)B_0 - i\gamma M'_{xy}(t)\Delta B(t) + i\gamma M_z(t)B'_{xy}(t) + i\Omega M'_{xy}(t) - \frac{M_{xy}(t)}{T2} && (8.20)\\
&= i(\Omega - \omega_0)M'_{xy}(t) - i\gamma M'_{xy}(t)\Delta B(t) + i\gamma M_z(t)B'_{xy}(t) - \frac{M_{xy}(t)}{T2} && (8.21)\\
& && (8.22)\\
\frac{dM'_z(t)}{dt} &= \frac{i\gamma}{2}\left(M_{xy}(t)\overline{B}_{xy}(t) - \overline{M}_{xy}(t)B_{xy}(t)\right) - \frac{M_z(t) - M_0}{T1} && (8.23)
\end{aligned}$$

Let $\Omega = \omega_0$ and apply RF pulses on resonance, along y' (i.e. $B'_x = 0$ and $B'_y = B'_1$), then:

$$\begin{cases}
\dfrac{dM'_x(t)}{dt} = \dfrac{-1}{T2}M'_x(t) + \gamma\Delta B(t)M'_y(t) - \gamma B_1(t)M'_z(t)\\
\dfrac{dM'_y(t)}{dt} = -\gamma\Delta B(t)M'_x(t) - \dfrac{1}{T2}M'_y(t)\\
\dfrac{dM'_z(t)}{dt} = \gamma B_1(t)M'_x(t) - \dfrac{1}{T1}M'_z(t) + \dfrac{M_0}{T1}
\end{cases} \tag{8.24}$$

From now on this set of equations will be referred to as BE.

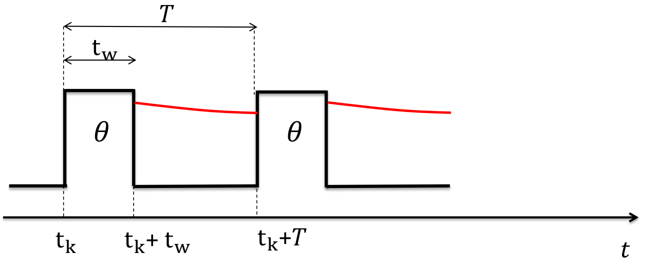

FIGURE 8.1: HRR pulse sequence used for the DNLM. Pulses are spaced T instants. The k-th pulse starts at time t_k and lasts t_w instants. It rotates $\mathbf{M}$ of an angle θ.

8.3 Discrete Time Nonlinear Model for Bulk Magnetization

A Discrete-time Nonlinear Model (DNLM) of the magnetization M as a function of ΔB was proposed in [19]. The motion of the magnetization vector M is obtained by successive application of a rotation matrix describing the effect of the RF pulse followed by another rotation matrix representing the effect of the field deviation ΔB. This model is suitable for the description of a HRR dynamics (see Chapter 6). The pulse sequence is shown in Figure 8.1. DNLM can be considered a discretisation of Bloch Equations with step equal to the inter-pulse time interval.

Let now permanently move to the rotating reference frame defined in the following as xyz (primes omitted for sake of compactness). The z axis is aligned along B_0 and the frame is rotating at speed $\Omega = \omega_0 = -\gamma B_0$, as in Figure 8.2. At time t_k, the magnetization is $\mathbf{M}(t_k)$ and a RF pulse is applied in the y direction. Let t_w be duration of each pulse. The electromagnetic pulse lasts then between t_k and $t_k + t_w$. Let θ be the angular displacement produced by the pulse. According to (3.26), it is given by:

$$\theta = -\gamma B_1 t_w \tag{8.25}$$

Let define $\mathbf{V}$, the matrix describing the rotation of the bulk magnetization in the xz plane along y, as:

$$\mathbf{V}(\theta) = \begin{bmatrix} \cos(\theta) & 0 & \sin(\theta) \\ 0 & 1 & 0 \\ -\sin(\theta) & 0 & \cos(\theta) \end{bmatrix} \tag{8.26}$$

The direction of application of each RF pulse is given by the sign of B_1. In particular, since pulses are applied in the $-y$ direction, one has to set set $B_1 < 0$. Since the rotation takest_w instants, one has:

$$\mathbf{M}(t_k + t_w) = V(\theta)\mathbf{M}(t_k) \tag{8.27}$$

Let now consider the drift in the transverse plane due to ΔB. It is given by:

$$\phi(t) = \int_{t_k+t_w}^{t_{k+1}} -\gamma \Delta B(p) dp \tag{8.28}$$

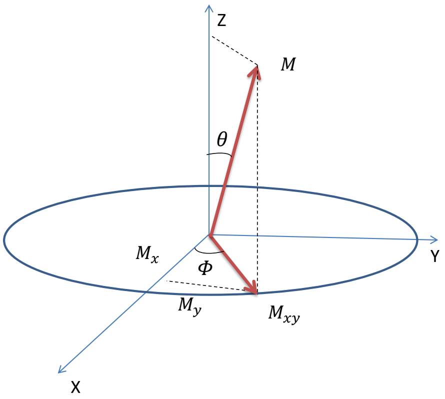

FIGURE 8.2: The xyz rotating reference frame. Each RF pulse rotates M of an angle θ. The field deviation generates a drift in the xy plane indicated as ϕ.

If ΔB is constant in the time interval $[t_k + t_w; t_{k+1}]$, it can be approximated as:

$$\phi = -\gamma T \Delta B \tag{8.29}$$

The rotation matrix describing the drift ϕ in each time period is:

$$\mathbf{W}(\phi) = \begin{bmatrix} \cos(\phi) & -\sin(\phi) & 0 \\ \sin(\phi) & \cos(\phi) & 0 \\ 0 & 0 & 1 \end{bmatrix} \tag{8.30}$$

To complete the model relaxation must be taken into account; so matrix **A** and vector **B** are introduced as function of $T1$ and $T2$.

$$\mathbf{A}(T1, T2) = \begin{bmatrix} e^{\frac{-T}{T2}} & 0 & 0 \\ 0 & e^{\frac{-T}{T2}} & 0 \\ 0 & 0 & e^{\frac{-T}{T1}} \end{bmatrix} \tag{8.31}$$

$$\mathbf{B}(T1) = \begin{bmatrix} 0 \\ 0 \\ M_0(1 - e^{\frac{-T}{T1}}) \end{bmatrix} \tag{8.32}$$

then:

$$\mathbf{M}(t_{k+1}) = \mathbf{A}(T1, T2)\mathbf{W}(\phi)\mathbf{M}(t_k + t_w) + \mathbf{B}(T1) \tag{8.33}$$

Finally, combining with (8.27), one gets to:

$$\mathbf{M}(t_{k+1}) = \mathbf{A}(T1, T2)\mathbf{W}(\phi)V(\theta)\mathbf{M}(t_k) + \mathbf{B}(T1) \tag{8.34}$$

According to HRR (see Chapter 6), $T << T1$,$T2$ and $\theta \approx 0$, constant. Then, moving to the dynamic system notation:

$$\begin{cases} \mathbf{M}(k+1) & = \mathbf{A}(T1,T2)\mathbf{W}(\phi)\mathbf{V}(\theta)\mathbf{M}(k) + \mathbf{B}(T1) \\ \phi & = -\gamma T \Delta B \end{cases} \tag{8.35}$$

which represents DNLM.
Note that the effect of the RF pulse comes before the drift since RF pulse acts in a negligible interval of time. Hence the two matrices are multiplied as $\mathbf{W}(\phi)\mathbf{V}(\theta)$.

8.3.1 Linearised Model

To properly drive the synthesis of a PID controller it is necessary to provide a Linearised Model (LM) of the system under control. This is the step that will be explored in this section. The equilibrium for the DNLM is found taking input $\overline{\phi} = 0$, corresponding to $\overline{\Delta B} = 0$; Solving (8.35), the magnetization at equilibrium $\overline{\mathbf{M}}$ is computed as:

$$\begin{cases} \overline{M_x} = \dfrac{-e^{-T/T2} sin\theta M_0 (1 - e^{-T/T1})}{1 - cos\theta (e^{-T/T1} + e^{-T/T2}) + e^{-T/T1} e^{-T/T2}} \\ \overline{M_y} = 0 \\ \overline{M_z} = \dfrac{(1 - e^{-T/T2} cos\theta) M_0 (1 - e^{-T/T1})}{1 - cos\theta (e^{-T/T1} + e^{-T/T2}) + e^{-T/T1} e^{-T/T2}} \end{cases} \tag{8.36}$$

This allows to compute a linearisation of DNLM around the equilibrium.

$$\mathbf{M}(k+1) \approx \overline{\mathbf{A}}\mathbf{M}(k) + \overline{\mathbf{B}}\Delta B(k) \tag{8.37}$$

with:

$$\overline{\mathbf{A}} = \mathbf{A}\mathbf{W}(\overline{\phi})\mathbf{V} \tag{8.38}$$

$$\overline{\mathbf{B}} = \begin{bmatrix} 0 \\ b_2 \\ 0 \end{bmatrix} \tag{8.39}$$

$$b_2 = \gamma T \frac{-e^{-T/T2} sin\theta M_0 (1 - e^{-T/T1})}{1 - cos\theta (e^{-T/T1} + e^{-T/T2}) + e^{-T/T1} e^{-T/T2}} \tag{8.40}$$

Finally, by introducing the output transformation:

$$M_y(z) = \overline{\mathbf{C}}\mathbf{M}(k) = [0\ 1\ 0]\mathbf{M}(k) \tag{8.41}$$

the transfer function between ΔB and M_y is:

$$\frac{M_y(z)}{\Delta B(z)} = \overline{\mathbf{C}}(z\mathbf{I} - \overline{\mathbf{A}})^{-1}\overline{\mathbf{B}} = \frac{b_2}{z - e^{-T/T2}} \tag{8.42}$$

8.4 Static Steady State Model and Linear Region

As the controller will be designed focusing on the above model it is important to define the limits of the linear region in terms of admissible ΔB (see Figure 8.3). If the field deviation exceeds this limit, regulation to zero may not be performed correctly as the error signal is no longer proportional to ΔB. In addition, the relation between M_y and ΔB is no longer bijective. Assume $\Delta B(k)$ remains constant for many samples. Let its value be ΔB_{ss}. Then $\mathbf{M}(k)$ will eventually reach a steady state condition. This can be imposed as follows:

$$\mathbf{M}(k+1) = \mathbf{M}(k) = \mathbf{M}_{ss} \tag{8.43}$$

Recall the hypothesis introduced for HRR (Chapter 6)

- T«$T1$,$T2$
- ϕ small
- $\theta \approx 0$

Then the steady state model can be expressed as:

$$\mathbf{M}_{ss} = \mathbf{A}_{ss}\mathbf{W}_{ss}\mathbf{V}_{ss}\mathbf{M}_{ss} + \mathbf{B}_{ss} \tag{8.44}$$

where the matrices $\mathbf{A}_{ss}$, $\mathbf{W}_{ss}$, ,$\mathbf{V}_{ss}$ and $\mathbf{B}_{ss}$ are obtained by means of Taylor expansion. In particular:

$$\mathbf{A}_{ss} = \begin{bmatrix} 1-\frac{T}{T2} & 0 & 0 \\ 0 & 1-\frac{T}{T2} & 0 \\ 0 & 0 & 1-\frac{T}{T1} \end{bmatrix} \tag{8.45}$$

$$\mathbf{B}_{ss} = \begin{bmatrix} 0 \\ 0 \\ M_0(\frac{T}{T1}) \end{bmatrix} \tag{8.46}$$

$$\mathbf{V}_{ss} = \begin{bmatrix} 1 & 0 & \theta \\ 0 & 1 & 0 \\ -\theta & 0 & 1 \end{bmatrix} \tag{8.47}$$

$$\mathbf{W}_{ss} = \begin{bmatrix} 1 & -\phi & 0 \\ \phi & 1 & 0 \\ 0 & 0 & 1 \end{bmatrix} \tag{8.48}$$

Solving for $\mathbf{M}_{ss}$:

$$\mathbf{M}_{ss} = (\mathbf{I} - \mathbf{A}_{ss}\mathbf{V}_{ss}\mathbf{W}_{ss})^{-1}\mathbf{B}_{ss} \tag{8.49}$$

with:

$$(\mathbf{I} - \mathbf{A}_{ss}\mathbf{V}_{ss}\mathbf{W}_{ss}) = \begin{bmatrix} \frac{T}{T2} & \phi(1-\frac{T}{T2}) & -\theta(1-\frac{T}{T2}) \\ -\phi(1-\frac{T}{T2}) & \frac{T}{T2} & \phi\theta(1-\frac{T}{T2}) \\ \theta(1-\frac{T}{T1}) & 0 & \frac{T}{T1} \end{bmatrix} \tag{8.50}$$

If the following approximations are introduced:

$$\begin{aligned} \frac{T}{T1} &\approx 0 \\ 1-\frac{T}{T2} &\approx 1 \\ \phi\theta &\approx 0 \end{aligned}$$

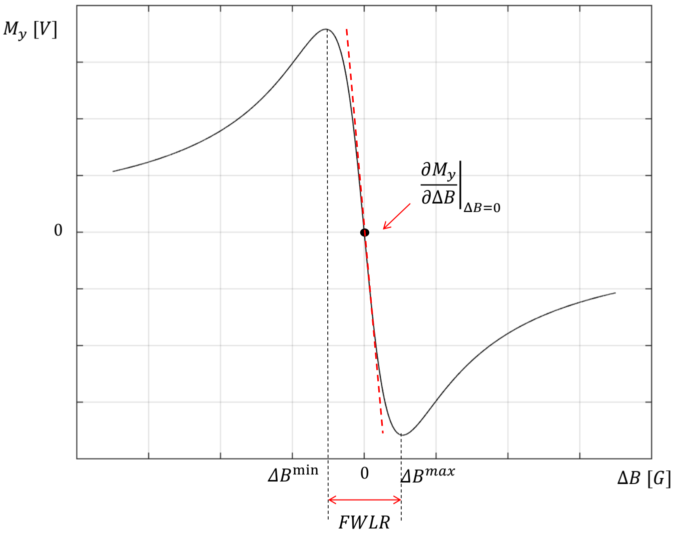

FIGURE 8.3: Plot of the curve relating the y component of the transverse magnetization at steady state to the magnetic field deviation. Note that the shape of the curve is that of a dispersion mode profile.

then:

$$(\mathbf{I} - \mathbf{A}_{ss}\mathbf{V}_{ss}\mathbf{W}_{ss}) \approx \begin{bmatrix} \frac{T}{T2} & \phi & -\theta \\ -\phi & \frac{T}{T2} & 0 \\ \theta & 0 & \frac{T}{T1} \end{bmatrix} \tag{8.51}$$

The steady state values for $\mathbf{M}_{ss}$ are then:

$$\begin{cases} M_{x_{ss}} = \dfrac{\frac{\theta}{T}T2M_0}{1+(\frac{\theta}{T})^2T1T2+(\gamma\Delta BT2)^2} \\ M_{y_{ss}} = \dfrac{-\gamma\Delta B\frac{\theta}{T}T2^2M_0}{1+(\frac{\theta}{T})^2T1T2+(\gamma\Delta BT2)^2} \\ M_{x_{ss}} = \dfrac{[1+(\gamma\Delta BT2)]^2M_0}{1+(\frac{\theta}{T})^2T1T2+(\gamma\Delta BT2)^2} \end{cases} \tag{8.52}$$

A plot of $M_{y_{ss}}$ as function of ΔB is shown in Figure 8.3. Note that the profile shows a linear behaviour just in a region around the perfect resonance condition. This is the region in which the lock system can be effectively used. Let define ΔB^{min} and ΔB^{miax} the values of field deviation corresponding respectively to the positive and negative peak of the dispersion curve. The Full Width of Linear Region (FWLR) can then be defined as:

$$FWLR = |\Delta B^{max} - \Delta B^{min}|. \tag{8.53}$$

Within this region, the curve can be approximated as linear and bijective.

8.5 Model Comparison: Simulated Step Response

This section is devoted to a detailed comparison of the NMR models presented above. Different simulations are performed to stress the hypotheses required by

γ $[rad/(s\ G)]$	$T1$ $[s]$	$T2$ $[s]$	M_0 $[V]$	T $[\mu s]$	θ $[°]$
26751.3	0.4276	0.03931	1	200	1.8

TABLE 8.1: Comparison of DNLM and LM: parameters of the NMR virtual sample and parameters of the lock sequence used for simulations.

Simulation	*Figure*	ΔB $[G]$
1	8.4	0.001, 0.005, 0.010
2	8.5	-0.001, -0.005, -0.010
3	8.6	-0.01, -0.02, -0.04

TABLE 8.2: Comparison of DNLM and LM: amplitude of field step disturbance.

the models and compare their predicted evolution of the M_y signal as response to different field disturbances.

8.5.1 Discrete time Non Linear Model and Linearised Model

In order to evaluate the performance of the models introduced in this chapter, a set of simulated step responses is performed to verify whether the linearisation around $\Delta B = 0$ provides a good approximation of DNLM in its linear region. Each simulation consists in generating a series of three field steps of increasing height applied to the two models. Comparison is carried out concerning the output M_y only, as LM were derived for that component only. The simulations are set up so that all the hypothesis which were introduced for DNLM are satisfied. Table 8.1 shows the parameters of the virtual sample; the overall field disturbance ΔB assumes value as reported in Table 8.2.

Plots in Figures 8.4 and 8.5 show the results for Simulation 1 and 2. The comparison clearly shows that LM is a good approximation of DNLM only if the input is close to the equilibrium one ($\Delta B \approx 0$). When the field deviation grows in magnitude the two models start behaving differently, in particular DNLM describes oscillations during the transient phase which cannot be obtained using a linear model. In addition, when ΔB approaches the limit of the linear region $[\Delta B^{min}; \Delta B^{max}]$, the predicted steady state values become appreciably different (0.16 V for LM versus 0.125 V for DNLM with $\Delta B = -10\ mG$). The nonlinear model in fact seems to provide less sensitivity to the field deviation and it is also slower in reaching the steady state value. Figure 8.6 instead shows the results of Simulation 3. In this case the disturbance gets so strong that the linear region limit is overcome and the dispersion signal starts reacting to ΔB in the wrong direction. This is evident when comparing the response of the third step to the previous two in DNLM. The linearisation instead keeps growing, providing a completely unaffordable estimation of the field deviation.

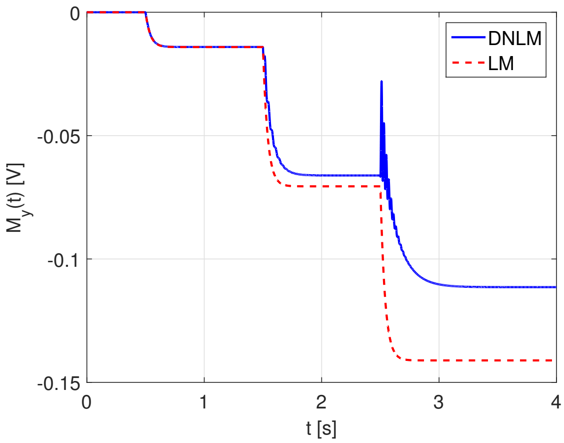

FIGURE 8.4: *Simulation 1*. Step response comparison for DNLM (blue, solid line) and LM (red, dashed line).

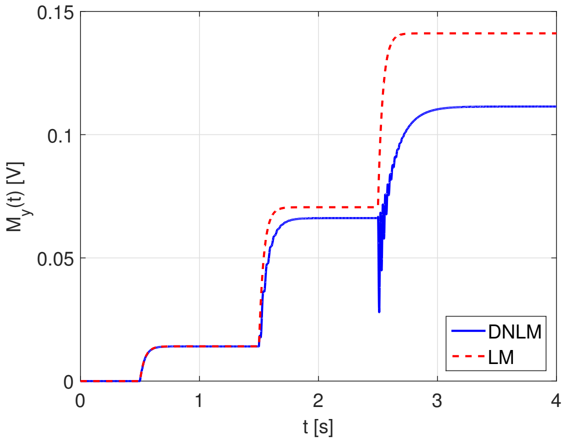

FIGURE 8.5: *Simulation 2*. Step response comparison for DNLM (blue, solid line) and LM (red, dashed line).

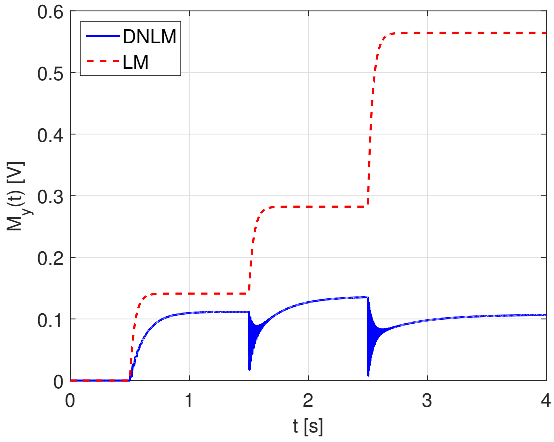

FIGURE 8.6: *Simulation 3*. Step response comparison for DNLM (blue, solid line) and LM (red, dashed line).

γ $[rad/(s\ G)]$	$T1$ $[s]$	$T2$ $[s]$	M_0 $[V]$	T $[\mu s]$	θ $[°]$
26751.3	0.4276	0.03931	1	200	1.8

TABLE 8.3: Comparison of BE and DNLM: parameters of the NMR virtual sample used for simulations.

Simulation	*Figure*	T $[\mu s]$	θ $[°]$	ΔB $[G]$
1	8.7	200	1.8	0.001, 0.005, 0.010
2	8.8, 8.9	200	1.8	0.01, 0.05, 0.10
3	8.10	2000	1.8	0.001, 0.005, 0.010
4	8.11	20000	1.8	0.01, 0.05, 0.10
5	8.12	200	27	0.001, 0.005, 0.010
6	8.13, 8.14	200	27	0.01, 0.05, 0.10

TABLE 8.4: Comparison of BE and DNLM: parameters of the lock sequence and amplitude of step disturbances used for simulations.

8.5.2 Bloch Equations and Discrete time Non Linear Model

In this section the response provided by DNLM, developed for the SSFP, is compared to the one obtained from the more general BE model. This step is very important since it is difficult to derive an equilibrium from Bloch model, as the second input is a square wave triggering the RF pulses which is always running. Therefore the possibility to use DNLM allows linearization (LM) and a much simpler approach for the synthesis of a controller. The set of simulations is designed to understand the limit of DNLM in describing the behavior of the bulk magnetization. So the hypothesis needed by DNLM are released step by step and the simulated response is compared to that provided by BE. The parameters of the virtual sample are reported in Table 8.3.

It is necessary to set up a proper pulse sequence for the BE so that the design of experiment is the same for both models. BE in fact requires as second input a square wave with inter-pulse interval equal to T and a pulse duration t_w computed according to Equation 3.26, where B_1 is a parameter of BE and θ is a parameter of DNLM. The parameters used in the simulations are reported in Table 8.4, where the reference to the respective plot are reported as well.

Simulation 1 compares the responses of the two models if all the requirements for DNLM are fulfilled. As expected, in this situation the two responses are exactly superimposed.

Simulation 2 introduces a strong disturbance, so that the hypothesis of small ϕ angles is released. Oscillations are present in both models during transients. The DNLM reaches a real steady state condition with no oscillations, while the BE keeps on oscillating around a steady state value, as shown in Figure 8.9. In addition the steady state values no longer grows as δB grows.

In *Simulation 3* the inter-pulse time T is increased, but it is still less than $T2$. The two responses are still fully overlapped.

With *Simulation 4* T is made comparable to $T2$. We expect no complete steady state free precession phenomenon here. Oscillations are evident in BE. Still, their average value seem to be related to the field deviation. Notice that the DNLM signal moves in the wrong direction: ΔB increases and M_y increases as well. This happens as disturbances exceed the linear region.

In *Simulation 5* instead θ is made bigger, trying to violate the hypothesis of having θ small. The two responses seem to be fully overlapped.
With *Simulation 6* a stronger disturbance ΔB is introduced. In this case both models keep on oscillating as Figure 8.14 clearly shows. Still, according to what stated before, not all oscillations are present in the discrete time model. As far as the line of tendency is concerned, it is maintained linear, with the dispersion signal M_y moving down as ΔB grows up.

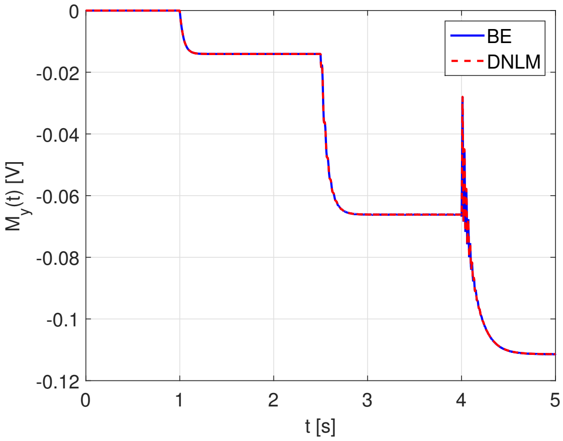

FIGURE 8.7: *Simulation 1*. Step response comparison for BE (blue, solid line) and DNLM (red, dashed line).

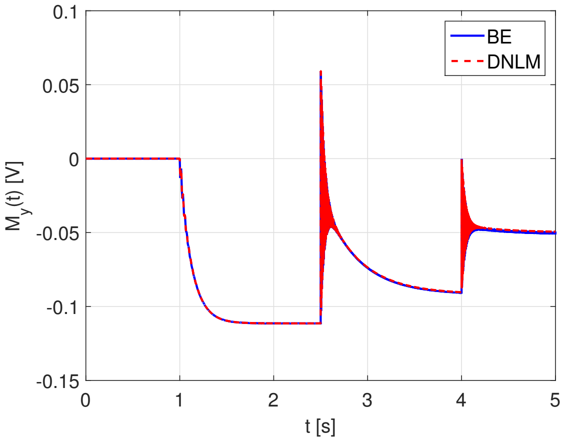

FIGURE 8.8: *Simulation 2*. Step response comparison for BE (blue, solid line) and DNLM (red, dashed line).

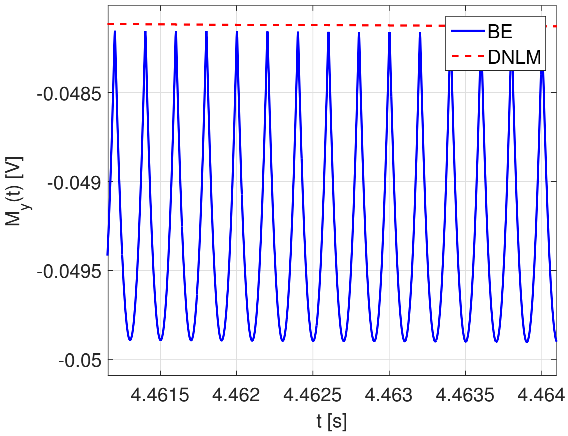

FIGURE 8.9: *Simulation 2*. Detail: DNLM does not take into account inter-pulse oscillations of the transverse magnetisation.

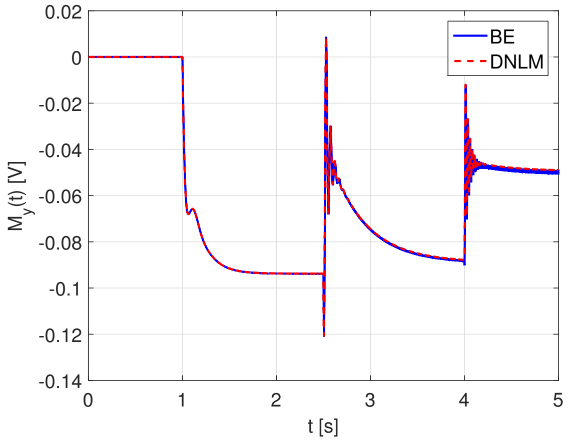

FIGURE 8.10: *Simulation 3*. Step response comparison for BE (blue, solid line) and DNLM (red, dashed line).

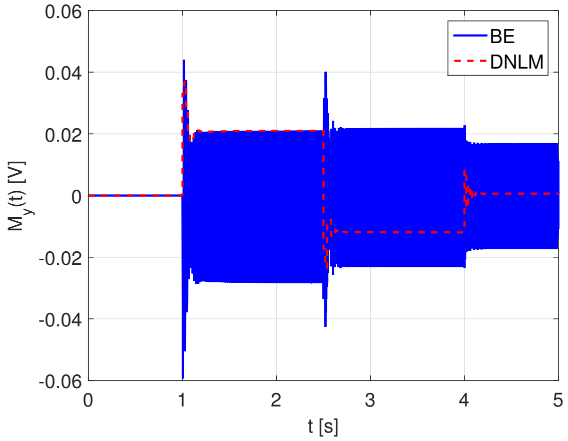

FIGURE 8.11: *Simulation 4*. Step response comparison for BE (blue, solid line) and DNLM (red, dashed line).

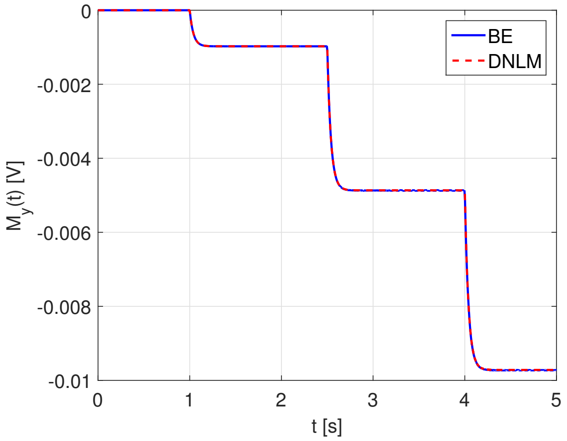

FIGURE 8.12: *Simulation 5*. Step response comparison for BE (blue, solid line) and DNLM (red, dashed line).

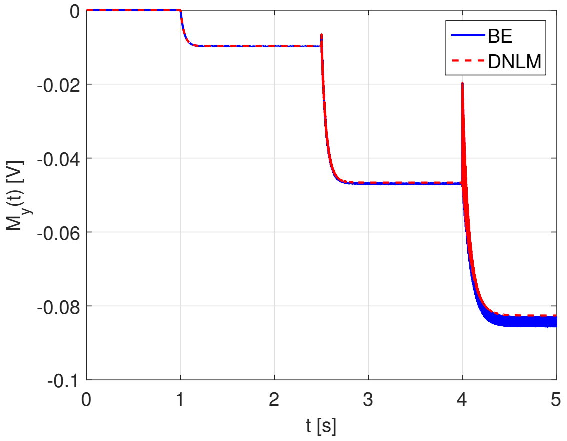

FIGURE 8.13: *Simulation 6*. Step response comparison for BE (blue, solid line) and DNLM (red, dashed line).

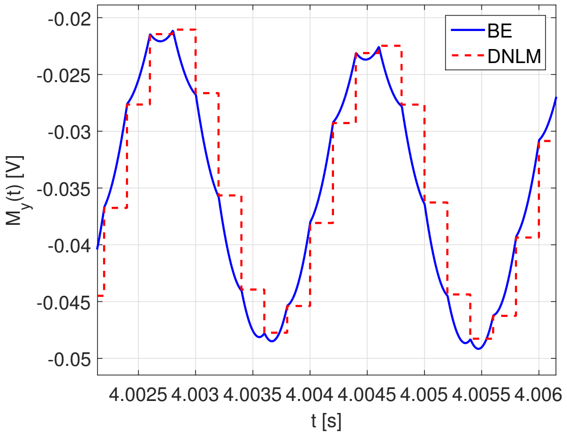

FIGURE 8.14: *Simulation 6*. Detail: when the strongest simulated disturbance acts on the system, both BE and DNLM oscillate around a steady state value. As expected, not all oscillations are present in the discrete time version.

Sample	*Trial*	T [μs]	θ [°]
1	1.1	100	4
1	1.2	100	8
1	1.3	200	8
1	1.4	200	8
2	2.1	100	4
2	2.2	100	8
2	2.3	200	8
2	2.4	200	8
3	3.1	100	4
3	3.2	100	8
3	3.3	200	8
4	4.1	100	5
4	4.2	100	9
4	4.3	200	9
5	5.1	100	4
5	5.2	100	8
5	5.3	200	8

TABLE 8.5: Details of lock sequences used for NMR trials.

Sample	γ [$rad/(s\ G)$]	$T1$ [s]	$T2$ [s]	$T2^*$ [s]	M_0 [V]
1	26751.3	0.06	0.02	0.000055	0.28
2	26751.3	0.007	0.002	0.000042	0.29
3	26751.3	0.18	0.056	0.000075	0.28
4	26751.3	2.37	2.14	0.000030	0.59
5	25166.2	1	0.8	0.000050	0.45

TABLE 8.6: Details of samples used for NMR trials.

8.6 Model Validation

For the purpose of validation, a set of NMR experiments is carried out relying on a permanent magnet providing a stable field of 500 G. The lock sequence is applied to different samples with different values of T and θ (for a detailed description of the trials refer to Tables 8.5 and 8.6). For gain evaluation, the response to a step field deviation $\Delta B = -0.235\ G$ is concerned and the predicted steady state values of M_y, ($\hat{SS}_{DNLM}$ and $\hat{SS}_{LM}$), are compared to the real ones (SS). Results are shown in Table 8.7. A comparison of real settling times (ST) to DNLM and LM estimated ones ($\hat{ST}_{DNLM}$ and $\hat{ST}_{LM}$) is also shown in Table 8.7. Note that the effect of each step disturbance ΔB is obtained moving the receiver frequency Ω of the system, according to 6.2. This allows to apply the same disturbance to the whole sample and have an accurate measure of the disturbance itself. Other ways of inducing ΔB, such as windings flown by currents, may not provide exact results. Since the disturbance is generated out of the sample, it may experience a different value of ΔB from the expected one. Moreover, windings may introduce their own time constant, which may result in a wrong estimation of the NMR one. Data collected from trials are filtered to remove high frequency measurement noise. The presence of offsets is removed as well.

Trial	$\hat{SS}_{LM}$ $[mV]$	$\hat{SS}_{DNLM}$ $[mV]$	SS $[mV]$	$\hat{ST}_{LM}$ $[s]$	$\hat{ST}_{DNLM}$ $[s]$	ST $[s]$
1.1	700	32	1.2	0.15	0.22	0.15
1.2	400	52	4	0.15	0.22	0.20
1.3	700	25	2.2	0.17	0.25	0.25
2.1	450	30	1.6	0.01	0.03	0.03
2.2	300	51	2.5	0.01	0.03	0.03
2.3	530	28	2.5	0.012	0.03	0.03

TABLE 8.7: Comparison of model-predicted steady state values of M_y to real ones after the application of a step field disturbance.

When comparing the results obtained from DNLM and LM to the data collected from real NMR experiments these considerations arise:

- the time constant of DNLM represents a good approximation of that of the real system;
- the time constant of LM represents an acceptable approximation of that of the real system, however it is slightly faster than both DNLM and the real data;
- the gain of both DNLM and LM heavily overestimates the gain of the real system.

The explanation for this error can be found in the field inhomogeneity, which is not taken into account by any of the previous models. They are in fact macroscopic models, intended to describe the evolution of the bulk magnetization vector, without considering the evolution of the small components which sum up into the **M** vector itself. In presence of a non-homogeneous field, the curve in Figure 8.3 shows a reduction of the slope in the linear region and a widening of the latter. The settling time instead is not affected by the non-homogeneity of the magnetic field. This phenomenon is consistent with the collected data.

8.7 Bloch-Based Isochromat Model

All the models previously introduced do not consider the effect of non-homogeneous magnetic field. They are macroscopic models, intended to describe the evolution of the bulk magnetization vector, without considering the evolution of the small components which sum up into the **M** vector itself. Recall that the effect of field inhomogeneity is a quicker loss of coherence of spins (see Chapter 5). This affects the shape of the absorption spectrum which is wider and shorter than the homogeneous case. This means that more frequencies around the Larmor one are involved in the resonance process. Each of these frequencies can be associated to a group of spins, called isochromats (see Chapter 5), which see the same field value along the z axis. In addition, under the former conditions, echoes are likely to grow, both as spin echoes and as stimulated ones. So, a model aiming to fully describe the NMR process should keep into account the separate behaviour of isochromats and then sum their contributions up to completely represent the evolution of the bulk magnetization. The idea is to run BE for each isochromat i to compute its contribution $\mathbf{m}_i$. Then **M** is obtained summing all individual contributions $\mathbf{m}_i$ with proper weights a_i. So it is possible to write:

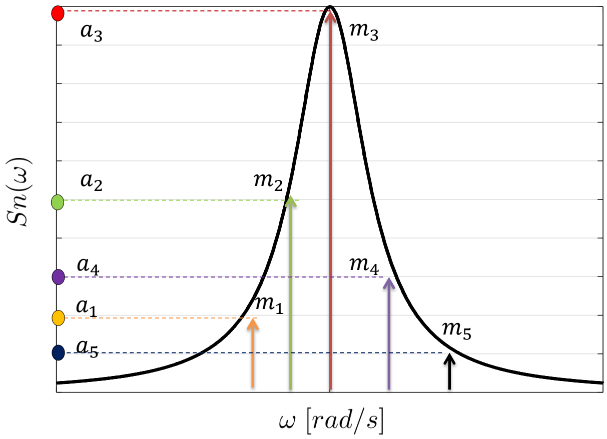

FIGURE 8.15: Graphical interpretation of isochromat decomposition used in BBIM.

$$\mathbf{M}(t) = \sum_i a_i \mathbf{m}_i(t) \tag{8.54}$$

The Lorentzian shape, centred at frequency ω_0, can be written as:

$$S(\omega) = \frac{T2^*}{1 + (T2^*(\omega - \omega_0))^2} \tag{8.55}$$

If an interval $[-\overline{\omega};\overline{\omega}]$ is considered, $S(\omega)$ can be normalized as follows:

$$Sn(\omega) = \frac{S(\omega)}{\sum_{-\overline{\omega}}^{\overline{\omega}} S(\omega)} \tag{8.56}$$

therefore one can define:

$$a_i = Sn(\omega_i) \tag{8.57}$$

The same approach is used for a quantitative investigation of the phenomena of Echo and SSFP [27, 36, 29]. In the following reference to this model will be made as *Bloch-based Isochromat Model* (BBIM).

To verify the correctness of the approach it is possible to perform simulations using Matlab. In particular with the aim to verify that the sensitivity of the dispersion signal to field deviation ΔB is reduced in the case of non-homogeneous field (i.e. $T2^* << T2$). Moreover, the system should present a wider linear region. Tables 8.8 and 8.9 resume the parameters used in this simulation, Figures 8.16a and 8.16b depict the results of simulation, Figures 8.17a and 8.17b show the two normalized absorption spectra.

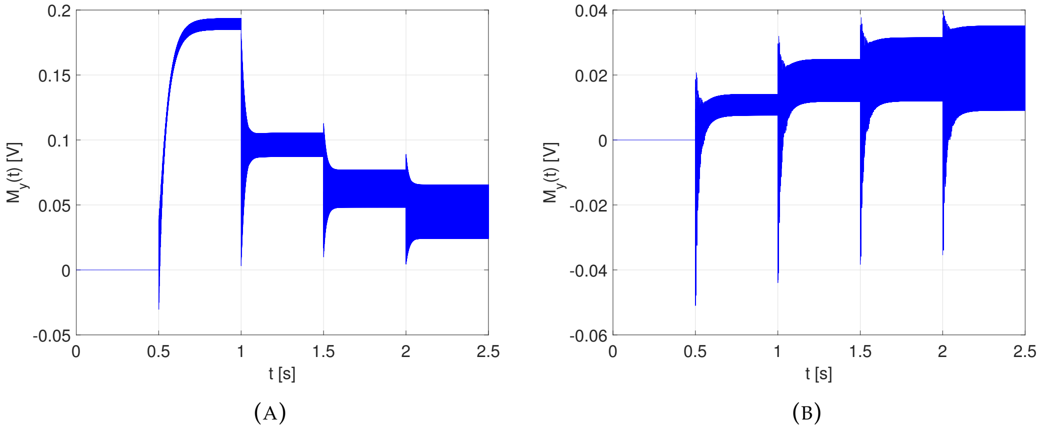

FIGURE 8.16: Simulation 1 (a) and Simulation 2 (b). *BBIM* simulations show the effect of field inhomogeneity on the SSFP of the virtual sample. The sensitivity to the field deviation and the width of the linear region are both affected.

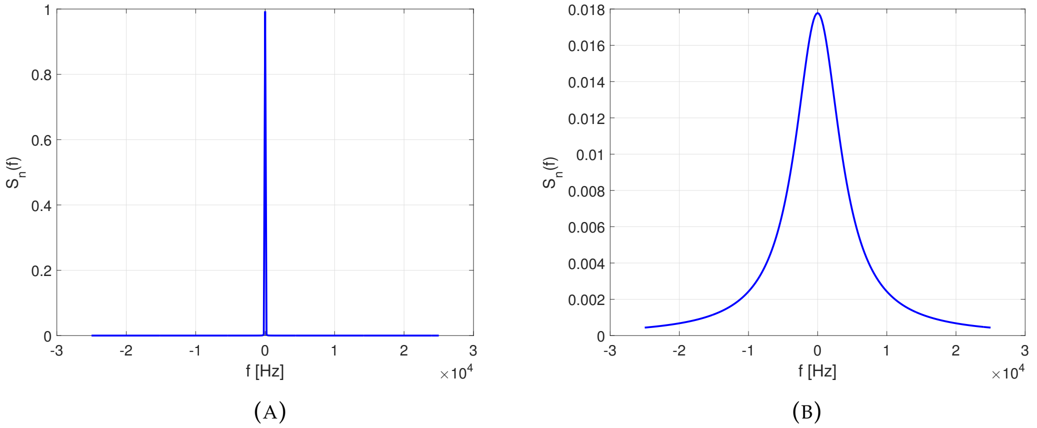

FIGURE 8.17: Normalized Lorentzian distributions of the isochromats in a strongly homogeneous field (a) and in a non-homogeneous field (b).

8.7.1 Model Validation

In order to validate BBIM a set of trials with different samples and different experimental parameters carried out. As for *LM* validation, trials are performed over the permanent magnet introduced in Chapter 7, and field steps ΔB are obtained acting on the receiver frequency. For comparison a field deviation of $\Delta B = -0.235\ G$ is considered since it lies in the centre of the linear region. Real data are filtered to remove high frequency noise. Moreover, they are affected by an offset due to non-perfect resonant condition or to the particular spatial distribution of field inhomogeneity in the sample. This offset is removed offline. The model predicted values are obtained

$\gamma\ [rad/(s\ G)]$	$T1\ [s]$	$T2\ [s]$	$T2^*\ [s]$	$M_0\ [V]$
26751.3	0.052	0.017	0.00004	1.6

TABLE 8.8: Parameters of the virtual sample used for BBIM simulations.

Trial	T [μs]	θ [°]	ΔB [G]	*Homogeneity*
1	100	4	-0.235, -0.470, -0.705, -0.940	T2
2	100	4	-0.235, -0.470, -0.705, -0.940	T2*

TABLE 8.9: Parameters of the experiment for BBIM simulation.

as the average of the steady state values of M_y. The details of trials are presented in Tables 8.6 and 8.5. The predicted and measured transverse magnetization steady state values are compared in Table 8.10. Figure 8.18a and 8.18b and Figure 8.19a and 8.19b compare the real and the simulated data for Trials 1.2 and 2.2.

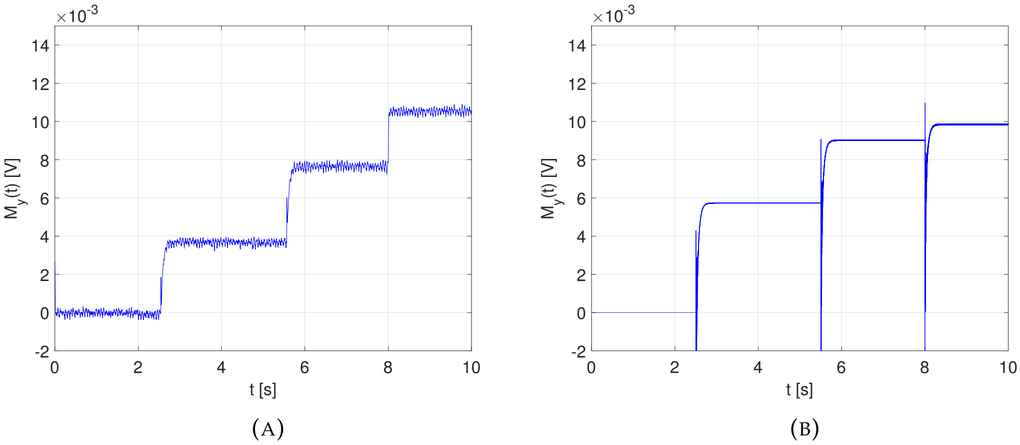

FIGURE 8.18: Trial 1.2. Behaviour of the transverse magnetization $M_y(t)$ in real experiment (a) and in the $BBIM$ simulated one (b).

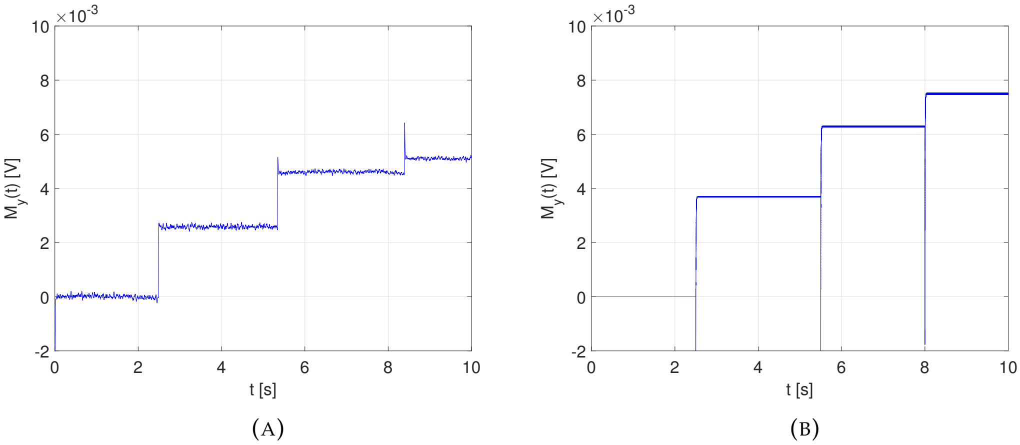

FIGURE 8.19: Trial 2.2. Behaviour of the transverse magnetization $M_y(t)$ in real experiment (a) and in the $BBIM$ simulated one (b).

The settling times of the model and of collected data are quite similar, as reported in Table 8.11. The gain is still overestimated but now results are much closer to that of real experiments (see Table 8.10). These trials show that the BBIM is inclined to slightly overestimate the actual gain of the system in the middle of the linear region. A possible explanation can be found in the choice of the shape used for the simulation: in fact the field inhomogeneity may turn the NMR spectrum into a non-perfectly Lorentzian shape. Another explanation lies in the estimation of parameters

$Trial$	$\hat{SS}_{BBIM}$ $[mV]$	SS $[mV]$
1.1	3.5	1.2
1.2	6	4
1.3	3	2.2
1.4	12	3
2.1	2.5	1.6
2.2	4	2.5
2.3	2	2.5
2.4	3	3
3.1	6	3
3.2	9	6
3.3	4.5	3
4.1	3	3
4.2	6	8
4.3	1	5
5.1	3.5	3
5.2	9	6
5.3	3	5

TABLE 8.10: Comparison of $\hat{SS}_{BBIM}$ to real SS after the application of a step field disturbance.

$Trial$	$\hat{ST}_{BBIM}$ $[s]$	ST $[s]$
1.1	0.22	0.12
1.2	0.22	0.20
1.3	0.25	0.25
2.1	0.03	0.03
2.2	0.03	0.03
2.3	0.03	0.03

TABLE 8.11: Comparison of $\hat{ST}_{BBIM}$ to real ST after the application of a step field disturbance.

$(T1\ ,T2\ ,T2^*\ ,\theta\ ,T\ ,M_0)$ which is always subject to measurement errors. Nevertheless, the results are much more affordable than those obtained from the former models.

Transfer Function Model

A model-based synthesis of a PID regulator typically requires a linear model describing the dynamics of the process under control. For this purpose, a tentative linearised model was derived in the previous Sections. Still, experimental validation demonstrated that such model was not suitable to describe dynamics of the lock experiment in case of non perfectly homogeneous field. BBIM carefully describes the dynamics of the lock experiment, but, on the contrary, can not be easily linearised and is therefore not suitable for control purposes. To overcome this limitation, a linear transfer function model describing the dynamic behaviour of the lock sensor can be identified by means of input-output identification techniques, exploiting BBIM model to collect data from simulations. The identification phase is set-up as follows:

- *Simulation of a step response around $\Delta B = 0$.* The system is first brought in SSFP on perfect resonance. Then, once the steady state condition is reached, a step variation of ΔB is applied. Let ΔB_{step} be the amplitude of the step, which must be chosen so that $|\Delta B_{step}| << \Delta B^{max}$. The $M_y(t)$ signal is collected at this point.

- *Filtering of output identification data.* The shape of the SSFP signal shows oscillations with fundamental harmonic at $\frac{1}{T}$, and harmonic content at higher frequencies [28]. From the sensor point of view, these oscillations represent measurement noise and must not be described by the linear model. A low-pass filtering procedure allows to reduce the impact of SSFP oscillations on the $M_y(t)$ signal.

- *Definition of the structure of the model.* The structure of the local model must be chosen according to the behaviour of the step response $M_y(t)$. A first order transfer function with no zero is used in case of monoexponential response. A second order transfer function with zero is used in case of more complex behaviours.

- *Identification of the parameters of the model via Constrained Least Square optimisation.* Constrained Least Square (CLS) optimisation allows to exploit input-output data to optimise the values of model parameters, in order to provide the best fit between model prediction and identification data. In case of a second order structure, it is possible to introduce constraints on the position of the zero according to the presence of an inverse response or an overshoot in the step response.

The CLS optimisation problem is expressed as follows [37]:

$$\begin{aligned} \hat{\mathbf{P}}^{CLS} &= min_{\mathbf{P}} (\mathbf{Y} - \hat{\mathbf{Y}}(\mathbf{P}))^\top (\mathbf{Y} - \hat{\mathbf{Y}}(\mathbf{P})) \\ & subject\ to : \mathbf{CP} \leq \mathbf{d} \end{aligned} \tag{8.58}$$

with $\mathbf{Y}$ the vector containing the measured $M_y(t)$ for each time instant t, $\hat{\mathbf{Y}}$ the vector containing the predicted $M_y(t)$ for each corresponding time instant t, $\mathbf{P}$ the vector of unknown parameters and $\mathbf{C}$ and $\mathbf{d}$ respectively a matrix and a vector of proper size to introduce polytopic constraints on $\mathbf{P}$.

The goodness of fit is evaluated with the following metric:

$$FIT = 100 \left(1 - \frac{||\mathbf{Y} - \hat{\mathbf{Y}}||_2}{||\mathbf{Y} - mean(\mathbf{Y})||_2}\right) \tag{8.59}$$

In case of single exponential response of M_y, the following first order transfer function is adopted:

$$G_{nmr}(s) = \frac{\mu_{nmr}}{1 + s\tau_{nmr}} \tag{8.60}$$

with the corresponding step response predictor $\hat{M}_y(t)$:

$$\hat{M}_y(t) = \mu_{nmr} \left(1 - e^{-t/\tau_{nmr}}\right) \tag{8.61}$$

In the other cases, a second order transfer function is adopted:

$$G_{nmr}(s) = \frac{\mu_{nmr}(1 + sT_{nmr})}{(1 + s\tau_{nmr_1})(1 + s\tau_{nmr_2})} \tag{8.62}$$

with the convention $\tau_{nmr_2} < \tau_{nmr_1}$ and the corresponding predictor:

$$\hat{M}_y(t) = \mu_{nmr} \left(1 - \tfrac{\tau_{nmr_1} - T_{nmr}}{\tau_{nmr_1} - \tau_{nmr_2}} e^{-t/\tau_{nmr_1}} + \tfrac{\tau_{nmr_2} - T_{nmr}}{\tau_{nmr_1} - \tau_{nmr_2}} e^{-t/\tau_{nmr_2}}\right) \tag{8.63}$$

In particular, in presence of an inverse response, the constraint $T_{nmr} < 0$ is introduced. In case of overshoot the constraint $T_{nmr} > \tau_{nmr_1}$ is instead introduced. Stability constraints $\tau_{nmr_1} > 0$ $\tau_{nmr_2} > 0$ are always present.

Chapter 9

Closed-Loop Design

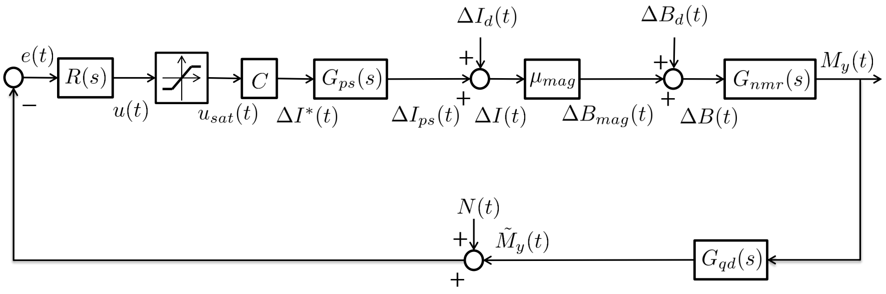

FIGURE 9.1: Block scheme with transfer function for the FFL. $u(t)$ is the voltage control action, $u_{sat}(t)$ is the saturated voltage control action, $\Delta I^*(t)$ is the current control action. $\Delta I(t)$ is the overall current deviation from the resonance condition; it is the sum of the current from the power supply, $\Delta I_{ps}(t)$, and the current disturbance $\Delta I_d(t)$; $\Delta B(t)$ is the overall field deviation seen by the NMR sample; it is the sum of the field deviation from the magnet, $\Delta B_{mag}(t)$, and the field disturbance $\Delta B_d(t)$; $M_y(t)$ is the y component of the transverse magnetization in the rotating frame, $\tilde{M}_y(t)$ is its low-pass filtered version; $N(t)$ is measurement noise; $e(t)$ is the error signal feeding the regulator.

The design of the closed-loop for the lock system should consider both the NMR lock sensor dynamics and the NMR hardware setup required to run the lock experiment. The scheme in Figure 9.1 shows the overall closed-loop setup for the FFL in terms of transfer functions. The regulator action $u(t)$ is the voltage output from a DAC converter and is turned into a current by means of a known conductance C. The current output is limited, therefore a saturation must be included. Note that it is modelled as the equivalent voltage saturation to ease an antiwindup implementation of the regulator. Let $u_{sat}(t)$ be the control action after the saturation block. The power supply features an internal control loop: the current control action is introduced by summing it to the overall current reference of the power supply. Let therefore denote the current control action as ΔI^*. The power supply unit is then modelled as a first order transfer function relating ΔI_{ps}, i.e. the power supply current deviation from the resonance condition, to ΔI^*:

$$G_{ps}(s) = \frac{\Delta I_{ps}\ [A]}{\Delta I^*\ [A]} = \frac{\mu_{ps}}{1 + s\tau_{ps}} \tag{9.1}$$

The magnet is instead modelled as a static gain:

$$\mu_{mag} = \frac{\Delta B_{mag}\ [G]}{\Delta I\ [A]} \tag{9.2}$$

with ΔB_{mag} the magnet field deviation from the resonance condition. The NMR receiver chain (the quadrature detector in particular) can be described by a low pass filter, that should be considered in the design of the control loop as well.

Note that, from the discussion in Chapter 8, the steady state value of M_{xy} in the rotating reference frame is proportional to the value of M_0. In addition, M_0 is measured trough the acquisition chain, therefore the value of M_0 already accounts for the gain $\mu_a cq$. In view of this consideration, the filter can be conceptually placed after the NMR lock sensor, as depicted in Figure 9.1. It can therefore be modelled as:

$$G_{qd}(s) = \frac{\tilde{M}_y\ [V]}{M_y\ [V]} = \frac{1}{1 + s\tau_{qd}} \tag{9.3}$$

where $\tilde{M}_y(t)$ is the low-pass filtered signal of $M_y(t)$. The overall process transfer function is then given by

$$G(s) = G_{qd}(s)G_{nmr}(s)\mu_{mag}G_{ps}(s)C \tag{9.4}$$

9.1 Synthesis of the Regulator

Once the process transfer function $G(s)$ is known, it is possible to tune a parameterised regulator, which must cope with the following requirements:

- stability of the closed-loop system;
- settling time as short as possible;
- rejection of current/field oscillations;
- perfect rejection of step current/field disturbances (at steady state).

For sake of generality, the synthesis of a PID regulator is discussed in this section. However, in some cases, a simpler PI regulator may be enough to face the requirements. The presence of the integrator of the PID allows to guarantee perfect compensation of step process disturbances (no derivative action is present in the process). In addition, the closed-loop bandwidth b_w is required to be the largest possible to provide the shortest settling time and as much rejection of process disturbances as possible. Still, the presence of measurement noise N limits the closed-loop bandwidth. Recall that the oscillations of the SSFP signal represent a source of measurement noise (see Section 8). When b_w is expressed in $[rad/s]$, it therefore holds:

$$b_w < \frac{2\pi}{T} \tag{9.5}$$

Equation (9.5) stresses the importance of T as design parameter. By reversing the inequality, it is possible to place a constraint on the choice of T according to the desired closed-loop bandwidth (i.e.according to the desired closed-loop settling time). Let consider a PID controller in the realisable form:

$$R(s) = \frac{\mu_r(1 + sT_{z1})(1 + sT_{z2})}{s(1 + s\tau_f)} \tag{9.6}$$

It is possible to use the two zeros of the PID to cancel the two slowest poles of $G(s)$, typically an NMR pole or the power supply one, while τ_{qd} typically resides at high frequency. τ_f is placed out of the desired bandwidth and may be used to improve filtering of measurement noise N. A careful choice of μ_r and τ_f allows to shape the loop function $L(s) = G(s)R(s)$ to provide the required disturbance rejection and settling time. The stability of the closed-loop system can instead be assessed by means of the *Bode Criterion* [38].

Regulators are implemented in a discrete-time way, by exploiting the full computation capability of the hardware, which results in $T_s = 25\ \mu s$. Discretisation of regulators is performed with *Tustin* method $s = 2(z - 1)/(T_s(z + 1))$ to guarantee that the stability is preserved (all asymptotically stable/stable continuous time poles are respectively mapped into asymptotically stable/stable discrete time poles).

Chapter 10

Experimental trials

To validate the preliminary results obtained in [25], a series of experimental trials are performed in this work. This section is first devoted to the description of both the main NMR experiment and the lock setup which are used to carry out experimental trials. Then the methodology described in Section 9 is applied to synthesise a PI regulator. The results of closed-loop experiments are finally presented and discussed.

10.1 NMR Lock Setup

The main magnetic field B_0 is generated by a Stelar s.r.l. manufactured resistive magnet [23], driven by IECO MPS 400 VERIFY power supply [34] (prototypes for IDentIFY EU Project). According to the manufacturer, the power supply is characterised by a 25 KHz bandwidth, with an internal control loop guaranteeing perfect tracking of step references. The analysis of the noise spectrum of the amplifier highlights the presence of some harmonic content at 50 $[Hz]$ and its multiples, up to 300 Hz. The main NMR experiment is carried out on a pure Galden sample, targeting the Fluorine F^{19} nucleus ($\gamma = 25166.2\ rad/(s\ G)$). The lock experiment is instead carried out targeting the Proton H^1 nucleus ($\gamma = 26751.3\ rad/(s\ G)$). Two different samples are tested: a silicone one and a copper sulphate one. Note that the gyromagnetic ratios of H^1 and F^{19} are not very distant in frequency (i.e. the two nuclei resonate at similar frequencies). To minimise the interference between the two experiments, two different probes are used for the main and lock experiment. These probes feature a magnetic shielding to protect the NMR samples from spurious RF pulses coming from the other experiment. The NMR parameters of interest of the two lock samples are reported in Table 10.1. Details of the lock sequences are instead reported in Table 10.2.

A PI controller is implemented on a Xilinx MicroBlaze microprocessor [39], embedded in the Xilinx Spartan FPGA board [39] hosting the firmware required for the NMR lock experiment. A minimum sampling time of $T_s = 25\ \mu s$ can be achieved with this implementation. The control action (voltage) is generated by a 16 bit DAC and is turned into current by means of a 5 Ω resistance. For safety issues, the current output is limited to ±500 mA. Due to the presence of this saturation, an antiwindup

Sample	γ $[rad/(s\ G)]$	$T1$ $[s]$	$T2$ $[s]$	$T2^*$ $[s]$	M_0 $[V]$
Silicone	26751.3	0.365	0.050	0.00026	0.385
Copper sulph.	26751.3	0.0017	0.0015	0.00011	0.4474

TABLE 10.1: Details of the lock samples.

Sample	T $[\mu s]$	θ $[deg]$
Silicone	60	9
Copper sulphate	50	9

TABLE 10.2: Details of the lock sequence.

scheme is adopted for the PI implementation. As already stated in Section 9, the corresponding voltage saturation is considered ($\pm 2.5\ V$). The current control action is then summed to the current reference of IECO power supply. Step and sinusoidal current disturbances $\Delta I_d(t)$ are artificially generated by an analog waveform generator and injected in the closed-loop by summing them to the reference of IECO power supply as well.

10.2 NMR Sensor Models

Transfer function models for the NMR sensor are now derived according to the methodology described in Section 8. Both silicone and copper sulphate cases are investigated. The NMR parameters of the two samples are reported in Table 10.1. An Inversion-Recovery (IR) experiment is used to estimate $T1$ [14], while a Carr Purcell Meiboom Gill (CPMG) experiment allows to estimate $T2$ in presence of a non-homogeneous B_0 [14]. $T2^*$ and M_0 are obtained by fitting a simple Free Induction Decay (FID) signal [14]. Table 10.2 shows instead the lock sequence parameters. All these parameters are required by BBIM to perform simulations of the NMR lock experiment.

10.2.1 Silicone

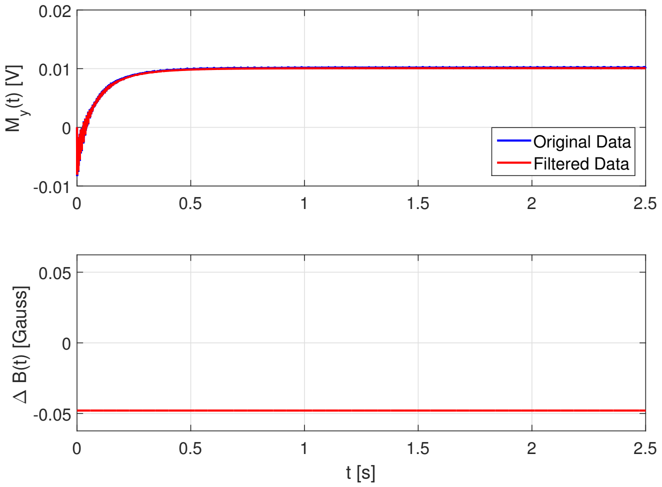

FIGURE 10.1: Silicone sample. Input-output data for CLS identification of the transfer function model. Top: $M_y(t)$ step response data from BBIM model and filtered data. Bottom: magnetic field deviation $\Delta B(t)$.

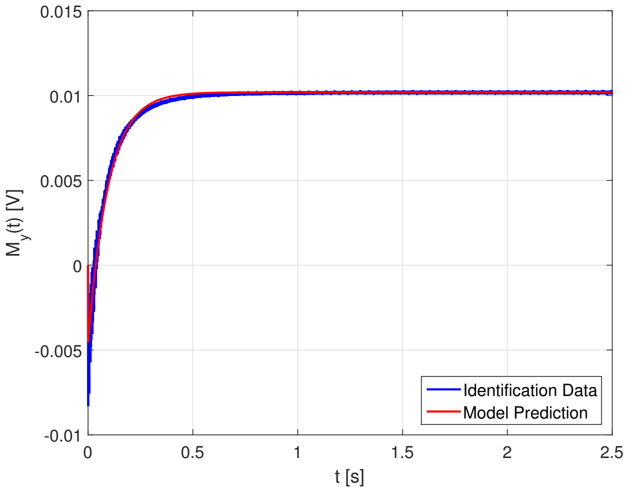

FIGURE 10.2: Silicone sample. Comparison of identification data $M_y(t)$ and transfer function model prediction $\hat{M}_y(t)$.

The dynamic behaviour of the Silicone sample stimulated with the lock sequence is simulated with BBIM model (details are reported in Tables 10.1 and 10.2). In particular, a step response experiment is simulated. The amplitude of the applied field step is $\Delta B_{step} = -0.048\ G$. The step is applied at time $t = 0\ s$ Figure 10.1 depicts the field step and the $M_y(t)$ response, which are used as input-output data for CLS identification. Figure 10.1 also shows $M_y(t)$ after low-pass filtering. A detail is depicted in Figure 10.3: note how the oscillations of the SSFP signal are removed after filtering. The behaviour of $M_y(t)$ clearly shows an inverse response. A second order system structure is then required, es defined in Equation (8.62), with the predictor reported in Equation (8.63). CLS identification allows to obtain the following values for the model parameters:

$$\begin{aligned} \mu_{nmr} &= -0.2127\ V/G \\ T_{nmr} &= -0.044\ s \\ \tau_{nmr_1} &= 0.0966\ s \\ \tau_{nmr_1} &= 0.0001\ s \end{aligned} \tag{10.1}$$

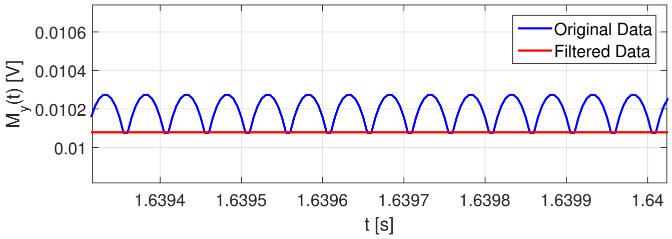

FIGURE 10.3: Silicone sample. Detail of input-output data for CLS identification of the transfer function model.

A comparison of the step response obtained from BBIM model and that predicted by $G_{nmr}(s)$ is reported in Figure 10.2. The goodness of fit results $FIT = 89\ \%$.

10.2.2 Copper Sulphate

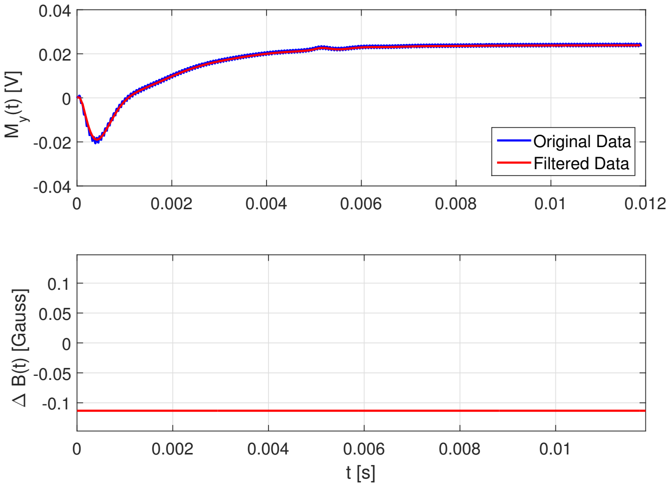

FIGURE 10.4: Copper sulphate sample. Input-output data for CLS identification of the transfer function model. Top: $M_y(t)$ step response data from BBIM model and filtered data. Bottom: magnetic field deviation $\Delta B(t)$.

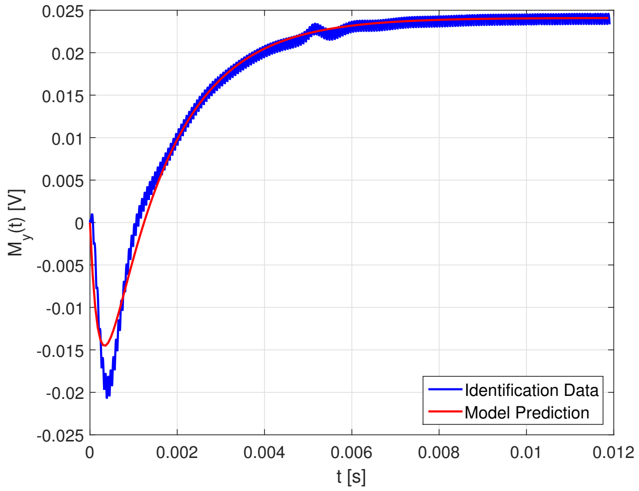

FIGURE 10.5: Comparison of identification data $M_y(t)$ and transfer function model prediction $\hat{M}_y(t)$.

A step response simulation is performed based on BBIM model. A field step of amplitude $\Delta B_{step} = -0.113\ G$ is applied at time $t = 0\ s$ to the copper sulphate sample, stimulated with the lock sequence (details are reported in Tables 10.1 and 10.2). The input-output data for CLS identification are reported in Figure 10.4. Again, $M_y(t)$ shows an inverse response. The second order system structure described in Equation (8.62) is then required, with the predictor reported in Equation (8.63). The parameters of the transfer function model obtained from CLS identification are then:

$$\begin{aligned} \mu_{nmr} &= -0.2128\ V/G \\ T_{nmr} &= -0.0015\ s \\ \tau_{nmr_1} &= 0.0015\ s \\ \tau_{nmr_1} &= 0.0002\ s \end{aligned} \tag{10.2}$$

Figure 10.5 shows a comparison of the step response obtained from BBIM model and that predicted by $G_{nmr}(s)$. The goodness of fit results $FIT = 88.5$ %.

10.3 Process Model

The whole process transfer function $G(s)$ is now derived for both NMR lock samples. As stated in Section 10.1, the IECO power supply guarantees perfect tracking of step current references, with a bandwidth of 25 KHz (157082 rad/s). Hence the parameters of Equation (9.1) can be set as:

$$\begin{aligned} \mu_{ps} &= 1 \\ \tau_{mag} &= \frac{1}{157082}\ s \end{aligned} \tag{10.3}$$

The quadrature detector low-pass filter is set to 40 KHz (251327 rad/s) for the closed-loop experiments. Its transfer function time constant can then be set as:

$$\tau_{qd} = \frac{1}{251327}\ s \tag{10.4}$$

It is important to note that both NMR lock samples (silicone and copper sulphate) show an inverse response in the step response experiment. This places an upper bound to the closed-loop bandwidth b_w, which is not likely to be higher than the frequency of the non-minimum phase zero of $G_{nmr}(s)$. In particular, in case of silicone, the zero is placed at 22.72 rad/s, while in case of copper sulphate it is placed at 674.3 rad/s. In view of this consideration, it is possible to neglect the dynamics of both $G_{ps}(s)$ and $G_{qd}(s)$, since their poles are placed at higher frequencies with respect to the expected closed-loop bandwidth b_w. In addition, since $\mu_{ps} = \mu_{qd} = 1$, it is possible to approximate:

$$G(s) \simeq G_{nmr}(s)\mu_{mag}C = \frac{\mu_g(1 + sT_{nmr})}{(1 + s\tau_{nmr_1})(1 + s\tau_{nmr_2})} \tag{10.5}$$

The NMR sensor dominates the overall dynamics of the system, while the gain is influenced by the magnet and the conductance. According to the manufacturer, the magnet is characterised by a gain $\mu_{mag} = 47\ G/A$, while the conductance results $C = 0.2\ S$. To sum up, the process transfer function in case of silicone can be expressed as:

$$G(s) = \frac{-2(1 - s0.044)}{(1 + 0.0966s)(1 + 0.0001s)} \tag{10.6}$$

while in case of copper sulphate it results:

$$G(s) = \frac{-2(1 - s0.0015)}{(1 + 0.0015s)(1 + 0.0002s)} \tag{10.7}$$

10.4 Experimental Validation Trials

The process models identified in the previous section are obtained by means of simulations only. In this section the process models are instead identified relying on real experimental data. Note that this would not be possible for the end-user of a lock system, therefore the regulators will be tuned according to the models derived in Section 10.3, and the procedure here discussed is only intended as a validation one. The steps required for the experimental trials are the same adopted for the simulated ones: the sample is stimulated with the lock sequence and brought in SSFP regime. The voltage control action $u(t)$ undergoes then a step variation. Both $u(t)$ and $M_y(t)$ are recorded as input-output data for identification, which is carried out by means of Matlab Identification Toolbox [33]. Data preprocessing is limited to the same low-pass filtering procedure also applied to the simulated data. The results are now presented for both NMR samples.

10.4.1 Silicone

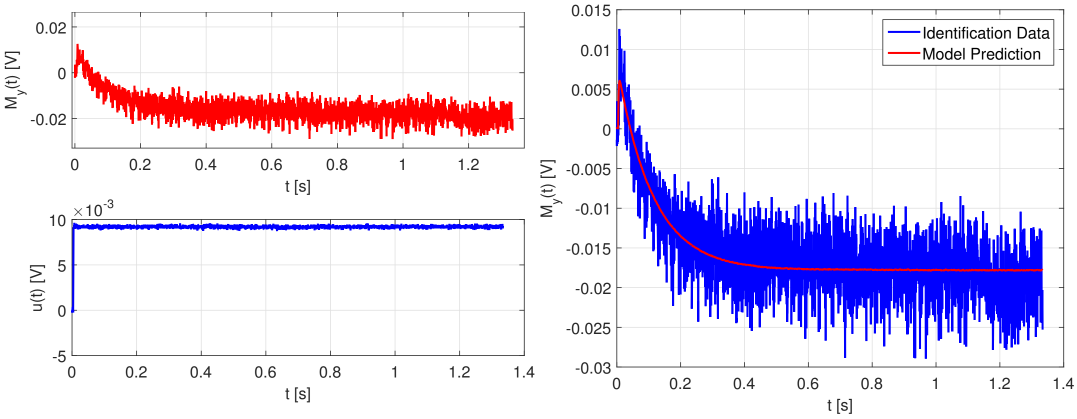

(A)

(B)

FIGURE 10.6: Silicone sample. (A) Experimental Input-output data for identification of the process model. Top: $M_y(t)$ step response data. Bottom: voltage control action $u(t)$. (B) Comparison of experimental identification data $M_y(t)$ and process model prediction $\hat{M}_y(t)$.

The step response experiment performed with the silicone sample is depicted in Figure 10.6a. As for the simulation, an inverse response is present in $M_y(t)$. The same second order structure is therefore adopted for the new identification based on experimental data. Both experimental and model predicted step response are reported in Figure 10.6b. Let $G_e(s)$ be the resulting process transfer function:

$$G_e(s) = \frac{-1.93(1 - s0.0434)}{(1 + 0.11s)(1 + 0.0014s)} \tag{10.8}$$

A comparison to Equation (10.6) highlights that the static gain, the non-minimum phase zero and the slow pole are closely identified, while the main difference is the fast pole.

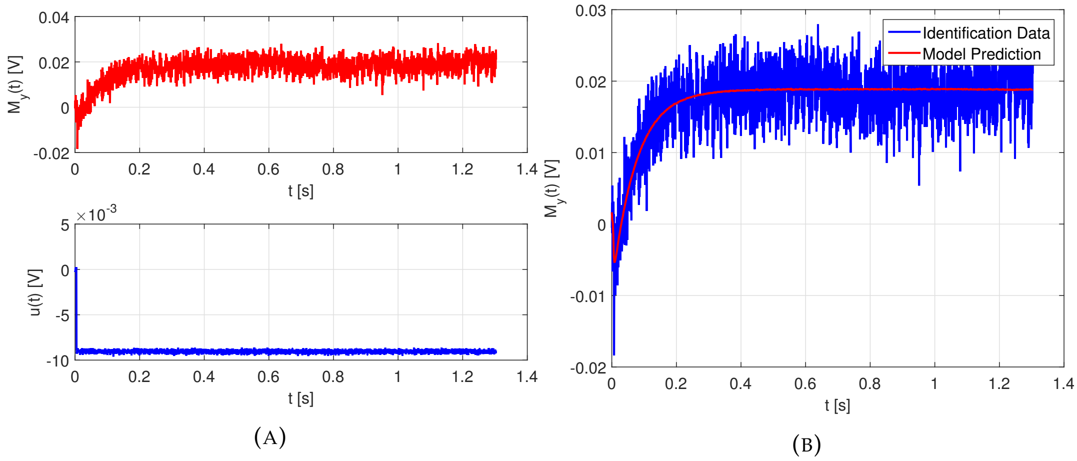

(A)

(B)

FIGURE 10.7: Copper sulphate sample. (A) Experimental Input-output data for identification of the process model. Top: $M_y(t)$ step response data. Bottom: voltage control action $u(t)$. (B) Comparison of experimental identification data $M_y(t)$ and process model prediction $\hat{M}_y(t)$.

10.4.2 Copper Sulphate

Figure 10.7a shows the step response experiment input-output signals, $u(t)$ and $M_y(t)$, in case of copper sulphate sample. As in the previous case, the experimental data are in agreement with the simulated ones and both the responses are characterised by the inverse response. The process model identified from the experimental data is then:

$$G_e(s) = \frac{-2.1(1 - s0.0271)}{(1 + 0.0747s)(1 + 0.0017s)} \tag{10.9}$$

while the one identified from simulation is reported in Equation (10.7). Figure 10.7b shows a comparison of the experimental step response and the one predicted by $G_e(s)$. Let now compare Equation (10.9) to Equation (10.7). In this case the simulated response is faster than the real one: all the time constants of Equation (10.7) are in fact shorter than those of Equation (10.9). The static gain is instead close to 2 in both cases. Recall that the synthesis of the regulator is based on Equation (10.7) only, therefore some mismatch may exist between the closed-loop performances predicted by the linear approximation and those obtained with real experiments.

10.5 Synthesis of the Regulator

The synthesis of the regulator, based on the process model $G(s)$ derived in Section 10.3, is now discussed for both lock samples. Note that, in both cases, the pole of $G(s)$ associated to τ_{nmr_2}, i.e. the one at higher frequency, is outside of the expected closed-loop bandwidth. It is therefore not necessary to compensate for its effect in the design of the loop function. This motivates the choice of implementing a PI regulator instead of a PID. The regulator transfer function can then be written as:

$$R(s) = \frac{\mu_r(1 + sT_{z1})}{s} \tag{10.10}$$

The synthesis is performed by setting:

$$\begin{aligned} T_{z1} &= \tau_{nmr_1} \\ \mu_r &= \frac{1}{\mu_g} b_w \end{aligned} \tag{10.11}$$

with

$$b_w = -\frac{1}{2}\frac{1}{T_{nmr}} \tag{10.12}$$

to keep b_w lower than the frequency of the non-minimum phase zero of $G(s)$.

10.5.1 Silicone

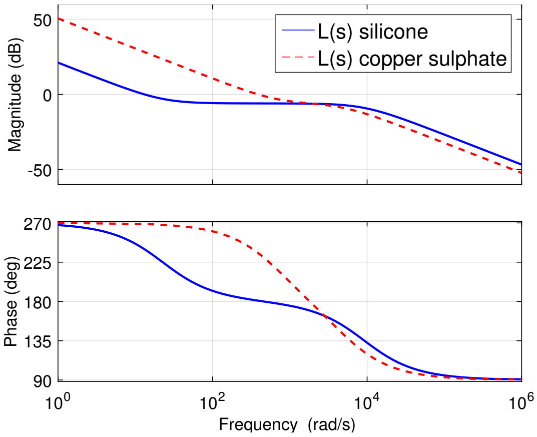

FIGURE 10.8: Loop functions $L(s)$ in case of silicone sample (solid, blue line), and of copper sulphate sample (dashed, red line).

The process transfer function in case of silicone sample is reported in Equation (10.6). By synthesising the regulator according to the previous considerations, one has:

$$\begin{aligned} \mu_r &= -5.68 \\ T_{z1} &= 0.0966\ s \end{aligned} \tag{10.13}$$

This allows to obtain a closed-loop bandwidth $b_w = 13.1\ rad/s$, with an expected closed-loop settling time of about 0.35 s. This stresses the fact that the choice of the NMR sample used for the lock experiment is crucial for the overall performances of the system. A careful design of the sample, without any inverse response - or with faster ones - may in fact allow to obtain better settling times and more rejection of process noise. With the lock sequence parameters adopted with the silicone sample (see Table 10.2), the measurement noise due to the SSFP signal is placed at 104720 rad/s. The design of $L(s)$ (see Figure 10.8) allows rejection of $-27\ dB$ of such measurement noise. The phase margin ϕ_m associated to the design results $\phi_m = 60°$, ensuring robust stability of the closed-loop (phase margin reduction due to discretisation is negligible).

10.5.2 Copper sulphate

In case of copper sulphate lock sample, the process transfer function is reported in Equation (10.7). The syntheses of the regulator results in:

$$\begin{aligned} \mu_r &= -168.575 \\ T_{z1} &= 0.0015\ s \end{aligned} \tag{10.14}$$

The associated closed-loop bandwidth is $b_w = 388\ rad/s$, with an expected closed-loop settling time of about $0.0119\ s$. With the lock sequence parameters adopted with the copper sulphate sample (see Table 10.2), the measurement noise due to the SSFP signal is placed at $125660\ rad/s$ and the loop function (see Figure 10.8) design allows $-34\ dB$ of attenuation. The phase margin ϕ_m associated to the design results $\phi_m = 55.5°$, ensuring robust stability of the closed-loop (phase margin reduction due to discretisation is negligible).

10.6 Closed-loop Trials

A set of closed-loop experiments is designed to assess the performances of the two loop functions design, with particular focus on the rejection of process disturbance, when dealing with the real process. Note that, with the current NMR hardware setup, the measurement noise at low frequency is relevant when compared to the measure of the current disturbance of the IECO power supply (see Section 9). Waiting for a new NMR receiver chain with reduced measurement noise, in order to test the controller design, an artificial current disturbance of significant amplitude is injected in the system. The current disturbance is introduced by means of an analog current waveform generator, whose output is summed to the power supply current reference. In particular, two different kind of experiments are performed: a step disturbance is injected to test the closed-loop settling time, while sinusoidal disturbance at different frequencies are useful to test the design of the loop function. Note that the amplitude of the current disturbances (about $500\ \mu A$ for step disturbances and $2\ mA$ for sinusoidal disturbances) is chosen so that the corresponding field disturbance (about $23.5\ mG$ and $94\ mG$, respectively) does not exceed the linear region of the NMR sensor.

10.6.1 Silicone

In case of NMR lock based on the silicone sample, according to the design described in Section 10.5, the expected closed-loop bandwidth is $b_w = 13.1\ rad/s$, corresponding to a settling time of about $0.35\ s$. Figure 10.9 shows the experimental response to a step current disturbance. The experimental evaluation results in about $0.1\ s$ of settling time, which is faster than expected from the linear approximation. Figures 10.10a and 10.10b show the open and closed-loop to a $1\ Hz$ sinusoidal disturbance, respectively. The effect on the feedback signal $M_y(t)$ is reduced of about 5 times by the closed-loop. This is slightly better than predicted by the loop function design, which has a magnitude of about $6\ dB$ at $1\ Hz$ (see Figure 10.8). Figures 10.10a and 10.10b show instead the open and closed-loop response to a $10\ Hz$ sinusoidal disturbance. In this case, the effect on the feedback signal $M_y(t)$ is not reduced by the closed-loop. This is consistent with the loop function design. Note that a DC current offset is present in the current disturbance. This offset is correctly compensated by the integral action featured in the closed-loop.

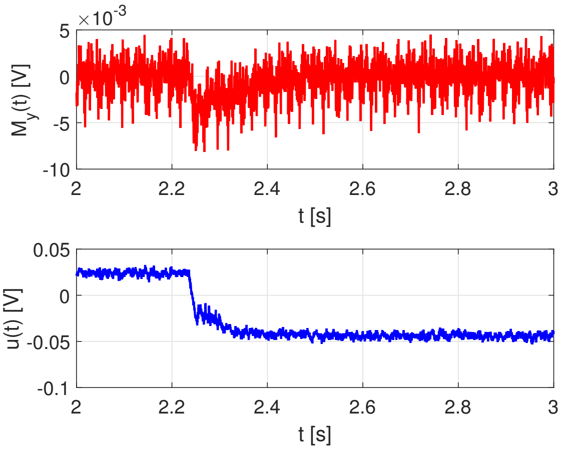

FIGURE 10.9: Silicone sample. Closed-loop response to a current step disturbance. Top: feedback signal $M_y(t)$ Bottom: voltage control action $u(t)$.

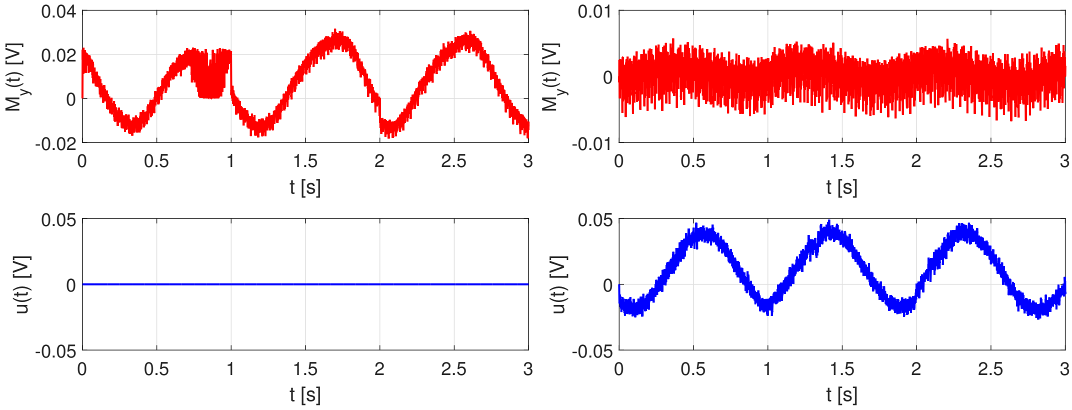

(A) (B)

FIGURE 10.10: Silicone sample. Open-loop (A) and closed-loop (B) response to a 1 Hz sinusoidal disturbance. Top: feedback signal $M_y(t)$ Bottom: voltage control action $u(t)$.

10.6.2 Copper Sulphate

The expected closed-loop bandwidth and settling time in case of copper sulphate sample are $b_w = 388\ rad/s$ and $0.0119\ s$, respectively. The experimental results obtained with the application of a current step disturbance are reported in Figure 10.12. The closed-loop settling time can be experimentally valued as $0.015\ s$, that it slightly longer than expected. Figures 10.13a and 10.13b show the open and closed-loop response to a $10\ Hz$ sinusoidal disturbance. In this case, the effect on the feedback signal $M_y(t)$ is reduced of a factor 3 by the closed-loop. This is consistent with the loop function design, which should provide $14\ dB$ of rejection at $10\ Hz$. Figures 10.14a and 10.14b show the open and closed-loop response to a $50\ Hz$ sinusoidal disturbance. The loop function has magnitude $1.8\ dB$ at $50\ Hz$, providing a slight reduction of the effect of sinusoidal noise, as verified in the experiment (factor 1.3 of reduction). The open and closed-loop responses to a $100\ Hz$ current disturbance are instead depicted in Figure 10.15a and 10.15b, with no appreciable rejection of noise, as expected from the loop function design.

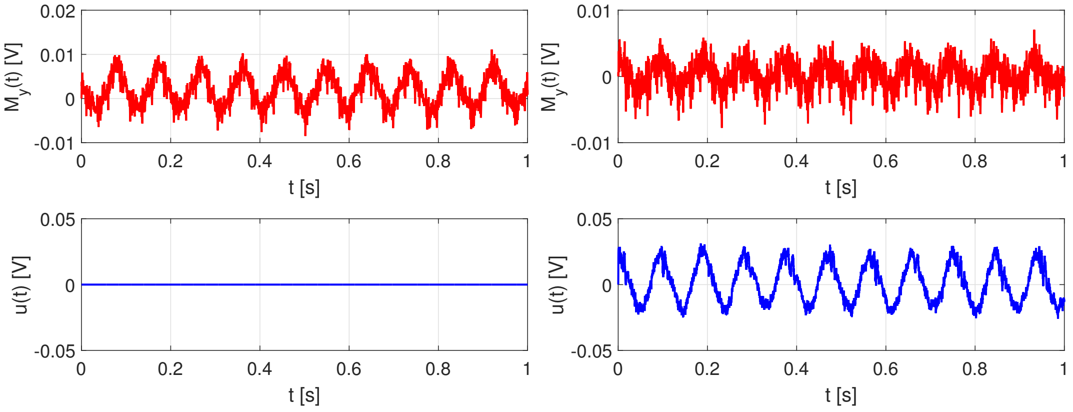

(A) (B)

FIGURE 10.11: Silicone sample. Open-loop (A) and closed-loop (B) response to a 10 Hz sinusoidal disturbance. Top: feedback signal $M_y(t)$ Bottom: voltage control action $u(t)$.

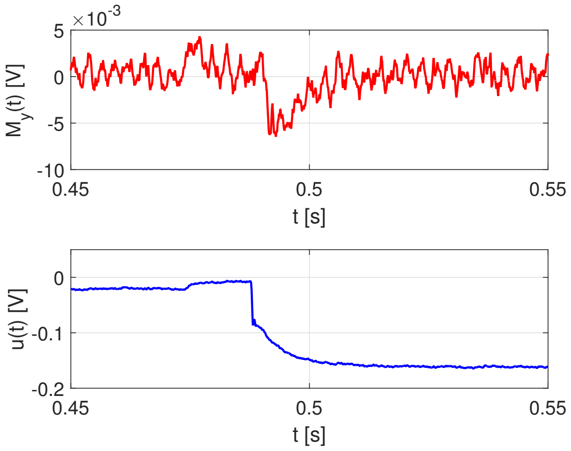

FIGURE 10.12: Copper sulphate sample. Closed-loop response to a current step disturbance. Top: feedback signal $M_y(t)$ Bottom: voltage control action $u(t)$.

10.7 Effect of Lock System on the Main NMR Experiment

The final aim of the NMR lock system is improving the results of the main NMR experiment which runs in parallel. For this purpose, a series of NMR experiments is performed without NMR lock first, then repeated with the lock system based on copper sulphate, in presence of external current disturbances. The choice of copper sulphate is motivated by the better performances obtained in Section 10.6.2. The main NMR experiment is carried out on a pure Galden sample, targeting the Fluorine F^{19} nucleus ($\gamma = 25166.2\ rad/(s\ G)$) at a magnetic field $B_0 = 1880\ G$, corresponding to a resonance frequency of about 8 MHz. Each experiment consists in a series of standard S1P sequences, generating a standard $T2^*$ decay of the recorded NMR signal [14]. A S1P experiment runs on resonance if the imaginary component of the quadrature detected NMR signal is zero, and the real component shows an exponential decay. Figure 10.16a shows the main NMR signal in presence of the 10 Hz sinusoidal current disturbance. According to the analysis carried out in Section 10.6.2, the lock system should appreciably improve the results by rejecting the current oscillations. The results of the NMR experiment with the same disturbance

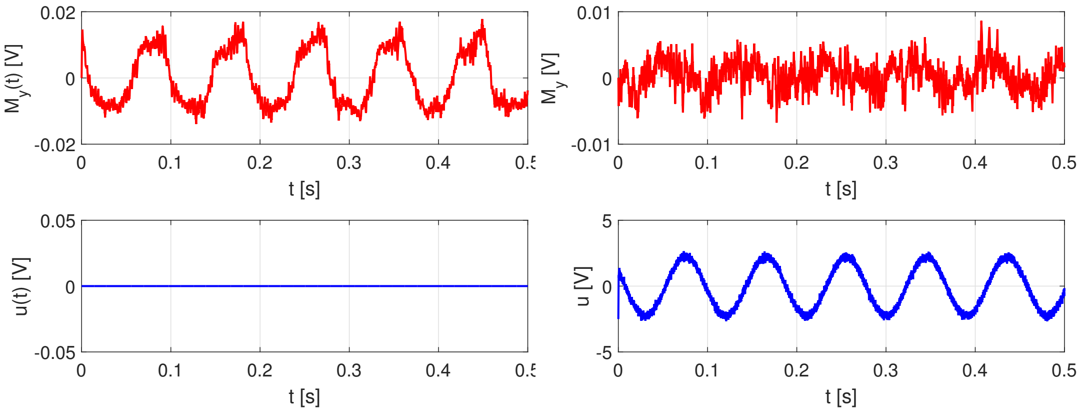

(A) (B)

FIGURE 10.13: Copper sulphate sample. Open-loop (A) and closed-loop (B) response to a 10 Hz sinusoidal disturbance. Top: feedback signal $M_y(t)$ Bottom: voltage control action $u(t)$.

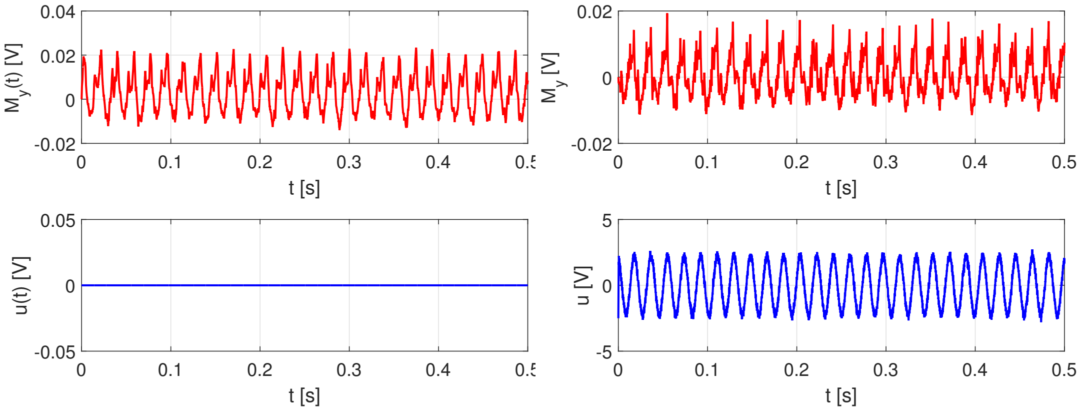

(A) (B)

FIGURE 10.14: Copper sulphate sample. Open-loop (A) and closed-loop (B) response to a 50 Hz sinusoidal disturbance. Top: feedback signal $M_y(t)$ Bottom: voltage control action $u(t)$.

and the lock system are depicted in Figure 10.16b. Note how the imaginary component of the NMR signal is closer to zero with respect to the open-loop case, and the exponential shape of the real component. The experiment is repeated with a 50 *Hz* sinusoidal current disturbance. Results are depicted in Figures 10.17a and 10.17b. The presence of the lock system still improves the results, but some oscillations are still present in the NMR signal, since the current disturbance is just slightly rejected by the closed-loop.

As stated before, the experiment runs on resonance if the imaginary signal is zero. Therefore, a possible way to quantitatively evaluate the effect of the lock system is to consider the power $\mathbb{P}$ of that signal, with $\mathbb{P}$ defined as follows:

$$\mathbb{P}[z] = \frac{1}{N+1} \sum_{n=0}^{N} |z(n)|^2 \tag{10.15}$$

where $z(n)$ is a generic discrete-time signal. Table 10.3 reports a comparison of the power of the imaginary part of the NMR in the two trials discussed in this section.

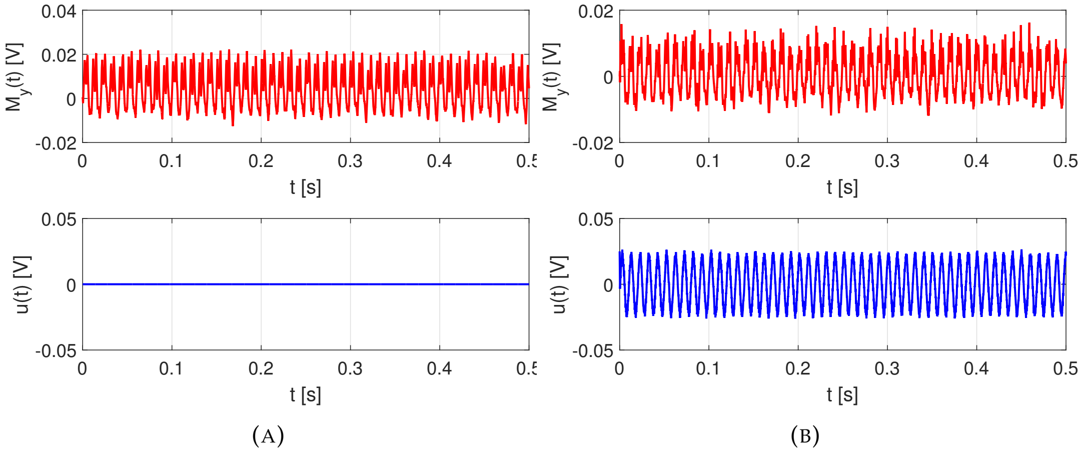

FIGURE 10.15: Copper sulphate sample. Open-loop (A) and closed-loop (B) response to a 100 Hz sinusoidal disturbance. Top: feedback signal $M_y(t)$ Bottom: voltage control action $u(t)$.

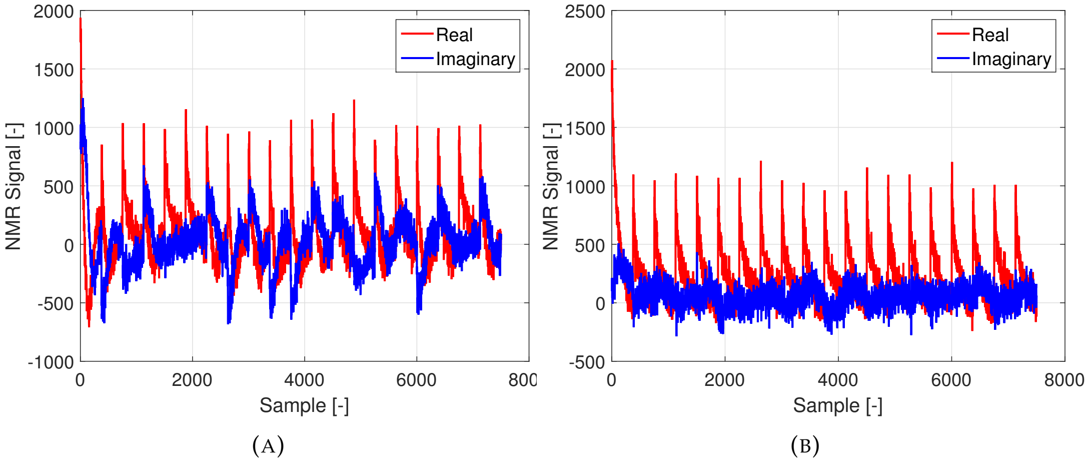

FIGURE 10.16: Copper sulphate sample. Main NMR experiment without lock system (A) and with lock system (B), in presence of a 10 Hz sinusoidal disturbance.

In both cases, the presence of the lock system allows to reduce the power with respect to the no lock case. As expected from the loop function design and as already shown by the closed-loop trials, the lock is more effective with the 10 Hz sinusoidal disturbance.

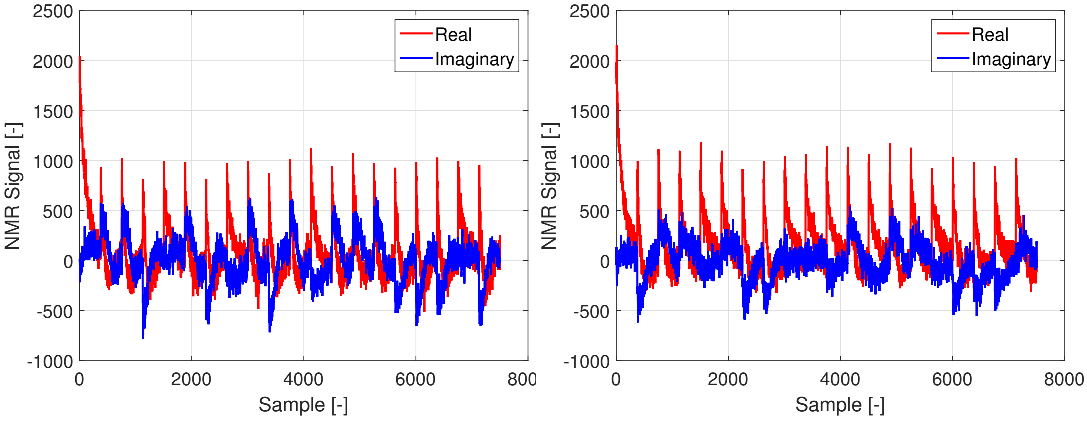

(A) (B)

FIGURE 10.17: Copper sulphate sample. Main NMR experiment without lock system (A) and with lock system (B), in presence of a 50 Hz sinusoidal disturbance.

Noise Frequency $[Hz]$	*Img Power Without Lock* $[-]$	*Img Power With Lock* $[-]$
10	57300	13800
50	49200	31200

TABLE 10.3: Power of imaginary component of NMR signal with and without lock system, in presence of external current disturbance.

Chapter 11

Conclusion and Future Work

This work aims to provide a complete description of an NMR Lock system by means of mathematical models and to define a proper methodology for the synthesis of a parametric regulator. The Lock system must in fact fulfil a set of requirements in terms of stability, perfect tracking of a magnetic field reference and maximum settling time of the magnetic field. To obtain this goal it is necessary to analyse all the different aspects of the process under control, ranging from the hardware necessary to perform the NMR experiment to the physics of NMR. The first part of this thesis is therefore devoted to a quantitative, detailed analysis of the NMR phenomenon. This allows to master the subject even in complex situations such as the presence of a non-homogenous magnetic field. Furthermore, the different approaches to the problem of lock are explored, so that the most promising in terms of fulfilling the requirement is chosen. Attention is then moved to the hardware which allows to perform a correct NMR Lock experiment. Great effort is devoted to the modelling of the NMR phenomenon. Different models are investigated and their response compared to real NMR trials performed in collaboration with Stelar s.r.l. The result is a parameterised model which allows the system to work independently on the substances used for the NMR experiment. In the end a methodology for the synthesis of a PID regulator is proposed. Two lock sensors are designed and their linear models are obtained from simulated data. Experimental data are collected to evaluate the correctness of the procedure. The lock control loop is then designed, on the basis of the sensor model and on models of the hardware needed to perform the NMR lock experiment. Two PI regulators are tuned accordingly. Closed-loop trials confirm the correctness of the approach, providing results in agreement with the loop function design. Standard NMR experiments are also performed with and without the designed lock system and highlight the benefit of its introduction. The next step of the research will consist in applying the proposed methodology to develop an external lock system for proton FFC NMR, with the lock experiment performed on fluorine. This will require the engineering of a proper fluorine sample allowing to efficaciously perform the lock experiment, and a dedicated receiver channel with high SNR. Moreover, FFC NMR, where the B_0 field quickly cycles over different values, introduces a further difficulty since the virtual sensor for the measure of the magnetic field deviation may exhibit a different dynamic behaviour during the ramp from the relaxation to the acquisition field. In case this effect can not be properly handled with the robustness of the control design, ad hoc solutions should be developed.

Part II

Service Pressure Regulation in Water Distribution Newtorks

Chapter 12

Introduction

Due to its benefits in terms of leakage reduction [40], pipe burst abatement [41, 42] and infrastructure life extension, pressure control has recently been widely adopted in the management of water distribution networks (WDNs). After a WDN has been divided into zones of homogeneous elevation (pressure zones) for facilitating pressure regulation [43], local and remote real time control (RTC) can be adopted to drive a control valve installed in each pressure zone. The difference between local and remote RTC lies in the source of the measurements used for service pressure regulation. Local RTC is carried out by controlling a variable at the valve site (i.e. the pressure head at the valve outlet) [44, 45, 46, 47]. Remote RTC, instead, is carried out by taking as controlled variable the pressure head at the critical node, i.e. the node with minimum average pressure [48, 49, 50, 51, 52]. While being more burdensome in terms of installation costs, remote RTC is often more cost-effective in the long run [52]. In fact, it enables service pressure regulation to meet WDN demand variations in time. RTC controllers can serve as low-level controllers in hierarchical control schemes, where a high-level optimal control strategy defines the pressure setpoints for the different pressure zones, according to an economic cost-benefit evaluation over the whole network [53, 54, 55, 56, 57, 58, 59]. The operation of remote RTC can be summarized as follows. At each control time step, the pressure head is measured at the remotely controlled node. By making use of suitable algorithms operating on the pressure head measurements, a programmable logic controller sets the new suitable device setting to obtain the desired pressure at the remote node. In the works of Campisano et al. [48, 49, 50], simple proportional algorithms were used for valve control. Based on physical considerations on the WDN, Creaco and Franchini [51] developed a more effective algorithm that also makes use of the water discharge measurement in the pipe equipped with the control device. Finally, Creaco [60] and Page et al. [61] showed that implementing water discharge prediction inside the control algorithm of Creaco and Franchini [51] may be beneficial in terms of error on the controlled variable with respect to the set point and of total variations of the device setting. The benefits stand out above all when the random fluctuations of demand are insignificant compared to its hourly variations [60]. The algorithms by Campisano et al. [48, 49, 50], Creaco and Franchini [51], Creaco [60] and Page et al. [61] were all developed considering sufficiently large control time steps, e.g. order of magnitude of some minutes, across which WDN behaviour can be approximated as a sequence of steady states. The aim of this work is instead investigating the possibility of improving the regulation performance by reducing the sampling time of the control system (down to 1 second). This requires taking into account the dynamic behaviour of the WDN. Different model-based algorithms (Proportional-Integral and Linear Quadratic Gaussian Controllers) are tuned and tested, and their performance evaluated with simulations in two different case studies. The algorithm by Creaco and Franchini [51] is used as benchmark for comparison. Results related to this part

of the Thesis are published in [62].
This part of the Thesis starts providing the reader with some basic concepts of hydrodynamics (Chapter 13) and both a physical and mathematical detailed description of the unsteady flow in elastic pipes (Chapter 14). The case studies are then introduced in Chapter 15, along with their mathematical models, which are used for simulations. Then the control algorithms are introduced and the tuning process described in detail (Chapter 16). Chapter 17 is devoted to an in-depth analysis of stability and robustness of frequency domain control algorithms that allows to improve the tuning strategy. Finally, an extensive comparison of results is reported in the final chapter of this work.

Chapter 13

Basics of Hydrodynamics

This preliminary chapter is devoted to the introduction of the basic concepts of hydrodynamics which will be exploited in the following chapters to formulate a complete mathematical model for the plant under consideration. Further details can be found in [43, 63]

13.1 Fluid Motion

Let consider a fluid in motion, which can described by its flow field. Then it is possible to introduce the concepts of flow lines, flow tubes and fluid threads, and characterise different regimes of fluid motion. *Flux lines* are in each point of the flow field, instant by instant, the lines tangent to the velocity vector (see Figure 13.1). Consider now a closed curve that is not a flow line, and draw the flow lines through each point of the considered curve. Such set of flow lines is called *flow tube*. A flow tube is characterised by no flow throughout any of its points. An example is depicted in Figure 13.2 If, in addition, the closed curve defining the flow tube encircles an infinitesimal area dA, then the flow tube is called *flow thread*.
Flow can then be characterised according to its behaviour in time. In particular, a fluid is characterised by a *steady flow* condition if both geometric and cinematic properties do not change in time, in each cross section. This also means that velocity is constant in each point of the flow field. In addition, if geometric and cinematic properties are also constant throughout all the cross sections, the steady flow is said to be *uniform*. On the contrary, if the geometric and cinematic properties of the flow do change in time, flow is said to be *unsteady*, and is characterised by time varying velocities in each point of the flow field.

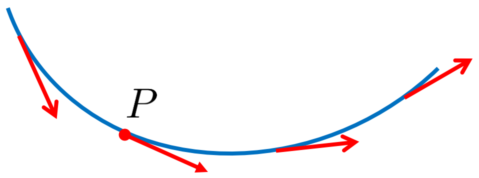

FIGURE 13.1: A flow line is tangent to the velocity vector in each point P of the flow field.

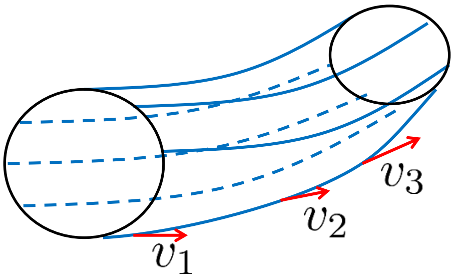

FIGURE 13.2: A flow tube example: black lines represent the closed curve, blue lines are flux lines.

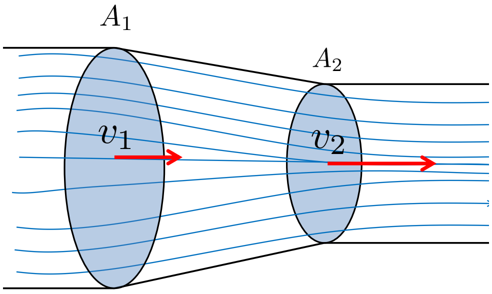

FIGURE 13.3: Pipe with variable cross section.

13.2 The Continuity Equation

The *mass conservation principle* states that the overall mass characterising a system can not be altered by any transformation (nuclear phenomena excluded), and represent the most basic principle of hydrodynamics. Consider an infinitesimal volume dV, crossed by the flow. Then the mass conservation principle states that the mass of fluid entering such volume must equal the mass of fluid leaving it. In general, the fluid density ρ can change due to changes in the fluid temperature or pressure. For sake of simplicity, assume that ρ is constant in the following, if not differently stated. For each section of the flow, it is possible to express the volume of fluid crossing the section in an infinitesimal time instant dt as:

$$dV = Svdt \tag{13.1}$$

where v is the average fluid velocity in the section and S is the area of the section. The flow Q is then defined as:

$$Q = \frac{dV}{dt} = Sv \tag{13.2}$$

Consider now the situation depicted in Figure 13.3, and suppose a steady flow condition. It is then possible to compute the flow in sections 1 and 2, Q_1 and Q_2 , as:

$$Q_1 = S_1 v_1 \quad Q_2 = S_2 v_2 \tag{13.3}$$

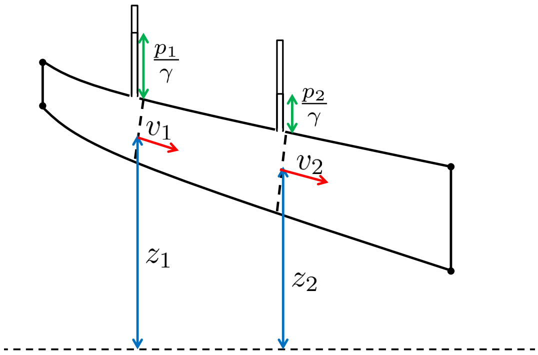

FIGURE 13.4: Pipe with variable cross section.

Due to the steady flow hypothesis, flow velocity does not change in time, therefore flow is also constant in time. Then:

$$Q_1 = Q_2 = Q = constant \tag{13.4}$$

With reference to flow threads, it is possible to express the continuity equation for steady flow conditions as:

$$\frac{dQ}{ds} = 0 \tag{13.5}$$

with s the curvilinear coordinate defined along the fluid thread. In case of unsteady flow, instead, the flow is *not* constant along all the fluid thread.

13.3 The Energy Conservation Principle

The *energy conservation principle* is the second basic principle of hydrodynamics. It states that the overall energy of an isolated system does not change in time; energy can only be transformed from one form to another. With reference to Figure 13.4, let consider two sections of the pipe, and assume an ideal fluid (characterised by no friction), in steady flow condition. Assume also that the fluid does not exchange energy with the surroundings. Then the energy of the fluid at section 1 has to equal the energy at section 2. In general, the overall amount of energy of the fluid can be expressed as the sum of three main contributions:

- *potential energy due to the geodetic altitude*. It is computed as:

  $$E_p = mgz \tag{13.6}$$

  where m is the fluid mass, g is gravity and z is the geodetic altitude of the fluid with respect to a reference plane $z = 0$;

- *potential energy due to pressure*. It is computed as:

  $$E'_p = mg\frac{p}{\gamma} \tag{13.7}$$

  where m is the fluid mass, g is gravity, p is pressure and γ is the specific weight of the fluid;

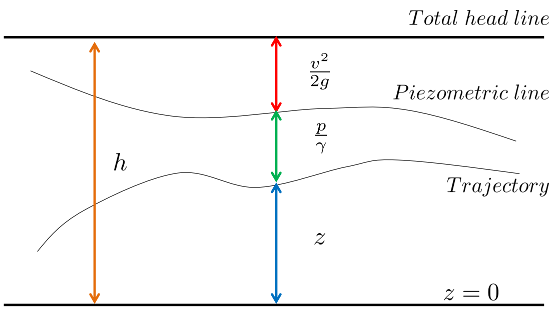

FIGURE 13.5: Graphical representation of Bernoulli equation for an ideal fluid.

- *kinetic energy*. It is computed as:

$$E_k = \frac{1}{2}mv^2 \tag{13.8}$$

where m is the fluid mass, v is the velocity of the fluid.

The overall energy of the fluid is the sum of these three contributions, which is constant in time and space under the assumptions of steady flow and ideal fluid. The overall energy H is called *total head*, and can be computed by means of *Bernoulli's equation* as follows:

$$H = mgz + mg\frac{p}{\gamma} + \frac{1}{2}mv^2 = constant \tag{13.9}$$

Dividing Equation 13.9 by the mass m it is possible to compute the total head of the fluid thread h:

$$h = z + \frac{p}{\gamma} + \frac{v^2}{2g} = constant \tag{13.10}$$

Note that, with this formulation, h is expressed in *meters*. Finally, Bernoulli's equation applied to an ideal fluid thread can be written as:

$$\frac{dH}{ds} = 0 \tag{13.11}$$

with s the curvilinear coordinate defined along the fluid thread. In case of unsteady flow, instead, the total head is *not* constant along all the fluid thread.

13.4 Total Head Line and Piezometric Line

Let now consider the Bernoulli equation for an ideal fluid, as expressed in Equation 13.10. Note that the three terms are expressed in *meters*, and can be identified as:

- *geodetic altitude*, the altitude of the fluid with respect to a reference plane $z = 0$;
- *piezometric height*, the ratio of the pressure p and the fluid specific weight γ;
- *kinetic height*, the ratio of the squared velocity v^2 and twice the gravity acceleration g.

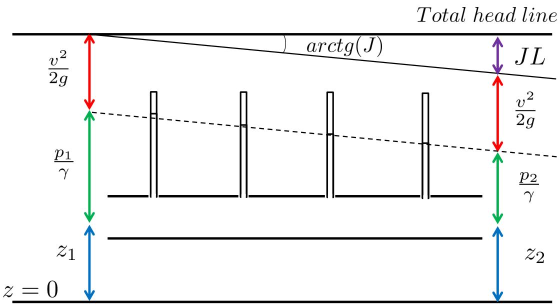

FIGURE 13.6: Graphical representation of Bernoulli equation for a real fluid.

The *piezometric altitude* is the sum of geodetic altitude z and piezometric height, and represents the potential energy of the fluid thread. The sum of the piezometric altitude and of the kinetic height gives the total head h, the overall energy of the fluid thread. Both the piezometric altitude and the total head can be graphically represented as lines: this interpretation is resumed in Figure 13.5, where the reference plane for the geodetic altitude is $z = 0$.

Let now consider a *real* fluid and introduce the effect of viscous friction in Bernoulli's equation. Viscous friction arises both from the interaction between fluid particles and between fluid particles and the internal surface of the pipe. The situation is depicted in Figure 13.6, where a horizontal pipe is considered for sake of clarity. In this case, the fluid dissipates part of its energy as friction while flowing along the pipe, and the piezometric line is no longer parallel to the reference plane. For a real fluid in steady flow conditions, the piezometric line is a straight line with slope $-J$, with J the *friction slope*, defined as follows:

$$J = \frac{\Delta h}{L} \tag{13.12}$$

with L the length of the pipe and Δh the head loss across the pipe. It represents the head loss per unit length. Note that, in steady flow conditions, the total head line is parallel to the piezometric line, therefore the total head line is also a straight line with slope $-J$. It is then possible to formulate Bernoulli's equation applied to a real fluid thread:

$$\frac{dH}{ds} = -J \tag{13.13}$$

with s the curvilinear coordinate defined along the fluid thread.

Chapter 14

Elastic Unsteady Flow

This chapter is devoted to a detailed description of the unsteady flow in elastic conditions, also known as *water hammer effect*. The phenomenon is first analysed with a conceptual example, then by means of a rigorous mathematical description which will allow to develop a proper simulation environment for the case studies presented in this work. With elastic flow, two main effects have to be considered: the fluid density can not be considered constant, mainly due to the effect if pressure. In addition, the pipes the fluid is flowing through can also undergo elastic deformation, again due to pressure. Let consider 14.1, which depicts a conceptual case study that allows to qualitatively introduce the water hammer effect. The system under consideration is composed of a reservoir, acting as a source node, an elastic pipe, and a shutter placed at the end of the pipe, where the shutter is completely open. The fluid initially flows from the reservoir to the end of the pipe with velocity v_0. Pressure $h_0 = p_0/\gamma$ is initially determined by the reservoir, and is common to all sections of the pipe. Suppose now that the shutter is suddenly closed. Let this happen at time $t = 0$. This means that fluid velocity at the end of the pipe must become null. This in turn means that pressure increases to balance the inertia of the fluid. Let this pressure increase be denoted as Δp. The increase in the pressure generates an increase in the fluid density, which finally results in elastic deformation of the pipe. The perturbation of the flow conditions ($v_0 = 0$ and $h = (p_0 + \Delta p)/\gamma$) starts travelling upstream the pipe with speed $-c$, called *celerity*, which mainly depends on the characteristics of the pipe. This can be interpreted as a pressure wave moving through the pipe. As the wave reaches the reservoir, it is reflected and propagates towards the end of the pipe with celerity c. Pressure is restored at $h = h_0$, but, to obtain this, the fluid speed is reversed (i.e. $v = -v_0$). When the perturbation reaches the shutter, the fluid speed is again set to zero. This generates a pressure decrease of $-\Delta p$, which propagates along the pipe in the upstream direction. Once it reaches the reservoir, it is reflected again to restore the pressure. Fluid velocity is again reversed, and gets value $v = v_0$. When the perturbation reaches the shutter, the initial conditions are restores, and the process repeats periodically. Note that, when dealing with a real fluid characterised by the presence of friction, part of the energy is consumed in the process, which finally settles to a new equilibrium condition, which differs from the initial one.

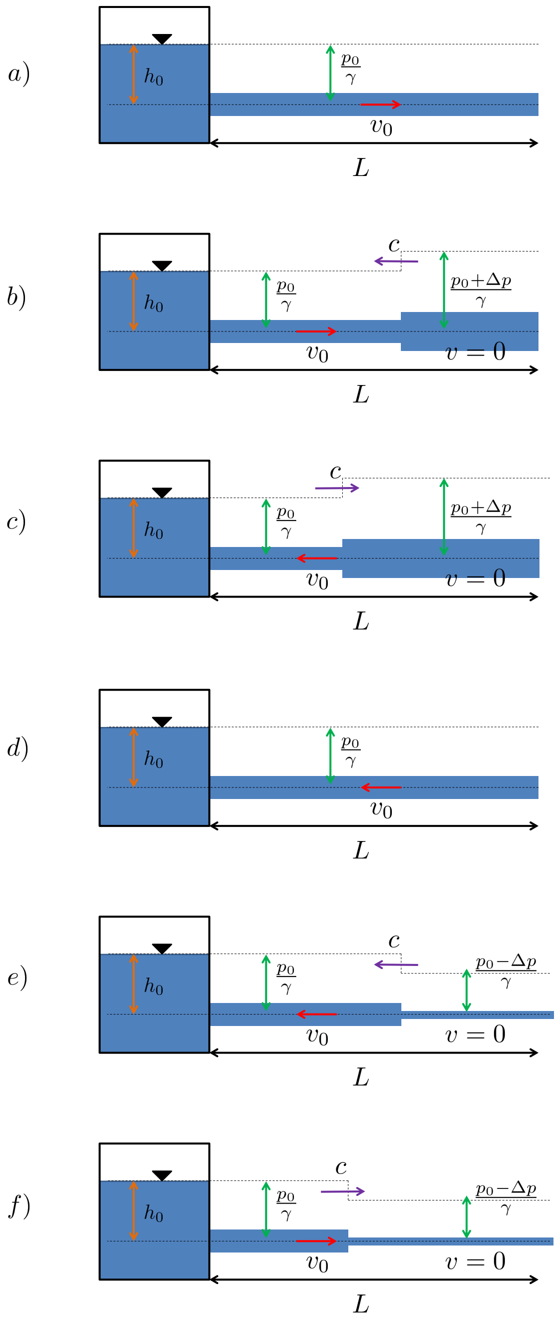
a)
h_0
$\frac{p_0}{\gamma}$
v_0
L
b)
h_0
c
$\frac{p_0}{\gamma}$
$\frac{p_0+\Delta p}{\gamma}$
v_0
$v = 0$
L
c)
h_0
c
$\frac{p_0}{\gamma}$
$\frac{p_0+\Delta p}{\gamma}$
v_0
$v = 0$
L
d)
h_0
$\frac{p_0}{\gamma}$
v_0
L
e)
h_0
c
$\frac{p_0}{\gamma}$
$\frac{p_0-\Delta p}{\gamma}$
v_0
$v = 0$
L
f)
h_0
c
$\frac{p_0}{\gamma}$
$\frac{p_0-\Delta p}{\gamma}$
v_0
$v = 0$
L

FIGURE 14.1: Conceptual example of the water hammer effect.

14.1 Elastic Unsteady Flow Equations

In case of unidimensional elastic unsteady flow, the continuity equation and the work energy principle discussed in the previous chapter are expressed as follows:

$$\begin{cases} \dfrac{\partial H}{\partial x} + \dfrac{1}{gA}\dfrac{\partial Q}{\partial t} + J = 0 \\ \dfrac{\partial H}{\partial t} + \dfrac{c^2}{gA}\dfrac{\partial Q}{\partial x} = 0 \end{cases} \tag{14.1}$$

where Hp $[m]$ and Q $[m^3/s]$ are the pressure head and the flow discharge along the pipe, x $[m]$ is the position along the pipe, t $[s]$ is time, A $[m^2]$ is the pipe cross-section area, g $[m/s^2]$ is the gravity acceleration constant, c $[m/s]$ is the wave celerity, J is the friction slope [43].

The wave celerity c can be computed as:

$$c = \left(\frac{\frac{\epsilon}{\zeta}}{1 + \frac{\epsilon d}{Es}} \right)^{\frac{1}{2}} \tag{14.2}$$

where ϵ $[Pa]$ and ζ $[kg/m^3]$ are water bulk modulus and density; E $[Pa]$, d $[m]$ and s $[m]$ are pipe modulus of elasticity, diameter and thickness.

The pipe friction slope can be evaluated according to the *Darcy-Weisbach* formula:

$$J = 10.29 \frac{n^2|Q|Q}{d^{5.33}} \tag{14.3}$$

where n $[s/m^{\frac{1}{3}}]$ is the Gauckler–Manning coefficient and d $[m]$ is the pipe diameter. Note that this expression was originally developed for steady flow. In case of unsteady flow, a correction factor has to be applied to obtain a better description of the energy loss.

14.1.1 Method of Characteristics

Equation 14.1 represents a system of partial differential equations, where the independent variables are the time t and the position along the pipe x. The *method of characteristics* allows to transform the unsteady flow equations in a set of ordinary differential equations [63], as now discussed.
Consider the following combination of Equations 14.1:

$$g\left(\frac{\partial H}{\partial x} + \frac{1}{gA}\frac{\partial Q}{\partial t} + J\right) + \lambda\left(\frac{\partial H}{\partial t} + \frac{c^2}{gA}\frac{\partial Q}{\partial x}\right) = 0 \tag{14.4}$$

By rearranging terms it is possible to write it as:

$$g\frac{\partial H}{\partial x} + \lambda\frac{\partial H}{\partial t} + \frac{1}{A}\frac{\partial Q}{\partial t} + \lambda\frac{c^2}{gA}\frac{\partial Q}{\partial x} + gJ = 0 \tag{14.5}$$

with λ a linear combination term.
It is also possible to write:

$$\begin{aligned}\frac{dH}{dt} &= \frac{\partial H}{\partial t} + \frac{\partial H}{\partial x}\frac{dx}{dt} \\ \frac{dQ}{dt} &= \frac{\partial Q}{\partial t} + \frac{\partial Q}{\partial x}\frac{dx}{dt}\end{aligned} \tag{14.6}$$

and pick λ such that:

$$\frac{dx}{dt} = \frac{g}{\lambda} = \frac{\lambda c^2}{g} \tag{14.7}$$

In this way the linear combination can be written as:

$$\lambda\frac{dH}{dt} + \frac{1}{A}\frac{dQ}{dt} + gJ = 0 \tag{14.8}$$

where λ assumes the following values:

$$\lambda = \pm\frac{g}{c} \tag{14.9}$$

and the corresponding relation between space and time is given by:

$$\frac{dx}{dt} = \pm c \tag{14.10}$$

In the (x, t) plane, Equation 14.10 represent two straight lines with slopes $1/c$ and $-1/c$, called *characteristic lines*, which coincide with the discontinuities of the solution of the differential problem. From a physical point of view, they instead represent the travel of perturbations.

In particular, when considering the positive characteristic C^+, Equation 14.8 can be rewritten as:

$$dH + \frac{c}{gA}dQ + Jcdt = 0 \tag{14.11}$$

by setting:

$$\frac{dx}{dt} = c \tag{14.12}$$

If instead the negative characteristic C^- is considered, it is possible to write:

$$dH - \frac{c}{gA}dQ - Jcdt = 0 \tag{14.13}$$

by setting:

$$\frac{dx}{dt} = -c \tag{14.14}$$

14.2 Integration of Unsteady Flow Equations

By introducing the hypothesis of constant celerity c, the characteristic lines can be integrated as:

$$\pm\, c = \frac{\Delta s}{\Delta t} \tag{14.15}$$

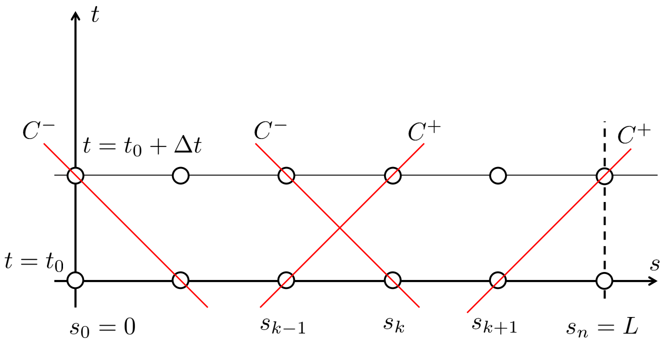

FIGURE 14.2: Representation of characteristic lines for the integrated equations of elastic unsteady flow, applied to a pipe of length L.

where Δs is the modulus of the space travelled by the perturbation in a time interval Δt. The integration of equations 14.11 and 14.13 along the characteristic lines results:

$$\begin{aligned} &\left(H_{s,t+\Delta t} - H_{s-1,t}\right) + \frac{c}{gA}\left(Q_{s,t+1} - Q_{s-1,t}\right) + c\Delta t J(Q_{s-1,t}) = 0 \;\; (C^+) \\ &\left(H_{s,t+\Delta t} - H_{s+1,t}\right) + \frac{c}{gA}\left(Q_{s,t+1} - Q_{s+1,t}\right) - c\Delta t J(Q_{s+1,t}) = 0 \;\; (C^-) \end{aligned} \tag{14.16}$$

Consider now a pipe of lenght L, and subdivide it into n sections, each of length Δs. Equation 14.16 allow to determine pressure heads and flow values in each section of the pipe at each finite timestep Δt. Spatial and temporal steps must be related according to Equation 14.15. A typical procedure consists in defining the spatial step and computing the resulting temporal step. With reference to Figure 14.2, it is possible to compute pressure head and flow in the generic section s_k as follows:

$$\begin{aligned} &\left(H_{s_k,t+\Delta t} - H_{s_{k-1},t}\right) + \frac{c}{gA}\left(Q_{s,t+\Delta t} - Q_{s_{k-1},t}\right) + c\Delta t J(Q_{s_{k-1},t}) = 0 \;\; (C^+) \\ &\left(H_{s,t+\Delta t} - H_{s_{k+1},t}\right) + \frac{c}{gA}\left(Q_{s,t+\Delta t} - Q_{s_{k+1},t}\right) - c\Delta t J(Q_{s_{k+1},t}) = 0 \;\; (C^-) \end{aligned} \tag{14.17}$$

By adding and subtracting Equations 14.17, it is possible to obtain:

$$\begin{cases} H_{s_k,t+\Delta t} &= \frac{1}{2}\left(H_{s_{k-1},t} + H_{s_{k+1},t}\right) + \frac{c}{2gA}\left(Q_{s_{k-1},t} + Q_{s_{k+1},t}\right) + \\ & + \frac{c\Delta t}{2}\left[J(Q_{s_{k+1},t}) - J(Q_{s_{k-1},t})\right] \\ Q_{s_k,t+\Delta t} &= \frac{1}{2}\left(Q_{s_{k-1},t} + Q_{s_{k+1},t}\right) + \frac{c}{2gA}\left(H_{s_{k-1},t} + H_{s_{k+1},t}\right) + \\ & + \frac{c\Delta t}{2}\left[J(Q_{s_{k+1},t}) - J(Q_{s_{k-1},t})\right] \end{cases} \tag{14.18}$$

which allow to compute pressure H and flow Q at time $t + \Delta t$ in each section s_k from the knowledge of pressure H and flow Q at time t in each section of the pipe. The complete solution to the problem requires then the definition of boundary conditions. In particular,it is required to provide the values of H and Q at time $t = t_0$ in each section of the pipe (*time boundary conditions*) and the values of H and Q at the beginning and end of the pipe for each time $t \geq 0$ (*space boundary conditions*). Note that, for space boundary conditions, it is just required to know the value of Q or H, since it is possible to compute the missing one by applying the equation describing the single characteristic line that interests such boundary point. Such conditions can be introduced as imposed pressure heads due to the presence of tanks or as imposed flow values due to the users' demand.

Chapter 15

Case Studies and Numerical Model for Plant Simulations

The RTC algorithms developed in this work are tested with two different WDN topologies. In both cases, nodal demands are generated at the temporal scale of 1 s, making use of statistic models for demand pulse generation [64]. All the proposed demand profiles follow patterns that keep into account human daily routine. Three main peaks can be identified in the daily profiles: one in the morning, one close to midday and an evening one, while demand is typically lower during night time. The profile would be flatter during day time in presence of industrial activities, whose demand is more uniform during working hours.

Case Study A, which is depicted in Figure 15.1, is represented by a simple water distribution system, with a tank acting as a source node and a pipe connecting it to a single demanding node. The tank provides a constant pressure of 50 m. The time behaviour of the demand is depicted in Figure 15.2. No leakage is considered in this system. A pressure control valve (PCV) is installed 250 m downstream the source node. The valve closure speed was set to obtain the full valve closure from the completely open position in 100 s. For control purposes, pressure is measured in the middle of the pipe. The control goal is regulation of the pressure in the middle of the pipe at $h_{sp} = 29\ m$.
To test the robustness of regulation, simulations are repeated introducing different offsets in the demand profile. The offsets range in the interval $[-0.03; 0.05]$ $[m^3/s]$ and take into account seasonal variations of the demand. For Case Study A, a 2 hour simulation is also performed to evaluate the behaviour of the controller in presence of a step variation ($+\ 0.03$ $[m^3/s]$) of the demand, to simulate the opening of a fire hydrant or a sudden break in the pipe.

Case Study B is represented by the skeletonized WDN of a town with about 30,000 inhabitants in Northern Italy. The network is made up of 27 nodes (26 nodes

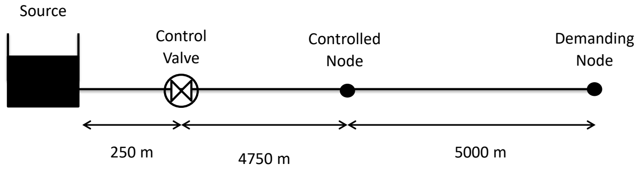

FIGURE 15.1: Case Study A: topology of the water distribution system.

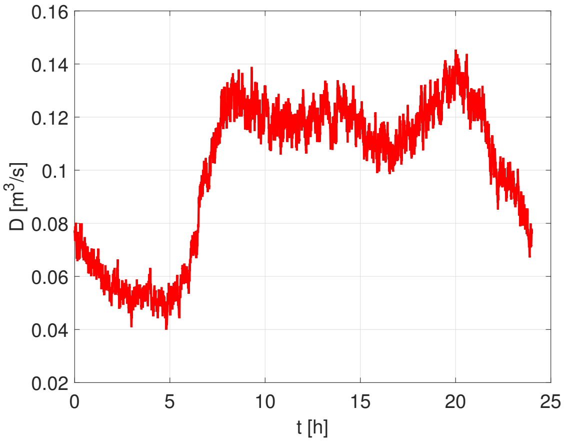

FIGURE 15.2: Case Study A: demand profile.

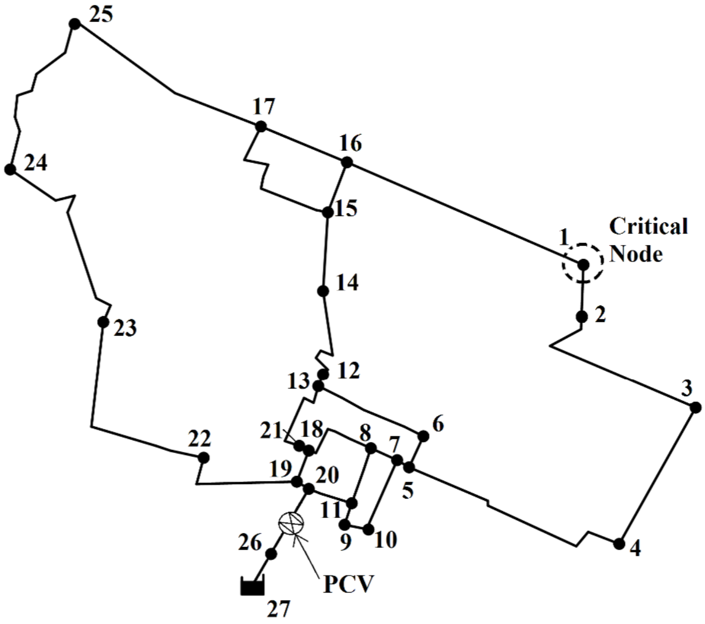

FIGURE 15.3: Case Study B: topology of the WDN

with unknown head with ground elevation of 0 m a.s.l. and 1 source node with ground level of 35 m a.s.l.) and 32 pipes. The complete topology is depicted in Figure 15.3. In this case study, two demand patterns are considered [60], leading to two different trends of the total WDN demand (see Figure 15.4a): a flatter trend (profile A) and a more peaked trend (profile B). This is done to analyse robustness of RTC with respect to different nodal demand behaviours. The source pressure head profile is instead reported in Figure 15.4b. Other features of network nodes and pipes are reported in [64]. A PCV with diameter of 250 mm is installed in pipe 26-20 linking the source to the rest of the network. In the RTC, the critical node 1 is chosen as controlled node. The pressure set point value for the critical node is $h_{sp} = 25\ m$. The valve moves from a completely open to a completely closed position in 300 s.

The two case studies represent processes with different dynamic behaviours. The dynamics of Case Study A is in fact mainly determined by the water hammer effect, whose impact on RTC is not completely clear, in particular when the control algorithm is implemented with short sampling times (instability events that arouse in

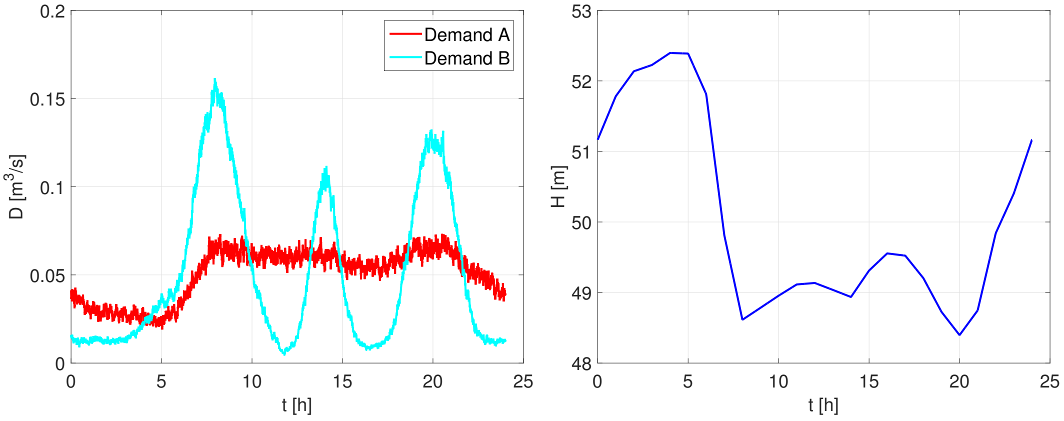

(A) (B)

FIGURE 15.4: Case Study B: (A) Demand profiles. (B) Source pressure head profile.

real plants have been studied in similar situations in [65] and [66]). On the other hand, the dynamic behaviour of Case Study B is given by its complex topology, while the water hammer effect is expected to play a minor role.

15.1 Numerical Model for Plant Simulations

The WDN behaviour is described by means of elastic unsteady flow modelling described in the previous Chapter. This enables proper analysis of the hydraulic transients due to rapid nodal demand and/or valve setting variations.

To account for leakage from WDN pipes, the leakage outflow per unit length, $q\ [m^2/s]$, is considered:

$$q = \alpha_{leak} h_p^{\gamma} \tag{15.1}$$

where $\alpha_{leak}\ [m/s]$ and $\gamma\ [-]$ are the leakage coefficient and exponent, respectively. As for leakage evaluation, exponent γ is set to 1, typical value for plastic pipes [67]. Coefficient $\alpha_{leak}\ [-]$ is set to 0 and $9.4\ 10^{-9} m/s$ to obtain a leakage percentage rate of 0% and 20%, in the two case studies, respectively. The leakage term is introduced in the unsteady flow equations as follows:

$$\begin{cases} \dfrac{\partial h_p}{\partial x} + \dfrac{1}{gA}\dfrac{\partial Q_p}{\partial t} + J & = 0 \\ \dfrac{\partial h_p}{\partial t} + \dfrac{c^2}{gA}\dfrac{\partial Q_p}{\partial x} + \dfrac{c^2 q}{gA} & = 0 \end{cases} \tag{15.2}$$

where h_p and q_p are the pressure head and the flow in the generic pipe p. The pipe friction slope can be evaluated as in Equation 21.1. Pipe friction slopes are then increased using the correction proposed by Pezzinga in [68], to account for the unsteady flow effects.

The solution of the water hammer partial differential equations through the method of the characteristics, with suitable boundary conditions are assigned in correspondence to source and demanding nodes, where fixed total pressure head and demands are prescribed, respectively. The continuity equation is introduced as well for boundary conditions, i.e. the sum of the water discharges entering the generic demanding node through the connected pipes equals the nodal outflow, at each time integration step. The instantaneous demand at each WDN node is evaluated using the stochastic bottom-up approach proposed in [64]. The outflow to the nodal users is evaluated by multiplying the instantaneous demand by the correction factor proposed in [69], to account from the dependence of nodal outflow on service pressure. This factor is a function of the ratio of the instantaneous pressure head h to the desired pressure head h_{sp} and ranges from 0 to 1.

The effect of the control valve is modelled by considering no link at the valve site and setting nodal inflow at the upstream end at:

$$Q_{up} = \sqrt{\frac{2g}{\xi(\alpha)}} A \sqrt{\Delta H_{valve}} \tag{15.3}$$

and the inflow at the downstream end is set, instead, to:

$$Q_{down} = Q_{up} \tag{15.4}$$

where ξ is the valve head loss coefficient, ΔH_{valve} is the head drop in the valve and α is the valve closure setting, ranging from 0 (fully open) to 1 (fully closed). The valve head loss coefficient is a growing function of α. This function is typically made available by the valve manufacturer.

Chapter 16

Pressure Control Strategies Based on Dynamic Models

In this section different control strategies synthesized on linear dynamic models of the plant are introduced. All the presented algorithms use an approximated linear model identified around a suitable working point of the system under control. The control algorithms are tested with simulations on the complete process models, as described in Chapter 15. To quantify and compare their performances, three metrics are introduced. All signals in the loop are sampled with a 1 s sampling time. Let k be the current discrete-time instant. Let $h(k)$ be the measured pressure, h_{sp} be the pressure setpoint, $\alpha(k)$ be the valve closure and $\Delta\alpha(k) = \alpha(k) - \alpha(k-1)$ be the variation of the valve closure over a single sampling time. Let $e(k) = h(k) - h_{sp}$ be the error of the controlled pressure head at time instant k. Then the metrics can be defined as follows:

- $Mean|e(k)|\ [m]$. The *regulation error*, which evaluates the proximity of the pressure to the desired setpoint.
- $\sum |\Delta\alpha(k)|\ [-]$. The *cost of control*, which impacts on the energy required to perform regulation and on wear of actuators.
- $\%\ of\ Displacement\ Instants\ [-]$, measuring valve activity in terms of percentage of time instants during which the actuator is in motion.

Regulators will be tuned to minimise the regulation error. Then, if possible, tuning will be refined to reduce the control cost without degrading the regulation error.

16.1 Working Points

The first step of a model-based synthesis is the definition of a nominal working point, typically an equilibrium of the system. When a mathematical description of the process is available in state-space form, it is possible to find its equilibria by requiring the state derivatives to be zero, when inputs are set to a constant value (i.e. by requiring a steady state condition to be reached). The mathematical modelling of the WDN introduced in Section 15.1 allows the detailed description and simulation of the dynamics of the system, but is too complex to be put in state-space form. However, the nominal working point can be found experimentally by means of simulations.

For this purpose, a Multi-Input Single-Output (MISO) system must be considered in both case studies. Input signals are:

- $\alpha(t)$, the valve closure ($[-]$).

- $H(t)$, the source pressure head ($[m]$).
- $D_i(t)$, the water demand ($[m^3/s]$) at node i.

The output is the pressure $h(t)$ (expressed in $[m]$) measured at the desired point of the WDN.
Note that $\alpha(t)$ is the only control variable, since we assume no possibility of controlling the source pressure $H(t)$. Consequently, $H(t)$ and $D_i(t)$ represent stochastic disturbances acting on the process. Typical profiles of $H(t)$ and $D(t)$ are depicted in Figure 15.2 for Case Study A, with $D(t)$ the demand of the single demanding node. Figure 15.4a shows the profiles for Case Study B, with $D(t)$ representing the overall demand of the WDN, i.e.:

$$D(t) = \sum_{i=1}^{N_{nodes}} D_i(t) \tag{16.1}$$

where N_{nodes} is the number of demanding nodes in the WDN. In the definition of the working point, the average values of typical $H(t)$ and $D_i(t)$ profiles are considered as input to the system.

Case Study A

The control goal in Case Study A is to perform a pressure regulation at $h_{sp} = 29\ m$ at the controlled node, which is placed in the middle of the pipe. Simulations allow to define the value of α which results in the desired pressure, when the exogenous inputs acting on the system are the average value of the source pressure head $H(t)$ and the average value of the demand $D(t)$. The working point for Case Study A is then defined by the tuple $WP_A = (\overline{\alpha}, \overline{H}, \overline{D}, \overline{h})$:

$$WP_A = \begin{cases} \overline{\alpha} = 0.694 \\ \overline{H} = 50\ m \\ \overline{D} = 0.1\ m^3/s \\ \overline{h} = 29\ m \end{cases} \tag{16.2}$$

Case Study B

The control goal in Case Study B is to perform the pressure regulation at $h_{sp} = 25\ m$ at the controlled node, which coincides with node 1. The average value of the source pressure head and demand must be used in the simulations. Note that, in the case of multiple demanding nodes, it is necessary to consider the average value of each demand profile $D_i(t)$. The tuple $WP_B = (\overline{\alpha}, \overline{H}, \overline{D}_1, ..., \overline{D}_{N_{nodes}}, \overline{h})$ is then the working point for Case Study B:

$$WP_B = \begin{cases} \overline{\alpha} = 0.619 \\ \overline{H} = 39.6\ m \\ \overline{D}_1 = 0.0014\ m^3/s \\ ... \\ \overline{D}_{N_{nodes}} = 0.0007\ m^3/s \\ \overline{h} = 25\ m \end{cases} \tag{16.3}$$

Remark: Demand profiles A and B share the same average values for each $D_i(t)$, therefore it is not necessary to define two different working points for Case Study B.

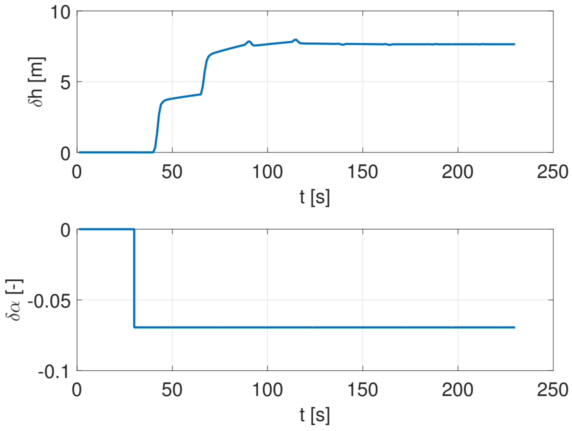

FIGURE 16.1: Case Study A: identification data. Top: pressure variation $\delta h(t)$. Bottom: valve variation $\delta\alpha(t)$.

16.2 Dynamic Models

The synthesis of regulators requires a dynamic model relating the valve closure $\alpha(t)$ to the pressure $h(t)$. Since analytical linearization is too complex in view of the complexity of the nonlinear model, black-box identification, based on simulated data collected on the simulator, has been exploited for the definition of a local model describing the dynamics of the system around the equilibrium. The identification phase is set-up as follows:

- *Simulation of a step response of the WDN around the working point.* The system is first brought around the desired working point. Then, once at steady state, a 10% step variation of α is applied (the valve speed limit is disabled for this simulation). Let $\Delta\alpha_{step}$ be the amplitude of the step.
- *Buildup of input-output identification data.* A local model must be identified, therefore it is necessary to construct variation signals $\delta\alpha(t) = \alpha(t) - \overline{\alpha}$ and $\delta h(t) = h(t) - \overline{h}$ as input-output data. The former signal represents the input of the linearised system, the latter its output.
- *Definition of the structure of the model.* The structure of the local model must be chosen according to the behaviour of the step response $\delta\alpha(t)$.
- *Identification of the parameters of the model.* Matlab Identification Toolbox [33] allows to use input-output data to optimise the values of parameters, to provide the best fit between model prediction and identification data.
- *Validation.* The model prediction is compared against simulations of step responses of the WDN. Different step amplitudes are used to validate the model.

Case Study A

A step response simulation around WP_A allows to obtain the input-output identification data shown in Figure 16.1. The step response does not show any overshoot, inverse response or oscillation. Still, a pure delay is present, and coincides with the time required by the pressure wave generated from the valve to reach the pressure sensor. The celerity of the wave is known, therefore the delay τ_a can be computed as:

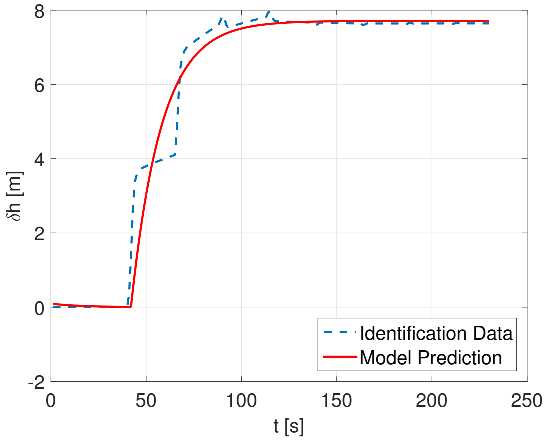

FIGURE 16.2: Case Study A: comparison of model and system output with identification data.

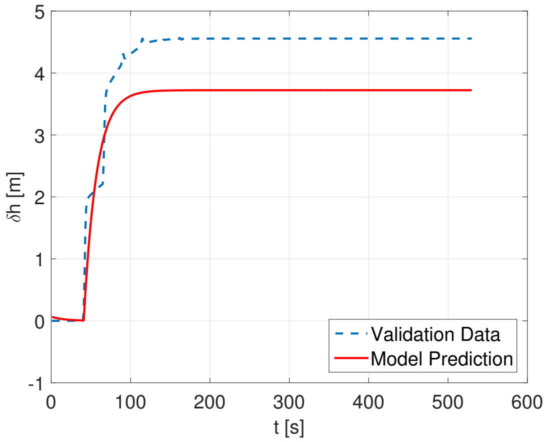

FIGURE 16.3: Case Study A: comparison of model and system output with validation data.

$$\tau_a = \frac{L_{v-s}}{c} \tag{16.4}$$

where L_{v-s} is the distance between the valve and the sensor and c is the celerity of the wave.

The structure chosen for the model (a continuous time transfer function, with s the Laplace variable) and the values of its parameters are reported in (16.5). Figure 16.2 shows a comparison between the model output and the identification data.

$$\begin{aligned} G_a(s) &= \frac{\mu_a e^{-s\tau_a}}{1+sT_a} \\ \mu_a &= -107.27\ m \\ T_a &= 16\ s \\ \tau_a &= 11\ s \end{aligned} \tag{16.5}$$

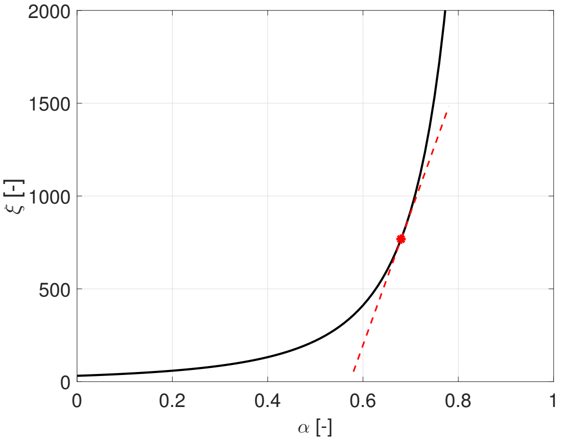

FIGURE 16.4: The local loss coefficient ξ as function of the valve closure α and the straight line tangent to the curve in the working point.

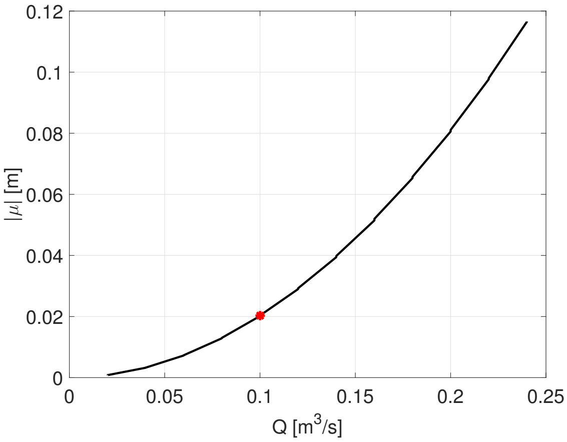

FIGURE 16.5: Absolute value of the gain of the linearised system μ_a as function of the flow Q.

Validation is performed by simulating the step response with different step amplitudes and comparing the results to the response predicted by the model. In particular, Figure 16.3 shows the response to a 5% step in α. The model does not exactly predict the gain of the system, due to the presence of some nonlinearities.
Let us consider (15.3), where α does not directly affect the pressure loss, but appears through ξ. The relation between ξ and α, depicted in Figure 16.4, is strongly nonlinear. A formal linearisation procedure would approximate the relation with the slope of the tangent to the curve in correspondence of the working point ($\frac{d\xi}{d\alpha}|_{\alpha=\overline{\alpha}}$). The proposed procedure approximates it as $\frac{\Delta\xi}{\Delta\alpha_{step}}$, which depends on the amplitude of the step applied during the identification phase.
Equation (21.1) shows instead that the pressure variation generated by a step $\Delta\alpha_{step}$ also depends on the flow Q. In particular, the absolute value of the pressure variation increases with the square of the flow. Figure 16.5 depicts the relation between the absolute value of the gain of the linearised system ($|\mu_a|$) and the flow Q. The relation is obtained by repeating the identification procedure at different values of Q, with same values of $\overline{\alpha}$ and $\Delta\alpha_{step}$.
Nevertheless, the two nonlinearities do not cumulate, but are likely to cancel each other in closed-loop. In fact, whenever the flow Q increases, the pressure h would decrease. The valve closure α must then decrease to compensate for the pressure

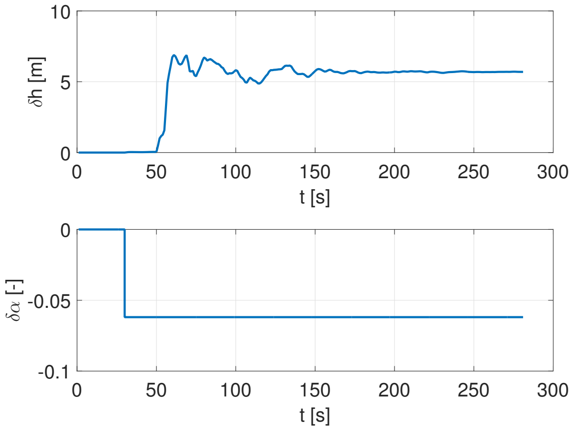

FIGURE 16.6: Identification data for Case Study B. Top: pressure variation $\delta h(t)$. Bottom: valve variation $\delta \alpha(t)$.

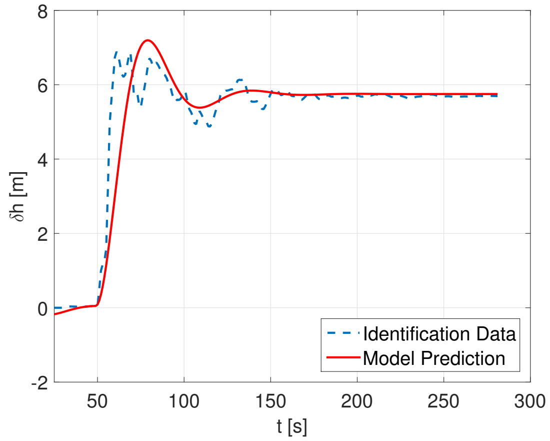

FIGURE 16.7: Case Study B: Comparison of model and system output with identification data.

loss. An increase in Q then results in a decrease in α. When considering this effect in terms of gain of the linearised system, an increase in Q means an increase in the gain, but the resulting decrease in α means a decrease in the gain. On the other hand, if Q decreases, the pressure h increases and α must be increased, thus the two effects still compensate each other. Still, in case of $\alpha \approx 1$, the ξ nonlinearity is dominant and is not mitigated by the Q one. Note that this is not likely to happen in real situations: $\alpha \approx 1$ would be required when $D \approx 0$, but this never happens due to leakage. On the contrary, when $\alpha \approx 0$, the Q nonlinearity dominates. In view of these considerations, it is still important to synthesise regulators providing sufficient margin of robustnes, and setup simulations to test the robustness of the regulators.

Case Study B

The previous procedure can be applied to Case Study B. Figure 16.6 shows the identification step response around WP_B. Some oscillations are present in the response, due to the effect of pressure waves coming from different paths of the WDN. This motivates the introduction of a second order transfer function model with complex conjugate poles. The pure delay is still present, but its computation can no longer be made by means of a structural analysis of the WDN, and must be treated as a parameter for the identification problem. The overall structure chosen for the model

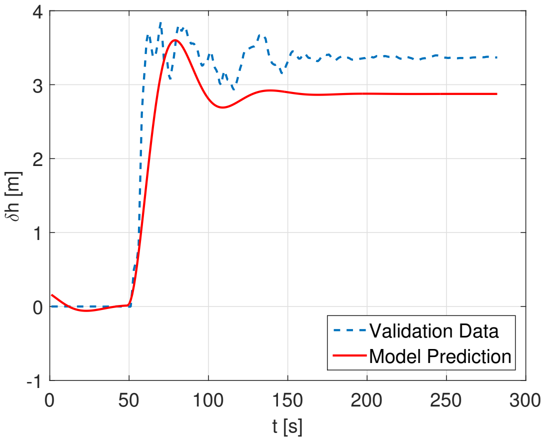

FIGURE 16.8: Case Study B: Comparison of model and system output with validation data.

and the values of its parameters are reported in (16.6). Figure 16.7 shows a comparison between the model output and the identification data. Validation is depicted in Figure 16.8. The applied step is $\Delta\alpha_{step} = 5\%$ (a 10% step was used for identification). The considerations about gain nonlinearities which were introduced for Case Study A still hold for Case Study B.

$$G_b(s) = \frac{\mu_b e^{-s\tau_b}}{1 + 2\zeta_b s/\omega_b + s^2/\omega_b^2}$$

$$\begin{aligned} \mu_b &= -92.86\ m \\ \zeta_b &= 0.4 \\ \omega_b &= 0.1\ rad/s \\ \tau_b &= 19\ s \end{aligned} \tag{16.6}$$

16.3 Control

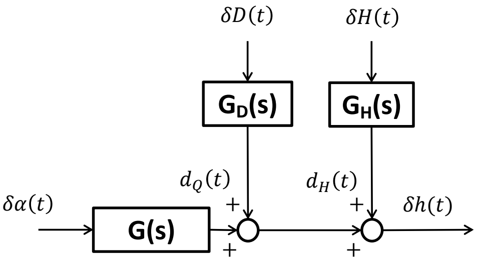

FIGURE 16.9: SISO system for control purposes.

The main goal is regulation to the setpoint h_{sp} of the pressure $h(t)$, in presence of process disturbances generated by the effect of exogenous inputs $H(t)$ and $D_i(t)$.

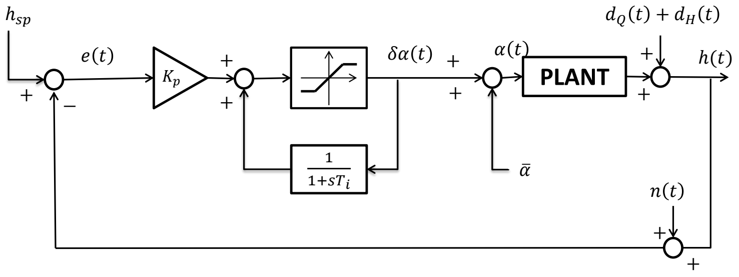

FIGURE 16.10: Antiwindup control scheme for PI regulators.

In this situation, it is possible to refer to a Single-Input Single-Output (SISO) system, whose behaviour around the working point can be described by the local, linear models derived in Section 16.2. Regulators are then synthesised on the basis of $G_a(s)$ and $G_b(s)$, requiring the closed-loop bandwidth to be the largest possible, while providing robustness to gain and phase variations. The SISO system and the linear framework considered for the control design are depicted in Figure 16.9, where $\delta H(t)$ and $\delta D(t)$ are the source pressure and nodal demand variation signals from their working point values. Then $d_H(t)$ is the disturbance generated by $\delta H(t)$ through the dynamic relation $G_H(s)$, and $d_Q(t)$ the disturbance generated by $\delta D(t)$ through the dynamic relation $G_D(s)$. Note that the knowledge of $G_H(s)$ and $G_D(s)$ is not required by the control algorithms proposed in this work.

Note that, every time the value of D_i changes, a pressure wave is generated from the corresponding demanding node and propagates throughout the WDN. A reflected wave is generated as well when the primary one reaches the end of a pipe or the control valve. This effect is particularly important in Case Study A, since the wave propagates and gets reflected through a single pipe. The same holds every time the value of α changes, with the primary wave propagating from the valve towards the demanding node.

The same effect is present in the more complex WDN considered for case Study B. Still, due to the presence of many possible paths for the pressure waves, the power is distributed over a number of harmonics and is expected to have less impact on closed-loop performance. Some realistic measurement noise $n(t)$ is present in Case Study B as well.

All regulators are implemented in a discrete-time way, by exploiting the full capability of the measurement system in terms of sampling time, which results in $T_s = 1\ s$. Discretisation of regulators is performed by adopting the *Tustin* method $s = 2(z-1)/(T_s(z+1))$ to guarantee that the stability is preserved (all asymptotically stable/stable continuous time poles are respectively mapped into asymptotically stable/stable discrete time poles). The design and test of the different control schemes based on the dynamic model derived in Section 16.2 are presented in the following subsections.

16.4 PI Regulators

A Proportional-Integral (PI) control action $u(t)$ can be expressed as follows [38]:

$$u(t) = K_p e(t) + K_i \int e(t)dt \tag{16.7}$$

where $e(t)$ is the error signal. Moving to the *Laplace* domain, one has:

$$U(s) = K_p E(s) + \frac{K_i}{s} E(s) \tag{16.8}$$

with s the Laplace variable, $F(s)$ the Laplace transform of a generic time domain signal $f(t)$. The transfer function of the regulator can be written as follows:

$$R(s) = \frac{U(s)}{E(s)} = K_p + \frac{K_i}{s} = \frac{K_p s + K_i}{s} = K_i \frac{1 + s\frac{K_p}{K_i}}{s} \tag{16.9}$$

By defining $T_i = K_p / K_i$ and $\mu_r = K_i$, one has:

$$R(s) = \mu_r \frac{1 + sT_i}{s} \tag{16.10}$$

By properly shaping the loop transfer function $L(s) = G(s)R(s)$, it is possible to cope with the different control requirements. Note that, when no derivative action is present, an integrator in $L(s)$ ensures perfect tracking of step reference signals and complete rejection of step process disturbances. Still, the presence of a saturation of the control action (recall $\alpha \in [0;1]$) calls for an antiwindup implementation of the PI regulator, to avoid undershoots/overshoots which may completely empty the WDN. The overall control scheme is depicted in Figure 16.10. Note that the model of the saturation affects $\delta\alpha$. It must be therefore implemented as $\delta\alpha \in [1 - \overline{\alpha}; -\overline{\alpha}]$. Stability of the resulting closed-loop systems can be assessed by means of the *Bode Criterion* [38].

Case Study A

Let the model of the system be described by (16.5). It is then possible to set:

$$\begin{aligned} T_i &= T_a \\ \mu_r &= \frac{\omega_c}{\mu_a} \end{aligned} \tag{16.11}$$

where ω_c is the desired closed-loop bandwidth expressed in rad/s.
The resulting loop transfer function $L(s)$ is:

$$L(s) = \frac{\omega_c}{s} e^{-s\tau} \tag{16.12}$$

The only free design parameter is ω_c, which must be chosen according to the design specifications.

A first PI is tuned by requiring $\omega_c = 0.0314\ rad/s$. In the following, this algorithm will be referred to as PI_{na}. The resulting loop function $L(s)$ is depicted in Figure 16.11. The associated phase margin, including the effect of the pure delay,

$Demand$ $Offset$ $[m^3/s]$	$Displacement$ $Instants$ [%]	$\sum\|\Delta\alpha\|$ $[-]$	$Mean\|e(k)\|$ $[m]$
-0,03	100	223,21	2,29
-0,02	100	169,05	1,73
-0,01	100	93,63	1,03
0	100	38,33	0,51
0,01	100	35,02	0,49
0,02	100	33,49	0,48
0,03	100	32,48	0,48
0,04	100	31,78	0,49
0,05	100	31,3	0,5

TABLE 16.1: Case Study A: performance of PI_{na} algorithm for different demand offsets.

$Demand$ $Offset$ $[m^3/s]$	$Displacement$ $Instants$ [%]	$\sum\|\Delta\alpha\|$ $[-]$	$Mean\|e(k)\|$ $[m]$
-0,03	100	8,57	1,12
-0,02	100	7,96	1,02
-0,01	100	7,55	0,94
0	100	7,24	0,89
0,01	100	7,01	0,85
0,02	100	6,83	0,82
0,03	100	6,7	0,8
0,04	100	6,62	0,78
0,05	100	6,56	0,78

TABLE 16.2: Case Study A: performance of PI algorithm for different demand offsets.

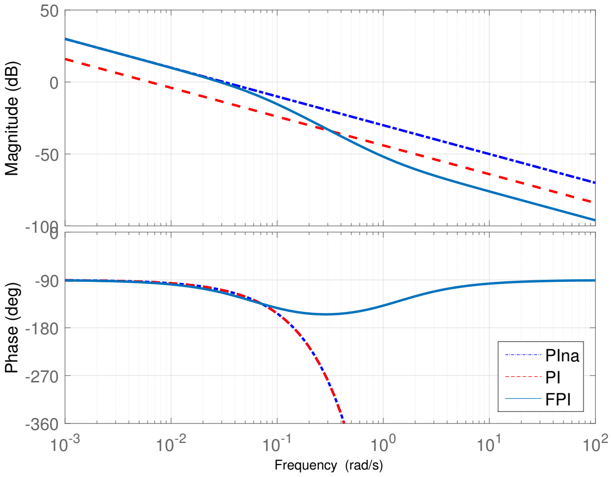

FIGURE 16.11: Case Study A: design of loop functions for PI_{na}, PI and FPI regulators.

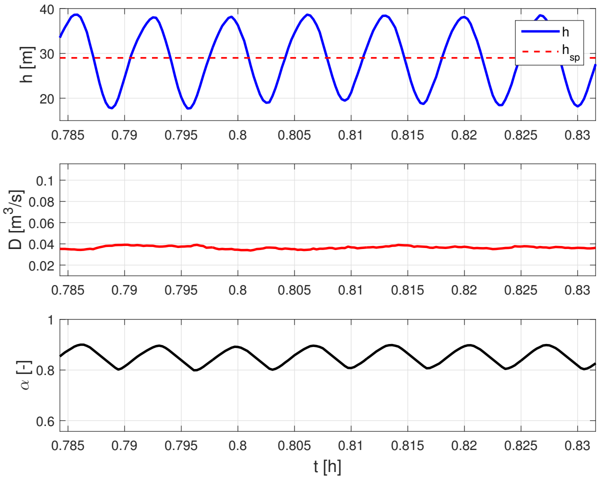

FIGURE 16.12: Case Study A: closed-loop simulation with PI_{na} and demand offset -0.03 m^3/s. Top: pressure $h(t)$ and pressure setpoint h_{sp}. Middle: demand $D(t)$. Bottom: valve closure $\alpha(t)$.

results $\phi_m = 70°$, ensuring robust stability of the closed-loop and very little oscillations in the closed-loop step response. Phase margin reduction due to discretisation is negligible.

Table 16.1 shows the results of closed-loop simulations with PI_{na}. Note that, for negative demand offset values, the cost of regulation grows very high and the regulation error gets worse. This is due to the presence of a pressure wave with frequency

$$f_w = \frac{1}{25} = 0.04 \; Hz \tag{16.13}$$

propagating through the pipe. The effect is shown in Figure 16.12, with reference to a simulation with demand offset of -0.03 m^3/s. Recall that a pressure wave is generated every time the valve setting α changes. Such wave propagates through the pipe and gets reflected once it reaches the demanding node, hitting the pressure sensor again while moving back towards the valve. When the controller tries to compensate for the pressure variation, a new wave is generated and reflected. In addition, with very low values of the demand $D(t)$, the regulator sets values of

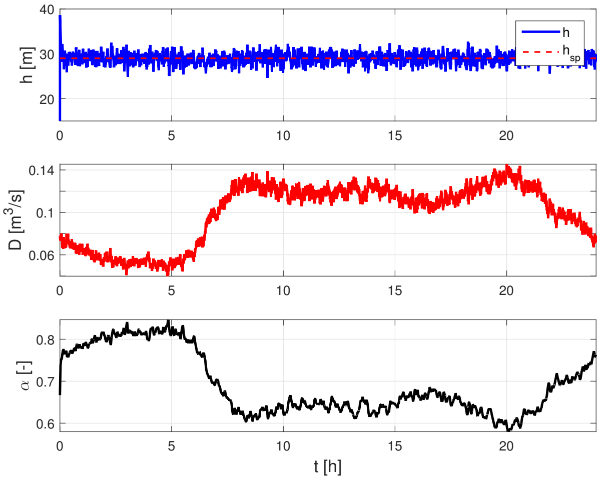

FIGURE 16.13: Case Study A: closed-loop simulation with PI algorithm. Top: pressure $h(t)$ and pressure setpoint h_{sp}. Middle: demand $D(t)$. Bottom: valve closure $\alpha(t)$.

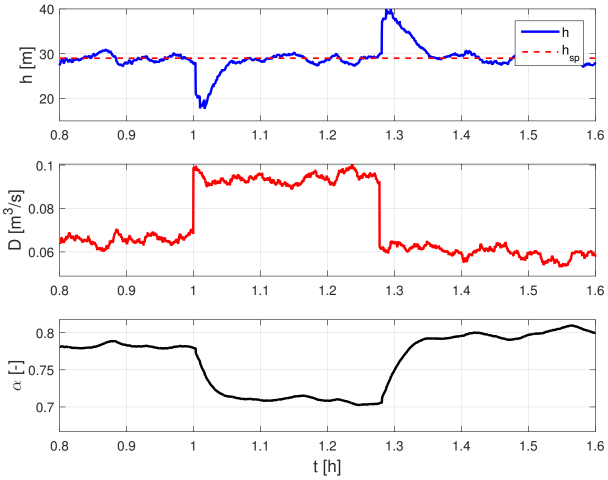

FIGURE 16.14: Case Study A: closed-loop simulation with PI algorithm and opening of a fire hydrant. Top: pressure $h(t)$ and pressure setpoint h_{sp}. Middle: demand $D(t)$. Bottom: valve closure $\alpha(t)$.

α which get close to 1. According to the effect of gain nonlinearities described in Section 16.3, the ξ nonlinearity dominates and the gain of the process increases. This in turn means that the closed-loop bandwidth is enlarged and that the regulator tries to compensate the effect of the pressure wave propagating through the pipe, instead of filtering it. By doing so, other waves at the same frequency are generated. Other works instead suggest that the observed oscillations are the result of the phase margin reduction which occours due to the enlarged closed-loop bandwidth [47, 65, 66].

A retuning of the regulator is therefore necessary. A possibility is to reduce the closed-loop bandwidth. A second attempt is then made with $\omega_c = 0.0063\ rad/s$. The new phase margin is $\phi_m = 86°$ (phase margin reduction due to discretisation is negligible). The new PI will be referred to simply as PI. Results are reported in Table 16.2. Figure 16.13 shows the main signals of the control-loop for a whole day simulation with the nominal demand profile. Figure 16.14 shows the response of the system in presence of an additional step disturbance $D_s(t) = 0.03\ m^3/s$. This

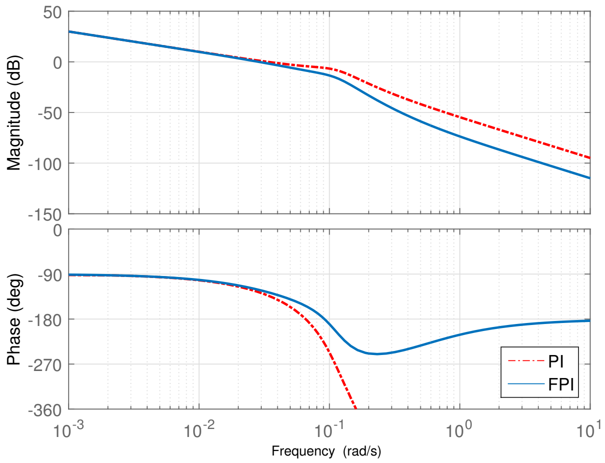

FIGURE 16.15: Case Study B: design of loop functions for PI and FPI regulators.

$Demand$ $Profile$	$Displacement$ $Instants$ $[\%]$	$\sum\lvert\Delta\alpha\rvert$ $[-]$	$Mean\lvert e(k)\rvert$ $[m]$
A	100	33.5	0.7
B	98	22.9	0.55

TABLE 16.3: Case Study B: Performance of PI algorithm for different demand profiles.

simulation mimics real situations, such as a sudden break of a pipe or the opening of a fire hydrant. The control system manages to bring the pressure back to the setpoint without any oscillation in about 300 s.

Case Study B

For Case Study B, the local model of the system is reported in (16.6). A possible tuning is:

$$\begin{aligned} T_i &= \frac{1}{2\omega_b} \\ \mu_r &= \frac{\omega_c}{\mu_b} \end{aligned} \tag{16.14}$$

with

$$\omega_c < \omega_b$$

.

The best results are obtained with $\omega_c = 0.0314$ rad/s. Phase margin results $\phi_m = 48°$: the closed loop system is asymptotically stable but some damped oscillations may be present in the closed-loop step response. The Bode diagram of the loop function $L(s)$ is depicted in Figure 16.15 (phase margin reduction associated to the discretisation can be neglected). The proposed tuning tries to find a balance in the trade off between phase margin and loop function attenuation right after ω_c, where a non negligible resonance peak exists. The phase margin must be sufficient

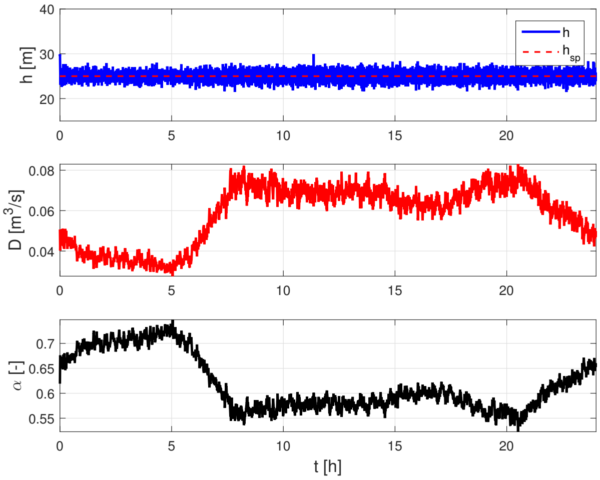

FIGURE 16.16: Case Study B: closed-loop simulation with PI algorithm and demand profile A. Top: pressure $h(t)$ and pressure setpoint h_{sp}. Middle: demand $D(t)$. Bottom: valve closure $\alpha(t)$.

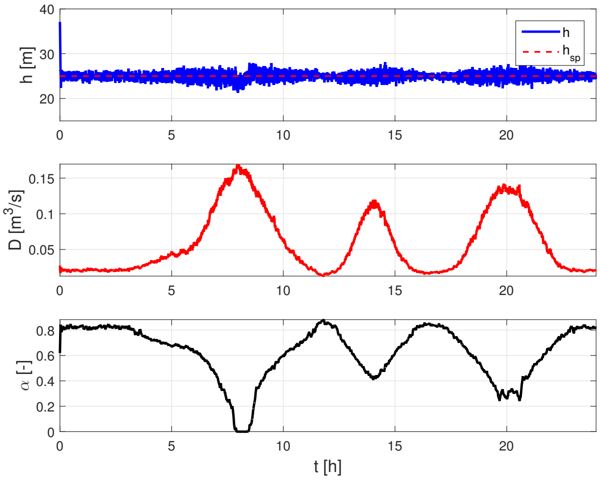

FIGURE 16.17: Case Study B: closed-loop simulation with PI algorithm and demand profile B. Top: pressure $h(t)$ and pressure setpoint h_{sp}. Middle: demand $D(t)$. Bottom: valve closure $\alpha(t)$.

to generate just small oscillations in the closed-loop response and to provide some robustness to model uncertainty. On the other hand, $|L(j\omega)|_{dB}$ should not be too close to the 0 dB axis to provide some robustness against the gain variations discussed in the paper. In fact, if the attenuation is not enough, an increase in the gain could move ω_c after the resonance peak thus possibly spoiling the stability of the closed-loop system. The results of the simulations with the two demand profiles are presented in Table 16.3 and depicted in Figures 16.16 and 16.17.

16.5 Filtered PI Regulators and Smith Predictor

According to the previous considerations, it may be possible to improve the PI performance by introducing a low pass filter to enhance rejection of noise at frequency f_w. The overall regulator $R(s)$ can then be considered as the cascade of a PI controller, as described in Section 16.4, and the filter given by the transfer function $R_f(s)$,

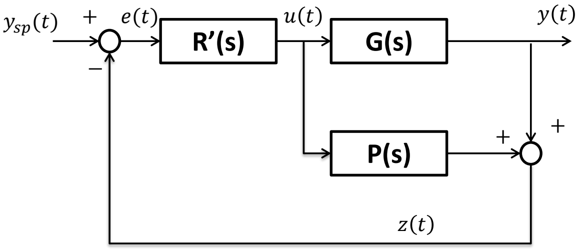

FIGURE 16.18: Control scheme with Smith Predictor.

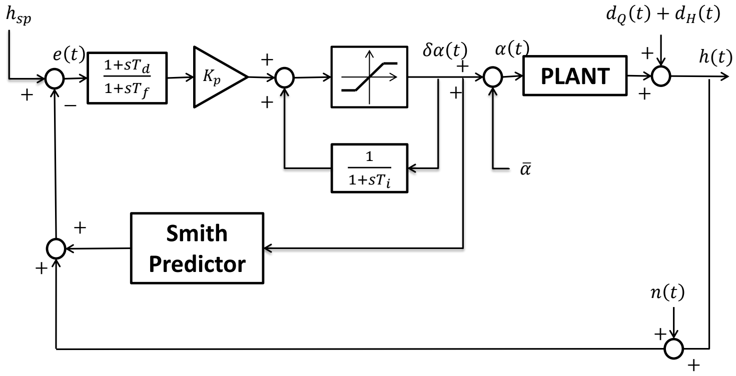

FIGURE 16.19: Antiwindup control scheme for *FPI* regulators with Smith Predictor.

reported in (16.15).

$$R_f(s) = \frac{(1+sT_d)}{(1+sT_f)} \tag{16.15}$$

When the filtering pole is placed just outside of the closed-loop bandwidth, the phase margin of the system can be reduced significantly. The zero of $R_f(s)$ can be used to reduce the phase margin loss. In the following of the paper, this algorithm will be referred to as *FPI* (Filtered PI). Since the system under control is characterised by the presence of a pure delay, it is also possible to compensate for its effect on the phase margin by introducing a Smith Predictor (SP), which is now presented.

Consider an asymptotically stable SISO system with transfer function

$$G(s) = G'(s)e^{-s\tau} \tag{16.16}$$

where $G'(s)$ is a rational transfer function. Then, with reference to the control scheme in Figure 16.18, it is possible to neglect the presence of the pure delay $e^{-s\tau}$ in the design of the regulator $R'(s)$ when

$$P(s) = (1-e^{-s\tau})G'(s) \tag{16.17}$$

The effect of the scheme is to obtain a feedback with a *prediction* $z(t) = y(t+\tau)$ of the controlled variable $y(t)$.

The overall control scheme for the *FPI* algorithm with antiwindup implementation and Smith Predictor is depicted in Figure 16.19.

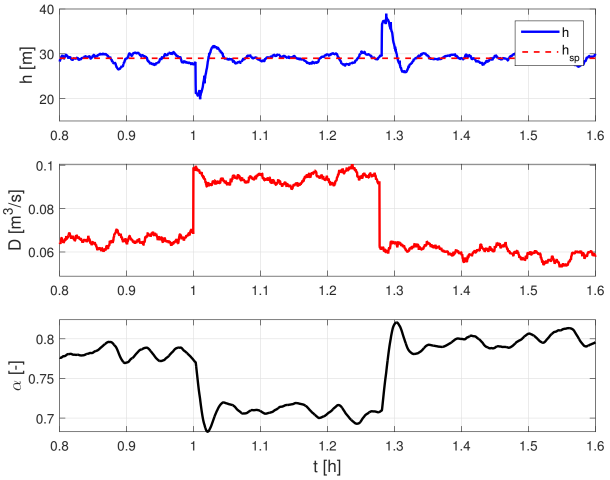

FIGURE 16.20: Case Study A: closed-loop simulation with FPI algorithm and opening of a fire hydrant. Top: pressure $h(t)$ and pressure setpoint h_{sp}. Middle: demand $D(t)$. Bottom: valve closure $\alpha(t)$.

Demand Profile $[m^3/s]$	*Displacement Instants* [%]	$\sum \lvert\Delta\alpha\rvert$ $[-]$	$Mean \lvert e(k)\rvert$ $[m]$
-0,03	100	15	0,74
-0,02	100	14,1	0,69
-0,01	100	13,46	0,66
0	100	12,98	0,64
0,01	100	12,62	0,62
0,02	100	12,34	0,6
0,03	100	12,18	0,56
0,04	100	12,11	0,59
0,05	100	12,11	0,59

TABLE 16.4: Case Study A: performance of FPI algorithm for different demand offsets.

Case Study A

In Case Study A it is possible to compute the frequency f_w of the pressure wave as described in (16.13). The PI_{na} algorithm presented in Section 16.4 can be extended to provide more rejection of noise at frequency f_w. The best design of the filter $R_f(s)$ is obtained by setting:

$$\begin{aligned} T_d &= \frac{1}{5}\frac{1}{2\pi f_w} \\ T_f &= 20T_d \end{aligned} \tag{16.18}$$

which provides $30dB$ of rejection of the pressure wave. The bode diagram of the overall loop function $L(s)$ is reported in Figure 16.11. The closed-loop bandwidth is approximately $\omega_c = 0.0314\ rad/s$. Thanks to the Smith Predictor, the phase margin results $\phi_m = 67°$ (by neglecting the effect of discretisation), ensuring robust stability of the closed-loop and very little oscillations in the closed-loop step response.

$Demand$ $Profile$	$Displacement$ $Instants$ $[\%]$	$\sum\lvert\Delta\alpha\rvert$ $[-]$	$Mean\lvert e(k)\rvert$ $[m]$
A	100	11.4	0.74
B	98	9.6	0.62

TABLE 16.5: Case Study B: Performance of FPI algorithm for different demand profiles.

Note that, in contrast with the closed-loop bandwidth reduction introduced for the PI algorithm, the proposed filter design limits the closed-loop bandwidth in case of increase in the process gain, while keeping the nominal closed-loop bandwidth almost unchanged. Result of whole day simulations are reported in Table 16.4. Simulation of fire hydrant opening is instead shown in Figure 16.20. Regulation to h_{sp} is faster than the PI case but shows a little overshoot/undershoot. In the following, this algorithm will be simply referred to as FPI.

Case Study B

The WDN considered in Case Study B shows a complex topology with many possible paths connecting the control valve to the controlled node. Cycles are also present. Many pressure waves are therefore generated when a variation of the status of the valve occurs. In addition, each demanding node generates waves which propagate through the network. It is then very difficult to identify the frequencies of such waves. Still, a possible design for the $R_f(s)$ placing the filtering pole right after the closed-loop bandwidth and then placing the zero in an arbitrary position to improve the phase margin. The Smith Predictor described in the previous section is still included in the design. Let therefore:

$$\begin{aligned} T_f &= \frac{0.6}{\omega_c} \\ T_d &= 0.1 T_f \end{aligned} \tag{16.19}$$

With the PI tuned as in Section 16.4, with $\omega_c = 0.0314\ rad/s$, the overall regulator provides a phase margin $\phi_m = 59°$. The effect of discretisation on the phase margin is negligible. The corresponding loop function is reported in Figure 16.15. A comparison of the loop functions obtained with the PI and the FPI algorithms highlights that the FPI results in a reduced magnitude in correspondence of the resonance peak, which is outside of the closed-loop bandwidth and in turn present in the control sensitivity function as well. The overall effect is a reduction of the associated actuator oscillations. Table 16.5 reports the results of simulations of the WDN in closed loop with the FPI algorithm.

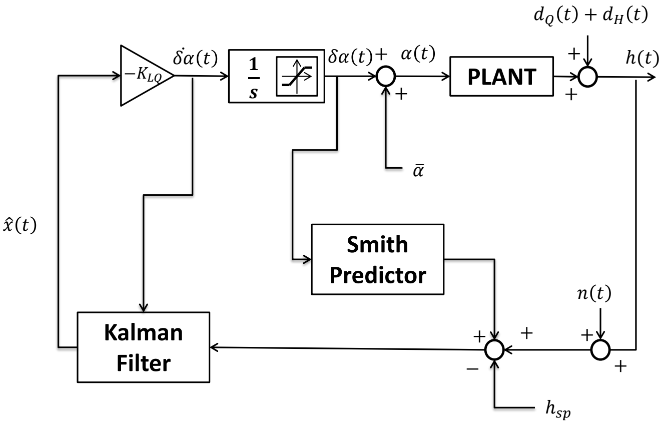

FIGURE 16.21: Control scheme for the LQG regulator, featuring integral action and Smith Predictor

16.6 Linear Quadratic Gaussian Control

Linear Quadratic Gaussian (LQG) control is one of the most common optimal control techniques. Optimal control allows to formulate control problems as optimisation ones, explicitly taking into account cost/benefit trade-offs in the synthesis of the controller. In particular, LQG control is the combination of a Linear Quadratic (LQ) state-feedback controller and a Kalman Filter (KF) for estimation of nonmeasurable states. In particular, the LQG schemes developed in this work features a discrete time, infinite horizon LQ regulator and a steady-state KF. The main results of infinite horizon LQ control are summarised in Theorem 2, while Theorem 3 discusses the steady-state KF [70].

Theorem 2. Consider a linear, discrete time system described by:

$$\mathbf{x}(k+1) = \mathbf{A}\mathbf{x}(k) + \mathbf{B}\mathbf{u}(k) \tag{16.20}$$

and the infinite horizon quadratic cost function:

$$\begin{aligned} &J = \sum_{k=0}^{\infty}(\mathbf{x}^\top(k)\mathbf{Q}\mathbf{x}(k) + \mathbf{u}^\top(k)\mathbf{R}\mathbf{u}(k)) \\ &\text{with} \\ &\mathbf{Q} \geq 0 \quad \mathbf{R} > 0 \end{aligned} \tag{16.21}$$

If the pair $(\mathbf{A}, \mathbf{B})$ is reachable, and the pair $(\mathbf{A}, \mathbf{Cq})$ is observable, with $\mathbf{Q} = \mathbf{Cq}^\top\mathbf{Cq}$, then, the optimal control law is given by

$$\mathbf{u}(k) = -\mathbf{K}_{LQ}\mathbf{x}(k) \tag{16.22}$$

with

$$\mathbf{K} = (\mathbf{R} + \mathbf{B}^\top\overline{\mathbf{P}}\mathbf{B})^{-1}\mathbf{B}^\top\overline{\mathbf{P}}\mathbf{A} \tag{16.23}$$

where $\overline{\mathbf{P}}$ is the unique positive definite solution of the stationary Riccati Equation

$$\mathbf{P}\text{=}\mathbf{A}^\top\mathbf{P}\mathbf{A} + \mathbf{Q} - \mathbf{A}^\top\mathbf{P}\mathbf{B}(\mathbf{R} + \mathbf{B}^\top\mathbf{P}\mathbf{B})^{-1}\mathbf{B}^\top\mathbf{P}\mathbf{A} \tag{16.24}$$

The closed-loop system

$$\mathbf{x}(k+1) = (\mathbf{A} - \mathbf{B}\mathbf{K}_{LQ})\mathbf{x}(k) \tag{16.25}$$

is asymptotically stable.

Theorem 3. Assume that the considered system is described by:

$$\begin{cases} \mathbf{x}(k+1) = \mathbf{A}\mathbf{x}(k) + \mathbf{B}\mathbf{u}(k) + \mathbf{w}(k) \quad \mathbf{x}(0) = \mathbf{x}_0 \\ y(k) = \mathbf{C}\mathbf{x}(k) + n(k) \end{cases} \tag{16.26}$$

with $\mathbf{w}(k)$ and $n(k)$ respectively process and measurement noise. Let $\mathbf{w}(k)$ be white, Gaussian with zero mean and covariance $\mathbf{Q}_k$. Analogously, let $n(k)$ be white, Gaussian with zero mean and covariance R_k. Let also assume that the two noises are not correlated.
If the pair $(\mathbf{A}, \mathbf{Bq})$, with $\mathbf{Bq}$ such that $\mathbf{Q}_k = \mathbf{Bq}^\top \mathbf{Bq}$, is reachable and that the pair $(\mathbf{A}, \mathbf{C})$ is observable, the optimal state estimator is then given by:

$$\begin{aligned} \hat{\mathbf{x}}(k+1|k+1) = {} & \mathbf{A}\hat{\mathbf{x}}(k|k) + \mathbf{B}\mathbf{u}(k) + \\ & + \mathbf{L}[y(k+1) - \mathbf{C}(\mathbf{A}\hat{\mathbf{x}}(k|k) + \mathbf{B}\mathbf{u}(k))] \end{aligned} \tag{16.27}$$

with

$$\mathbf{L} = \overline{\mathbf{P}}\mathbf{C}^\top [\mathbf{C}\overline{\mathbf{P}}\mathbf{C}^\top + R_k]^{-1} \tag{16.28}$$

where $\overline{\mathbf{P}}$ is the unique positive definite solution of the stationary Riccati Equation

$$\mathbf{P} = \mathbf{A}\mathbf{P}\mathbf{A}^\top + \mathbf{Q}_k - \mathbf{A}\mathbf{P}\mathbf{C}^\top [\mathbf{C}\mathbf{P}\mathbf{C}^\top + R_k]^{-1}\mathbf{C}\mathbf{P}\mathbf{A} \tag{16.29}$$

The estimator is asymptotically stable, i.e. the eigenvalues of $(\mathbf{A} - \mathbf{L}\mathbf{C})$ have modulus less than 1. Note that the eigenvalues of the overall closed-loop system are those of $(\mathbf{A} - \mathbf{B}\mathbf{K}_{LQ})$ and of $(\mathbf{A} - \mathbf{L}\mathbf{C})$, so that the closed-loop stability is guaranteed.

Figure 16.21 shows the overall closed-loop setup for the implementation of the *LQG* control used in this paper. As for *PI* and *FPI* algorithms, the regulator is tuned according to linear models derived in Section 16.2. Note that an integrator is introduced in the loop, providing a twofold contribution. On one hand, it allows to synthesise the LQ regulator with control action u coinciding with the derivative of the valve closure variation $\delta\alpha$. This in turn means that the derivative appears (in its discrete-time version) in the cost function, providing a more direct way to weight the performance metric $\sum |\Delta\alpha|$. On the other hand, with a SISO system without any derivative action, the presence of the integrator in the control loop ensures complete rejection of step process disturbances and perfect tracking of step references. Accumulation in the integrator is limited to the interval $[1-\overline{\alpha}; -\overline{\alpha}]$, to account for saturation of the control action and avoid integral windup.
Let $\mathbf{A}$, $\mathbf{B}$, and $\mathbf{C}$ be a realisation of (16.5) or (16.6). To introduce the integral action as described in Figure 16.21, the system is extended as:

$$\mathcal{A} = \begin{bmatrix} 0 & 0 \\ \mathbf{B} & \mathbf{A} \end{bmatrix} \quad \mathcal{B} = \begin{bmatrix} 1 \\ 0 \end{bmatrix} \quad \mathcal{C} = \begin{bmatrix} 0 & \mathbf{C} \end{bmatrix} \tag{16.30}$$

The LQ and KF are then synthesised over the extended system $(\mathcal{A}, \mathcal{B}, \mathcal{C})$, discretised with step of 1 s and a Zero-Order Hold algorithm. The control scheme also features

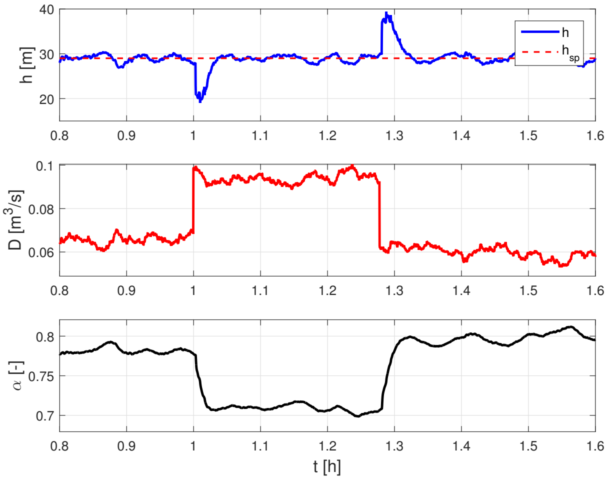

FIGURE 16.22: Case Study A: closed-loop simulation with *ILQG* algorithm and opening of a fire hydrant. Top: pressure $h(t)$ and pressure setpoint h_{sp}. Middle: demand $D(t)$. Bottom: valve closure $\alpha(t)$.

Demand Profile $[m^3/s]$	*Displacement Instants* [%]	$\sum \lvert\Delta\alpha\rvert$ $[-]$	$Mean\lvert e(k)\rvert$ $[m]$
-0,03	100	13,4	0,84
-0,02	100	12,42	0,77
-0,01	100	11,77	0,73
0	100	11,32	0,7
0,01	100	11	0,68
0,02	100	10,75	0,66
0,03	100	10,6	0,65
0,04	100	10,5	0,65
0,05	100	10,5	0,65

TABLE 16.6: Case Study A: performance of *ILQG* algorithm for different demand offsets.

the Smith Predictor developed in Section 16.5 for pure delay compensation. In the following of this work, this algorithm will be denoted as *ILQG*.

Case Study A

Simulations with the water distribution system of Case Study A and *ILQG* algorithm provided the results shown in Table 16.6. Simulation of hydrant opening is depicted in Figure 16.22. Regulation to the setpoint is performed in about 250 s, with no oscillations in the response. The values of tuning parameters are:

$$\mathbf{Q} = \begin{bmatrix} 10^{-4} & 0 \\ 0 & 10^{-8} \end{bmatrix} \quad \mathbf{R} = 1 \quad \mathbf{Q}_k = 0.005\mathbf{I}_{2\times 2} \quad R_k = 1$$

where the non-zero elements in $\mathbf{Q}$ weight respectively the state of the integrator and the state of the linearised system.

Demand Profile	*Displacement Instants* [%]	$\sum\lvert\Delta\alpha\rvert$ [$-$]	$Mean\lvert e(k)\rvert$ [m]
A	100	20	0.7
B	98	15	0.6

TABLE 16.7: Case Study B: Performance of *ILQG* algorithm for different demand profiles.

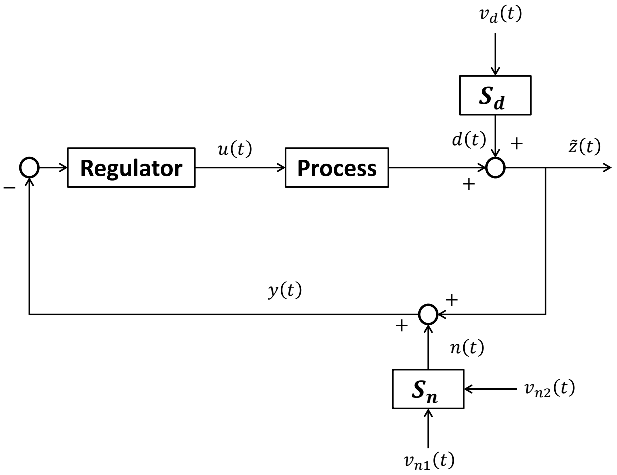

FIGURE 16.23: Control scheme for LQG control with disturbances prefiltering.

Case Study B

For the WDN considered in case Study B, the best results are obtained with

$$\mathbf{Q} = \begin{bmatrix} 10^{-3} & 0 & 0 \\ 0 & 10^{-8} & 0 \\ 0 & 0 & 10^{-8} \end{bmatrix} \quad \mathbf{R} = 1 \quad \mathbf{Q}_k = 0.00005\mathbf{I}_{3\times 3} \quad R_k = 1$$

Performance metrics are reported in Table 16.7.

16.7 Linear Quadratic Gaussian Control with Shaping Functions

Note that, for Case Study A, it is particularly interesting to bring in the *LQG* algorithm the same concepts introduced with the *FPI* one: an enhanced filtering at frequency f_w, and a limitation on the increase in the closed-loop bandwidth in case of increased gain of the process (see Section 16.5). This result can be achieved by means of a control scheme with disturbances prefiltering, as in Figure 16.23.
Let v_d, v_{n1}, v_{n2} be uncorrelated white noises, and let S_d and S_n be asymptotically stable systems producing the stationary noises $d(t)$ and $n(t)$. The process is described

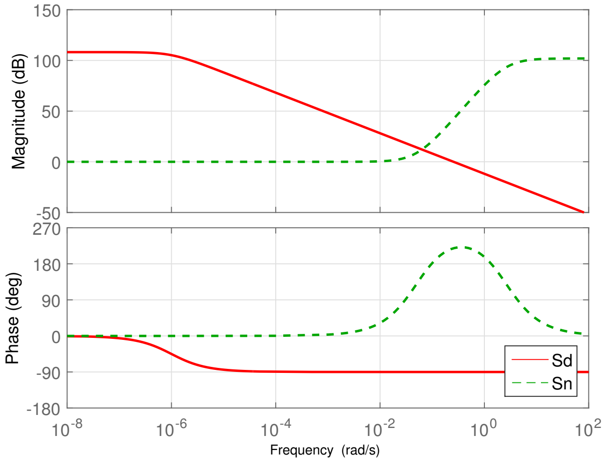

FIGURE 16.24: Shaping functions used for disturbances prefiltering.

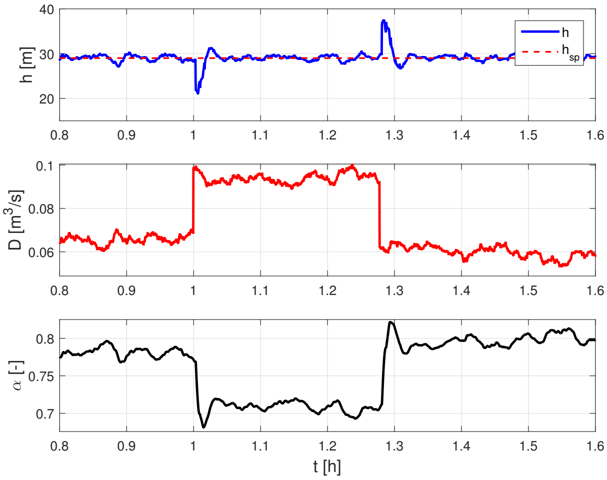

FIGURE 16.25: Case Study A: closed-loop simulation with $ILQG - SF$ algorithm and opening of a fire hydrant. Top: pressure $h(t)$ and pressure setpoint h_{sp}. Middle: demand $D(t)$. Bottom: valve closure $\alpha(t)$.

by:

$$\begin{cases} \dot{\mathbf{x}}(t) & = \mathcal{A}\mathbf{x}(t) + \mathcal{B}u(t) \\ \tilde{z}(t) & = \mathcal{C}\mathbf{x}(t) + d(t) \\ y(t) & = \tilde{z}(t) + n(t) \end{cases} \tag{16.31}$$

while S_d and S_n are described by:

$$\begin{cases} \dot{\mathbf{x}}_d(t) & = \mathbf{A}_d\mathbf{x}_d(t) + \mathbf{B}_d v_d(t) \\ d(t) & = \mathbf{C}_d\mathbf{x}_d(t) \end{cases} \tag{16.32}$$

and

$$\begin{cases} \dot{\mathbf{x}}_n(t) & = \mathbf{A}_n\mathbf{x}_n(t) + \mathbf{B}_n v_{n1}(t) \\ n(t) & = \mathbf{C}_n\mathbf{x}_n(t) + v_{n2}(t) \end{cases} \tag{16.33}$$

Now define:

Demand Profile $[m^3/s]$	*Displacement Instants* [%]	$\sum \lvert\Delta\alpha\rvert$ $[-]$	*Mean* $\lvert e(k)\rvert$ $[m]$
-0,03	100	23	0,56
-0,02	100	22,1	0,53
-0,01	100	21,47	0,52
0	100	21	0,51
0,01	100	20,73	0,51
0,02	100	20,5	0,51
0,03	100	20,37	0,51
0,04	100	20,36	0,51
0,05	100	20	0,52

TABLE 16.8: Case Study A: performance of $ILQG - SF$ algorithm for different demand offsets.

$$\bar{\mathbf{x}}(t) = \begin{bmatrix} \mathbf{x}(t) \\ \mathbf{x}_d(t) \\ \mathbf{x}_n(t) \end{bmatrix} \quad \bar{\mathcal{A}} = \begin{bmatrix} \mathcal{A} & 0 & 0 \\ 0 & A_d & 0 \\ 0 & 0 & A_n \end{bmatrix} \quad \bar{\mathcal{B}} = \begin{bmatrix} \mathcal{B} \\ 0 \\ 0 \end{bmatrix} \tag{16.34}$$

$$\bar{\mathbf{v}}(t) = \begin{bmatrix} 0 & 0 \\ B_d & 0 \\ 0 & B_n \end{bmatrix} \begin{bmatrix} v_d(t) \\ v_{n1}(t) \end{bmatrix} \quad \bar{\mathcal{C}} = \begin{bmatrix} \mathcal{C} & C_d & C_n \end{bmatrix}$$

and the enlarged system:

$$\begin{cases} \dot{\bar{\mathbf{x}}}(t) & = \bar{\mathcal{A}}\bar{\mathbf{x}}(t) + \bar{\mathcal{B}}u(t) + \bar{\mathbf{v}}(t) \\ y(t) & = \bar{\mathcal{C}}\bar{\mathbf{x}}(t) + v_{n2}(t) \end{cases} \tag{16.35}$$

Assuming that the covariance $Q_{k_{n2}}$ of v_{n2} is positive definite, then (16.35) fulfils the conditions required for the design of a stabilizing LQG regulator.
This algorithm is implemented on a discretised version of (16.35) and will be referred to as $ILQG - SF$. Shaping functions S_d and S_n can be chosen to place the power of measurement noise $n(t)$ from f_w towards higher frequencies and process noise $d(t)$ towards lower frequencies. Figure 16.24 depicts the chosen shapes and (16.36) reports the mathematical expressions.

$$\begin{aligned} \omega_w &= 2\pi f_w \\ S_d(s) &= \frac{\omega_w\, 10^6}{(1 + s10^6)} \\ S_n(s) &= \frac{(1 + s/(5\omega_w))^3}{(1 + s/(0.1\omega_w))^3} \end{aligned} \tag{16.36}$$

With weights reported in (16.37), the regulation error improves significantly.

$$\mathbf{Q} = \begin{bmatrix} 1 & 0 & 0 & 0 & 0 & 0 \\ 0 & 10^{-12} & 0 & 0 & 0 & 0 \\ 0 & 0 & 0.26 & 0 & 0 & 0 \\ 0 & 0 & 0 & 0 & 0 & 0 \\ 0 & 0 & 0 & 0 & 0 & 0 \\ 0 & 0 & 0 & 0 & 0 & 0 \end{bmatrix} \quad R = 1 \tag{16.37}$$

$$\mathbf{Q}_k = 0.05\mathbf{I}_{6\times 6} \quad R_k = 1$$

Performance metrics are reported in Table 16.8. Figure 16.25 shows the fire hydrant opening simulation. Regulation is slightly faster than the standard $ILQG$ case, but shows some minor overshoot.

Chapter 17

Stability Analysis and PI Design Based on Higer Order Models

The main aim of this Chapter is to demonstrate that the use of linear, local models with higher order allows to properly describe the high frequency behaviour of the plant, which can not be captured by standard, low order models such as the typical first or second order ones used in the previous Chapter. As it will be discussed with both case studies A and B, the frequency response of the plant shows in fact many resonance peaks at high frequency. This may spoil the results of the stability and robustness analysis based on low order models, if the desired closed-loop bandwidth is too high in frequency.

The higher order models can be obtained from the step response data. In particular, Matlab Identification Toolbox is used to identify the values of the parameters of $\tilde{G}(s)$, a higher order transfer function. The higher order model prediction should better match the high frequency oscillations of the step response of the system. For the PI and FPI-SP algorithms, the higher order model $\tilde{G}(s)$ can be adopted in order to tune ω_c (i.e. the gain of the regulator) directly on the model, with no need for trial and error procedures on the plant.

The higher order model is also useful to understand how FPI-SP algorithms can reduce the cost of control, by a better analysis of the control sensitivity function.

17.1 PI Gain Design Based on Higher Order Models

Let focus on the PI_{na} algorithm, as introduced in 16. Recall that, when the PI_{na} algorithm is applied to the plant, it performs well for nominal demand profile or higher mean values, but becomes unstable and introduces large oscillations when the demand drops to lower values, as reported in Figure16.12. Note that the stability analysis performed during the tuning phase is based on a *model* of the system, which is by definition an approximation of the real process. In particular, as shown in Figure 17.1, the linear model $G_{ah}(s)$ only provides a low frequency approximation of the dynamics of the system. Moreover, due to the nonlinearity of the process under control, such linear model is only valid locally, in a neighbourhood of the working

	$PIna$	PI
ϕ_m	70°	86°
K_m	4.6	22.6

TABLE 17.1: Robustness indicators for the PI_{na} and PI RTC algorithms based on $L(s)$.

	$PIna$	PI
ϕ_m	59.5°	80.6°
K_m	1.9	9.5

TABLE 17.2: Robustness indicators for the PI_{na} and PI RTC algorithms based on $\tilde{L}(s)$.

point. Consequently, the stability results hold in such neighbourhood only. This is particularly interesting since the simulations show that the PI_{na} algorithm becomes unstable with very low values of the flow through the pipe (that is when the system moves very far from the nominal working point).

In order to extend the stability analysis and quantitatively understand the cause of the recorder instability, the robustness indicators are now evaluated and the analysis repeated around the working point characterised by low flow, by means of a higher order model.

Figure 17.3 shows the identification data and the output predicted by $\tilde{G}_{ah}(s)$, a transfer function of higher order, whose parameters are identified from the data by means of Matlab Identification Toolbox. Note how the model prediction now closely follows the time evolution of the pressure.

Figure 17.4 shows the Bode diagram for $\tilde{G}_{ah}(s)$. A comparison of the Bode diagrams of $G_{ah}(s)$ and $\tilde{G}_{ah}(s)$ (respectively Figure 17.2 and 17.4) highlights in $\tilde{G}_{ah}(s)$ the presence of a number of resonance peaks at high frequency. This behaviour can not be captured by the simpler first order transfer function $G_{ah}(s)$, which instead decreases with slope -20dB/decade.

Let us now analyse the Bode diagrams of the loop function, $\tilde{L}_{PIna}(s)$, obtained applying the PI regulator to $\tilde{G}_{ah}(s)$, as in Figure 17.4. The hypotheses for the application of Bode criterion are fulfilled: $\mu_L > 0$ and $\phi_m > 0$, therefore asymptotic stability can again be concluded around the nominal working point.

The robustness indicators obtained from $\tilde{L}_{PIna}(s)$ are reported in Table 17.2. Note that, while the phase margin was just slightly overestimated, the gain margin is strongly overestimated by the simpler G_{ah} model. This is due to the presence of the resonance peaks, which bring the Bode diagram of $\tilde{L}(s)$ much closer to the 0 dB axis than expected.

The last step of this analysis consists in repeating the procedure at a different working point, characterised by very low flow and very high values of α. These are the conditions that bring PI_{na} to instability. In particular, let define the low flow working point WP^{lf}:

$$WP^{lf} = \begin{cases} \overline{\alpha} = 0.88 \\ \overline{H} = 50\ m \\ \overline{D} = 0.03\ m^3/s \\ \overline{h} = 29\ m \end{cases} \tag{17.1}$$

The step response identification data, obtained performing the simulated experiment around WP^{lf}, are reported in Figure 17.5. The same Figure shows also the model prediction obtained from $\tilde{G}^{lf}_{ah}(s)$, again a transfer function of higher order. Figure 17.6 shows the Bode diagrams of $\tilde{G}^{lf}_{ah}(s)$ and highlights that both the static gain and the height of resonance peaks have increased, with respect to $\tilde{G}_{ah}(s)$.

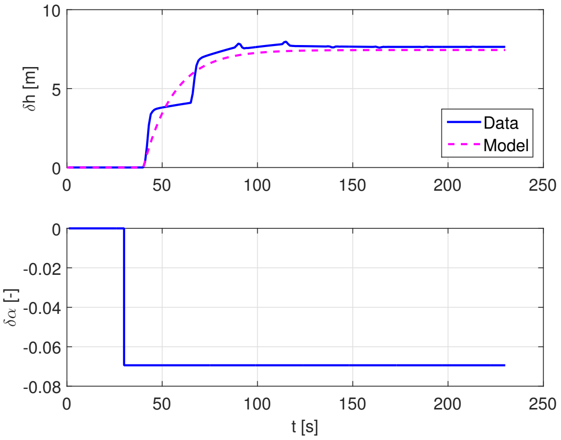

FIGURE 17.1: Step response identification data and model prediction. Top: measured (solid, blue line) and predicted (magenta, dashed line) pressure variation $\delta h(t)$. Bottom: valve variation $\delta\alpha(t)$.

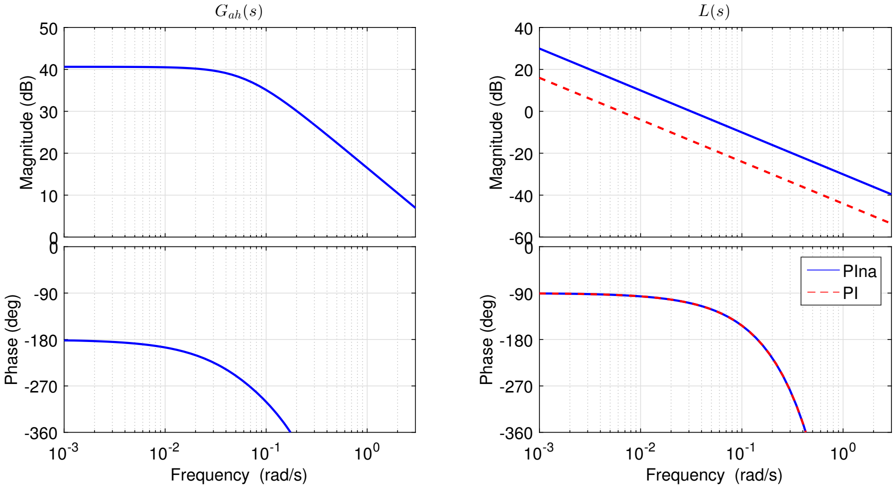

FIGURE 17.2: Left: Bode diagram of $G_{ah}(s)$. Right, blue solid line: Bode diagram of $L(s)$ with PI_{na} algorithm. Right, red dashed line: Bode diagram of $L(s)$ with PI algorithm.

Let now try to verify stability from the analysis of the Bode diagrams of the loop function $\tilde{L}^{lf}(s)$ (see Figure 17.6). Note that the Bode diagram of $\tilde{L}^{lf}_{PIna}(s)$ is now crossing the 0 dB axis many times. The Bode criterion can not be applied to prove stability. In order to draw some conclusions about the stability of the PI_{na} algorithm, it is necessary to rely on the Nyquist plot of $\tilde{L}^{lf}_{PIna}(s)$, which is depicted in Figure 17.7. Note that, in this case, the point -1 is encircled many times by the Nyquist plot, while $Np = 0$, therefore the feedback system is unstable, explaining the large oscillations which arise in the low flow simulations.
A detail of the oscillations is reported in Figure 16.12. Note that the period of the oscillation ($T_w = 25\ s$) is consistent with the frequency of the more pronounced resonance peak of $\tilde{G}^{lf}_{ah}(s)$ (and $\tilde{L}^{lf}_{PIna}(s)$), which is located around 0.26 rad/s.

The stability analysis performed above suggests that instability may arise from an increase in the gain of the process, combined with the presence of multiple resonance peaks. The first order model can not capture this phenomenon, and the design

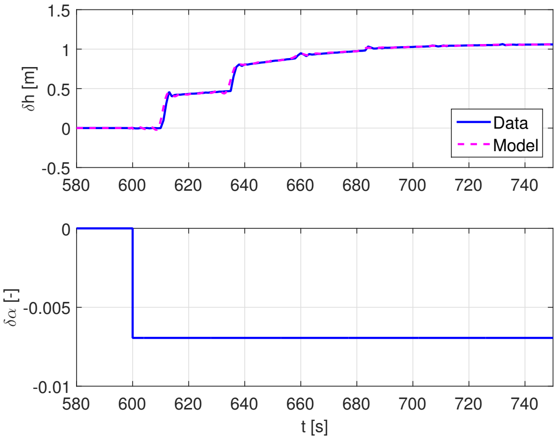

FIGURE 17.3: Step response identification data and model prediction from $\tilde{G}_{ah}(s)$. Top: measured (solid, blue line) and predicted (magenta, dashed line) pressure variation $\delta h(t)$. Bottom: valve variation $\delta\alpha(t)$.

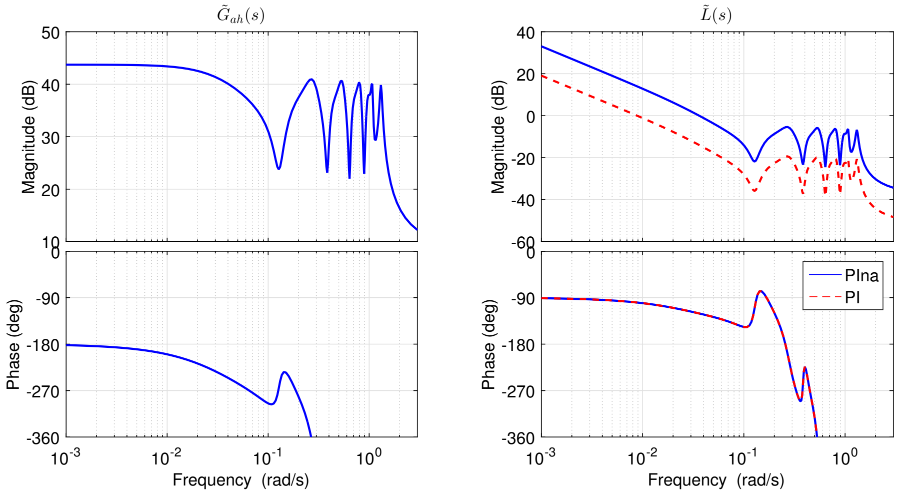

FIGURE 17.4: Left: Bode diagram of $\tilde{G}_{ah}(s)$. Right, blue solid line: Bode diagram of $\tilde{L}(s)$ with PI_{na} algorithm. Right, red dashed line: Bode diagram of $\tilde{L}(s)$ with PI algorithm.

of regulator based on such model results inaccurate. In particular, the gain of the regulator has to be tuned with a trial and error procedure. However, the same analysis suggests that the higher order models can be useful tools in the design of the regulator gain, allowing to avoid the trial and error procedure. This section proposes an example of retuning of the PI_{na} algorithm, based on the higher order models. Let consider the retuning referred to as PI algorithm, with the loop function $L_{PI}(s)$ given by:

$$L_{PI}(s) = \frac{0.0063}{s} e^{-11s} \tag{17.2}$$

with $\omega_c = 0.0063\ rad/s$ and phase margin $\phi_m = 86°$. The Bode diagrams of $L_{PI}(s)$ is depicted in Figure 17.2. Note that the new loop function only differs from the old one in the closed-loop bandwidth, which is higher in the $PI_{na}(s)$ case.

This new ω_c was chosen by verifying stability and robustness using the higher order models identified before, around both WP and WP^{lf}. Figure 17.4 shows the Bode diagram for $\tilde{G}_{ah}(s)$ and the Bode diagrams of the loop function $\tilde{L}_{PI}(s)$ associated to WP. The hypotheses for the application of Bode criterion are fulfilled, since

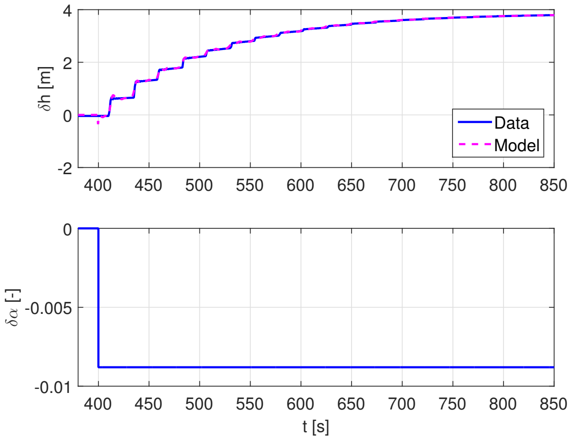

FIGURE 17.5: Step response identification data and model prediction from $\tilde{G}^{lf}_{ah}(s)$. Top: measured (solid, blue line) and predicted (magenta, dashed line) pressure variation $\delta h(t)$. Bottom: valve variation $\delta\alpha(t)$.

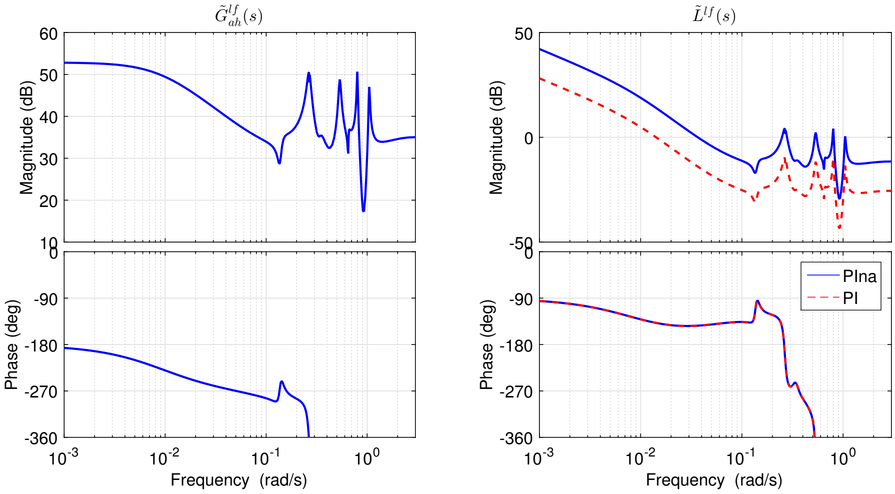

FIGURE 17.6: Left: Bode diagram of $\tilde{G}^{lf}_{ah}(s)$. Right, blue solid line: Bode diagram of $\tilde{L}^{lf}(s)$ with PI_{na} algorithm. Right, red dashed line: Bode diagram of $\tilde{L}^{lf}(s)$ with PI algorithm.

$\mu_L > 0$ and $\phi_m > 0$, and asymptotic stability can again be concluded around the nominal working point. The robustness indicators obtained from $\tilde{L}_{PI}(s)$ are reported in Table 17.2. Note how the gain margin is increased by the gain reduction, and how the distance between resonance peaks and the 0 dB axis is increased.

Let now consider the low flow working point WP^{lf}, and the associated higher order model $\tilde{G}^{lf}_{ah}(s)$, whose Bode diagrams are reported in Figure 17.5. The same Figure also shows the Bode diagrams of the corresponding loop function $\tilde{L}^{lf}_{PI}(s)$, obtained with the application of the new PI algorithm. The Bode diagram fulfils the hypotheses of Bode criterion, which can be successfully applied to prove asymptotic stability of the feedback system.

Figure 17.7 also shows the Nyquist diagram for $\tilde{L}^{lf}_{PI}(s)$, which is still far from encircling the point -1, thus providing again some degree of robustness.

When applied to the plant, the new PI algorithm delivers satisfactory results, without any stability issue in all the simulated scenarios.

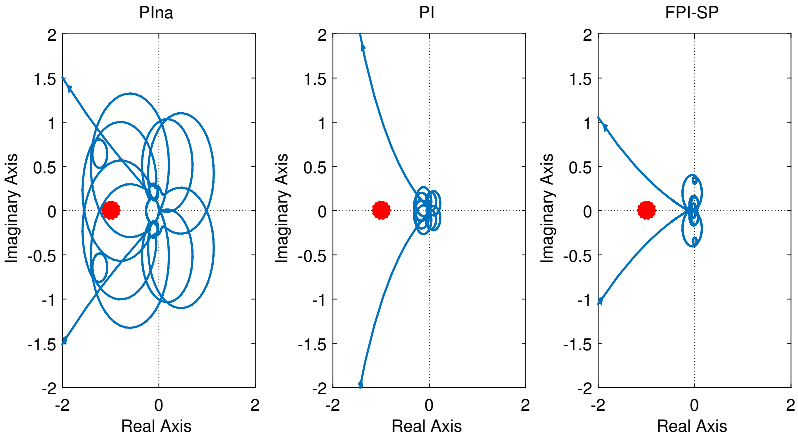

FIGURE 17.7: Nyquist diagrams of $\tilde{L}^{lf}(s)$. Left: PI_{na} algorithm. Centre: PI algorithm. Right: $FPI - SP$ algorithm.

Remark. Let consider the stability analysis of the PI algorithm in nominal conditions, based on the nominal first order model. Figure 17.2 shows the loop function $L_{PI}(s)$. The phase margin results $\phi_m = 86°$, while the phase margin loss associated to the discretisation results $\phi_d = -0.18$ °. The Bode criterion can again be applied to prove the asymptotic stability of the feedback system.
Let now focus on the robustness indicators evaluated in the nominal case, with the first order model: Table 17.1 highlights the increase in the gain margin, with respect to the previous tuning. A comparison with Table 17.2 (robustness indicators evaluated with the higher order model) again stresses how the analysis based on the first order model heavily overestimates the gain margin provided by the closed-loop system.

The analysis of stability and robustness of the Proportional Integral RTC algorithms performed in the previous sections allows making some remarks:

- The instability of a nominally stable RTC algorithm can be caused by the combined action of the gain nonlinearities and the high frequency resonance peaks of the process.
- A low order model as $G_{ah}(s)$ can not capture such high frequency resonant behaviour, while a higher order model like $\tilde{G}_{ah}(s)$ may provide a better description of the dynamics of water distribution system. When a higher order model is available, the tuning of the regulators can be successfully performed on the model, with no need for trial and error procedures. Still, in some real experimental scenarios, it may be difficult to obtain an accurate higher order model.
- For these reasons, when based on a low order model, the RTC algorithm must be tuned so that *both* phase and gain margin provide a wide degree of robustness to the design, or consider the vectorial stability margin.
- Both Bode and Nyquist diagrams can be useful tools to analyse stability and evaluate robustness of the control design.

In addition, it was shown in the previous Chapters that it is possible to improve the design of the Proportional Integral algorithm by introducing a Filtering action and a Smith Predictor. These elements were originally introduced to filter high frequency harmonics and reduce the cost of control as the cumulative motion of the PCV. Still, the stability analysis performed in this work highlights that robustness is also enhanced by this new design, as discussed in the following section.

17.2 Improving Robustness and Cost of Control with FPI-SP RTC Algorithms

This section highlights how stability and robustness could benefit from the introduction of a lowpass filter and a Smith Predictor in the design of the RTC algorithm. In addition, an detailed explanation of how this design allows to reduce the cost of control is given, based on the same higher order model used for the stability analysis.

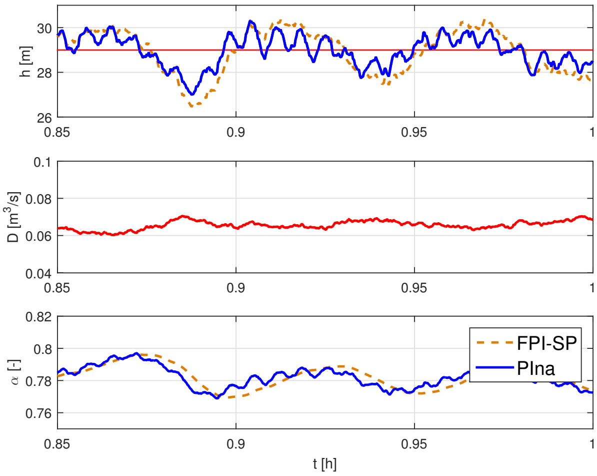

FIGURE 17.8: Closed-loop simulation with $PIna$ (blue, solid line) and $FPI - SP$ (orange, dashed line) algorithms. Top: pressure $h(t)$ and pressure setpoint h_{sp}. Middle: demand $D(t)$. Bottom: valve closure $\alpha(t)$.

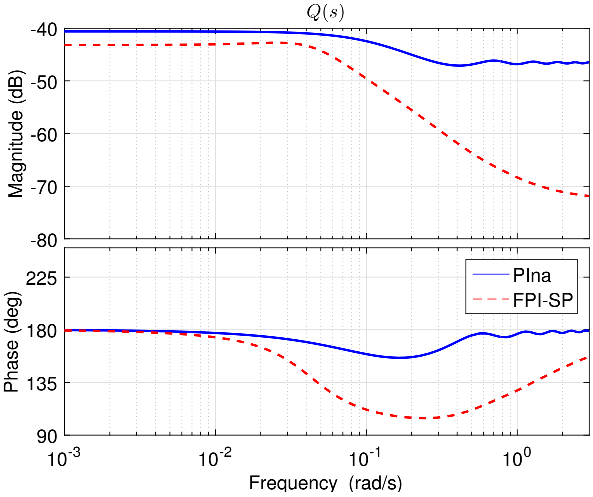

FIGURE 17.9: Control sensitivity functions for the $PIna$ (solid, blue line) and $FPI - SP$ (red, dashed line) algorithms.

17.2.1 Stability Analysis of FPI-SP RTC Algorithm

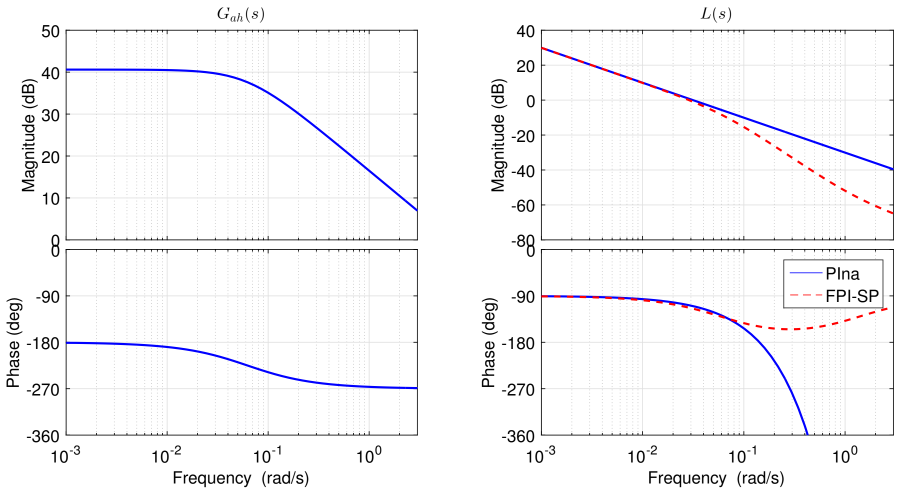

FIGURE 17.10: Left: Bode diagram of $G_{ah}(s)$. Right, blue solid line: Bode diagram of $L(s)$ with PI_{na} algorithm. Right, red dashed line: Bode diagram of $L(s)$ with $FPI-SP$ algorithm.

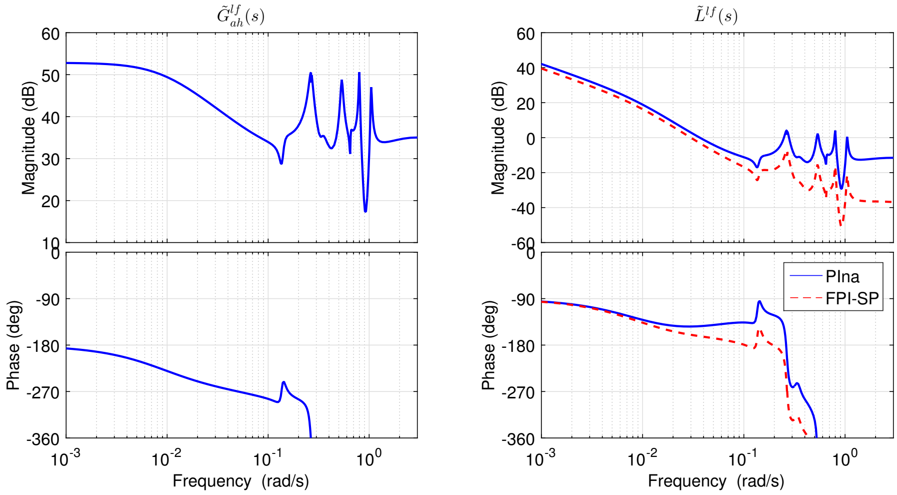

FIGURE 17.11: Left: Bode diagram of $\tilde{G}^{lf}_{ah}(s)$. Right, blue solid line: Bode diagram of $\tilde{L}^{lf}(s)$ with PI_{na} algorithm. Right, red dashed line: Bode diagram of $\tilde{L}^{lf}(s)$ with $FPI-SP$ algorithm.

Stability and Robustness of $FPI-SP$ algorithm are now evaluated according to the procedure introduced in this work. The nominal stability can be proven by means of the Bode criterion, since $\mu_L > 0$ and $\phi_m = 67^\circ > 0$. In addition, one has $K_m = \infty$, since the phase of $L_{FPI-SP}(s)$ never reaches -180°. The phase margin loss associated to the discretisation results $\phi_d = -0.9\ ^\circ$. In comparison to the PI_{na} algorithm, it is possible to note that the gain margin is heavily increased, while maintaining the phase margin and ω_c almost unchanged.
From a practical point of view this means that the robustness of the algorithm is increased without reducing the bandwidth of the closed-loop, which in turns impacts on the regulation performances, as instead happened for the PI algorithm. The last step is repeating the analysis around WP^{lf}, to prove stability at low flows. Let $\tilde{L}^{lf}_{FPI_SP}(s)$ be the loop transfer function, obtained from the application of the $FPI-SP$

algorithm to the higher order model $\tilde{G}_{ah}^{lf}(s)$; its Bode diagram is reported in Figure 17.11. Note that, while the critical frequency ω_c is almost coinciding for both PI_{na} and $FPI-SP$ algorithm, it is still possible to prove stability of $FPI-SP$ by means of Bode criterion, since the resonance peaks which cause instability of PI_{na} are not crossing the 0 dB axis. In addition, some robustness margin is left to face further variations of the process model. The same result can be obtained from the inspection of the Nyquist plot (see Figure 17.7), and the application of the Nyquist theorem.

Remark: Note that the loop functions reported in Figure 17.10 slightly differ in the static gain. This is due to the presence in $FPI-SP$ of the Smith Predictor based on the nominal process model $G_{ah}(s)$, whose static gain is in turn different from that of $\tilde{G}_{ah}^{lf}(s)$.

17.2.2 Cost of Control of FPI-SP RTC Algorithm

As it was demonstrated in the previous chapters, the RTC algorithm benefits from the new elements in terms of cost of control, evaluated as the overall motion of the PCV during the trial. The filtering action in the regulator transfer function improves rejection of high frequency harmonics of the error signal. This means that the regulator does not try to compensate them, reducing the required motion of the valve, as shown in Figure 17.8. This effect can be considered during the design phase by addressing the *control sensitivity function*, which is defined as:

$$Q(s) = \frac{U(s)}{Y^*(s)} = \frac{R(s)}{1+L(s)} \tag{17.3}$$

In case of Smith Predictor, it is defined as:

$$Q(s) = \frac{U(s)}{Y^*(s)} = \frac{R'(s)}{1+L(s)} \tag{17.4}$$

with $R'(s)$ defined according to Equation (17.5), and $L(s)$ according to Equation (17.6):

$$R'(s) = \frac{R(s)}{1+P(s)R(s)} \tag{17.5}$$

$$L(s) = G(s)\frac{R(s)}{1+P(s)R(s)} = G(s)R'(s) \tag{17.6}$$

A comparison of the control sensitivity functions associated to the PI_{na} and $FPI-SP$ algorithms is presented in Figure 17.9. The two transfer functions are computed with $G(s) = G_{ah}(s)$. Note that the $FPI-SP$ algorithm shows a reduced control sensitivity at high frequency with respect to the PI_{na} algorithm.

17.3 Water Distribution Network

The aim of this section is to show that the analysis proposed in this work can also be applied to case study B, when the step response experiment performed around a working point would suggest to use a first order model as approximation.

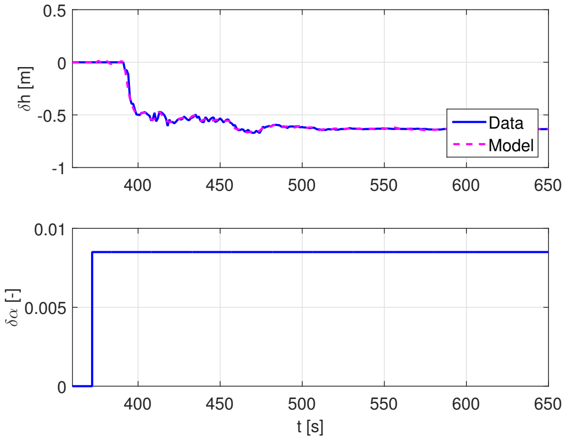

FIGURE 17.12: Step response identification data and model prediction from $\tilde{G}_{ah}(s)$. Top: measured (solid, blue line) and predicted (magenta, dashed line) pressure variation $\delta h(t)$. Bottom: valve variation $\delta\alpha(t)$.

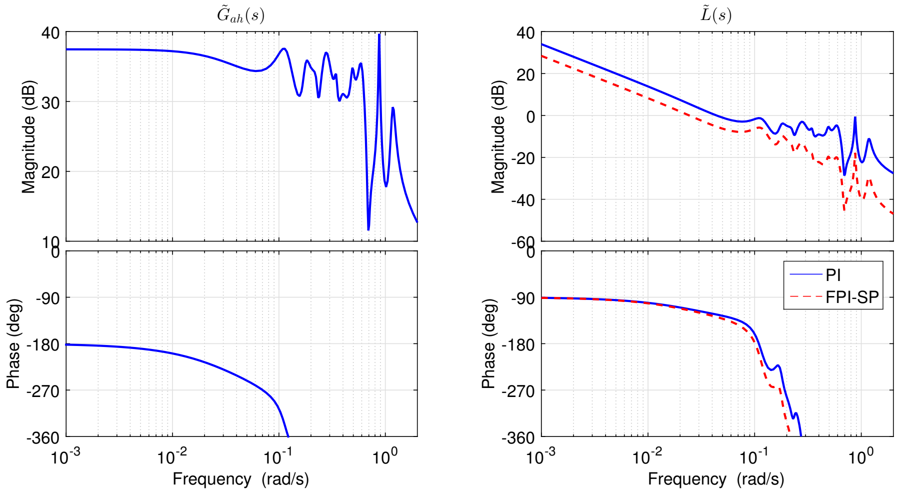

FIGURE 17.13: Left: Bode diagram of $\tilde{G}_{ah}(s)$. Right, blue solid line: Bode diagram of $\tilde{L}(s)$ with a PI algorithm. Right, red dashed line: Bode diagram of $\tilde{L}(s)$ with a FPI-SP algorithm.

17.3.1 Stability and Robustness Analysis

According to the proposed design procedure, a step response experiment, performed in nominal conditions, leads to the following local model:

$$G_{ah}(s) = \frac{-74.7e^{-18s}}{(1+14.4s)} \tag{17.7}$$

A possible tuning for the PI algorithm is then:

$$R_{PI}(s) = \frac{0.00067(1+14.4s)}{s} \tag{17.8}$$

A possible $FPI - SP$ extension is instead:

$$R_{FPI}(s) = \frac{0.00067(1+14.4s)}{s}\frac{1+1.25s}{1+12.5s} \tag{17.9}$$

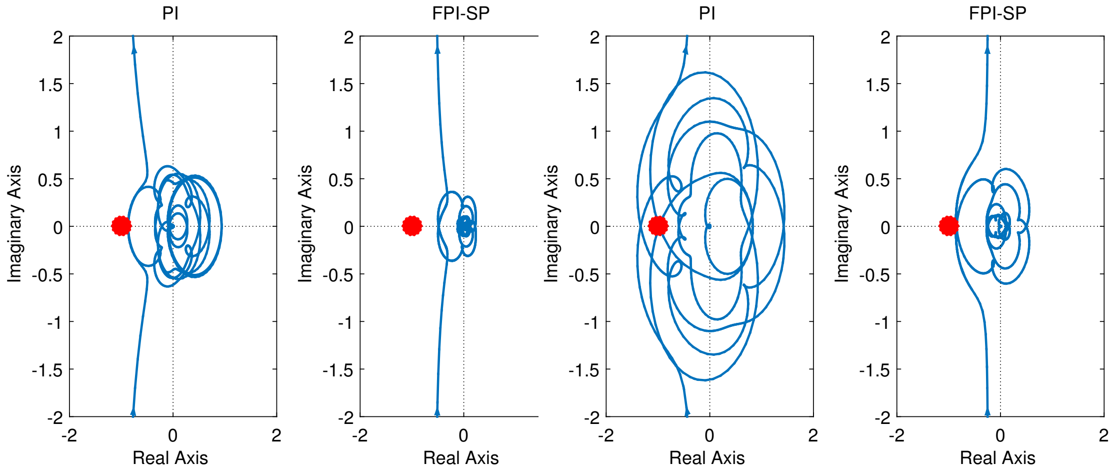

(A)

(B)

FIGURE 17.14: WDN: (a) Nyquist diagrams of $\tilde{L}(s)$. Left: PI algorithm. Right FPI-SP algorithm. (b) Nyquist diagrams of $\tilde{L}^{hf}(s)$. Left: PI algorithm. Right FPI-SP algorithm.

	PI	$FPI-SP$
ϕ_m	56.5°	64.5°
K_m	1.15	2

TABLE 17.3: WDN: robustness indicators for the PI and $FPI-SP$ RTC algorithms based on $\tilde{L}(s)$.

with the Smith Predictor based on $G_{ah}(s)$. The two regulators are implemented in a discrete time way. Discretisation is performed with Tustin method to ensure that stability properties of $R(s)$ are preserved. The chosen sampling time is 1 s, which is consistent with Nyquist Sampling Theorem [38]. The phase margin loss associated to the discretisation results $\phi_d = -1.44$ ° for both algorithms.

The stability analysis here reported is based on the identification of the higher order model $\tilde{G}_{ah}(s)$ from the same step response experiment used to identify $G_{ah}(s)$. The identification data and the model prediction are reported in Figure 17.12. The Bode diagram of $\tilde{G}_{ah}(s)$ is depicted in Figure 17.13. Note that high frequency resonance peaks are present also in this case, with even lower damping than in the WDS case. This makes the peaks even more pronounced, with a magnitude of the Bode diagram that is higher than that of the static gain of the transfer function itself, despite a more accurate pressure-driven modelling of the WDN (as suggested in [68] and [69]). The same Figure also shows the Bode diagrams of $\tilde{L}(s)$ obtained with the application of the PI and $FPI-SP$ algorithms proposed above. Stability can be proven with Bode criterion, and, again, note how the $FPI-SP$ algorithm manages to improve the filtering of high frequency harmonics and increase the gain margin, with no significant reduction of the closed-loop bandwidth or phase margin reduction. Figure 17.14a shows the Nyquist plot for the two algorithms, to highlight their overall robustness as distance from the point -1. Note how the PI algorithm is dangerously close to the point -1, while $FPI-SP$ provides more robustness.

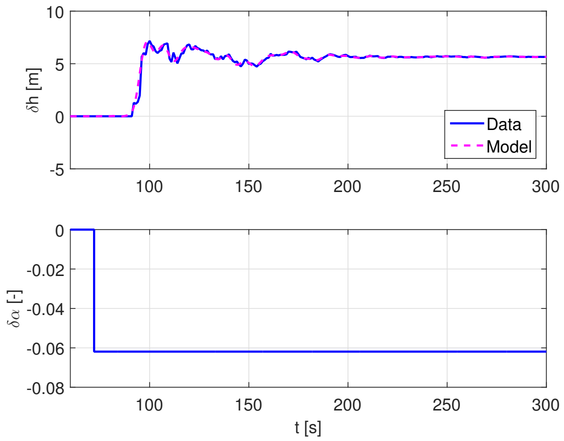

FIGURE 17.15: WDN: Step response identification data and model prediction from $\tilde{G}_{ah}^{hf}(s)$. Top: measured (solid, blue line) and predicted (magenta, dashed line) pressure variation $\delta h(t)$. Bottom: valve variation $\delta\alpha(t)$.

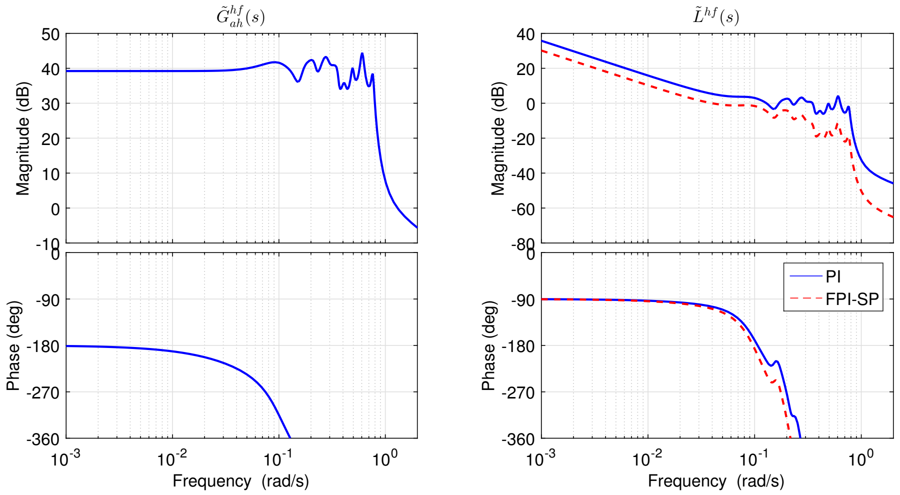

FIGURE 17.16: WDN: Left: Bode diagram of $\tilde{G}_{ah}^{hf}(s)$. Right, blue solid line: Bode diagram of $\tilde{L}^{hf}(s)$ with a PI algorithm. Right, red dashed line: Bode diagram of $\tilde{L}^{hf}(s)$ with a $FPI-SP$ algorithm.

Due to the complex topology, the distributed nature of the WDN and the pressure dependent outflow from the demanding nodes, the local behaviour of the system may be changing a lot when considering different working points, not just in the static gain, but in a more complex and unpredictable way. For these reasons, the robustness of the RTC algorithms is of fundamental importance and should be tested around different working points. As an example, let us repeat the analysis at a working point characterised by a higher average of the total demand (let denote the related models with apex hf). The identification data and the model prediction are reported in Figure 17.15. The Bode diagram of $\tilde{G}_{ah}^{hf}(s)$ is depicted in Figure 17.16. The loop functions $\tilde{L}^{hf}(s)$, associated to the two control algorithms, are reported in the same Figure. The Bode criterion can be used to prove $FPI-SP$ stability while, in the case of the PI algorithm, the Bode diagram of $\tilde{L}^{hf}(s)$ crosses the $0\ dB$ axis many times, thus contradicting one of the hypotheses required by the criterion. Stability of the PI algorithm must be therefore discussed from the Nyquist plot of the

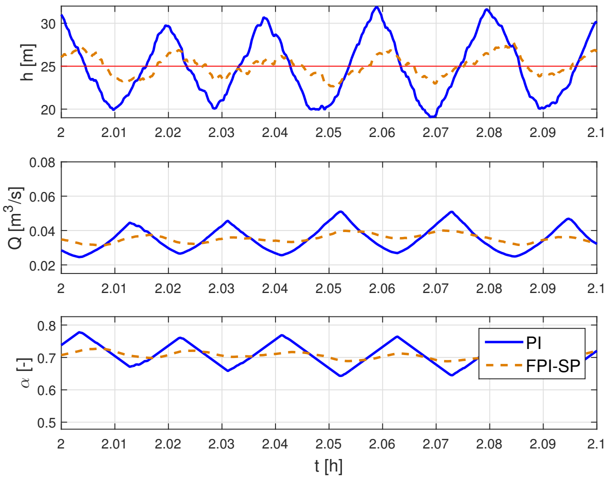

FIGURE 17.17: WDN: Closed-loop simulation with PI (blue, solid line) and $FPI - SP$ (orange, dashed line) algorithms. Top: pressure $h(t)$ and pressure setpoint h_{sp}. Middle: flow discharge at the valve site $Q(t)$. Bottom: valve closure $\alpha(t)$.

associated loop function, which is reported in Figure 17.14b, and highlights that the algorithm leads to instability around the considered working point. When considering the Nyquist plot of $FPI - SP$ loop function it is possible to understand how the algorithm is still stable, even if closer to the instability condition. Figure 17.17 shows a simulation of the WDN around the working point with higher total demand, with both control algorithms. As expected from the analysis, the PI algorithm leads to instability: note how the speed of the PCV is always saturated during control. On the contrary, the $FPI - SP$ algorithms is correctly working, even if some minor oscillations are generated in the service pressure.

17.4 Discussion of Results

The analysis performed in this Chapter suggests that the instability of PI/FPI-SP algorithms can be caused by the presence of multiple resonance conditions that may not be described by the model used in the design of the regulator, concurrently with a consistent nonlinearity of the gain of the process under control. When possible, it is therefore advisable to base the regulator design on higher order models, which better describe the dynamics of the process around the working point. In particular, a higher order model allows to understand the presence of non de-amplified closed-loop oscillations at various frequencies, which can affect stability in presence of gain uncertainty. The different resonance peaks in the open-loop transfer function $G(s)$ should be carefully considered in the design of the loop function $L(s)$ to properly evaluate stability, robustness and overall dynamic performances of the control algorithm. In case this is not possible, wide robustness margins must be provided in the design of the feedback system. For this purpose, it is shown that the introduction of a low-pass filter and a Smith Predictor can significantly improve the robustness of the control scheme, while, at the same time, help reducing the cost of control. It is also advisable to consider auxiliary working points characterised by different values of flow discharge and repeat the analysis to ensure stability and robustness even in critical situations.

Chapter 18

Discussion of Results and Future Work

The results of simulations introduced in Chapters 18.1 and 16 are now discussed and compared. In addition, results are also compared to those obtained with a different control approach, based on physical considerations on steady state conditions in WDNs, which is now briefly introduced. Note that this controller is usually applied with control time steps of the order of magnitude of some minutes. This makes the performance comparison particularly interesting, since it can highlight if the reduced sampling time introduced in this work can be useful in improving the overall control performances.

18.1 Pressure Control Strategy Based on Steady State Models

The algorithm aims to correct the local head loss coefficient ξ of the valve, which is an increasing function of α, as derived from the specific valve curve $\xi(\alpha)$ provided by the valve manufacturer. Then $\Delta\xi$, i.e. the variation of ξ applied by the regulator, is equal to:

$$\Delta\xi = K\frac{2gA^2}{Q^2}e \tag{18.1}$$

where A $[m^2]$ is the cross area of the pipe equipped with the valve. Q $[m^3/s]$ is the measured water flow in the same pipe. Finally, K is a constant that is tuned by trial and error. Once $\Delta\xi$ is computed, the $\alpha(\xi)$ curve can be used to define to new valve setting α. The values of e and Q to be used for assessing $\Delta\xi$ are the average values measured during the previous control time step. For both case studies, the algorithm is applied with a time step of 180 s. Let refer to this algorithm as $P\ on\ \xi$. Further details about this algorithms can be found in [51].

Case study A

The results of simulations described in Section 15 are reported in Table 18.1. The best value of the controller constant K is experimentally determined as $K = 0.862$. Figure 18.1 depicts the closed-loop simulation of a fire hydrant opening. Pressure is restored in about 600 s by $P\ on\ \xi$ algorithm.

Case study B

Table 18.2 shows the results of simulations, with the two different demand profiles introduced in Section 15. The controller constant was set to $K = 0.4$ to obtain the best results for Case Study B.

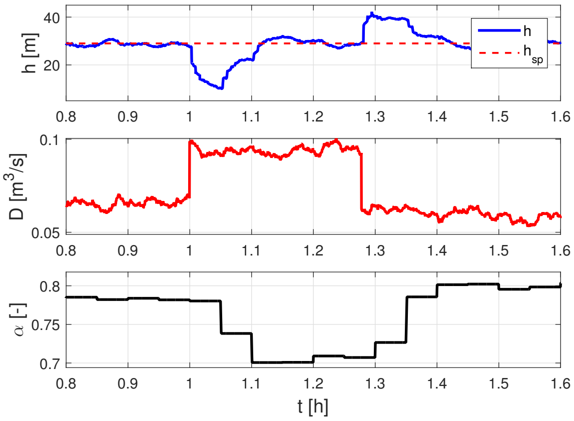

FIGURE 18.1: Case Study A: closed-loop simulation with $P\ on\ \xi$ algorithm and opening of a fire hydrant. Top: pressure $h(t)$ and pressure setpoint h_{sp}. Middle: demand $D(t)$. Bottom: valve closure $\alpha(t)$.

$Demand$ $Offset$ $[m^3/s]$	$Displacement$ $Instants$ $[\%]$	$\sum\|\Delta\alpha\|$ $[-]$	$Mean\|e(k)\|$ $[m]$
-0,03	0,68	3,17	2,31
-0,02	0,69	3,19	1,94
-0,01	0,70	3,24	1,68
0	0,71	3,33	1,50
0,01	0,73	3,69	1,25
0,03	0,78	3,98	1,16
0,04	0,81	4,36	1,08
0,05	0,88	4,89	1,01

TABLE 18.1: Performance of $P\ on\ \xi$ algorithm for different demand offsets.

18.2 Analysis of Performances

To make comparison easier, results of Case Study A are reported in Figure 18.2 and Figure 18.3, where respectively the regulation error ($Mean|e(k)|$) and the cost of control ($\sum|\Delta\alpha|$) are plot as function of the demand offset. Recall that regulators were tuned to obtain the best regulation error first. Then, if possible, tuning was changed to improve the control cost without degrading the regulation error. The algorithms accounting for the dynamics of the system work with a control sampling time of 1 s, trying to compensate for the instantaneous variations of the pressure generated by demand and source pressure variations. The percentage of displacement instants is therefore always 100%. All these algorithms outperform the $P\ on\ \xi$ algorithm in term of regulation error. Note that $P\ on\ \xi$ regulation performance suffers more from demand offset variations, while the other algorithms provide more constant results. The $ILQG-SF$ stands out, providing the best regulation error, with very little variations due to the demand offset. FPI and $ILQG$ follow with similar performance. The PI algorithm could not properly rejects pressure wave noise and could only be applied with a reduced closed-loop bandwidth, thus is the less performing

$Demand\ Profile$	$Displacement\ Instants$ [%]	$\sum\lvert\Delta\alpha\rvert$ [−]	$Mean\lvert e(k)\rvert$ [m]
A	2	3.37	1.06
B	2.75	5.55	0.98

TABLE 18.2: Case Study B: Performance of $PI\ on\ \xi$ algorithm for different demand profiles.

$Control\ Algorithm$	$Displacement\ Instants$ [%]	$\sum\lvert\Delta\alpha\rvert$ [−]	$Mean\lvert e(k)\rvert$ [m]
PI	100	33.5	0.7
$FPI\ with\ SP$	100	11.4	0.74
$ILQG\ with\ SP$	100	20	0.7
$P\ on\ \xi$	2	3.37	1.06

TABLE 18.3: Case Study B: performance comparison of algorithms tested on the WDN with Demand A.

$Control\ Algorithm$	$Displacement\ Instants$ [%]	$\sum\lvert\Delta\alpha\rvert$ [−]	$Mean\lvert e(k)\rvert$ [m]
PI	98	22.9	0.55
$FPI\ with\ SP$	98	9.6	0.62
$ILQG\ with\ SP$	98	15	0.6
$P\ on\ \xi$	2.75	5.55	0.98

TABLE 18.4: Case Study B: performance comparison of algorithms tested on the WDN with Demand B.

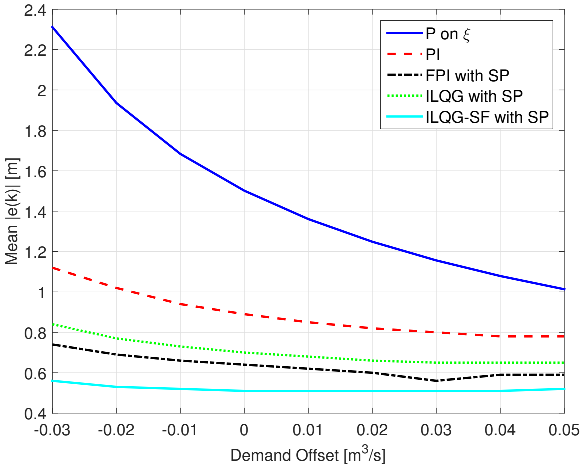

FIGURE 18.2: Case Study A: regulation error as function of the demand offset.

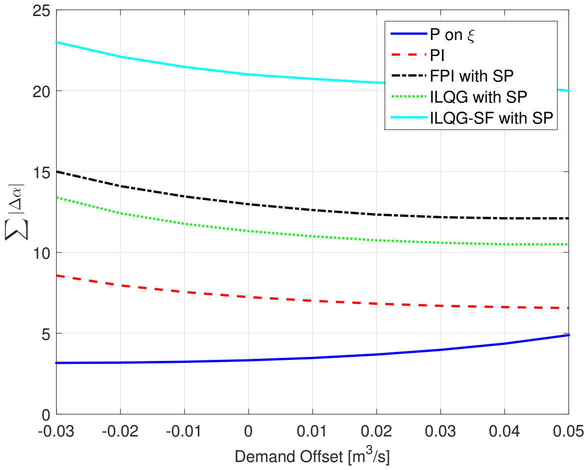

FIGURE 18.3: Case Study A: cost of control as function of the demand offset.

algorithm of the family. As expected, the cost of control grows with better regulation performances: the control valve has to move more when trying to compensate for faster disturbances. The new algorithms perform well also in the rejection of a demand step variation, with satisfying settling times and no or very little oscillations in the response, as discussed in Chapter 16 (fire hydrant opening simulations).

The results for Case Study B are summarised in Tables 18.3 and 18.4. Recall that a single tuning of the control algorithm was performed to cope with two different demand trends. Considerations about the percentage of displacement instants still hold. Note that a displacement instants of 98% is obtained with demand profile A because of saturation of the actuator (see Figure 16.16 as example). Again, all the new algorithms outperform the $P\ on\ \xi$ benchmark. The best regulation performance is delivered by the PI algorithm. The power of pressure waves, which were responsible for its bad performance in Case Study A, is now distributed over many harmonics. The PI could then be used with larger closed-loop bandwidths. Still, the cost of regulation is quite high when compared to $ILQG$ algorithm, which provides almost the same regulation performance with a significant reduction of control cost. Note that the results achieved with the $ILQG - SF$ algorithm are not reported because do not improve the one achieved without the shaping functions. The FPI

algorithm instead further reduces the control cost, at the price of slightly worse regulation error.

All control algorithms improve the results of the benchmark algorithm in terms of regulation error in presence of pulsed nodal demand. On average, the reduction in the regulation error adds up to about 40%. Pressure is quickly regulated to the setpoint even in presence of demand step variations.

In addition, in case of a PI or $FPI - SP$, the detailed analysis performed in Chapter 17 with the two different case studies motivates the use of a higher order model that captures the multiple resonant behaviour of the plant and allows to properly analyse stability and robustness of the control design. The proposed analysis also suggests that the higher order model can be an useful tool to complement the regulator design phase. In fact, while the first order model requires a trial and error procedure for the tuning of the gain of the regulator, the higher order model allows to tune the regulator directly on the model. Finally, the higher order model allows to explain in depth the benefits of the $FPI - SP$ design, both in terms of robustness and improved control sensitivity. A final remark concerns the implementation of the proposed algorithms in a real WDN framework. Note that all the algorithms require very low computational power and can be easily implemented on low power devices. Their application in the field is viable in all the cases where the increase in control cost, which may cause the more rapid wearing of the control valve, is not a limiting factor. Another fundamental requirement for the application of these algorithms operating with a sampling time of 1 s is the possibility to transfer continuously the pressure head signal from the remote note to the control valve site. This is easy in new WDNs, where wiring is already present alongside pipes. In old WDNs, where the absence of wiring alongside pipes makes wireless communication necessary, the use of control algorithms operating with longer sampling times may be preferable. The study of the presented algorithms with longer settling times is left as future work.

Part III

Model Predictive Control of a Laboratory Scale Overhead Travelling Crane Affected by Deadzone Nonlinearity

Chapter 19

Introduction

The control of plants with actuators showing a nonlinear behaviour (saturation, deadzone, hysteresis, backlash...) is one of the most common issues in the industrial framework. Mechanical actuators in fact may not only show intrinsic nonlinear behaviour, but are also subject to an unavoidable ageing process which alters their dynamic. This results in a nonlinear and uncertain behaviour and consequently in poor control performances. This work focuses on a plant with DC motors whose dynamic is characterised by the presence of a non-symmetric deadzone and a saturation of the control signal. According to the literature, the problem can be faced in different ways, also relying on approaches which were developed for different types of nonlinearities. Among these techniques adaptive control [71, 72], Nonlinearity Inversion [73, 72, 74] and Hybrid MPC [75, 76]) are worth mentioning. Our aim is to implement and investigate two different control schemes based on Model Predictive Control (MPC) which are able to cope with the nonlinearity of the actuators.

The choice of MPC as the fundamental layer for control strategies is motivated by its flexibility: MPC allows to directly use process models, for example empirically derived from experiments, to explicitly consider state and input constraints in the control formulation. Defining a complete MPC controller requires then:

- a process model;
- input, output and state constraints;
- a cost function J defined over a finite horizon N ("prediction horizon");
- an optimisation algorithm;
- the application of the so-called "Receding Horizon (RH) Principle".

At any time instant k, based on the available process information, RH requires to solve the optimisation problem (optimise J) with respect to the future control sequence $\mathbf{u}_{[k,\ldots,k+N-1]} = [u(k), \ldots, u(k+N-1)]$ and then to apply its first element only. Then, at time instant $k+1$, basing on the new process information, a new optimisation problem is solved over the temporal window $[k+1, k+N]$ and the procedure is repeated [70]. Standard MPC algorithms can be easily used to introduce a saturation of the control input, but can not be used to directly address the problem of the deadzone. More sophisticated MPC algorithms are needed to manage its presence. In particular our first choice is Hybrid MPC, which allows to consider the deadzone directly in the dynamics of the plant. This requires to introduce in the optimisation problem logic constraints and variables that can be first translated into mathematical constraints with integer variables and then solved by means of Mixed-Integer solvers [77]. Examples of Hybrid MPC developed for nonlinear actuators handling

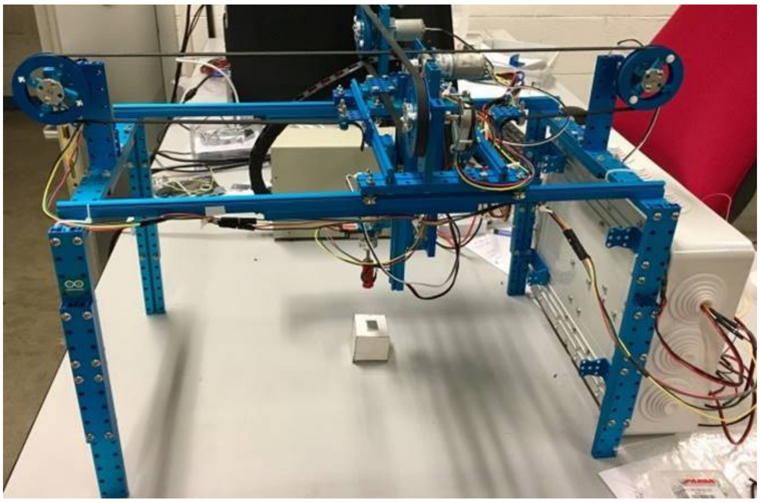

FIGURE 19.1: The laboratory scale overhead travelling crane used for experiments.

can be found in [75, 78, 76]. The second approach instead relies on constrained MPC and on the introduction of an inverse deadzone model, as described in [79]. In the following this will be referred as *Equivalent Saturation (ES) MPC*. This approach is investigated in [74] and [80]. There the authors claim that further research is needed to assess the algorithm performance in presence of model uncertainties. In addition, no extensive experimental ES validation has been performed in conjunction with an MPC controller.

The contribution of this work is twofold:

- the robustness analysis of both Hybrid and ES MPC;
- the experimental validation of the two algorithms on a laboratory scale overhead travelling crane exhibiting severe nonlinearities.

The analysis highlights that the two approaches can produce comparable results applied under nominal conditions. On the other side Hybrid MPC seems to behave more robustly when in presence of unmodelled nonlinearities. The results here discussed have been published as [81].

Chapter 20

Plant Description and Model Identification

A laboratory scale version of an overhead travelling crane (see Figure 19.1) is used for the experimental trials in this work. The crane allows to pick up and release a small load by means of a small electromagnet. Motion is allowed in all the three dimensions (x, y, z), with the same hardware configuration on the three motion axis (results for the $x - axis$ only will be reported, since the other two share a similar behaviour and do not provide any extra information to the discussion). The process was entirely built in the Process Control laboratory of University of Pavia, and features the following hardware:

- the crane structure, which is realised using Makeblock components [82].
- a 9V DC motor equipped with a belt, used as actuator (Makeblock components);
- a quadrature encoder (CUI AMT-102V), used to sense the position and the direction of motion.

The system is driven by means of Arduino Mega circuit board and interfaced with Matlab Real Time Toolbox for control purposes. The input to the process is the voltage over the DC motor. This will be used as control variable. The load position represents instead the output of the process.

The main goal of the control system is then to place the load as precisely as possible in the desired position, while avoiding any oscillations during motion. Note that the encoder shows a granularity that results in a linear position measurement error bounded by $[-0.1; +0.1]$ cm. The actuation instead shows a non-symmetric deadzone behaviour that is evident when supplying a purely sinusoidal input voltage to the DC motor and collecting the corresponding position (see Figure 20.1 as example). Note that the position drifts in the negative direction: a wider extension of the deadzone for positive voltages can then be expected. In addition, due to physical limitations, control voltages are constrained in a limited range, introducing a saturation effect on the control action. In the following of this section a mathematical description of nonlinearities affecting the actuation is introduced and the overall model identification phase is discussed.

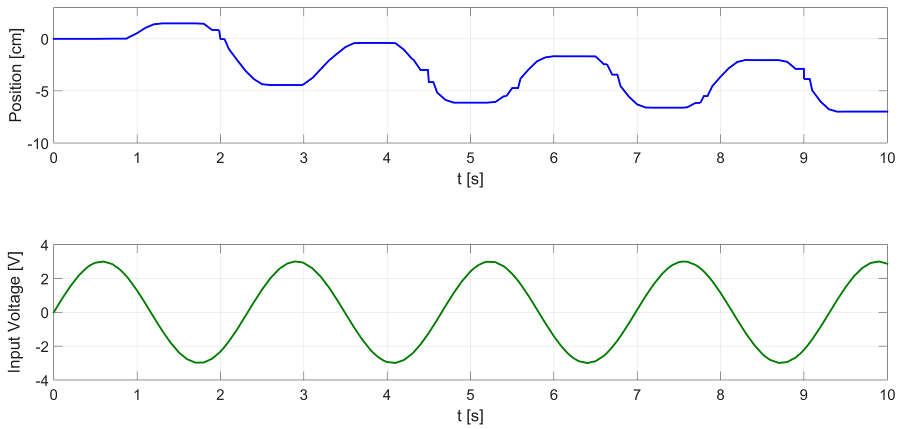

FIGURE 20.1: System response to a sinusoidal input.

20.1 Deadzone

The first step required for system modelling is the definition of the limits of the deadzone. It can be expressed as follows:

$$u_{dz}(t) = \begin{cases} u(t) - high & \text{if } u(t) \geq high \\ 0 & \text{if } low < u(t) < high \\ u(t) - low & \text{if } u(t) \leq low \end{cases} \tag{20.1}$$

and is depicted as in Figure 20.2.a. Recall that the plant shows a non-symmetric deadzone. Deadzone identification is carried out experimentally, by applying a weak slew rate voltage ramp (with a positive slope first, then with a negative one) to the DC motor and verifying the input voltage value corresponding to the instant in which the system starts moving. Measures are repeated with the load placed in different positions and a "conservative" model is defined by choosing the maximum *high* and the minimum *low* measured values:

$$\begin{aligned} low &= -2.4\ V \\ high &= 2.6\ V \end{aligned}$$

20.2 Saturation

Figure 20.2.b depicts a general signal saturation, which can be defined as:

$$u_{sat}(t) = \begin{cases} u_{max} & \text{if } u(t) \geq u_{max} \\ u(t) & \text{if } u_{min} < u(t) < u_{max} \\ u_{min} & \text{if } u(t) \leq u_{min} \end{cases} \tag{20.2}$$

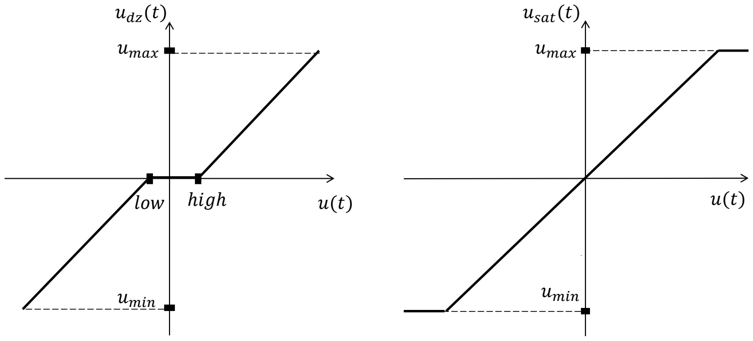

FIGURE 20.2: Left: a generic deadzone acting on signal $u(t)$. Right: a generic saturation acting on signal $u(t)$.

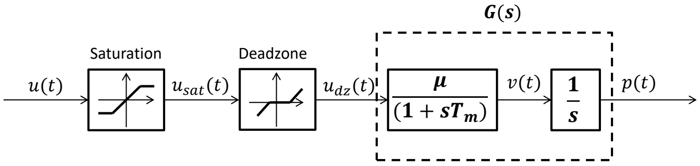

FIGURE 20.3: Block scheme for the the actuator. Signals in the scheme: $u(t)$ is a generic voltage input to the actuator; $u_{sat}(t)$ is the saturated voltage input; $u_{dz}(t)$ is the voltage input after the deadzone; $v(t)$ is the speed; $p(t)$ is the position. Note that mixed notation is used.

The voltage control input of the considered plant shows a saturation whose limits are given by:

$$u_{max} = 9\ V$$
$$u_{min} = -9\ V$$

20.3 DC Motor

As previously stated, a 9V DC motor is used as the main actuator for each axis in the plant. Angular motion is turned into linear motion by means of a belt pulley. The typical DC motor Input-Output models (with the control voltage as input and the linear speed as output) are two poles transfer functions, where the "slow" pole is related to the mechanical time constant of the motor, while the "fast" pole is related to its electrical time constant [83]. Preliminary tests show that the electrical pole can be neglected in our case. An integrator is then introduced to move from speed to position. To sum up, the model for the linear part of the actuator can be written as follows:

$$G(s) = \frac{P(s)}{U_{dz}(s)} \frac{[cm]}{[V]} = \frac{\mu}{s(1+sT_m)} \tag{20.3}$$

where μ $[cm/V]$ is the static gain and T_m $[s]$ is the motor mechanical time constant. The scheme of the whole actuator is presented in Figure 20.3, with a complete definition of signals.

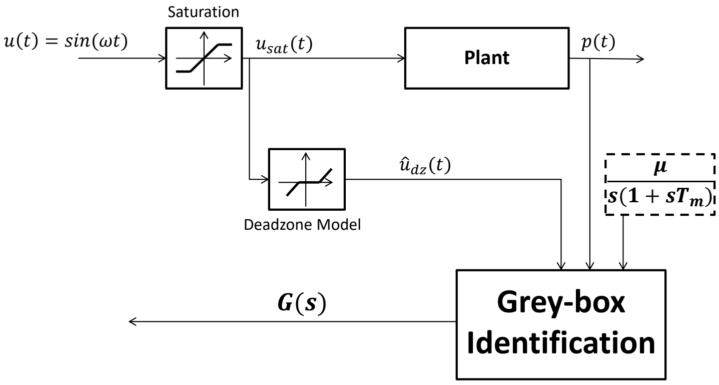

FIGURE 20.4: Conceptual block scheme for grey-box identification.

Under the hypothesis of having the nonlinearity confined to deadzone and saturation, and that the model of the deadzone is sufficiently reliable, a grey-box identification can be setup (see Figure 20.4) to define proper values for the parameters of the above physically based model. The dataset can be obtained in three steps:

- inject a series of sinusoidal inputs $u(t) = sin(\omega t)$ at different frequencies ω into the motor (avoiding saturation) and collect the position $p(t)$ as output;
- apply the same input to the deadzone model to obtain an estimate of $u_{dz}(t)$. Let this signal be defined as $\hat{u}_{dz}(t)$;
- build the input-output dataset with $\hat{u}_{dz}(t)$ as input and $p(t)$ as output signals.

With the help of Matlab Identification Toolbox [33], the estimated values for the parameters in $G(s)$ are:

$$\begin{aligned} \mu &= 15.3187\ cm/V \\ T_m &= 0.2920\ s \end{aligned}$$

The validation is performed by comparing the predicted to the real position signals as depicted in Figure 20.5.

It is important to note that a state space model in the form

$$\begin{cases} \dot{\mathbf{x}}(t) & = \mathbf{A}\mathbf{x}(t) + \mathbf{B}u_{dz}(t) \\ y(t) & = \mathbf{C}\mathbf{x}(t) \\ \mathbf{x}_0 & = \mathbf{x}(0),\ t \geq 0 \end{cases}$$

will be used in the development of both MPC controllers in the paper, therefore an additional step is required to move from the transfer function model to the state space (realisation). It follows:

$$\mathbf{x}(t) = \begin{bmatrix} p(t) \\ v(t) \end{bmatrix} \quad \mathbf{A} = \begin{bmatrix} 0 & 1 \\ 0 & \frac{-1}{T_m} \end{bmatrix} \quad \mathbf{B} = \begin{bmatrix} 0 \\ \frac{\mu}{T_m} \end{bmatrix} \quad \mathbf{C} = \begin{bmatrix} 1 & 0 \end{bmatrix} \tag{20.4}$$

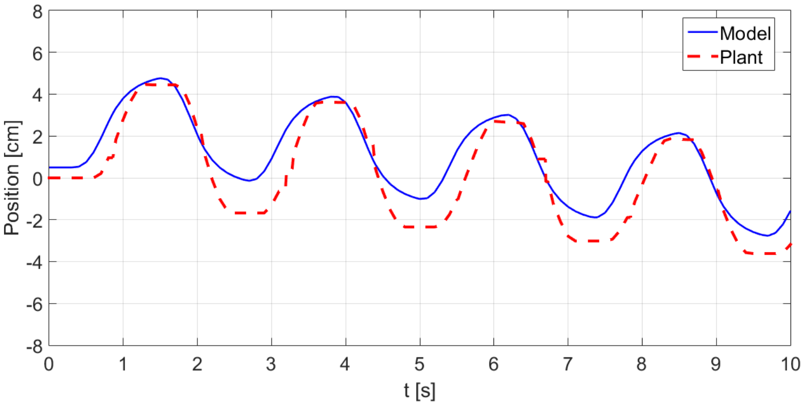

FIGURE 20.5: Validation of $G(s)$. The dashed, red line is the real position from the Plant, the solid, blue line is the predicted position from $G(s)$.

Since the control will be developed in a discrete-time framework, it is also necessary to discretise the system. A sample time $T_s = 0.1\ s$ is chosen according to the model time constant T_m and Nyquist theorem. Note that MPC controllers may be quite demanding in terms of computation time, therefore a conservative choice is made in this respect. In the following of the paper reference will be made to the discrete time versions of matrices $\mathbf{A}, \mathbf{B}, \mathbf{C}$ as $\mathbf{A}_d, \mathbf{B}_d, \mathbf{C}_d$ obtained with a Zero-Order Hold approximation:

$$\mathbf{A}_d = e^{\mathbf{A}T_s} \quad \mathbf{B}_d = \mathbf{B}\int_0^{T_s} e^{\mathbf{A}\tau} d\tau \quad \mathbf{C}_d = \mathbf{C} \tag{20.5}$$

Chapter 21

MPC General Framework

This section is devoted to a preliminary definition of the MPC controller which will be extended as Hybrid or ES one in the following of the paper. Let J be the general cost function as defined in (21.1), with p_r the position reference signal and $Q \geq 0$, $R > 0$, $N > 0$ generally defined parameters which will be specified for the Hybrid (subscript "h") and ES (subscript "es") cases.

$$J(\mathbf{x}(k), \mathbf{u}_{[k,...,k+N-1]}, N) = \sum_{i=0}^{N-1} (||\mathbf{C}_d \mathbf{x}(k+i) - p_r||_Q^2 + ||u(k+i)||_R^2) \tag{21.1}$$

where $\mathbf{u}_{[k,...,k+N-1]} = [u(k), ..., u(k+N-1)]$ is the future control sequence defined from instant k and $||\mathbf{g}||_{\mathbf{M}}^2$ is the square norm of a vector $\mathbf{g}$ weighted by a matrix $\mathbf{M}$. Then the resulting Finite Horizon Optimal Control Problem (FHOCP) at time instant k is reported in (21.2)-(21.4).

$$\begin{aligned} & min_{\mathbf{u}_{[k,...,k+N-1]}} J(\mathbf{x}(k), \mathbf{u}_{[k,...,k+N-1]}, N) \\ & subject\ to \end{aligned} \tag{21.2}$$

$$\mathbf{x}(k+1) = \mathbf{A}_d \mathbf{x}(k) + \mathbf{B}_d u(k) \tag{21.3}$$

$$\begin{gathered} \begin{bmatrix} p_{min} \\ v_{min} \end{bmatrix} \leq \mathbf{x}(k) \leq \begin{bmatrix} p_{max} \\ v_{max} \end{bmatrix} \\ u_{min} \leq u(k) \leq u_{max} \\ \forall k = 1, \ldots, N-1 \end{gathered} \tag{21.4}$$

The constraint values are defined according to hardware limitations and experimental considerations:

$$\begin{aligned} p_{min} &= -16\ cm \quad p_{max} = 16\ cm \\ v_{min} &= -5\ cm/s \quad v_{max} = 5\ cm/s \\ u_{min} &= -9\ V \quad u_{max} = 9\ V \end{aligned} \tag{21.5}$$

Let $\mathbf{u}^*_{[k,...,k+N-1|k]}$ be the optimal solution of the FHOCP at time instant k. The RH principle is then applied so that the actual control action given as output, $u_{mpc}(k)$, is the first element of the optimal control sequence $\mathbf{u}^*_{[k,...,k+N-1|k]}$. When the solution to the optimisation problem requires more time than available, it is possible to rely on the Explicit implementation of the MPC: the optimisation is solved *offline*, and the solution is parametrised with respect to the initial condition of the system and to the setpoint. In the following subsection the fundamental results for multi-parametric programming and Explicit MPC [84] are briefly reported.

21.1 Multiparametric Programming and Explicit MPC

Explicit MPC requires to solve the FHOCP (21.2)-(21.4) offline for every combination of initial conditions $\mathbf{x}(k)$ and position references p_r satisfying the constraints (recall that p_r is the position reference and must be therefore subject to $p_{min} \leq p_r \leq p_{max}$). Let then define $\gamma(k) = [\mathbf{x}(k)^\top \ p_r]^\top$ as the vector of parameters for the optimisation problem with the associate set of constraints. The optimal control action must then be *parametrised* with respect to $\gamma(k)$ (i.e. the dependency of $u_{mpc}(k)$ on $\gamma(k)$ is made *explicit*). An explicit implementation of MPC means then solving a *multi-parametric programming problem*.

21.1.1 Multiparametric Programming

Consider a general mathematical program:

$$\begin{aligned} J^*(\gamma) =& min_{\mathbf{u}} J(\gamma, \mathbf{u}); \\ & subject\ to: \\ & g(\gamma, \mathbf{u}) \leq 0 \end{aligned} \tag{21.6}$$

where $\mathbf{u}$ is the optimisation vector and γ is the vector of parameters.
Multiparametric programming aims at studying the behaviour of the value function $J^*(\gamma)$ and the optimizer $\mathbf{u}^*(\gamma)$ as the parameters γ vary. The result is a partitioning of the parameter space in *critical regions*: in each critical region the optimality conditions do not change, so that $\mathbf{u}^*$ can be straightforwardly expressed in terms of γ. Let Γ_f be the set of parameters for which (21.6) is feasible, and let Γ_i be polyhedral subsets of Γ_f such that $\bigcup_i \Gamma_i = \Gamma_f$. Each Γ_i is then associated to a closed form formula that allows to compute the value of the optimiser $\mathbf{u}^*(\gamma)$ whenever $\gamma \in \Gamma_i$.
When addressing a Quadratic Programming (QP) problem like (21.2)-(21.4), special properties of $J^*(\gamma)$ and $\mathbf{u}^*(\gamma)$ can be derived: Theorem 1 summarises the main results for multiparametirc Quadratic Programming (mp-QP) [85].

Theorem 1. *Consider the multiparametric quadratic program*

$$\begin{aligned} J^*(\gamma) =& min_{\mathbf{u}} \frac{1}{2}\mathbf{u}^\top \mathbf{H}\mathbf{u} + \gamma^\top \mathbf{F}^\top \mathbf{u} + \frac{1}{2}\gamma^\top \mathbf{Y}\gamma \\ & subject\ to: \\ & \mathbf{G}\mathbf{u} \leq \mathbf{W} + \mathbf{S}\gamma \end{aligned} \tag{21.7}$$

with γ the vector of parameters and $\mathbf{u}$ the vector of optimisation variables. Then the set Γ_f of parameters γ for which the problem is feasible is a polyhedral set, the value function J^* is continuous, convex, and piecewise quadratic, and the optimizer $\mathbf{u}^*$ is piecewise affine and continuous.

21.1.2 Explicit MPC

It is straightforward to show that (21.1) can be rewritten as proposed in (21.7) by setting:

$$\begin{aligned} \mathbf{u}(k) &= [u(k)\ u(k+1)\ \dots\ u(k+N-1)]^\top \\ \gamma(k) &= [\mathbf{x}(k)^\top\ p_r]^\top \end{aligned}$$

where the dependence of **u** and γ on the time instant k is introduced.
According to Theorem 1, the MPC controller obtained from (21.2)-(21.4) can then be represented in a totally equivalent way as:

$$u_{mpc}(\gamma(k)) = \mathbf{f}_i\gamma(k) + \mathbf{g}_i \ \text{ if } \ \gamma(k) \in \Gamma_i \tag{21.8}$$

where Γ_i are polyhedral subsets of Γ_f, $\mathbf{f}_i$ and $\mathbf{g}_i$ are a vector of proper size and a scalar defining the affine control law over the subset Γ_i. Once the explicit solution is available, online computations at time instant k are reduced to:

- find $\Gamma_{\bar{i}}$ such that $\gamma(k) \in \Gamma_{\bar{i}}$;
- compute $u_{mpc}(\gamma(k)) = \mathbf{f}_{\bar{i}}\gamma(k) + \mathbf{g}_{\bar{i}}$.

This result can be straighfowardly applied to ES. Still, some further consideration must be introduced for the Hybrid case, where the presence of binary variables forces to solve a Mixed-Integer Quadratic Programming problem (MIQP).

21.1.3 Explicit Hybrid MPC

When dealing with Hybrid MPC, the optimisation vector contains binary variables and the associated explicit formulation requires to solve a multiparametric MIQP (mp-MIQP). In this case, the partition associated to Γ_f may be non-polyhedral. To overcome this problem, it is possible to consider the mp-MIQP problem as being composed of a number of standard mp-QP subproblems, each one characterised by a possible combination of the values of binary variables. According to Theorem 1, a polyhedral partition of Γ_f is associated to each mp-QP subproblem. Note that in this case regions associated to different subproblems can overlap (i.e. $\gamma(k)$ can fall in more than a single region Γ_i). Possible Γ_i overlapping are maintained and the value of function J^* on each Γ_i must be stored.
The optimiser can be retrieved online as follows [77]:

- find all candidate regions Γ_i such that $\gamma(k) \in \Gamma_i$;
- compute J_i^* for all candidate regions;
- find the region $\Gamma_{\bar{i}}$ associated to $J_{\bar{i}}^* = min_i\,(J_i^*) = J^*$;
- compute $u_{mpc}(\gamma(k)) = \mathbf{f}_{\bar{i}}\gamma(k) + \mathbf{g}_{\bar{i}}$.

Remark: Matlab Hybrid Toolbox was used to formulate the MPC optimisation problems (both the QP and the MIQP) as multiparametric ones. As described in 20, Matlab Real Time Toolbox was used to communicate with the Arduino boad and drive the overhead travelling crane. Still, Explicit Controllers made available by the Hybrid Toolbox can not be used in such a real-time environment. A Matlab function was then developed to implement the online computations necessary to retrieve the optimiser from the solution of the multiparametric programming problem, as described in this Section. This controller is based on a point location algorithm to recover the control law, ensuring that the optimal control move is applied to the plant at any time instant.

21.2 Kalman Filter and Speed Estimation

Since only the encoder output (position) is available, an observer is needed to provide the MPC controller an estimation of the whole state. For this purpose, a steady-state Kalman filter is included in the control scheme. Let introduce process and measurement noise, respectively $\mathbf{w}(k)$ and $n(k)$, in the description of the system:

$$\begin{cases} \mathbf{x}(k+1) & = \mathbf{A}_d\mathbf{x}(k) + \mathbf{B}_d u_{dz}(k) + \mathbf{w}(k) \quad \mathbf{x}(0) = \mathbf{x}_0 \\ y(k) & = \mathbf{C}_d\mathbf{x}(k) + n(k) \end{cases} \tag{21.9}$$

Let $\mathbf{w}(k)$ be white, Gaussian with zero mean and covariance $\mathbf{Q}_k = 0.1\mathbf{I}_{2\times 2}$. Analogously, let $n(k)$ be white, Gaussian with zero mean and covariance $R_k = 1$. Let also assume that the two noises are not correlated. Note that u_{dz} (see Figure 20.3) represents a sort of "effective input voltage" and is not an existing, measurable signal: the Kalman filter is then fed by its estimation, $\hat{u}_{dz}(k)$, coming from the deadzone model. This implies that $\mathbf{w}(k)$ must also take into account model uncertainty of the deadzone block. Provided that the pair $(\mathbf{A}_d, \mathbf{B}_q)$, with $\mathbf{B}_q$ such that $\mathbf{Q}_k = \mathbf{B}_q\mathbf{B}_q^\top$, is reachable and that the pair $(\mathbf{A}_d, \mathbf{C}_d)$ is observable, the optimal state estimator [70] is then given by:

$$\begin{aligned} \hat{\mathbf{x}}(k+1|k+1) = {} & \mathbf{A}_d\hat{\mathbf{x}}(k|k) + \mathbf{B}_d\hat{u}_{dz}(k) + \\ & + \mathbf{L}[y(k+1) - \mathbf{C}_d(\mathbf{A}_d\hat{\mathbf{x}}(k|k) + \mathbf{B}_d\hat{u}_{dz}(k))] \end{aligned} \tag{21.10}$$

with

$$\mathbf{L} = \overline{\mathbf{P}}\mathbf{C}_d^\top[\mathbf{C}_d\overline{\mathbf{P}}\mathbf{C}_d^\top + R_k]^{-1}$$

where $\overline{\mathbf{P}}$ is the unique positive definite solution of the stationary Riccati Equation

$$\mathbf{P} = \mathbf{A}_d\mathbf{P}\mathbf{A}_d^\top + \mathbf{Q}_k - \mathbf{A}_d\mathbf{P}\mathbf{C}_d^\top[\mathbf{C}_d\mathbf{P}\mathbf{C}_d^\top + R_k]^{-1}\mathbf{C}_d\mathbf{P}\mathbf{A}_d$$

Now it is possible to implement an MPC algorithm based on the state estimation provided by the steady-state Kalman filter.

Chapter 22

Simulations and Experiments

22.1 Hybrid MPC Controller

The first control approach under investigation is the Hybrid MPC, since it allows to straightforwardly include the presence of the deadzone in the model used in the MPC by relying on the so called *Mixed Logical Dynamics* (MLD) formulation:

$$\begin{cases} \mathbf{x}(k+1) & = \mathbf{A}_d\mathbf{x}(k) + \mathbf{B}_{d1}u(k) + \mathbf{B}_{d2}\delta(k) + \mathbf{B}_{d3}\mathbf{z}(k) \\ y(k) & = \mathbf{C}_d\mathbf{x}(k) + \mathbf{D}_{d1}u(k) + \mathbf{D}_{d2}\delta(k) + \mathbf{D}_{d3}\mathbf{z}(k) \\ \mathbf{E}_2\delta(k) + \mathbf{E}_3\mathbf{z}(k) & \leq \mathbf{E}_1u(k) + \mathbf{E}_4\mathbf{x}(k) + \mathbf{E}_5 \end{cases} \tag{22.1}$$

where $\mathbf{x}(k)$ is the state vector of the system, $u(k)$ is the input, $y(k)$ is the output, $\delta(k)$ is a vector of auxiliary binary variables and $\mathbf{z}(k)$ is a vector of continuous auxiliary variables. $\mathbf{A}_d, \mathbf{B}_{d1}, \mathbf{B}_{d2}, \mathbf{B}_{d3}, \mathbf{C}_d, \mathbf{D}_{d1}, \mathbf{D}_{d2}, \mathbf{D}_{d3}, \mathbf{E}_1, \mathbf{E}_2, \mathbf{E}_3, \mathbf{E}_4, \mathbf{E}_5$ are matrices of proper size. It is possible to show that binary variables work as boolean ones under a proper set of constraints [77]: this allows to introduce logical conditions in system dynamics. Equation (22.1) is then part of the constraints in the MPC optimisation problem, which results in a Mixed-Integer Problem (MIP). Note that this class of problems is computationally demanding and ad hoc solvers [86, 87] are needed to obtain a proper solution. As a consequence, the horizon N_h of the Hybrid MPC is tipically limited, in particular when the adopted sampling time is short, leaving a short time for the online computation of the optimal control sequence.

22.1.1 Problem Formulation

A Hybrid model including the deadzone in the system dynamics will be now derived. Consider the deadzone definition (20.1): this represents a piecewise-affine function defined over three regions. It is then possible to introduce three *binary* variables $\delta_1(k), \delta_2(k)$ and $\delta_3(k)$ and associate each of them to one of the possible regions of the deadzone as in Figure 22.1. The additional constraint of having a single $\delta_i(k)$ valued "1" at each time instant k must be introduced as well:

$$\begin{aligned} u(k) \geq high &\implies \delta_1(k) = 1 \\ low < u(k) < high &\implies \delta_3(k) = 1 \\ u(k) \leq low &\implies \delta_2(k) = 1 \\ \delta_1(k) + \delta_2(k) + \delta_3(k) &= 1 \end{aligned} \tag{22.2}$$

Note that (22.2) can be rewritten according to the notation in (22.1) by properly defining the $\mathbf{E}_1, \mathbf{E}_2, \mathbf{E}_3, \mathbf{E}_4, \mathbf{E}_5$ matrices.

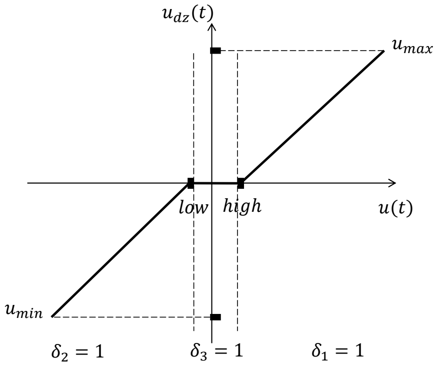

FIGURE 22.1: A generic deadzone acting on signal $u(k)$ as a piecewise-affine function associated to logical conditions.

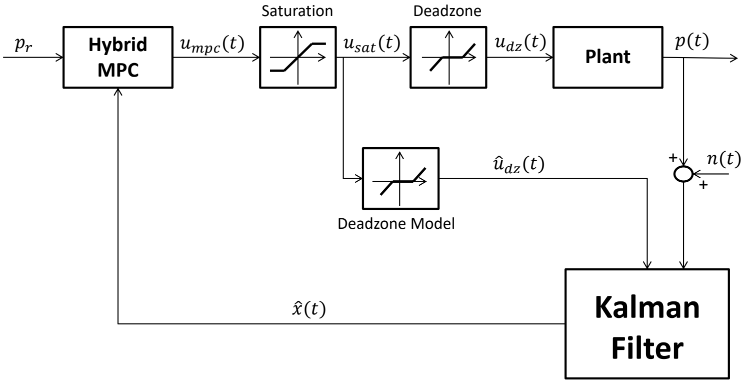

FIGURE 22.2: Block scheme for Hybrid MPC approach.

The Hybrid MPC controller is then defined by introducing the Q_h, R_h, N_h parameters in (21.1) and replacing the dynamics constraints of (21.4) with (22.1), where:

$$\mathbf{z}(k) = \delta(k)u(k)$$

$$\begin{aligned} \mathbf{B}_{d1} &= \mathbf{B}_d \\ \mathbf{B}_{d2} &= \begin{bmatrix} -\mathbf{B}_d high & -\mathbf{B}_d low & \mathbf{0}_{2\times 1} \end{bmatrix} \\ \mathbf{B}_{d3} &= \begin{bmatrix} \mathbf{0}_{2\times 2} & -\mathbf{B}_d \end{bmatrix} \\ \mathbf{D}_{d1} &= 0 \quad \mathbf{D}_{d2} = 0 \quad \mathbf{D}_{d3} = 0 \end{aligned} \tag{22.3}$$

Remark: The definition of $\mathbf{E}_1, \mathbf{E}_2, \mathbf{E}_3, \mathbf{E}_4, \mathbf{E}_5$, which account for (22.2) is not reported here. The controllers are in fact implemented using Matlab Hybrid Toolbox [77], that allows the user to work with *logic* variables and automatically performs the substitution with *binary* ones by introducing the necessary constraints. The overall control scheme is depicted in Figure 22.2. *Remark*: The controller is implemented in the *explicit* way, as described in 21.1.3.

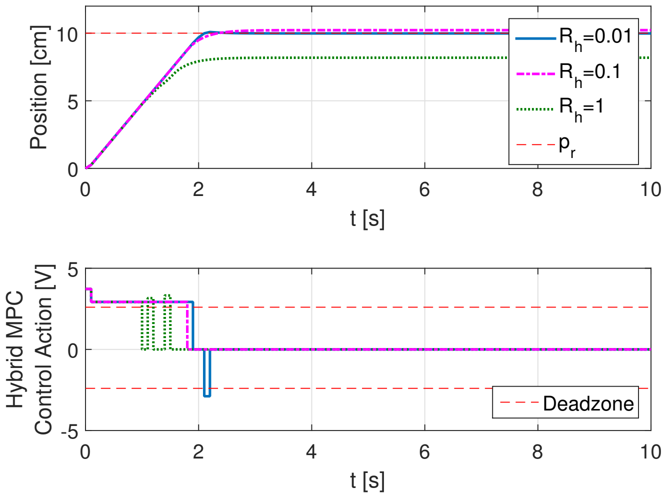

FIGURE 22.3: Hybrid MPC. Above: plot of simulated position $p(t)$.
Below: plot of simulated MPC control action $u_{mpc}(t)$.

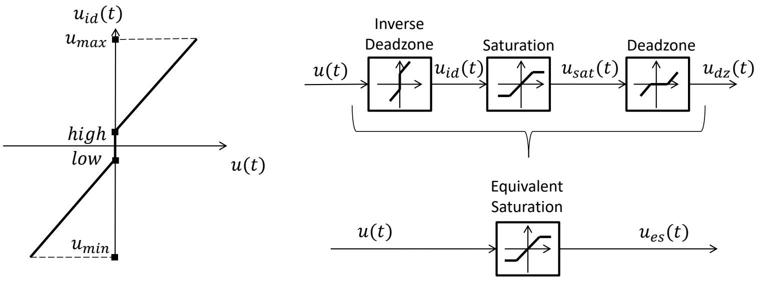

FIGURE 22.4: Left: inverse deadzone applied to a generic signal $u(t)$.
Right: equivalence of signals $u_{es}(t)$ and $u_{dz}(t)$.

22.1.2 Simulations

A set of simulations allows to define a first tuning of MPC parameters Q_h, R_h, N_h. Measurement noise is included in the simulations as a bounded random number generator in the interval $[-0.1; 0.1]$ to mimic the encoder limited resolution. The Kalman filter is used for state estimation, as discussed in 21.2. The explicit MPC computational honour limits $N_h = 5$. Control should be tuned as to reach the desired setpoint with the highest precision as possible while avoiding any oscillation or abrupt motion that can be dangerous for the load or for the crane structure itself. A settling time of few seconds is admissible. The best tuning is then obtained with $Q_h = 1, R_h = 0.01, N_h = 5$. Figure 22.3 shows the plot of signals $p(t)$ and $u_{mpc}(t)$ according to scheme in Figure 22.2, with different values of R_h. The solid, blue lines depict the signals of the chosen tuning. The position reaches the setpoint with no oscillations and with a very limited steady state error even in presence of measurement noise. The settling time is about 2 s. Note that higher values of R_h result in a steady-state tracking error.

22.2 MPC with Equivalent Saturation

This section focuses on the implementation of a constrained MPC controller based on the approach suggested in [74]. In particular, with the deadzone definition in

(20.1), it is possible to define the *Inverse Saturation* (see Figure 22.4.a) as follows:

$$u_{id}(t) = \begin{cases} u(t) + high & \text{if } u(t) > 0 \\ 0 & \text{if } u(t) = 0 \\ u(t) + low & \text{if } u(t) < 0 \end{cases} \tag{22.4}$$

Let the real plant saturation be defined as in (20.2), then it is possible to show that $u_{dz}(t)$, the fictitious signal after the cascade *Inverse deadzone - Saturation - Deadzone*, is equivalent to $u_{es}(t)$ (See Figure 22.4.b), which is defined as:

$$u_{es}(t) = \begin{cases} u_{max} - high & \text{if } u(t) \geq u_{max} - high \\ u(t) & \text{if } u_{min} - low < u(t) < u_{max} - high \\ u_{min} - low & \text{if } u(t) \leq u_{min} - low \end{cases} \tag{22.5}$$

This means that the MPC can be built as if the plant showed a simple saturation, therefore a constrained MPC can be enough to face the situation. This reduced computational complexity allows to increase the prediction horizon, which in turn helps improving the stability of the system [70].

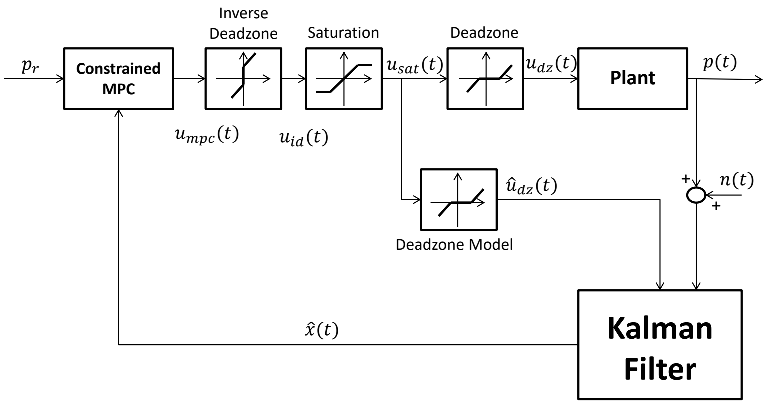

FIGURE 22.5: Block scheme for ES MPC approach.

22.2.1 Problem Formulation

This section will be devoted to the definition of the constrained MPC controller based on the ES approach. Figure 22.5 shows the overall control scheme for the ES MPC. Let J_{es} be the cost function as defined in (21.1), where Q_{es}, R_{es}, N_{es} are introduced. Then the resulting FHOCP is defined by replacing the saturation limits of (21.4) with the equivalent saturation ones:

$$u_{min} - low \leq u(k) \leq u_{max} - high \tag{22.6}$$

Remark: The controller is implemented in the *explicit* way, as described in 21.1.

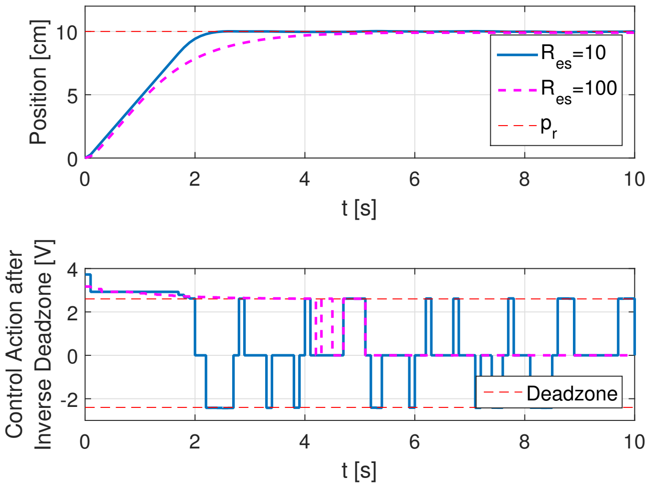

FIGURE 22.6: ES MPC. Above: plot of simulated position $p(t)$. Below: plot of simulated control action $u_{id}(t)$.

22.2.2 Simulations

As for the Hybrid MPC, the first step is defining a base tuning for Q_{es} and R_{es} parameters by means of simulations. The prediction horizon N_{es} is initially set to 10 steps. According to the control specifications presented in 22.1.2, the best results are obtained by setting $Q_{es} = 1, R_{es} = 10, N_{es} = 10$. Note that the two MPC control schemes are built upon different systems: similar (Q_h, R_h) and (Q_{es}, R_{es}) couples would produce very different results. It is therefore not surprising that very different tunings are needed to provide similar performances of the two control schemes. Figure 22.6 shows plots for the position $p(t)$ and control input $u_{id}(t)$ to the plant for different values of R_{es}. A solid, blue line is used for the chosen tuning. Simulations are performed including measurement noise on $p(t)$ and the Kalman filter. The adopted control strategy manages to bring the load to the setpoint in about 2 s, without any appreciable oscillation despite of measurement noise. Still, some chattering is present in the control action: note that this control voltage is actually given as output, but has no effect on the plant because of the deadzone.

22.3 Robustness with Respect to Deadzone Model Uncertainties

This section is devoted to an evaluation of the performances of the two control schemes introduced before when some uncertainty is present in the deadzone model. In particular, focus is on the case where the deadzone width is overestimated, since the authors expect this to be closely represent our situation (20.1). The study is performed by means of simulations where a constant error is introduced in the deadzone limits, so that the real deadzone is:

$$u_{dz}(t) = \begin{cases} u(t) - 2.4 & \text{if } u(t) \geq 2.4 \\ 0 & \text{if } -2.1 < u(t) < 2.4 \\ u(t) + 2.1 & \text{if } u(t) \leq -2.1 \end{cases} \tag{22.7}$$

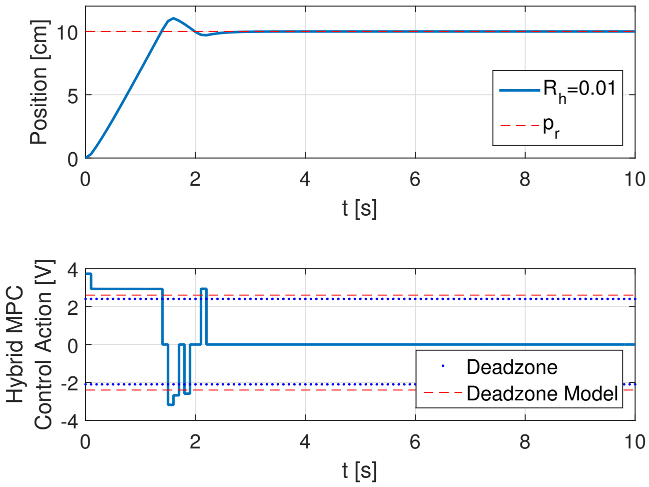

FIGURE 22.7: Hybrid MPC with uncertain deadzone. Above: plot of simulated position $p(t)$. Below: plot of simulated MPC control action $u_{mpc}(t)$.

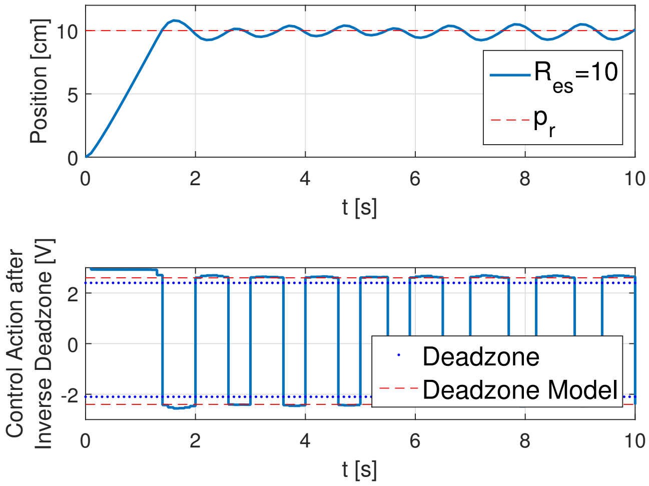

FIGURE 22.8: ES MPC with uncertain deadzone. Above: plot of simulated position $p(t)$. Below: plot of simulated control action $u_{id}(t)$.

22.3.1 Hybrid MPC

Figure 22.7 shows the behaviour of the Hybrid MPC controller as tuned in 22.1.2 in presence of deadzone model uncertainties. Some oscillations are present in $p(t)$. They are due to the combined action of deadzone uncertainty and measurement error. Still, after the initial transient, the signal settles around the setpoint with a tolerable error. No re-tuning is then needed in the Hybrid case.

22.3.2 Equivalent Saturation MPC

The behaviour of the ES MPC controller is reported in Figure 22.8. The result is not admissible since the position is always oscillating. This requires a re-tuning phase of the controller. The new weights are $Q_{es} = 1, R_{es} = 1000, N_{es} = 10$. *Remark:* Note that a chattering removal strategy is introduced by placing a small threshold ($u_{th} = 0.01V$) on the control signal $u_{id}(t)$, which is set to zero whenever its magnitude does not overcome the threshold. The need for this kind of algorithm was suggested by [79] and [73] to deal with the discontinuity in the deadzone inverse,

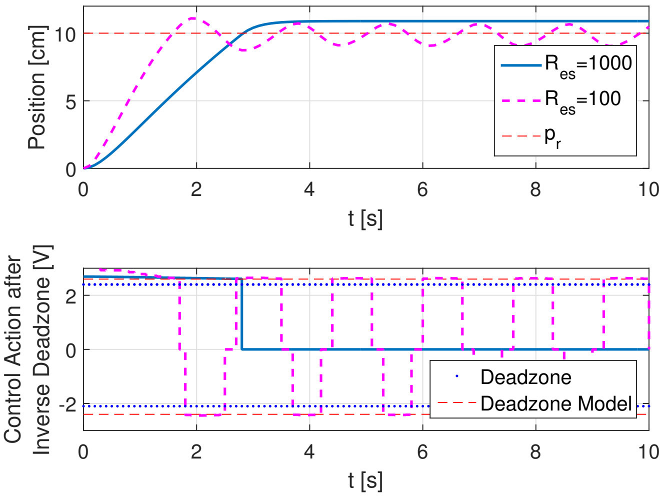

FIGURE 22.9: ES MPC with uncertain deadzone (re-tuning). Above: plot of simulated position $p(t)$. Below: plot of simulated control action $u_{id}(t)$.

which contributes to the chattering. After the re-tuning phase, simulations are repeated and results are reported in Figure 22.9. The results from the chosen tuning is depicted with a blue, solid line. Oscillations have been removed to the price of an increased steady-state error which is not negligible. Chattering of the control action has been removed as well. Note that $R_{es} = 100$ (dashed, magenta line in Figure 22.9) is not sufficient to ensure no permanent oscillations in the response. The increase of N_{es} instead does not introduce any appreciable improvement of the performance of the controller.

22.3.3 Comparison and Remarks

The results of simulations presented in this section suggest that the Hybrid controller outperforms the ES controller in presence of deadzone model uncertainties. Note that ES strategy is more likely to work just around the limits of the deadzone, therefore a moderate or even null predicted control action may result in an appreciable real one because of deadzone overestimation (see Figure 22.8). This generates the wide oscillations of the position seen in Figure 22.8. In the case of ES MPC, the problem is mitigated by introducing the anti-chattering technique. The second correction needed by ES is the increase of R_{es}, that has the effect of reducing the aggressiveness of the control action. Both modifications have as drawback degraded steady-state performances. The Hybrid controller is instead more "conservative" by construction: it in fact weights in J_h the actual voltage control action $u_{mpc}(t)$. On the contrary, the ES strategy weights in J_{es} the deviation of the control action from the deadzone (model) limit, $\hat{u}_{dz}(t)$, while the voltage "boost" from the inverse deadzone block comes at no price.

22.4 Experimental Results

The performances of the two controllers with real experiments on the overhead travelling crane are evaluated in this section. Loop closure is obtained by interfacing the Arduino platform to Matlab Real Time Toolbox: a UDP style packets exchange is setup to collect measures from the encoder and to deliver the control action to the

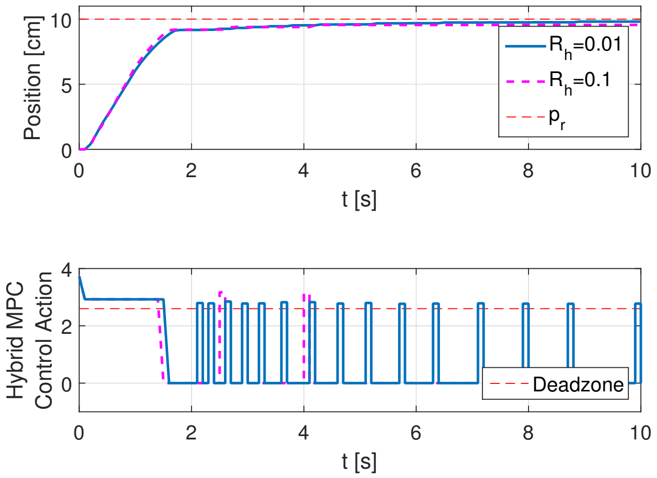

FIGURE 22.10: Hybrid MPC real experiments. Above: plot of position $p(t)$. Below: plot of MPC control action $u_{mpc}(t)$.

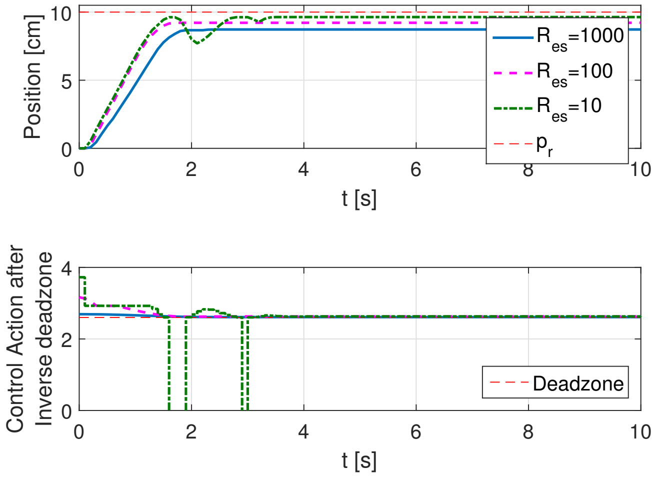

FIGURE 22.11: ES MPC real experiments. Above: plot of position $p(t)$. Below: plot of actual control action $u_{id}(t)$.

DC motor. The control schemes are those used for simulations, with the Kalman filter discussed in 21.2 used for load speed estimation.

22.4.1 Hybrid MPC

Figure 22.10 shows the plot of signals $p(t)$ and $u_{mpc}(t)$, according to the control scheme presented in Figure 22.2, with different R_h values. The solid, blue line is obtained with parameters defined in simulation (22.3.1). The magenta, dashed line is related to a re-tuning of the controller with the following parameters: $Q_h = 1, R_h = 0.1, N_h = 5$. Note that the responses of the two controllers is quite similar, with the $R_h = 0.01$ case providing a better steady-state error but with long settling time. The $R_h = 0.1$ case instead provides a tolerable steady state error (about 3 %), which is definitively reached in about 4 s. This is consistent with what stated in the previous sections: a higher value of R_h makes the controller admit some steady-state error but increases the robustness of the controller: no oscillations are in fact present in the transient response with the Hybrid controller.

22.4.2 Equivalent Saturation MPC

The results obtained with the ES MPC controller with anti-chattering, as tuned in 22.3.2, are now presented (see Figure 22.11, solid, blue line). Note that a wide steady state error is present in the closed-loop response. As discussed before, this is due to a high value of R_{es} parameter. A new tuning is done with the goal of obtaining a tolerable steady-state error while avoiding the presence of oscillations. Figures 22.11 depicts the new results obtained with ES MPC parameters set to $Q_{es} = 1, R_{es} = 100, N_{es} = 10$ (magenta, dashed line), and $Q_{es} = 1, R_{es} = 10, N_{es} = 10$ (green, dotted line). The steady-state error is again too wide to be of any practical interest in the $R_{es} = 100$ case. Some oscillation is instead present in the $R_{es} = 10$ response, but the steady-state error (about 5 %) can now be comparable to that obtained with the Hybrid MPC. Any further decrease of R_{es} introduces wider oscillations which may be dangerous for the plant. It is also important to point out that the input signal to the plant ($u_{id}(t)$) is always non-zero, despite of the anti-chattering strategy which places a threshold on the minimum control action coming from the MPC. This means that the controller is actually giving some voltage to the plant, but this is not enough to make the load move. Figure 22.11 clearly shows how the control action $u_{id}(t)$ is really close to the boundary of the deadzone model, which is uncertain. In this case, even if the deadzone was defined in a conservative way, some unmodelled nonlinearity prevents the load from moving.

Chapter 23

Conclusions and Future Work

This paper compares the performance of an Hybrid MPC controller to those of an Equivalent Saturation MPC by means of simulations and real experiments. The results suggest that the two controllers can be tuned to obtain similar behaviours. Still, the Hybrid MPC seems to be more robust with respect to model uncertainties, since it seldom works around the limits of the deadzone. As a consequence, the Hybrid controller does not practically require any heavy retuning while moving from simulations to the real, uncertain environment. This is instead the case of ES MPC, which is typically working around the limits of the deadzone, thus resulting less robust to model uncertainties. Also note that unmodelled nonlinearities introduce oscillations in the ES responses. For this particular case it is then possible to state that Hybrid MPC outperforms the ES one. Still, the ES MPC controller shows a reduced computational complexity, which allows to introduce a longer horizon and -possibly-terminal weight and constraint. Longer horizons may in fact help to preserve feasibility of the FHOCP and therefore stability of the closed-loop [70]. This is where ES may introduce some noticeable advantage. Some further investigation is then needed to evaluate the two schemes with final weight and constraint: this is left as future work.

Chapter 24

Conclusion

In this Thesis, control theory techniques were successfully applied in very different applications, in the context of Industry 4.0. In particular, three different control problems were faced with frequency domain, optimal and model predictive control approaches: magnetic field regulation in FFC NMR experiments, service pressure regulation in WDNs and control of a laboratory scale overhead travelling crane affected by deadzone nonlinearity.

The problem of magnetic field regulation in FFC NMR was faced with the Field Frequency Lock approach: a parallel NMR experiment allows to sense every magnetic field deviation from the resonance condition. A PID regulator was tuned to close the control loop with the signal provided by the NMR sensor. To this end, a digital twin of the whole process was developed, with a combination of physically based models (mainly for NMR) and grey box transfer function models identified from experimental data. The digital twin was then exploited both to optimise the design of the NMR sensor, and to develop the PID control strategy. Finally, the closed-loop approach was successfully tested on the real plant, thus allowing to improve the results obtained from FFC NMR experiments.

As for the previous case study, a digital twin of the process was available to study service pressure regulation in WDNs , with both frequency domain and optimal control strategies working at high sampling rates. In this case, the control performance of the different control algorithms was evaluated by accounting for both regulation error and cost of control. A careful tuning procedure, based on local, linear models of the process allowed to reach a satisfactory balance of the above requirements. In particular, this work highlighted the need for models characterised by high order to properly capture the high frequency behaviour of the plant and develop strategies to improve robustness and performance of the overall closed-loop.

Finally, two different MPC algorithms were developed to control the chart of a laboratory scale overhead travelling crane, whose actuators are affected by a severe deadzone. The two algorithms were based on the two different approaches to handle the nonlinearity: on one side, a hybrid MPC embeds a model of the deadzone in the system description, resulting in a Mixed Integers optimisation problem; on the other side, a nonlinearity inversion block is used to compensate for the effect of the deadzone, and a constrained linear MPC is introduced which only takes into account saturation of the control action. Simulations and experiments on the plant were performed to evaluate and compare the performances of the two control schemes, highlighting pros and cons of the two approaches.

In all cases, the work was carried out by adopting the Industry 4.0 approach. First, a digital twin of the plant was developed, starting from physical knowledge of the process and, when possible, on a number of field experiments for model identification and validation. The control strategies were then conceived and studied on the digital twin and finally applied to the real process (with the exception of the

WDN case study). Experimental trials provided control performances consistent with those expected from simulations. In this respect, satisfactory results were obtained in all the applications which were faced in this Thesis, thus stressing the importance and the positive impact of the application of control theory in the Industry 4.0 environment. In fact, while the Industry 4.0 approach opens wide possibilities in terms on sensing, communication and actuation capabilities, it also seeks after a proper application of control theory to get the best from these possibilities.

Bibliography

[1] M. Hermann, T. Pentek, and B. Otto. “Design principles for industrie 4.0 scenarios”. In: *2016 49th Hawaii international conference on system sciences (HICSS)*. IEEE. 2016, pp. 3928–3937.

[2] T. Stock and G. Seliger. “Opportunities of sustainable manufacturing in industry 4.0”. In: *Procedia Cirp* 40 (2016), pp. 536–541.

[3] Y. Liao et al. “Past, present and future of Industry 4.0-a systematic literature review and research agenda proposal”. In: *International journal of production research* 55.12 (2017), pp. 3609–3629.

[4] K. Zhou, T. Liu, and L. Zhou. “Industry 4.0: Towards future industrial opportunities and challenges”. In: *2015 12th International conference on fuzzy systems and knowledge discovery (FSKD)*. IEEE. 2015, pp. 2147–2152.

[5] S. Vaidya, P. Ambad, and S. Bhosle. “Industry 4.0–a glimpse”. In: *Procedia Manufacturing* 20 (2018), pp. 233–238.

[6] A. Gilchrist. *Industry 4.0: the industrial internet of things*. Apress, 2016.

[7] A. J.C. Trappey et al. “A review of essential standards and patent landscapes for the Internet of Things: A key enabler for Industry 4.0”. In: *Advanced Engineering Informatics* 33 (2017), pp. 208–229.

[8] J. Lee, H. Kao, and S. Yang. “Service innovation and smart analytics for industry 4.0 and big data environment”. In: *Procedia Cirp* 16 (2014), pp. 3–8.

[9] C. Yen et al. “Advanced manufacturing solution to industry 4.0 trend through sensing network and cloud computing technologies”. In: *2014 IEEE International Conference on Automation Science and Engineering (CASE)*. IEEE. 2014, pp. 1150–1152.

[10] M. Brettel et al. “How virtualization, decentralization and network building change the manufacturing landscape: An Industry 4.0 Perspective”. In: *International journal of mechanical, industrial science and engineering* 8.1 (2014), pp. 37–44.

[11] J. Lee, B. Bagheri, and H. Kao. “A cyber-physical systems architecture for industry 4.0-based manufacturing systems”. In: *Manufacturing letters* 3 (2015), pp. 18–23.

[12] N. Jazdi. “Cyber physical systems in the context of Industry 4.0”. In: *2014 IEEE international conference on automation, quality and testing, robotics*. IEEE. 2014, pp. 1–4.

[13] D. Ivanov et al. “A survey on control theory applications to operational systems, supply chain management, and Industry 4.0”. In: *Annual Reviews in Control* (2018).

[14] J. Keeler. *Understanding NMR spectroscopy*. John Wiley & Sons, 2011.

[15] J. P. Hornak. *The Basics of NMR. 1997*. Rochester Institute of Technology, Center for Imaging Science., 1997.

[16] N. E. Jacobsen. *NMR spectroscopy explained: simplified theory, applications and examples for organic chemistry and structural biology*. John Wiley & Sons, 2007.

[17] S. E. Van Bramer. "An Introduction to NMR Concepts". In: *Journal of Chemical Education* 79.4 (2002), p. 528.

[18] Elster A. D. and Burdette J. H. *Questions and Answers in Magnetic Resonance Imaging*. Mosby Inc, 1994.

[19] J. Samra. "A field-frequency lock implemented with a sampled-data feedback control algorithm derived from a small-signal NMR model". MA thesis. The Pennsylvania State University, 2008.

[20] S. Kan et al. "Automatic NMR field-frequency lock - pulsed phase locked loop approach". In: *Review of Scientific Instruments* 49.6 (1978), pp. 785–789.

[21] R. Kimmich. *Field-cycling NMR Relaxometry: Instrumentation, Model Theories and Applications*. Royal Society of Chemistry, 2018.

[22] G. Ferrante and S. Sykora. "Technical aspects of fast field cycling". In: *Adv Inorg Chem* 57 (2005), pp. 405–470.

[23] *Stelar website*. https://www.stelar.it/. Accessed: 2018-08-24.

[24] *Identify website*. https://www.identify-project.eu/. Accessed: 2018-08-24.

[25] G. Galuppini et al. "Towards a Model-Based Field-Frequency Lock for NMR". In: *IFAC-PapersOnLine* 50.1 (2017), pp. 13020–13025.

[26] G. Galuppini et al. "Towards a Model-Based Field-Frequency Lock for Fast-Field Cycling NMR". In: *Applied Magnetic Resonance* (2019), pp. 1–23.

[27] Colnago Luiz Alberto Bagueira de Vasconcelos Azeredo R. and M. Engelsberg. "Quantitative analysis using steady-state free precession nuclear magnetic resonance". In: *Analytical chemistry* 72.11 (2000), pp. 2401–2405.

[28] H.Y. Carr. "Steady-state free precession in nuclear magnetic resonance". In: *Physical Review* 112.5 (1958), p. 1693.

[29] E. L. Hahn. "Spin echoes". In: *Physical review* 80.4 (1950), p. 580.

[30] D.I. Hoult, R.E. Richards, and P. Styles. "A novel field-frequency lock for a superconducting spectrometer". In: *Journal of Magnetic Resonance* 30.2 (1978), pp. 351–365.

[31] D. Jiang et al. "The Digital Field-Frequency Lock System of High-Resolution NMR Spectrometer". In: *Electrical and Control Engineering (ICECE), 2010 International Conference on*. IEEE. 2010, pp. 2328–2331.

[32] P. Baldrighi et al. "Digital nuclear magnetic resonance acquisition channel". In: *2008 11th EUROMICRO Conference on Digital System Design Architectures, Methods and Tools*. IEEE. 2008, pp. 399–404.

[33] L. Ljung. *System identification toolbox: for use with MATLAB: user's guide*. Math Works, 1991.

[34] *IECO website*. http://www.ieco.fi/. Accessed: 2018-08-24.

[35] F. Bloch. "Nuclear induction". In: *Physical review* 70.7-8 (1946), p. 460.

[36] T. B. Moraesa and L. A. Colnago. "Simulação de Sinais de RMN Através das Equações de Bloch". In: *Quim. Nova* 37.8 (2014), pp. 1410–1416.

[37] T. Söderström and P. Stoica. *System identification*. Prentice-Hall, Inc., 1989.

[38] D. E Seborg et al. *Process dynamics and control*. John Wiley & Sons, 2010.

[39] *Xilinx website*. https://www.xilinx.com/. Accessed: 2018-08-24.

[40] M. Farley and S. Trow. *Losses in water distribution networks*. IWA publishing, 2003.

[41] J. Thornton and A. Lambert. "Managing pressures to reduce new breaks". In: *Water* 21.December 2006 (2006), pp. 24–26.

[42] A. Lambert, M. Fantozzi, and J. Thornton. "Practical approaches to modeling leakage and pressure management in distribution systems–progress since 2005". In: *Proceedings of the 12th Int. Conf. on Computing and Control for the Water Industry-CCWI2013*. 2013.

[43] T. M. Walski et al. *Advanced water distribution modeling and management*. Haestad press, 2003.

[44] S. L. Prescott and B. Ulanicki. "Improved control of pressure reducing valves in water distribution networks". In: *Journal of hydraulic engineering* 134.1 (2008), pp. 56–65.

[45] N. Fontana et al. "Real-Time Control of Pressure for Leakage Reduction in Water Distribution Network: Field Experiments". In: *Journal of Water Resources Planning and Management* 144.3 (2017), p. 04017096.

[46] N. Fontana et al. "Real-Time Control of a PRV in Water Distribution Networks for Pressure Regulation: Theoretical Framework and Laboratory Experiments". In: *Journal of Water Resources Planning and Management* 144.1 (2017), p. 04017075.

[47] T. Janus and B. Ulanicki. "Improving Stability of Electronically Controlled Pressure-Reducing Valves through Gain Compensation". In: *Journal of Hydraulic Engineering* 144.8 (2018), p. 04018053.

[48] A. Campisano, E. Creaco, and C. Modica. "RTC of valves for leakage reduction in water supply networks". In: *Journal of Water Resources Planning and Management* 136.1 (2009), pp. 138–141.

[49] A. Campisano, C. Modica, and L. Vetrano. "Calibration of proportional controllers for the RTC of pressures to reduce leakage in water distribution networks". In: *Journal of Water Resources Planning and Management* 138.4 (2011), pp. 377–384.

[50] A. Campisano et al. "Field-oriented methodology for real-time pressure control to reduce leakage in water distribution networks". In: *Journal of Water Resources Planning and Management* 142.12 (2016), p. 04016057.

[51] E. Creaco and M. Franchini. "A new algorithm for real-time pressure control in water distribution networks". In: *Water Science and Technology: Water Supply* 13.4 (2013), pp. 875–882.

[52] E. Creaco and T. Walski. "Economic Analysis of Pressure Control for Leakage and Pipe Burst Reduction". In: *Journal of Water Resources Planning and Management* 143.12 (2017), p. 04017074.

[53] G. Cembrano et al. "Optimal control of a water distribution network in a supervisory control system". In: *Control engineering practice* 8.10 (2000), pp. 1177–1188.

[54] C. Ocampo-Martinez et al. "Application of predictive control strategies to the management of complex networks in the urban water cycle [Applications of Control]". In: *IEEE Control Systems* 33.1 (2013), pp. 15–41. ISSN: 1066-033X.

[55] C. Ocampo-Martinez et al. “Hierarchical and decentralised model predictive control of drinking water networks: Application to barcelona case study”. In: *IET control theory & applications* 6.1 (2012), pp. 62–71.

[56] J.M. Grosso et al. “Chance-constrained model predictive control for drinking water networks”. In: *Journal of process control* 24.5 (2014), pp. 504–516.

[57] J. M. Grosso et al. “Stochastic model predictive control approaches applied to drinking water networks”. In: *Optimal Control Applications and Methods* 38.4 (2017), pp. 541–558.

[58] J.M. Grosso et al. “On the Assessment of Tree-Based and Chance-Constrained Predictive Control Approaches applied to Drinking Water Networks”. In: *IFAC Proceedings Volumes* 47.3 (2014). 19th IFAC World Congress, pp. 6240 –6245. ISSN: 1474-6670.

[59] R. Toro et al. “Tuning of Predictive Controllers for Drinking Water Networked Systems”. In: *IFAC Proceedings Volumes* 44.1 (2011). 18th IFAC World Congress, pp. 14507 –14512. ISSN: 1474-6670.

[60] E. Creaco. “Exploring Numerically the Benefits of Water Discharge Prediction for the Remote RTC of WDNs”. In: *Water* 9.12 (2017), p. 961.

[61] P. R. Page, A. M. Abu-Mahfouz, and S. Yoyo. “Parameter-less remote real-time control for the adjustment of pressure in water distribution systems”. In: *Journal of Water Resources Planning and Management* 143.9 (2017), p. 04017050.

[62] G. Galuppini et al. “Service pressure regulation in water distribution networks”. In: *Control Engineering Practice* 86 (2019), pp. 70–84.

[63] V. L. Streeter, E. B. Wylie, and K. W. Bedford. *Fluid mechanics, WCB*. 1998.

[64] E. Creaco et al. “Unsteady flow modeling of pressure real-time control in water distribution networks”. In: *Journal of Water Resources Planning and Management* 143.9 (2017), p. 04017056.

[65] B. Ulanicki and P. Skworcow. “Why PRVs tends to oscillate at low flows”. In: *Procedia Engineering* 89 (2014), pp. 378–385.

[66] T. Janus and B. Ulanicki. “Hydraulic modelling for pressure reducing valve controller design addressing disturbance rejection and stability properties”. In: Elsevier. 2017.

[67] J.E. Van Zyl and A.M. Cassa. “Modeling elastically deforming leaks in water distribution pipes”. In: *Journal of Hydraulic Engineering* 140.2 (2013), pp. 182–189.

[68] G. Pezzinga. “Evaluation of unsteady flow resistances by quasi-2D or 1D models”. In: *Journal of Hydraulic Engineering* 126.10 (2000), pp. 778–785.

[69] C. Ciaponi et al. “Procedure for defining a pressure-outflow relationship regarding indoor demands in pressure-driven analysis of water distribution networks”. In: *Water resources management* 29.3 (2015), pp. 817–832.

[70] L. Magni and R. Scattolini. *Advanced and multivariable control*. Pitagora, 2014.

[71] D.A. Recker et al. “Adaptive nonlinear control of systems containing a deadzone”. In: *Decision and Control, 1991., Proceedings of the 30th IEEE Conference on*. IEEE. 1991, pp. 2111–2115.

[72] M. Tian, G. Tao, and Y. Ling. “Adaptive dead-zone inverse for nonlinear plants”. In: *Decision and Control, 1996., Proceedings of the 35th IEEE Conference on*. Vol. 4. IEEE. 1996, pp. 4381–4386.

[73] S.W. Su et al. “Model predictive control of gantry crane with input nonlinearity compensation”. In: *International Conference on Control, Automation and Systems Engineering*. World Academy of Science, Engineering and Technology. 2009.

[74] M. Liñán and W.P. Heath. “Controller structure for plants with combined saturation and deadzone/backlash”. In: *Control Applications (CCA), 2012 IEEE International Conference on*. IEEE. 2012, pp. 1394–1399.

[75] H. Zabiri and Y. Samyudia. “A hybrid formulation and design of model predictive control for systems under actuator saturation and backlash”. In: *Journal of Process Control* 16.7 (2006), pp. 693–709.

[76] M. Herceg, M. Kvasnica, and M. Fikar. “Minimum-time predictive control of a servo engine with deadzone”. In: *Control Engineering Practice* 17.11 (2009), pp. 1349–1357.

[77] F. Borrelli, A. Bemporad, and M. Morari. *Predictive control for linear and hybrid systems*. Cambridge University Press, 2017.

[78] H. Zabiri and Y. Samyudia. “MPC design for constrained multivariable systems under actuator backlash”. In: *IFAC Proceedings Volumes* 37.9 (2004), pp. 643–648.

[79] M. Liñán and W.P. Heath. “Backlash compensation for plants with saturating actuators”. In: *Proceedings of the Institution of Mechanical Engineers, Part I: Journal of Systems and Control Engineering* (2017), p. 0959651817692471.

[80] M. Liñán and W.P. Heath. “MPC for plants subject to saturation and deadzone, backlash or stiction”. In: *IFAC Proceedings Volumes* 45.17 (2012), pp. 418–423.

[81] G. Galuppini, L. Magni, and D. M. Raimondo. “Model predictive control of systems with deadzone and saturation”. In: *Control Engineering Practice* 78 (2018), pp. 56–64.

[82] *Makeblock website*. `http://www.makeblock.com/`. Accessed: 2018-05-7.

[83] W. Leonhard. *Control of electrical drives*. Springer Science & Business Media, 2012.

[84] A. Alessio and A. Bemporad. “A survey on explicit model predictive control”. In: *Nonlinear model predictive control*. Springer, 2009, pp. 345–369.

[85] A. Bemporad et al. “The explicit linear quadratic regulator for constrained systems”. In: *Automatica* 38.1 (2002), pp. 3–20.

[86] IBM ILOG CPLEX. “V12. 1: User’s Manual for CPLEX”. In: *International Business Machines Corporation* 46.53 (2009), p. 157.

[87] A. et al. Makhorin. *GLPK (GNU linear programming kit)*. 2008.